UNIVERSITÀ DEGLI STUDI DI MILANO

Scuola di Dottorato in Fisica, Astrofisica e Fisica Applicata

Dipartimento di Fisica

Corso di Dottorato in Fisica, Astrofisica e Fisica Applicata

Ciclo XXVI

Di-tau topologies at ATLAS:
preparatory studies and search for Higgs boson decays
to two tau leptons during LHC Run-I

Settore Scientifico Disciplinare FIS/01-FIS/04

Supervisore: Dottoressa Donatella CAVALLI

Co-supervisore: Professor Attilio ANDREAZZA

Coordinatore: Professor Marco BERSANELLI

Tesi di Dottorato di:

Sofia Maria CONSONNI

Anno Accademico 2012-2013

Cover illustration:

ATLAS experiment event displays illustrating the subjects of this thesis.
An event with two hadronically decaying tau lepton candidates [1] is shown on the top left. Calorimeter energy deposits are clearly visible in the Electromagnetic (green) and Hadronic (red) calorimeters. On the bottom left an event with a secondary vertex in the Pixel detector [2]. On the top right a $Z \to \tau_\mu \tau_{\mathrm{had}}$ candidate event [3] and a VBF $H \to \tau_e \tau_{\mathrm{had}}$ candidate event [4] on the bottom right.

Contents

Introduction

The phenomenology of elementary particles and of their interactions is described by the Standard Model, which has a tremendous success in accounting for and predicting experimental observations. The explanation of the origin of particle masses has however long been a problem, with the most plausible natural solution, a mechanism proposed by Brout, Englert and Higgs in 1964, not experimentally confirmed for almost fifty years.

The fundamental phenomenological prediction of this mechanism is the existence of a further fundamental particle, the Higgs boson. Its discovery by the ATLAS and CMS collaborations in July 2012 is therefore a milestone in High Energy Physics and has marked the beginning of an intense campaign of characterisation of this new particle.

The study of the Higgs boson decay into two tau leptons in particular is of uttermost interest. Despite being experimentally challenging, the Higgs to two taus decay channel ($H \rightarrow \tau^+\tau^-$) offers in fact the best sensitivity to fundamental aspects of the theoretical predictions, such as the coupling of the Higgs Boson to fermionic particles. Moreover di-tau channels cover a fundamental role in extended Higgs sectors predicted in scenarios beyond the Standard Model.

The study of di-tau topologies is therefore a very important part of the physics program of the ATLAS experiment, operating at the Large Hadron Collider (LHC) at CERN. In this thesis several aspects of the study of di-tau topologies at ATLAS during Run-I are covered, ranging from preparatory studies to the actual search for $H \rightarrow \tau^+\tau^-$ decays. The thesis is organized as follows.

Chapter 1 is dedicated to an introductory overview of the Standard Model of elementary particles and their interactions, giving already emphasis to aspects that are relevant to the studies presented afterwards. An introduction to the Brout-Englert-Higgs mechanism and to Higgs boson phenomenology is given, together with a review of the discovery and measured properties results. The relevance of the study of the $H \rightarrow \tau^+\tau^-$ channel in this picture is shortly discussed as well.

Chapter 2 is made up of two main parts. The first one is dedicated to the description of the LHC collider and of the ATLAS experiment at CERN, together with the characteristics of the pp collision datasets collected during LHC Run-I. The second part gives an overview of the ATLAS event reconstruction techniques and of their performance. Even in this case emphasis is put on those aspects that are relevant to studies presented in this thesis.

In Chapter 3 a description of the main features of Higgs boson production and of its decay to two tau leptons is given. The description concentrates on the semileptonic channel, where one of the two tau leptons decays into a fully leptonic final state and the other to hadrons and a tau neutrino ($H \rightarrow \tau_{\mathrm{lep}}\tau_{\mathrm{had}}$), that is the topic of this work. The problem of mass reconstruction for this type of events is dealt with, presenting the results of the validation and preliminary studies for the improvement of a reconstruction algorithm employing the knowledge of the tau lepton decay kinematics that indicate possible improvements in mass resolution. Backgrounds in the search for $H \rightarrow \tau_{\mathrm{lep}}\tau_{\mathrm{had}}$ are described.

Chapter 4 describes the first ATLAS physics measurement in a di-tau topology: the $Z \rightarrow \tau^+\tau^-$ cross-section was measured in data collected during 2010. This measurement is particularly important since it was the first general rehearsal for di-tau searches at ATLAS. Methodology and theory uncertainty related aspects are described into detail. The $Z \rightarrow \tau^+\tau^-$ cross-section was measured with a total uncertainty of 10% and found to be in agreement with the Standard Model expectation as well as to measurements in other channels and in the CMS experiment.

In Chapter 5 and 6 my contributions to the reconstruction of hadronically decaying tau leptons are described. Hadronic tau decays are very important since they appear in $\sim 85\%$ of di-tau decays. They are reconstructed and identified in ATLAS making use of both tracking and calorimeter information.

Chapter 5 concentrates on tracking aspects, and in particular on the reconstruction of the particle passage point in the ATLAS Pixel detector. The performance on this aspect plays a key role in obtaining accurate track impact parameter and secondary vertex information, which is in turn used by identification algorithms of hadronically decaying tau leptons. The emphasis is put on the calibration and performance of the Pixel detector charge sharing algorithm and on the validation of a novel neural network clustering approach, which allowed improvements in the particle passage point resolution of up to $\sim 40\%$ in the best cases.

Chapter 6 instead is dedicated to the description of the energy calibration of hadronically decaying tau leptons. An overview of the calibration approach used during Run-I is given, together with a summary of the baseline uncertainty determination in 2011. An in-situ method used for the determination of the energy scale uncertainty is then presented, which allowed in 2011 to cross-check the pseudorapidity intercalibration of the tau energy scale within 3%.

Finally Chaper 7 gives an account of the method and expected results of a cut-based analysis for the search of $H \rightarrow \tau_{\mathrm{lep}}\tau_{\mathrm{had}}$. This analysis is intended as a support to the ATLAS $H \rightarrow \tau^+\tau^-$ analysis using multivariate techniques, and was developed in a continuous cross-talk with it. The ATLAS multivariate analysis has recently provided preliminary results with a $\sim 4\sigma$ evidence for the existence of $H \rightarrow \tau^+\tau^-$ decays. The analysis presented here has a lower sensitivity, since a more conservative cut-based approach was used and only the semilptonic channel, one of the possible $H \rightarrow \tau^+\tau^-$ decay channels, was covered. It has an expected $\sim 1.8\sigma$ sensitivity to a SM Higgs boson at $m_H = 125\,\mathrm{GeV}$.

The Standard Model of fundamental interactions

The present understanding of matter and forces is phenomenologically described by the Standard Model of fundamental interactions (SM). The SM has been developed during the last century within the context of gauge quantum field theories. Both matter and forces are described by means of a reasonably limited number of fields. The quanta of these fields are particles, which at present are believed to be fundamental. The SM has had an enormous success in explaining several phenomena, and its predictions are tested to precisions of down to 10^{-5} or more at the scales reached by experiments ($\sqrt{s} = 8$ TeV). A fundamental part of the SM is the spontaneous symmetry breaking mechanism responsible for the generation of the masses of particles, the Brout-Englert-Higgs mechanism (BEH). A key prediction of the SM as a consequence of the introduction of this mechanism is the existence of a massive scalar boson, the Higgs boson. This prediction has found its experimental confirmation in 2012-2013 in the measurements performed by the ATLAS and CMS experiments, operating at the Large Hadron Collider (CERN). The characteristics of the newly discovered boson are compatible with those predicted for the SM Higgs boson, but still many aspects need to be investigated, in particular the coupling to fermions. One of the most promising channels for the study of Higgs boson decays to fermions is the decay to pair of tau leptons, $H \rightarrow \tau^+ \tau^-$.

1.1 Standard Model basics

In this section a basic introduction to the SM is given. The Gauge Principle is explained to a larger extent, since the BEH mechanism was introduced to maintain the gauge theory nature of the SM.

1.1.1 Matter and fermion fields

In the SM matter is described by three families (or generations) of fermionic fields (spin $1/2$). Each family comprises two quarks and two leptons. Quarks interact strongly and, in ordinary matter, they are found only within bound states called hadrons, such as the proton and neutron that make up atomic nuclei. Leptons do not interact strongly, and can be found free or loosely bound, such as the electron in the atomic nucleus. Each fundamental fermion has its own anti-particle, which has the same characteristics except additive quantum numbers are opposite. Between families there exists a mixing

mechanism, which allows couplings between particles from different families. This is formalised by means of the CKM mixing matrix [5]. A scheme of the basic properties of fundamental fermions is shown in Table 1.1.

Fermions	Families			Electric Charge	Interactions
	1st	2nd	3rd	(e)	
Quarks	u	c	t	$+2/3$	Strong
					Weak
	d	s	b	$-1/3$	Electromagnetic
Leptons	ν_e	ν_μ	ν_τ	0	Weak
	e^-	μ^-	τ^-	-1	Weak and E.M.

Table 1.1: Elementary fermions in the SM.

Fermionic fields are observed to have symmetry properties, which are the key to our present understanding of the phenomenology of elementary particles.

1.1.2   The Gauge Principle

Symmetry involves the invariance of the system under a certain transformation. This can act on the field in the same way at all space-time points or in a different way. In the first case the transformation is called *global*, in the latter *local*. Global transformations though are somewhat unnatural, since they involve correlations between space-time points that are not causally connected. Therefore the introduction of a further field, that allows to preserve the invariance under the local transformation, is assumed as a good principle to build a physically meaningful theory. This principle takes the name of *gauge principle*, and theories built basing on it are *gauge theories*. Furthermore, gauge theories benefit from properties that make them very appealing for building a model of fundamental interactions. One of them is renormisability. In gauge theories divergences appearing in the calculations can systematically be eliminated. A nice example of the application of the *gauge principle* can be found in Quantum Electrodynamics (QED). In the classical theory the gauge invariance of electromagnetism comes as a consequence of Maxwell equations. This point of view can be reversed using the *gauge principle* so that electromagnetism arises naturally from the free theory. The free theory considered is that of a massless spin $1/2$ field, $\hat{\psi}$, described by the Lagrangian

$$\mathcal{L} = \bar{\hat{\psi}} i \gamma_\mu \partial_\mu \hat{\psi} \tag{1.1}$$

This Lagrangian displays a global U(1) symmetry, that is, it is invariant under the transformation

$$\hat{\psi}(\mathbf{x}, t) \rightarrow \hat{\psi}'(\mathbf{x}, t) = e^{-ieQ\hat{\chi}} \hat{\psi}(\mathbf{x}, t) \tag{1.2}$$

where $\hat{\chi} = \chi \mathbb{1}$, and χ is a real constant.

Asking for the system to be invariant under the local transformation, that is with $\chi = \chi(\mathbf{x}, t)$, it is necessary to make the replacement

$$\partial^\mu \to D^\mu = \partial^\mu + ieQ\hat{A}^\mu \tag{1.3}$$

with the new quantized field $\hat{A}^\mu$ transforming as

$$\hat{A}^\mu \to \hat{A}'^\mu = \hat{A}^\mu + \partial^\mu \chi \tag{1.4}$$

With this replacement the Lagrangian gains an extra term, that accounts for the electromagnetic coupling

$$\mathcal{L}_{\text{int}} = -eQ\bar{\hat{\psi}}\gamma_\mu\hat{\psi}\hat{A}^\mu \tag{1.5}$$

where e is the electromagnetic constant, related to the fine structure constant, and Q is the charge quantum number of the fermion field. One then needs just to add the kinetic term for the electromagnetic field to get the full Lagrangian that describes the behaviour of the spin $1/2$ matter field, of the spin 1 massless electromagnetic field and of their vectorial coupling.

The quantum of the electromagnetic field is the photon, and the electromagnetic interaction can be interpreted as the exchange of these quanta.

1.1.3   The Standard Model as a gauge theory: the gauge bosons

The SM is built in a way analogous to what has been outlined for QED. The symmetry underlying the SM is $\mathrm{SU}(3) \times \mathrm{SU}(2) \times \mathrm{U}(1)$. The $\mathrm{SU}(3)$ component of the theory is Quantum Chromodynamics (QCD), that describes strong interactions. The bosons arising when making the symmetry local take the name of gluons (g). The $\mathrm{SU}(2) \times \mathrm{U}(1)$ component instead is the electroweak model, which gives a unified description of electromagnetic and weak forces. The gauge bosons in this case are four. One is the photon (γ), the other three are massive vector bosons, $W^\pm$ and Z. Table 1.2 shows the gauge bosons present in the SM. More details about QCD and the electroweak model will be given in the next Sections 1.2, 1.3 and are nicely reviewed in Ref. [6], for what concerns the model itself, and Ref. [7] for its experimental foundations.

Interactions	Gauge Bosons	Electric charge	Mass (GeV)
Electromagnetic	Photon (γ)	0	$< 1 \times 10^{-18}$ eV
Weak	Vector Boson $W^\pm$	± 1	80.385 ± 0.015
	Vector Boson Z	0	91.1876 ± 0.0021
Strong	Gluons (g)	0	0

Table 1.2: Gauge bosons in the SM, mass values are taken from Ref. [8].

1.2   Quantum Chromodynamics selected topics

Quantum Chromodynamics is the gauge theory that describes strong interactions. It takes its name from the colour quantum number, which characterises the $SU(3)$ symmetry driving the dynamics. The only fermions carrying colour are quarks. Gluons carry colour too, and can therefore interact with each other. As a consequence of this fact the strong force has a short range.

A few topics in QCD, in particular related to physics at hadron colliders and that will be relevant in the following are outlined in Sections 1.2.1-1.2.4. Hadronic tau decays, that are obviously important in the context of this work, are instead treated separately in Sec. 1.6.1.
A useful review of QCD topics can be found in Ref. [8].

1.2.1   Running coupling

In the regimes of greatest interest at hadron colliders, and in particular of this work, it is convenient to treat QCD perturbatively. In this context observables are expressed in terms of the renormalized coupling $\alpha_s(\mu_R)$, where μ_R is an unphysical renormalisation scale. The renormalised coupling satisfies renormalisation group equations, that at first order have an analytic solution

$$\alpha_s(\mu_R^2) = \frac{12\pi}{(33 - 2n_f)} \cdot \left(\ln\left(\frac{\mu_R^2}{\Lambda^2}\right)\right) \tag{1.6}$$

where n_f is the number of fermions in the theory and Λ and energy scale parameter measured to be of order $\Lambda \sim 250\,\text{MeV}$. When one takes μ_R close to the scale of the momentum transfer Q in a given process, $\alpha_s(\mu_R^2 = Q^2)$ is indicative of the effective strength of the strong interaction in that process. Figure 1.1 shows the most recent theoretical predictions for $\alpha_s(\mu)$ and the measured values at various process scales μ.
The form of Equation 1.6 and the predictions shown in Figure 1.1 are among the greatest successes of QCD, because they allow to explain the behaviour of quarks at different scales. For small values of μ^2, $\alpha_s(\mu)$ becomes large. As a consequence the energy necessary to separate two coloured particles increases with their distance. This explains the phenomenon of confinement of the coloured quarks and gluons within hadrons. In the opposite regime, where μ^2 is large and the distance scale is small, quarks and gluons exhibit the behaviour known as asymptotic freedom. This behaviour is experimentally observed when probing the nucleon constituents in deep inelastic scattering experiments.

1.2.2   The parton model of hadronic interactions

The picture of hadrons that emerges from deep inelastic scattering experiments is that of composite particles, made up by quasi-free constituents, that are referred to as partons, confined within the hadron itself. Partons are not only quarks that carry the quantum numbers of the hadron (valence quarks), but also a sea of gluons and quark-antiquark pairs. The interaction of two hadrons is therefore a complex process, and its description
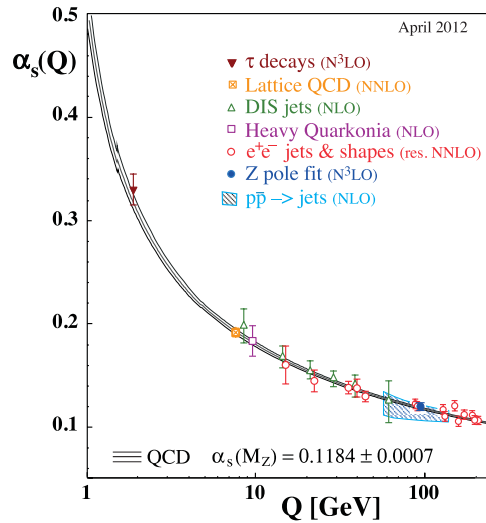
Figure 1.1: Summary of the values of $\alpha_s(\mu)$ at the μ values they are measured. The line shows the PDG average QCD prediction and the coloured band the $\pm\sigma$ limits. [8].

strongly depends on the scale at which it occurs. At the LHC the most interesting regime is that of large momentum transfers, where the interaction can be described, as a first approximation, as a parton-parton process. Since the centre-of-mass energy is large, the colliding protons can be described as collimated beams of partons, each one carrying a fraction x_i of the proton four-momentum p.

Parton density functions $f_i(x, \mu_F)$ describe the probability of finding parton i with four-momentum fraction between x and $x + dx$. The parton density functions (PDFs) depend on an arbitrary factorisation scale μ_F. This scale can be intuitively understood as the scale up to which emissions from the parton are absorbed in the PDFs. Such emissions are interpreted as a modification in the proton structure rather than part of the hard scattering process.

PDFs can not be calculated in perturbative QCD, and are therefore derived from fits to experimental data. Various approaches to the problem of extracting the PDFs exist, and this leads to different PDF sets. The most widespread used PDFs at the LHC are derived by the CTEQ [9], NNPDF [10], HERAPDF and MRS/MRST/MSTW [11] groups.

In this framework the inclusive production cross-section [1] of a particle A, $\sigma(h_1h_2 \rightarrow$

---

[1] In a purely mechanical context the rate of collision of point-like particles against an extended target is given by the flux of particles per unit area times the projection of the area perpendicular to the beam direction (cross-section). In high energy physics the concept of cross-section is extended from the purely geometrical one, and rather describes the physics of the interaction. The typical unit of cross-section is the *barn*(b), with $1b = 10^{-24} cm^2$. The rate of a process is given by the product of its cross-section times the beams instantaneous luminosity. If the instantaneous luminosity is integrated over time the total number of events can be obtained.

$A + X$) can be written as

$$\sigma(pp \to A+X) = \sum_{n=0}^{\infty} \alpha_s^n(\mu_R^2) \sum_{i,j} \int dx_1 dx_2 f_i(x_1, \mu_F^2) f_j(x_2, \mu_F^2) \times \widehat{\sigma}_{i,j \to A+X}^{(n)}(x_1 x_2 s, \mu_R^2, \mu_F^2)$$

$$(1.7)$$

where x_1 and x_2 are the four-momentum fractions of the interacting partons with respect to the parent hadron, the i and j indices run on all types of partons, and $\widehat{\sigma}$ is the cross-section of the relevant partonic process, that depends on the energy in the centre-of-mass of the two partons $\sqrt{x_i^a x_i^a s}$, and on the factorisation scale μ_F. The partonic cross-section depends on the renormalisation scale, as we have seen in the previous section for the coupling constant. The total cross-section does not depend on the renormalisation and factorisation scales. However if only N terms of the perturbative series, represented by the sum over the n index, are available, residual μ_R and μ_F dependences survive. Variations of the μ_R and μ_F scales allow to make estimates of the uncertainties on the predictions due to missing higher order terms.

1.2.3   Exclusive observables

Experiments do not observe partons, but rather hadronic final states, and many useful observables may have an exclusive character. This leads to some difficulties, that need specific care and tools to be met.

The first difficulty is related to the fact that in QCD calculations divergences appear in the limit where a soft or collinear additional particle is emitted. These divergences need to cancel in the calculation in order to yield a finite and physical result.
In perturbative fixed-order calculations, when going beyond the leading order (LO), the cancellation occurs only for infrared and collinear safe variables. These variables satisfy the property of not being changed by the addition of an infinitely soft or collinear particle in the final state. Interesting observables moreover may implicitly involve a veto on a part of the phase space, allowing only for partial cancellation of the divergences, and causing each α_s order to be accompanied by large logarithmic coefficients. The appearance of such logarithms can lead to poor convergence of the perturbative series, and therefore to an unreliable calculation. In these cases it may be possible to perform *resummed* calculations, that account for the dominant logarithmically enhanced terms to all orders in α_s.

The second difficulty arises from the fact experiments are often interested in observables depending on the details of the hadronic final state, for example when simulating the detector response to QCD events. Fully exclusive simulations of QCD events can be achieved making use of parton-shower Monte Carlo generators. In these generators the simulation of a chosen $2 \to 2$ hard-scattering process is followed by a *parton-shower* (PS). Gluon emissions or gluon splittings ($g \to q\bar{q}$) are generated, each at a scale lower than the previous one, following a distribution predicted by QCD. The shower can be continued down to a chosen scale where a *hadronisation model* can be used to convert partons into hadrons. The behaviour of the remnants of the incoming hadrons, the *underlying event*, is typically modelled by additional $2 \to 2$ scatterings.

Widespread used PS generators are PYTHIA6/8 [12, 13, 14], Herwig+Jimmy / Herwig++ [15, 16] and Sherpa [17]. Tunes for the modelling of the underlying event are usually taken care of directly by the experiments. Examples for the ATLAS experiment can be found in Refs. [18, 19]. Parton-shower Monte Carlo generators are extremely useful, but the shower may not provide the necessary accuracy in the prediction not only of exclusive observables but of simple detector acceptances as well. Schemes to match $2 \rightarrow n$ parton processes and NLO calculations with showers avoiding double counting exist and are implemented in programs publicly available. Examples of generators matched to a PS that are used in the following are ALPGEN [20], which is a multi-leg leading order generator, and MC@NLO [21] and POWHEG-BOX [22], that are next-to-leading order generators.

1.2.4 Jets

As a consequence of confinement, when a quark or gluon in a hadron undergoes a hard scattering process, it can not emerge as an isolated particle. The parton rather undergoes a hadronisation process, resulting in a jet of hadrons. The particles constituting the jet exhibit correlated kinematic properties, and therefore jets can be used as QCD probes. Moreover at hadron colliders interesting final states are often characterised by the presence of jets, which play therefore an important role for non strictly QCD measurements too.

In order to give a proper definition of a jet, that can be used to match predictions and measurements, both theory and experimental issues need to be considered. On the theory side a jet needs to be defined in an infrared and collinear safe way, be resilient to non-perturbative QCD effects, and be straightforward to implement in perturbative calculations. On the experimental side the requirements are that the jet final state should not be dominated by effects of efficiency, acceptance and resolution of the detector and it should be independent of the environment, in particular stable with luminosity. Moreover the jet definition should produce jets that are easy to calibrate, and allow for an efficient use of computational resources.

The jet-finding algorithms that best allow to preserve infrared and collinear safety are sequential recombination algorithms, and in particular the k_T family is the one of most widespread use at LHC experiments. The clustering is performed by choosing a distance measure between particles $d_{i,j}$ and between particles and the beam $d_{i,B}$

$$d_{ij} = \min(k_{ti}^{2p}, k_{tj}^{2p}) \frac{\Delta y^2 + \Delta \phi^2}{R^2} \tag{1.8}$$

$$d_{iB} = k_{ti}^{2p} \tag{1.9}$$

The distance measure depends on the particle transverse momentum k_t, its rapidity y and azimuthal angle ϕ. Moreover it is characterised by two parameters, p, that defines the algorithm and R, which is related to the typical jet size. The recombination starts from particles to form proto-jets. At each stage of the recombination proto-jets with smallest $d_{i,j}$ are recombined. If $d_{i,B}$ is smaller than any of the $d_{i,j}$ the proto-jet is taken

as a jet. Depending on the p parameter the algorithm has different properties. A relevant property of jets is the area, that quantifies the sensitivity to additional point-like or diffuse radiation. Different recombination jet algorithms are characterised by different behaviours of the area with, for example, the jet p_T. The jets of interest in this work are *anti-kt* jets, that is with $p = -1$. Anti-kt jets have the property of being approximately cones with constant radius R in (y, ϕ) space. Details on anti-kt jets can be found in Ref. [23], and a useful review of issues in jet physics can be found in Ref. [24]. Implementations used at LHC experiments are described in Refs. [25, 26].

1.3 Electroweak model selected topics

The electroweak model describes in a unified way electromagnetic and weak interactions. The relevant symmetry group is $SU(2)_L \times U_Y(1)$.

$SU(2)_L$ is the weak isospin group. The corresponding quantum numbers are the weak isospin T and the isospin third component T_3. The subscript "L" refers to the fact only left-handed particles couple to gauge boson. This property is encoded by assigning the left-handed and right-handed components of fermionic fields to different $SU(2)$ representations, and therefore assigning them different quantum numbers. The left- and right-handed components are defined as

$$\Psi_L = \frac{1 - \gamma_5}{2} \Psi \qquad \Psi_R = \frac{1 + \gamma_5}{2} \Psi \qquad (1.10)$$

where γ_5 is the chirality matrix.

The quantum number describing the couplings to the $U_Y(1)$ generators is the hypercharge Y, which is related to the electric charge and the third isospin component by the Gell-Mann Nijshima formula

$$Q = T_3 + \frac{Y}{2} \qquad (1.11)$$

Quantum number assignments to SM particles are summarised in Table 1.3.

Particle	T	T_3	Y	Q
$\nu_e \, \nu_\mu \, \nu_\tau$ left	$\frac{1}{2}$	$\frac{1}{2}$	-1	0
Negative charge $e \, \mu \, \tau$ left	$\frac{1}{2}$	$-\frac{1}{2}$	-1	-1
Negative charge $e \, \mu \, \tau$ right	0	0	-2	-1
$u \, c \, t$ left	$\frac{1}{2}$	$\frac{1}{2}$	$\frac{1}{3}$	$\frac{2}{3}$
$u \, c \, t$ right	0	0	$\frac{4}{3}$	$\frac{2}{3}$
$d \, s \, b$ left	$\frac{1}{2}$	$-\frac{1}{2}$	$\frac{1}{3}$	$-\frac{1}{3}$
$d \, s \, b$ right	0	0	$-\frac{2}{3}$	$-\frac{1}{3}$

Table 1.3: Quantum number assignments to the SM fermions. T is the weak isospin, T_3 the third isospin component, Y the hypercharge and Q the electric charge.

The charged $SU(2)_L$ generators are identified with the $W^\pm$ bosons. The neutral generators of $U(1)_Y$ and $SU(2)_L$ mix, and the actual physical states, the photon and the Z

boson, are superpositions of the generators. The mixing angle is the Weinberg angle θ_W, that allows to relate the $U(1)_Y$ and $SU(2)_L$ coupling constants, g' and g respectively

$$\sin \theta_W = \frac{g}{\sqrt{g^2 + g'^2}} \qquad \cos \theta_W = \frac{g'}{\sqrt{g^2 + g'^2}} \qquad (1.12)$$

$$e = g \sin \theta_W \qquad \frac{G_F}{\sqrt{2}} = \frac{g^2}{8m_W^2} \qquad (1.13)$$

to the constants describing the electromagnetic and weak interactions at low energy, e and G_F. The Weinberg angle was measured in a number of experiments and the world average for the sine of the effective angle is [8]

$$\sin^2 \theta_W = 0.23146(12) \qquad (1.14)$$

In the following a few selected topics in the context of the electroweak model are outlined. The problem of masses is at the origin of the introduction of the BEH mechanism in the SM, described later in Section 1.4.1. The properties of the Z boson are introduced since their precise measurements are among the strongest tests of the SM. Moreover, the study of the $Z \to \tau^+\tau^-$ process is a benchmark for the search of $H \to \tau^+\tau^-$. Z boson production processes at hadron colliders are therefore introduced as well.

1.3.1 Gauge boson and fermion masses

The phenomenology of weak interactions has long been described as a four-fermion point interaction with coupling constant [8]

$$\frac{G_F}{(\hbar c)^3} = 1.1663787(6) \times 10^{-5} \, \text{Gev}^{-2} \qquad (1.15)$$

This theory due to Fermi is able to accurately predict the phenomenology of β-decays. Comparing the couplings predicted by the Fermi theory, it is possible to obtain a prediction for the masses of the weak gauge bosons

$$m_W^2 = \frac{\pi \alpha}{\sqrt{2} \sin^2 \theta_W G_F} \qquad m_Z^2 = \frac{m_W^2}{\cos^2 \theta_W} \qquad (1.16)$$

This prediction was formulated before the actual discovery of the W and Z, and the match with the experimental measurements was a great impulse to the credibility of the electroweak model. So, unlike gluons and photons, the $W^\pm$ and Z bosons are massive. This poses and important problem, since in local gauge theories gauge bosons are predicted to be massless.

A problem with masses arises for what concerns fermions as well. Ordinary mass terms would in fact look like

$$\Delta \mathcal{L} = -m \left(\overline{f}_L f_R + \overline{f}_R f_L \right) \qquad (1.17)$$

Since f_L and f_R belong to different $SU(2)$ representations such term would violate global gauge invariance, and is therefore forbidden.

1.3.2   The Z boson: properties and Standard Model tests

The Z boson was discovered shortly after the W bosons in 1983 by the UA1 and UA2 experiments at the CERN $\mathrm{Sp\bar{p}S}$ collider [27, 28], and was rapidly characterised as being the Z boson predicted by the SM.

By the beginning of the '90s very high precision measurements became available from the experiments at the LEP e^+e^- collider at CERN (Aleph, Delphi, L3, Opal) and the SLD experiment at the SLC (SLAC) [29]. The large amount of data accumulated allowed to test to high precision the electroweak sector of the SM. In particular very high precision measurements were made of the Z boson mass, m_Z, its width Γ_Z, its coupling to fermions and the effective mixing angle for fermions $\sin^2\theta_W$.

The Z boson couplings to fermions are a combination of the $U_Y(1)$ and $SU(2)_L$ couplings, determined by the fermion quantum numbers and $\sin^2\theta_W$. The couplings are different for the left and right fermion components

$$g_L = T_3 - Q\sin^2\theta_W \qquad g_R = -Q\sin^2\theta_W \tag{1.18}$$

One can derive expressions for the axial and vector part of the coupling as well

$$g_V = T_3 - 2Q\sin^2\theta_W \qquad g_A = T_3 \tag{1.19}$$

Results of precision measurements at the Z peak are shown in Table 1.4. Figure 1.2 shows the experimental evidence that fixes the values of the axial coupling g_A and vector coupling g_V of the Z to the leptons.

Observable	Measurement	Standard Model Prediction
m_Z (GeV)	91.1875 ± 0.0021	91.1874 ± 0.0021
Γ_Z (GeV)	2.4952 ± 0.0023	2.4965 ± 0.0015
σ^0_{had} (nb)	41.540 ± 0.037	41.481 ± 0.014
R^0_l	20.767 ± 0.025	20.739 ± 0.018

Table 1.4: Properties of the Z boson as measured at LEP and SLC. m_Z is the Z boson mass, Γ_Z is the total Z width, σ^0_{had} is the peak cross-section for the production of a Z times the branching ratio for the decay to hadrons and R^0_l is the ratio of the partial width of the Z decaying to hadrons and a lepton pair. Figures are taken from Ref. [29].

The $Z \to \tau^+\tau^-$ process is the only process that allows to make measurements of the polarization of the Z boson decay products. At LEP the parameter $\sin^2\theta_W$ was measured exploiting the dependence of the tau polarisation on the cosine of the polar angle θ

$$\mathscr{P}_\tau(\cos\theta) = -\frac{\mathscr{A}_\tau(1+\cos^2\theta) + 2\mathscr{A}_e\cos\theta}{(1+\cos^2\theta) + 2\mathscr{A}_\tau\mathscr{A}_e\cos\theta} \tag{1.20}$$

where

$$\mathscr{A}_{\tau,e} = \frac{2g_{V\,\tau,e}\,g_{A\,\tau,e}}{g^2_{V\,\tau,e} + g^2_{A\,\tau,e}} \tag{1.21}$$
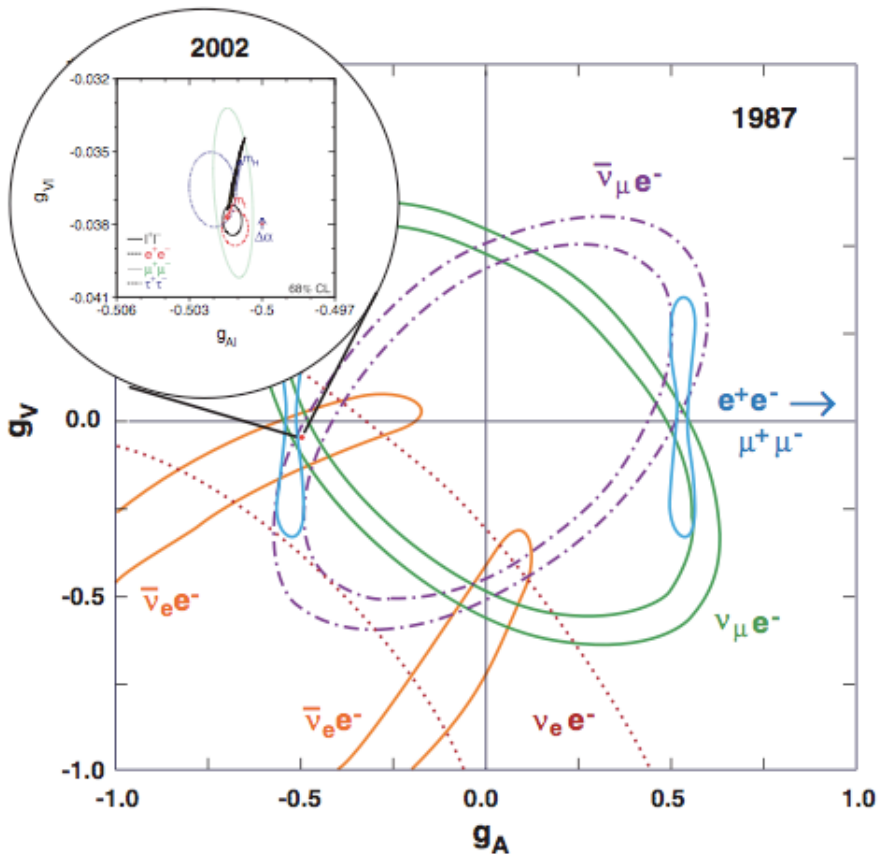
Figure 1.2: Values of the axial and vector part of the couplings of leptons to the Z. The big box shows the results of pre-LEP data from neutrino scattering and e^+e^- annihilation experiments, as they available in 1987. In the circle on the left measurements made at LEP and SLD are shown on a scale expanded by a factor 65 [29].

This is one of most accurate measurements of $\sin^2\theta_W$. The results of the measurements of $\sin^2\theta_W$ are shown in Table 1.5

Including data from LEP-II and TEVATRON a global SM fit was performed (see Ref. [30] and references therein). The results of the fit, shown in Figure 1.3, mark the success of the SM in describing the phenomenology of elementary particles.

1.3.3 Z boson production and decay at hadron colliders

At hadronic machines the Z boson is produced through the Drell-Yan process; the relevant diagrams are displayed in Figure 1.4. The main production process is due to $q\bar{q}$ annihilation, but the production can happen accompanied by a strongly interacting parton in the final state, resulting in a jet. The predicted $Z \to \tau^+\tau^-$ cross-section at the LHC

Measurement	$\sin^2 \theta_W$
Pole forward-backward asymmetries with leptons	0.23117 ± 0.00054
Tau polarisation	0.23202 ± 0.00057
Polarised forward-backward asymmetries	0.23141 ± 0.00065
Pole forward-backward asymmetry with b flavours	0.23225 ± 0.00038
Pole forward-backward asymmetry with c flavours	0.2322 ± 0.0010
Hadronic charge asymmetry	0.2321 ± 0.0010
Left right asymmetries	0.23109 ± 0.00029
Average LEP + SLD	0.23157 ± 0.00018

Table 1.5: Measurements of $\sin^2 \theta_W$ at LEP and SLC. The single measurements are explained into detail in Ref. [30].
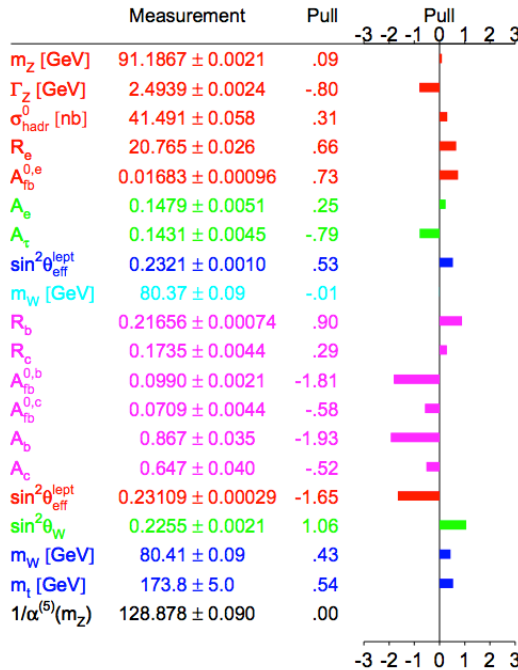

Figure 1.3: Results of the SM fit in Ref. [30].The pull is defined as the difference of the measurement and the Standard Model prediction.
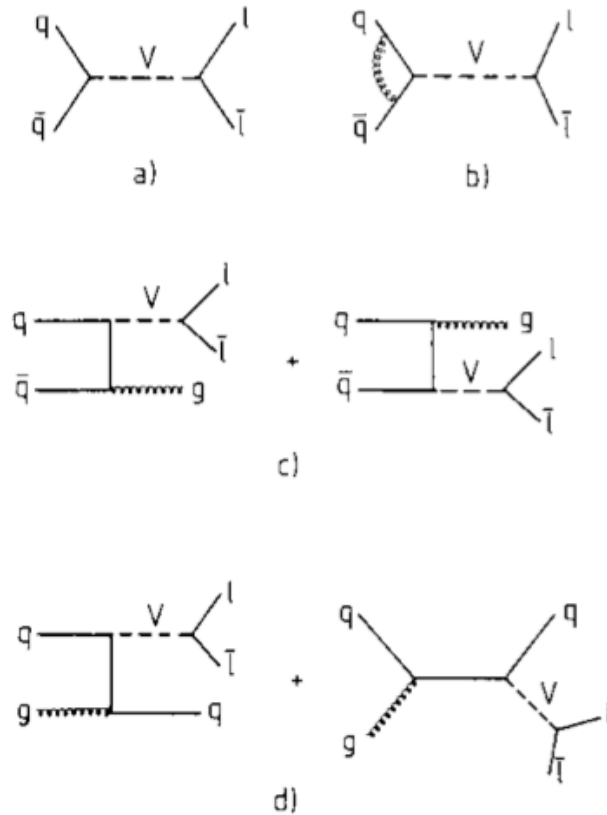
Figure 1.4: Feynman diagrams for the hadronic production of vector bosons V in QCD at LO and NLO. **(a)** Drell Yan (0th order), **(b)** QCD virtual correction, **(c)** QCD annhilation with gluon radiation, **(d)** QCD Compton process [31].

running at $\sqrt{s} = 7$ TeV and in an invariant mass window $[66, 116]$ GeV is 0.96 ± 0.05 nb [32, 33, 34]. The cross-section has been measured at LHC experiments by the ATLAS [35] and CMS [36, 37] collaborations. The results are shown in Figure 1.5(b) and are in good agreement with NNLO calculations.

The Z boson decays immediately after its production due to its large width. The detection therefore happens by the study of the decay products.
The main Z decay channels are shown in Table 1.6. The most favoured one is to a quark pair. At e^+e^- colliders this channel is accessible, but not at hadronic machines, due to the large background from QCD processes resulting in the production of jets. For the $Z \to \tau^+\tau^-$ channel the branching ratio is about 3.4%.
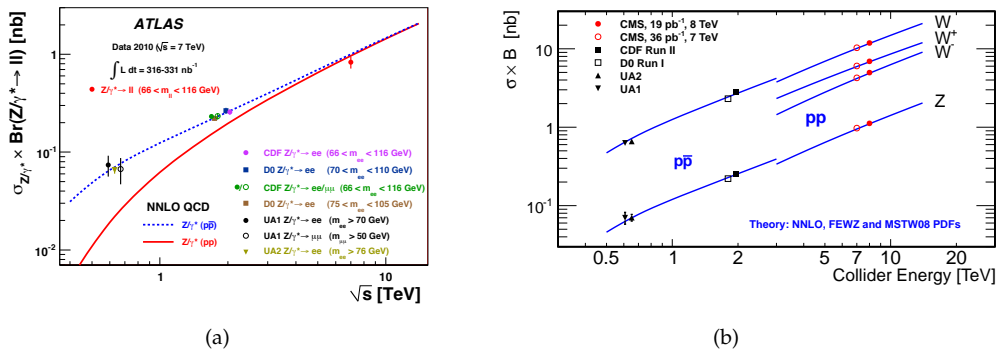
(a)

(b)

Figure 1.5: Inclusive Z boson production cross-sections as measured at the LHC by the (a) ATLAS [35] and CMS [36, 37] collaborations and at other hadron colliders, as a function of the centre-of-mass energy.

Decay mode	Fraction (Γ_i/Γ)
e^+e^-	$(3.363 \pm 0.004)\%$
$\mu^+\mu^-$	$(3.366 \pm 0.007)\%$
$\tau^+\tau^-$	$(3.370 \pm 0.008)\%$
l^+l^-	$(3.3658 \pm 0.0023)\%$
invisible	$(20.00 \pm 0.06)\%$
hadrons	$(69.91 \pm 0.06)\%$

Table 1.6: Main Z decay modes. Figures are taken from Ref. [8].

1.4 The Brout-Englert-Higgs mechanism and the Higgs boson

In the electroweak model there is an apparent problem with the masses of gauge vector bosons, as well as with the masses of fermions (see Sec. 1.3.1). The solution of these problems is provided in the SM by a minimal realisation of the mechanism first envisaged by Brout, Englert and Higgs in 1964. In Ref. [38] Brout and Englert first observed that gauge bosons can acquire a mass if the vacuum is degenerate with respect to the symmetry group of the theory, that is, when the symmetry is spontaneously broken. Higgs in Ref. [39, 40] showed that an essential feature of local gauge theories with spontaneous symmetry breaking is not only the appearance of masses for the gauge fields, but of massive scalar fields as well. The results of Higgs have been deepened by Guralnik, Hagen and Kibble in Ref. [41] and by Kibble in Ref. [42], who provided an extension to the case of non-Abelian gauge groups. Later on the mechanism was incorporated in the electroweak model [43, 44]. In the following a simple description of the realisation of the BEH mechanism in the SM is given. The phenomenology of the Higgs boson is then briefly summarised, before presenting the experimental evidences of its discovery and the first measurements performed by the ATLAS and CMS collaborations. Finally

the characteristics and relevance of the $H \to \tau^+\tau^-$ channel are discussed.

1.4.1 The mechanism and the Higgs boson

Spontaneous symmetry breaking arises in systems where the vacuum state is degenerate, such as a system with the potential illustrated in Figure 1.6. For these systems the Lagrangian is invariant under a certain symmetry operation, but the choice of a specific vacuum state among the possible ones, for which the field has a non-zero expectation value, causes a spontaneous breaking of the symmetry.
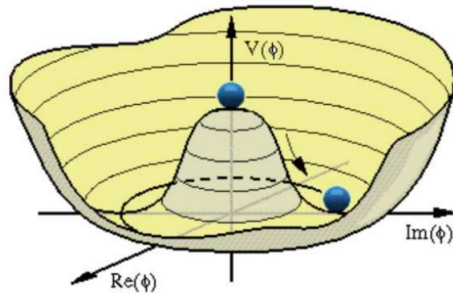

Figure 1.6: A prototypical effective 'mexican hat' potential that leads to spontaneous symmetry breaking [45].

In the SM just a new doublet of electrically neutral scalar fields, with hypercharge $Y = 1$ is introduced

$$\phi = \begin{pmatrix} \phi^+ \\ \phi^0 \end{pmatrix} \tag{1.22}$$

The Lagrangian for the doublet takes the form

$$\mathcal{L}_{\text{Higgs}} = (D_\mu \phi)^\dagger (D_\mu \phi) - V(\phi^\dagger \phi) \tag{1.23}$$

where the covariant derivative D_μ that appears in the kinetic term can be written as

$$D_\mu = i\partial_\mu - g\frac{\tau_a}{2}W_\mu^a - g'\left(-\frac{1}{2}\right)B_\mu \tag{1.24}$$

where B_μ is the gauge field of $U(1)_Y$, τ_a are the generators of $SU(2)_L$, and W_μ^a the correspondent fields. The potential that gives rise to the symmetry breaking is defined by two real parameters μ and λ

$$V(\phi^\dagger \phi) = -\mu^2 \phi^\dagger \phi + \lambda(\phi^\dagger \phi)^2 \tag{1.25}$$

A vacuum configuration is chosen as

$$\phi_0 = \frac{1}{\sqrt{2}} \begin{pmatrix} 0 \\ v \end{pmatrix} \tag{1.26}$$

The field can be expanded around this value

$$\phi = \frac{1}{\sqrt{2}} \begin{pmatrix} 0 \\ v + H(x) \end{pmatrix} \tag{1.27}$$

where the Higgs real valued field $H(x)$ appears. This particular expansion corresponds to a choice of gauge, the unitarity gauge, where the additional three degrees of freedom result absorbed by the gauge bosons.

Substituting this expression into Equation 1.23, mass terms appear, corresponding to

$$m_{W^\pm} = \frac{1}{2}vg \qquad m_Z = \frac{1}{2}v\sqrt{gg'^2} \qquad m_\gamma = 0 \tag{1.28}$$

The Higgs doublet has the right quantum numbers to allow for coupling terms of the form

$$-\lambda_e \left[(\nu_e, \bar{e})_L \begin{pmatrix} \phi^+ \\ \phi^0 \end{pmatrix} e_R + \bar{e}_R(\phi^-, \overline{\phi^0}) \begin{pmatrix} \nu_e \\ e \end{pmatrix}_L \right]$$

where the coupling costant λ_e is arbitrary and generates a mass term with $m_e = \lambda_e v/\sqrt{2}$. The same can be done for the other leptons and quarks. Terms mixing the families are allowed as well, so that the CKM matrix can be seen as a consequence of the BEH mechanism. The quantum of the scalar Higgs field is the Higgs boson, and the only additional free parameter added in the SM is its mass. The Higgs boson mass m_H is related to the potential parameter λ and vacuum expectation value v by

$$m_H = \sqrt{2\lambda}v \tag{1.29}$$

The couplings of the Higgs boson are determined once m_H is fixed, as a consequence production cross-sections and decay branching ratios can be determined as well. The couplings for the SM Higgs boson are, expressed in terms of the masses and of the vacuum expectation value,

$$g_{Hf\bar{f}} = \frac{m_f}{v} \qquad g_{HVV} = \frac{2m_V^2}{v} \tag{1.30}$$

$$g_{HHVV} = \frac{2m_V^2}{v^2} \qquad g_{HHH} = \frac{3m_H^2}{v} \qquad g_{HHHH} = \frac{3m_H^2}{v^2} \tag{1.31}$$

where m_f is the mass of fermion f, and m_V is the mass of V boson, where V stands either for the W or Z boson. The fact that the couplings are proportional to fermion masses and squared gauge boson masses is a fundamental SM prediction, crucial to verify in order to confirm that the BEH mechanism is at the origin of particle masses.

The description of the Higgs boson phenomenology in the following sections is largely based on Ref. [46].

1.4.2 Higgs boson decays

Higgs boson decay channels can have considerably different importances depending on m_H.

The Higgs partial decay width to a a pair of fermions f of mass m_f, $H \to f\bar{f}$, is given at tree level by

$$\Gamma_{f\bar{f}} = \frac{N_C G_F m_f m_H}{4\sqrt{2}\pi}\beta^3 \qquad \beta = \sqrt{1 - \frac{4m_f^2}{m_H^2}} \tag{1.32}$$

whereas for decays to a pair of on-shell vector bosons V of mass m_V, $H \to VV$

$$\Gamma_{VV} = \frac{G_F m_H^3}{16\sqrt{2}\pi}\delta_V\beta\left(1 - x_V + \frac{3}{4}x_V^2\right) \tag{1.33}$$

with

$$\delta_{W,Z} = 2, 1 \qquad \beta = \sqrt{1 - x_V} \qquad x_V = \frac{4m_V^2}{m_H^2} \tag{1.34}$$

finally decay modes to massless particles can proceed through loops, as shown in Figure 1.7 for $H \to \gamma\gamma$ decays.

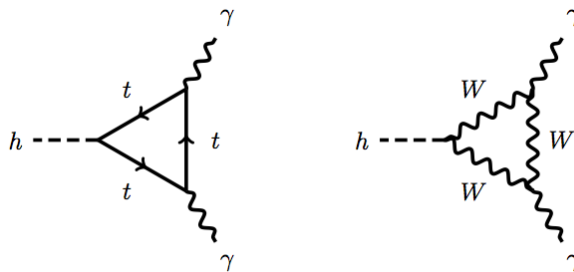**Figure 1.7:** Diagrams for the $H \to \gamma\gamma$ decay process.

Since the Higgs boson coupling depends on mass, the dominant loops are those where the top quark and W boson circulate. If heavy particles beyond the SM exist, they could manifest in this kind of loops. An analogous diagram, where the top quark is the only SM particle circulating in the loop, makes the process $H \to gg$ possible as well. The partial width for the $H \to \gamma\gamma$ decay is given by

$$\Gamma_{\gamma\gamma} = \frac{\alpha^2 g_F m_H^3}{128\sqrt{2}\pi^3}\left|\sum_i N_{c,i}Q_i^2 F_i\right| \tag{1.35}$$

where $N_{c,i}$ is the number of colours, Q_i the charge and F_i a factor depending on the particle spin.

Figure 1.8 shows the results obtained using HDECAY [47, 48, 49] and PROPHECY4F [50, 51, 52] which can be found in Ref. [53], and that include relevant QCD and electroweak corrections, as well as interference effects.

The first qualitative feature to be observed is that below the WW threshold only fermionic channels are open, and among these $H \to b\bar{b}$ is dominating due to its relatively large mass. $H \to \tau^+\tau^-$ decays immediately follow. $H \to gg$ and $H \to \gamma\gamma$ are suppressed since they proceed through loops. Partial widths for fermionic decays increase linearly with the mass. WW and ZZ decays are possible even below threshold, with the W and Z bosons produced off-shell. Even in this case the coupling remains the same, since it is proportional to the pole mass, and not the virtual q^2, but the width has a more complicated expression than Equation 1.33. The widths of the decays to pairs of vector bosons increase with the cube of m_H, and therefore WW decays remain dominant even when decays to top-quark pairs become kinematically allowed.
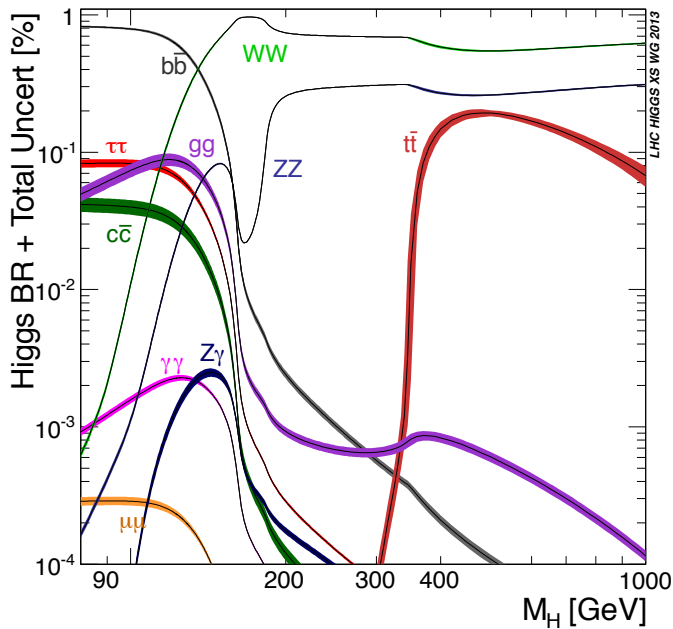

Figure 1.8: SM Higgs boson decay branching ratios as a function of m_H [53].

The uncertainties on the branching ratios shown due to missing higher orders and limited accuracy of the corrections are shown in Table 1.7.

1.4.3 Higgs boson production at the LHC

The Higgs boson can be produced by different mechanisms, whose importance depends on the type of collider. At the LHC, which is a pp collider, the main production modes are gluon-gluon fusion (ggF), vector-boson fusion (VBF), W/Z associated production (VH) and top-quark pair associated production (t$\bar{\text{t}}$H). The diagrams for the first relevant order of these processes are shown in Figure 1.9. The cross-sections as a function of mass for different centre-of-mass energies and different production modes at $\sqrt{s} = 8$ TeV are shown in Figures 1.10(a) and 1.10(b) respectively.

Partial width	QCD	Electroweak	Total
$H \to bb, cc$	~ 0.1-0.2%	~ 1-2% for $m_H \lesssim 135$ GeV	~ 1-2%
$H \to \tau\tau$		~ 1-2% for $m_H \lesssim 135$ GeV	~ 1-2%
$H \to t\bar{t}$	$\sim 5\%$	$\lesssim 2$-5% for $m_H < 500$ GeV	$\sim 5\%$
		$\sim 0.1(m_H/1\text{TeV})^4$ for $m_H > 500\text{GeV}$	~ 5-10%
$H \to gg$	$\sim 10\%$	$\sim 1\%$	$\sim 10\%$
$H \to \gamma\gamma$	$< 1\%$	$< 1\%$	$\sim 1\%$
$H \to WW/ZZ \to 4f$	$< 0.5\%$	$\sim 0.5\%$ for $m_H < 500\text{GeV}$	$\sim 0.5\%$
		$\sim 0.17(m_H/1\text{TeV})^4$ for $m_H > 500\text{GeV}$	~ 0.5-15%

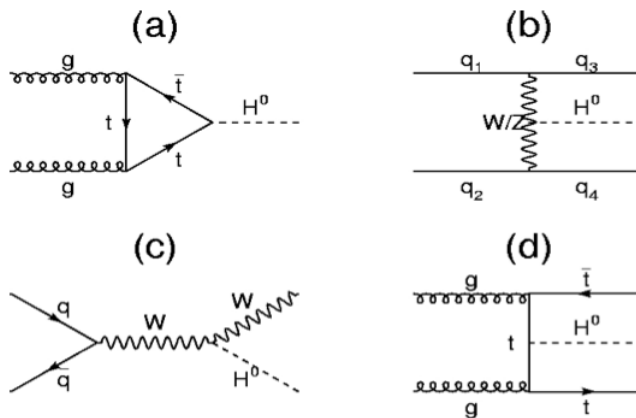**Table 1.7:** Estimate of theoretical uncertainties from missing higher orders on SM Higgs boson partial widths [54].

Figure 1.9: Diagrams for Higgs boson production at the LHC, (a) ggF, (b) VBF, (c) VH, (d) t$\bar{\text{t}}$H[46].

Since at the LHC pp collisions happen at a very high centre-of-mass energy ($\sqrt{s} = 7$ TeV or $\sqrt{s} = 8$ TeV), the LHC can naively be seen as a gluon collider. Therefore, even if the ggF process proceeds through loops, and should therefore be suppressed with respect to other production modes, it is actually the dominant mode.

VBF is a much rarer mode than ggF, but it is of a particular interest at the LHC, and for $H \to \tau^+\tau^-$ searches in particular. In this process the incoming quarks radiate two vector bosons (W/Z) that fuse to produce a Higgs boson. The Higgs boson decay products tend to be central in the detector, whereas the two quarks in the final state give rise to two jets forward in the detector. The reason for this is found in the W/Z propagator, $1/(Q^2 - m_{W/Z}^2)$. Since the process is t-channel, Q^2 is negative, and therefore the amplitude is least suppressed for small Q^2. This translates into large jet pseudorapidities being favoured. Additional jet activity would tend to be forward to the scattered quarks, since there is no coulour exchange between the incoming quarks. SM backgrounds (multi-jet production, W/Z production in association with jets, $t\bar{t}$ pair production) tend to have quite different
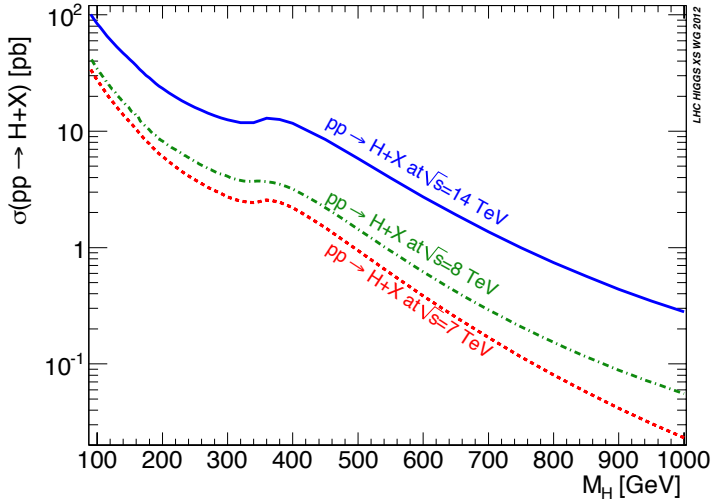
(a)
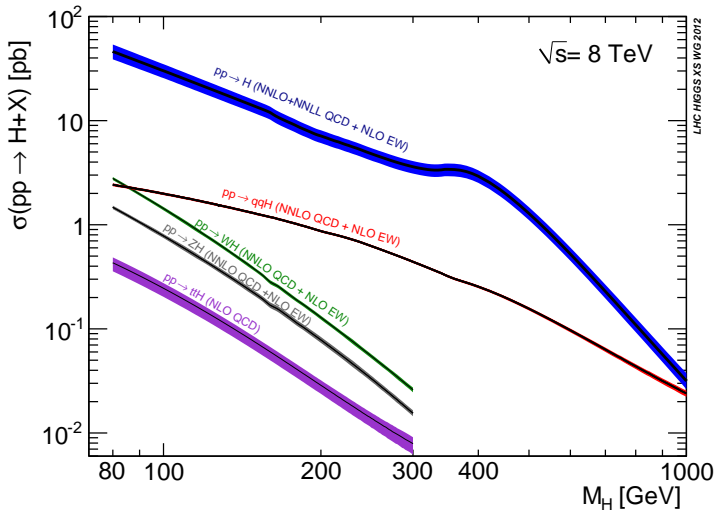
(b)

Figure 1.10: (a)total Higgs boson production cross-section for different centre-of-mass energies at a *pp* collider and (b) Higgs production cross-sections for single production modes [54, 55].

characteristics, with central jets and additional radiation. The characteristic topology of the VBF production process can therefore be exploited to suppress the backgrounds. A sketch of how a typical VBF event looks like in the detector is shown in Figure 1.11.
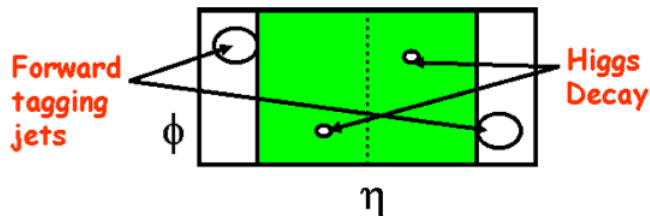

Figure 1.11: Sketch of a typical VBF event in the detector [46].

Production associated to a W or Z boson has a lower cross-section than VBF, but benefits from the very clear signature given by the presence additional leptons in the final state. Finally $t\bar{t}$H is the rarest production mode, with a complex signature characterised by several jets in the final state.

Theory uncertainties on production cross-sections is a complex topic, since analyses usually exploit exclusive variables, in particular the details of the jet final state, in order to get the best sensitivity. Examples are Higgs transverse momentum and additional final state jets variables. Part of the theory uncertainty therefore heavily depends on the analysis strategy employed. The most up to date prescriptions for production cross-sections values and uncertainties are found in Ref. [53].

1.5 Higgs boson discovery and first measurements

The hunt for the Higgs boson dates back to the '70s (an interesting historical profile of the Higgs boson is given in Ref. [45]), but only at the end of 1990s-begging of 2000s the Higgs boson was first cornered at experiments at the LEP e^+e^- collider [56] and Tevatron $p\bar{p}$ collider [57], and finally discovered by the ATLAS and CMS experiments. In July 2012 both the ATLAS and CMS experiments announced the observation of a new boson of mass ~ 125 GeV, in the context of Higgs searches [58, 59]. The observation of the excess was driven by the high mass resolution channels $H \to \gamma\gamma$ and $H \to ZZ^* \to 4l$, but the excess was confirmed by the $H \to W^+W^-$ channel as well. The observed local p_0 values, that is the probabilities that the background could produce a fluctuation greater than or equal to the excess observed in data, for the two experiments at the time are shown in Figure 1.12. In the following an equivalent formulation of p_0 in terms of number of standard deviations is referred to as significance.

The latest results unequivocally confirm the observation of a new boson of mass ~ 126 GeV. Furthermore measurements of the mass, couplings and spin-parity properties have been performed, that are all consistent with the SM expectations. It should be noted how $m_H \sim 126$ GeV is a very interesting mass point, where most decay channels are open and have a branching ratio large enough to be measured.
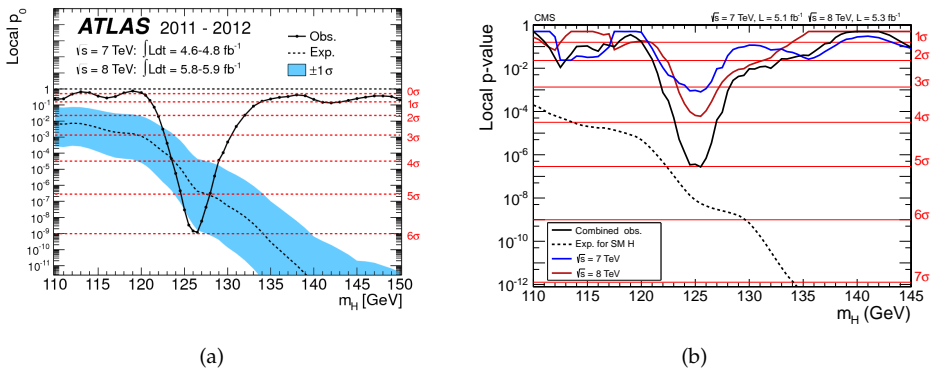
Figure 1.12: Observed local p_0 value as a function of m_H at the time of discovery. The dashed curve indicates the expected local p_0 under the hypothesis of a SM Higgs boson signal at that mass. (a) ATLAS experiment [58], (b) CMS experiment [59].

In the following, unless stated otherwise, the results shown were obtained from the analysis of the full 2011-2012 ATLAS and CMS datasets, which correspond to 4.7 fb^{-1} at $\sqrt{s} = 7$ TeV and 20.7 fb^{-1} at $\sqrt{s} = 8$ TeV for ATLAS and 4.9 fb^{-1} at $\sqrt{s} = 7$ TeV and 19.5 fb^{-1} at $\sqrt{s} = 8$ TeV for CMS. Part of the results were still preliminary and subject to updates at the time this thesis was written.

1.5.1 Observation in the boson channels

The $H \rightarrow \gamma\gamma$ signature is characterised by two high-p_T back-to-back photons, that can be resconstructed in a resonance. The background is given by $\gamma\gamma$-continuum, γ-jet and jet-jet production. The background is large, but its spectrum is steeply falling with mass and featureless, so that despite the small branching ratio for this channel (BR=$\sim 0.2\%$), it is one of the leading channels. Figure 1.13 shows the combined diphoton spectra after the full selection of the ATLAS [60, 61] and CMS [62] analyses. The ATLAS experiment observed the maximum deviation from the SM background expectation at a mass $m_H \sim$ 126.5 GeV. The observed significance of the excess at this mass is 7.4σ, to be compared with 4.3σ expected from a SM Higgs boson at this mass. The CMS experiment observed the excess at a mass $m_H \sim 125$ GeV. The CMS experiment pursued different analysis strategies: a multi-variate technique found an observed local significance of 3.2σ, with an expectation from a SM Higgs boson of 4.2σ, while for the cut-based approach the excess has a significance of 3.9σ (3.5σ expected).

The $H \rightarrow ZZ^* \rightarrow 4l$ channel (with $l = e/\mu$, BR=$\sim 0.1\%$) is the golden channel in the mass range where the excess is observed. The signature given by four leptons in the final state, coming from the decays of two Z bosons, is very distinctive. The background is small, mostly due to ZZ continuum. Figure 1.14 shows the four-lepton mass m_{4l} distribution selected in data for the ATLAS [60, 63] and CMS [64] experiments. The observed (expected from a SM Higgs boson) significance of the excess above the expected background is 6.6σ (4.4σ) at $m_H = 124.3$ GeV for the ATLAS experiment and 6.7σ (7.2σ) for
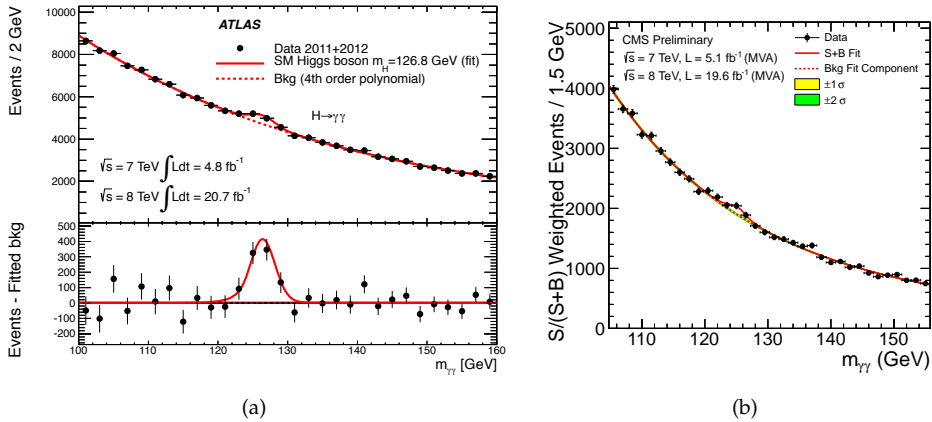
Figure 1.13: Invariant mass distribution of diphoton candidates after all selections (a) for the AT-LAS experiment inclusive analysis [60, 61]. (b) for the CMS experiment [62], MVA analysis, each event weighted by the S/(S+B) value of its analysis category.

the CMS experiment at $m_H = 125.8 \, \text{GeV}$.

At $m_H = 125 \, \text{GeV}$ the branching ratio of the $H \rightarrow W^+W^-$ channel is quite large, $\sim 20\%$, despite being below the real WW decay threshold. This channel has a clear signature given by the presence of two charged leptons and missing transverse momentum due to the neutrinos emitted in the W decays. However it is experimentally difficult due to the fact full mass reconstruction is not possible. The main backgrounds come from irreducible WW continuum, $t\bar{t}$ pairs and $W \rightarrow l\nu$. Figure 1.15(a) shows the transverse mass distribution of $H \rightarrow WW^* \rightarrow l\nu l\nu$ candidates for the ATLAS experiment [65]. Figure 1.15(b) shows the observed and expected significances for each Higgs mass hypothesis for the CMS experiment [66]. The observed (expected from a SM Higgs boson) significance of the excess above the expected background is 3.8σ (3.7σ) for the ATLAS experiment and 4.0σ (5.1σ) for the CMS experiment at $m_H = 125 \, \text{GeV}$.

1.5.2 Fermionic channels

Fermionic decay channels are experimentally very challenging. Both the $H \rightarrow b\bar{b}$ and $H \rightarrow \tau^+\tau^-$ channels suffer in the hadronic LHC environment from heavy backgrounds due to processes with jets in the final state. In order to extract the signal from the background specific Higgs production modes are targeted, in particular VBF and VH associated production.

Figure 1.16 shows the results of the ATLAS $H \rightarrow b\bar{b}$ analysis targeting the VH production mode [67]. Three channels were considered, according to the vector boson type and decay ($W \rightarrow l\nu$, $Z \rightarrow l^+l^-$, $Z \rightarrow \nu\bar{\nu}$), with different background compositions, and a categorisation based on the vector boson p_T was employed to maximise the sensitivity. No excess was observed, and a limit was set to the Higgs boson cross-section times the $H \rightarrow b\bar{b}$ branching ratio of 1.4 times the SM expectation (1.3 expected).
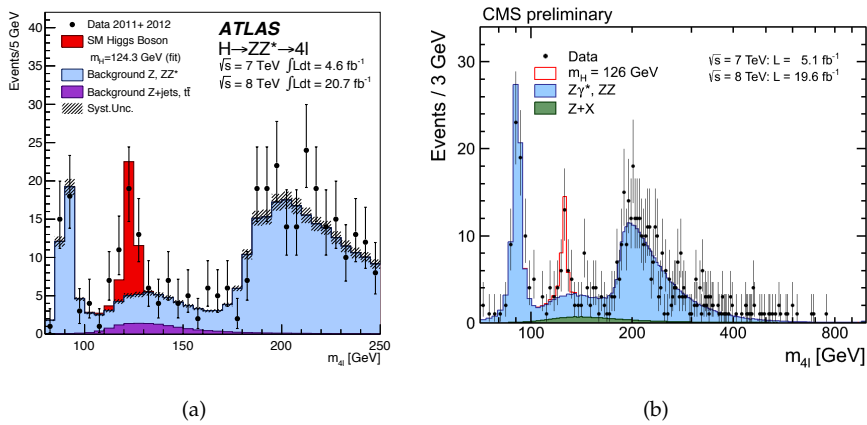
(a)   (b)

Figure 1.14: Distribution of m_{4l} for the selected $H \rightarrow ZZ^* \rightarrow 4l$ candidates in data. The estimated background is shown. (a) for the ATLAS experiment, the expected SM Higgs boson signal for $m_H = 124.3 \, \text{GeV}$ is shown [60, 63]. (b) for the CMS experiment the signal is for $m_H = 126 \, \text{GeV}$ [64].
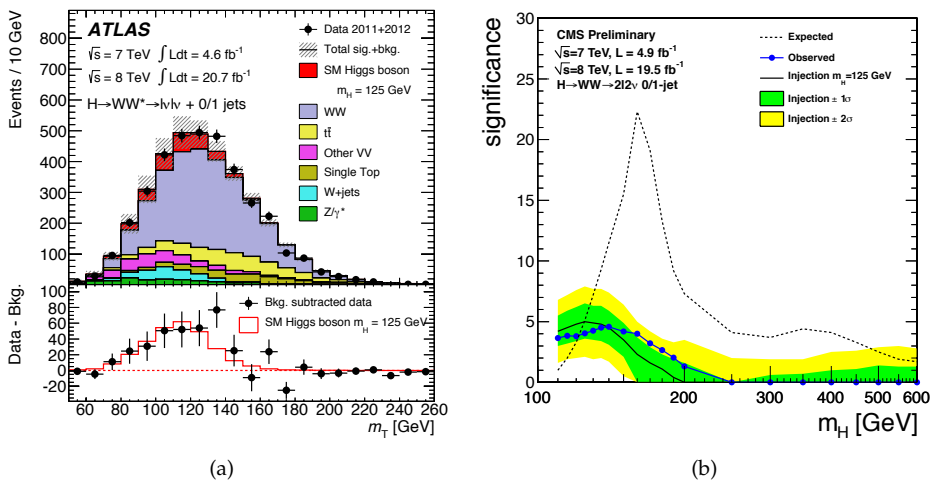

(a)   (b)

Figure 1.15: $H \rightarrow WW^* \rightarrow l\nu l\nu$ channel: (a) transverse mass distribution for the selected events, ATLAS experiment [65]. (b) observed and expected significances, CMS experiment [66].
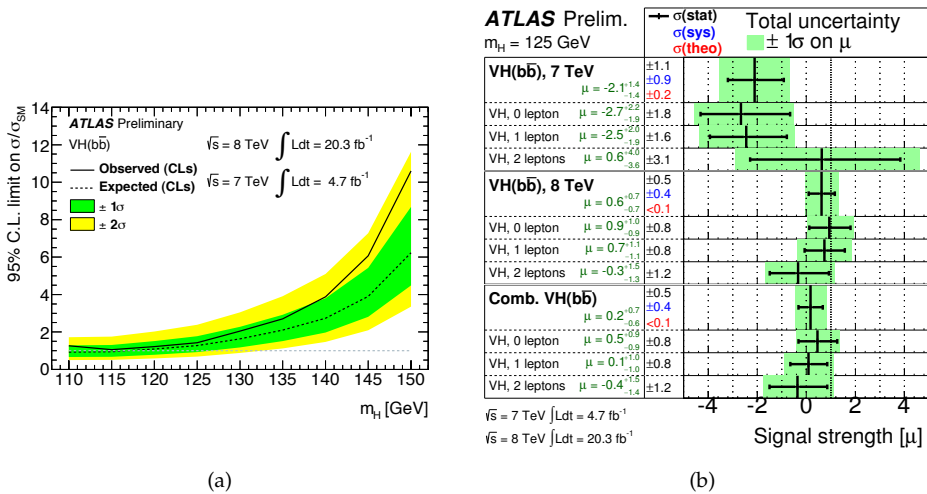
Figure 1.16: (a) expected (dashed) and observed (solid) 95% CL cross-section upper limits, normalised to the SM Higgs boson production cross-section, as a function of m_H for the ATLAS VH $H \to b\bar{b}$ channel. (b) summary of the fitted signal strength values for single channels and years [67].

Figure 1.17(a) shows the expected and observed 95% CL upper limits on the product of the VH production cross section times the $H \to b\bar{b}$ branching fraction, with respect to the SM expectation, obtained by the CMS experiment. Figure 1.17(b) shows expected and observed p_0 values. An excess of events above the expected background was observed, with a local significance of 2.1σ at $m_H = 125\,\mathrm{GeV}$, consistent with the expectation from the production of the standard model Higgs boson [68].

The study of the $H \to \tau^+\tau^-$ decay channels is possible mainly by targeting the VBF production mode and boosted Higgs topologies (for more details see Chapter 3). For preliminary results the two experiments both pursued analyses on six different channels (according to tau lepton decay modes) but preferring different strategies. ATLAS developed a multi-variate analysis approach, concentrating only on two very sensitive analysis categories. The CMS experiment instead adopted an approach based on sequential cuts, optimised in several analysis categories. Both the ATLAS and CMS experiment obtained evidence for the existence of $H \to \tau^+\tau^-$ decays.

For the ATLAS experiment the significance of the data excess over the background prediction at $m_H = 125\,\mathrm{GeV}$ is 4.1σ (3.2σ expected), and the measured $\mu = 1.4^{+0.5}_{-0.4}$ [4]. Figure 1.18(a) shows the distributions of event yields as a function of the logarithm of the signal over background ratio, obtained for each event in its bin of the multi-variate discriminant. The excess can be clearly seen. The signal predictions both for $\mu = 1$ and $\mu = 1.4$ are shown. Figure 1.18(b) instead shows the mass distribution for events from all channels and categories combined with weights $\ln(1 + S/B)$ (even in this case taken from bins of the multi-variate discriminant). The mass of the excess is comparable to that expected for a $m_H = 125\,\mathrm{GeV}$ SM Higgs boson.
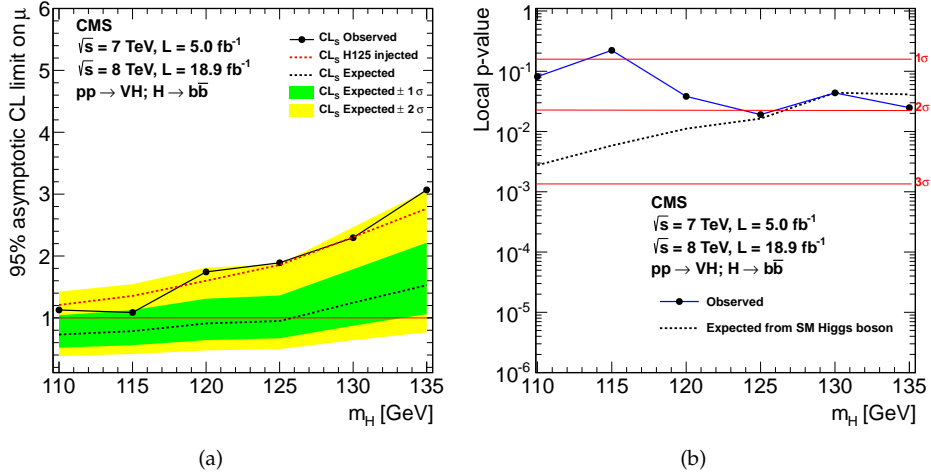
Figure 1.17: (a) Expected and observed 95% CL upper limits on the product of the VH production-cross section times the $H \rightarrow b\bar{b}$ branching fraction, with respect to the expectations for the standard model Higgs boson. (b) Local p_0 values for the background-only hypothesis to. [68].
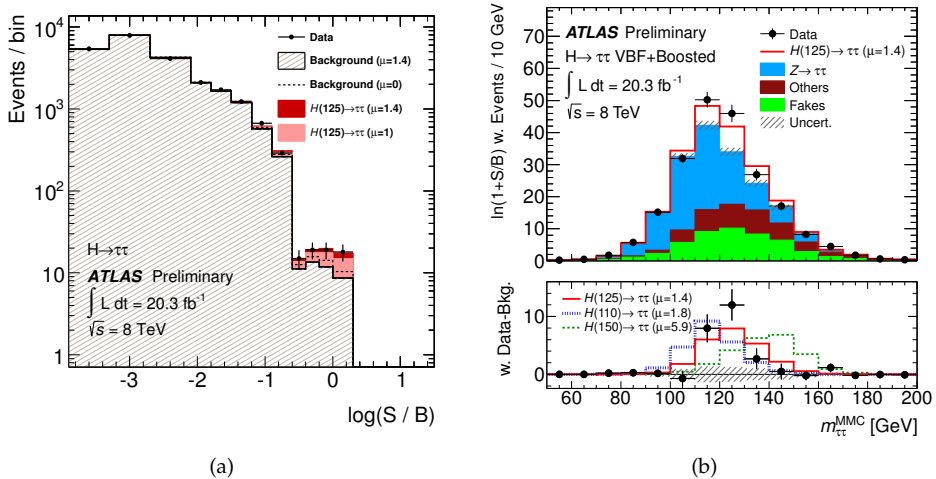

Figure 1.18: (a) Event yields in the ATLAS $H \rightarrow \tau^+\tau^-$ analysis as a function of $\log(S/B)$, where S (signal yield) and B (background yield) are taken from each event's bin in the multi-variate discriminant. (b) Mass distribution where events are weighted by $\ln(1 + S/B)$ [4].

The CMS experiment has found an excess $> 3\sigma$ in the range $110 < m_H < 130\,\text{GeV}$ (3.60σ observed and 3.38σ expected at $m_H = 125\,\text{GeV}$) [69]. Figure 1.19(a) shows the expected and observed p_0 values as a function of the Higgs boson mass, whereas Figure 1.19(b) shows the mass spectrum, obtained combining the different categories and channels according to the expected signal and signal-plus-background yield in each category.
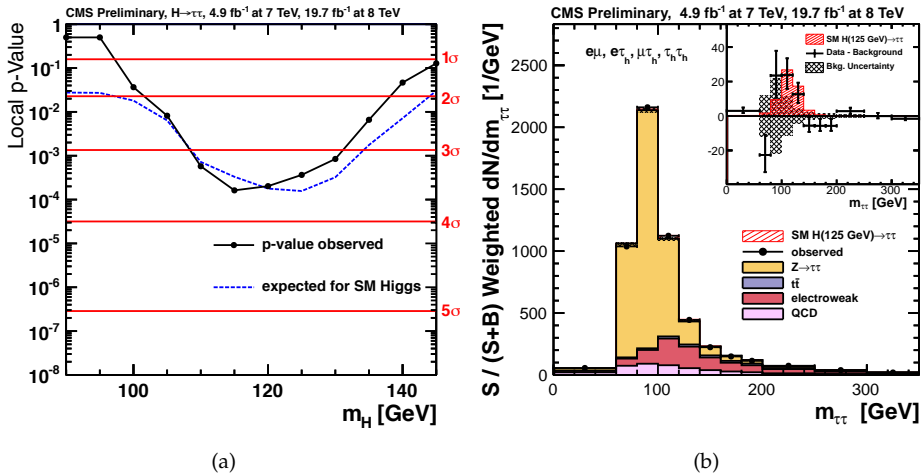

(a)   (b)

Figure 1.19: (a) Observed and expected local p_0 value and (b) combined observed and predicted di-tau mass distributions, weighted by the ratio between the expected signal and signal-plus-background yields in each category for the CMS $H \to \tau^+\tau^-$ analysis [69].

1.5.3   Mass and signal strength measurement

The mass of the observed state is measured by ATLAS [70] and CMS [71] using the high mass resolution channels $H \to \gamma\gamma$ and $H \to ZZ^* \to 4l$. The mass is measured to be

$$\text{ATLAS} \qquad m_H = 125.5 \pm 0.2(\text{stat})^{+0.5}_{-0.6}(\text{syst})\,\text{GeV} \qquad (1.36)$$

$$\text{CMS} \qquad m_H = 125.7 \pm 0.3(\text{stat}) \pm 0.3(\text{syst})\,\text{GeV} \qquad (1.37)$$

A first test of the compatibility of the observed excess with the SM expectation can be performed using the combined signal strength. A signal strength is a modifier of the signal yield with respect to the SM expectation. The signal yield can in fact be written as

$$n^k_{\text{signal}} = \left(\sum_i \mu_i \sigma_{i,\text{SM}} \times A^k_{if} \times \epsilon^k_{if} \right) \times \mu_f \times B_{f,\text{SM}} \times (L)^k \qquad (1.38)$$

where $\sigma_{i,\text{SM}}$ is the SM production cross-section for mode i and $\times B_{f,\text{SM}}$ the branching ratio for the decay channel f. For every analysis k the luminosity corresponding to the

used dataset is $\mathcal{L}^k$, the acceptance is A_{if}^k and the efficiency ϵ_{if}^k. μ_i and μ_f modify the SM expectations of the production cross-sections and decay branching ratios respectively. Signal strengths therefore test the compatibility between the background only hypothesis ($\mu = 0$) and the SM hypothesis ($\mu = 1$).

The combined signal strength is obtained by considering only one modifier μ for all production modes and fixing the decay branching ratios to the SM expectations.

The results obtained considering $m_H = 125.5$ by the ATLAS [60] and CMS [59] experiments are shown in Figure 1.20. The best combined μ values at this mass for the two experiments are

$$\text{ATLAS} \, (\gamma\gamma, WW^* \text{and} ZZ^*) \qquad \mu = 1.33^{+0.21}_{-0.18} \tag{1.39}$$

$$\text{CMS} \, (\gamma\gamma, b\bar{b}, \tau\tau, WW^* \text{and} ZZ^*) \qquad \mu = 0.80^{+0.14}_{-0.14} \tag{1.40}$$
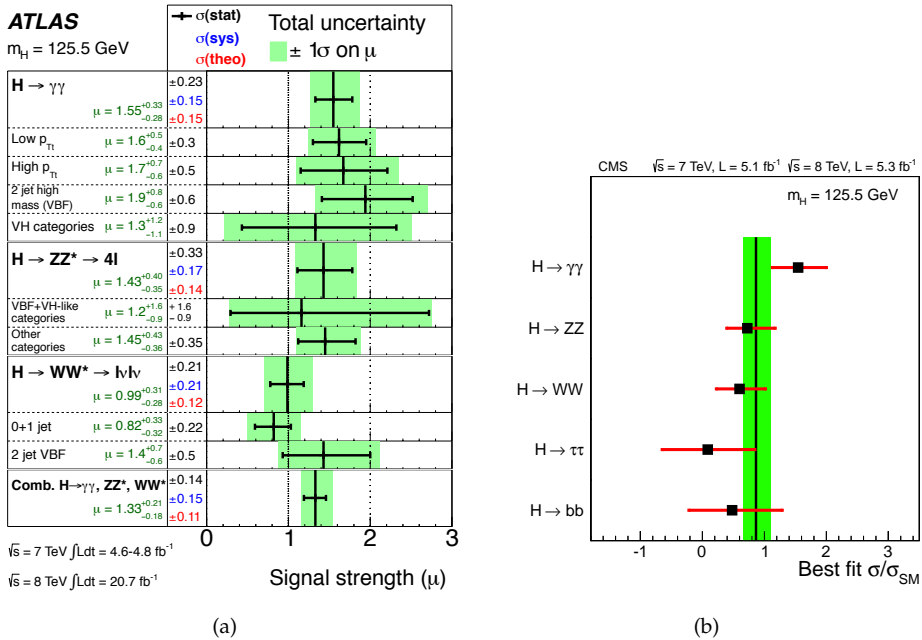

Figure 1.20: Best μ values for individual decay modes and for the combination for (a) ATLAS [60] and (b) CMS [59].

The overall compatibility with the SM Higgs boson expectation is at the 15% level.

1.5.4 Production modes

An important test of the SM is obtained considering separate signal strengths for the production modes described in Section 1.4.3. This test is possible since the categorisation of events in the analyses allows to enhance the sensitivity to individual production

mechanisms. A common signal strength for ggF and t$\bar{\text{t}}$H $\mu_{\text{ggH+t}\bar{\text{t}}\text{H}}$, and VBF and VH $\mu_{\text{VBF+VH}}$ was used. The first signal strength is sensitive to the couplings to fermions, whereas $\mu_{\text{VBF+VH}}$ is more sensitive to the coupling to bosons. The results of the ATLAS and CMS experiments are shown in Figure 1.21 and are consistent with the SM inside 95% contours for ATLAS and 65% contours for CMS. Evidence for the existence of the VBF production mode is at the 3.3σ level for ATLAS and 3.2σ for CMS.
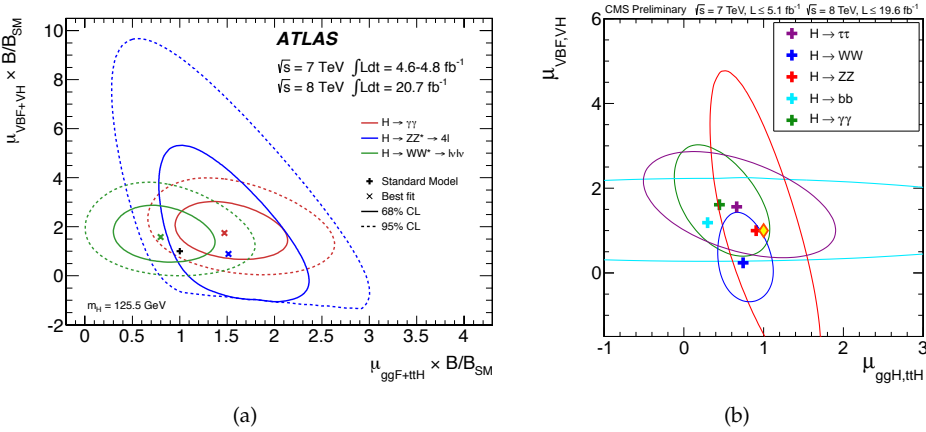

(a)   (b)

Figure 1.21: Likelihood contours for $\mu_{\text{ggH+t}\bar{\text{t}}\text{H}}$ and $\mu_{\text{VBF+VH}}$ for (a) ATLAS [60] and (b) CMS [71].

1.5.5 Couplings

To confirm that the state that is observed is indeed the Higgs boson it is crucial to test the couplings to SM particles. A coherent framework to test couplings was developed and can be found in Ref. [53]. Various tests were performed by the two experiments.

Vector boson versus fermion couplings. How the Higgs boson couples to fermions and bosons is a fundamental prediction of the theory. In particular it is interesting to test whether the Higgs boson couples to fermions too. The parameters of interest in this case are modifiers for the couplings to fermions and bosons k_V and k_F. Under the assumption there are no BSM contributions, the absence of coupling to fermions was excluded at more than 5σ level, mainly indirectly via the ggF production mode loop.

Custodial symmetry. The prediction that the couplings to the W and Z boson are the same was tested. The parameter of interest is the ratio λ_{WZ} between the two couplings.

Fermionic couplings. The CMS experiment probed the fermionic couplings specifically as well. The two parameters of interest are the ratios of couplings to down/up fermions λ_{du} and the ratio of couplings to leptons and quarks $\lambda_{l,q}$

BSM physics. Possible effects from BSM physics were investigated considering contributions of new particles in the loops and to the total width. In the first case the parameters of interest are the effective couplings to gluons and photons, k_g and k_γ. In the second case limits were set to the branching ratio to BSM particles $\mathrm{BR_{BSM}}$.

The results for the ATLAS and CMS experiments are shown in Figure 1.22 and are all in agreement with the SM expectations.
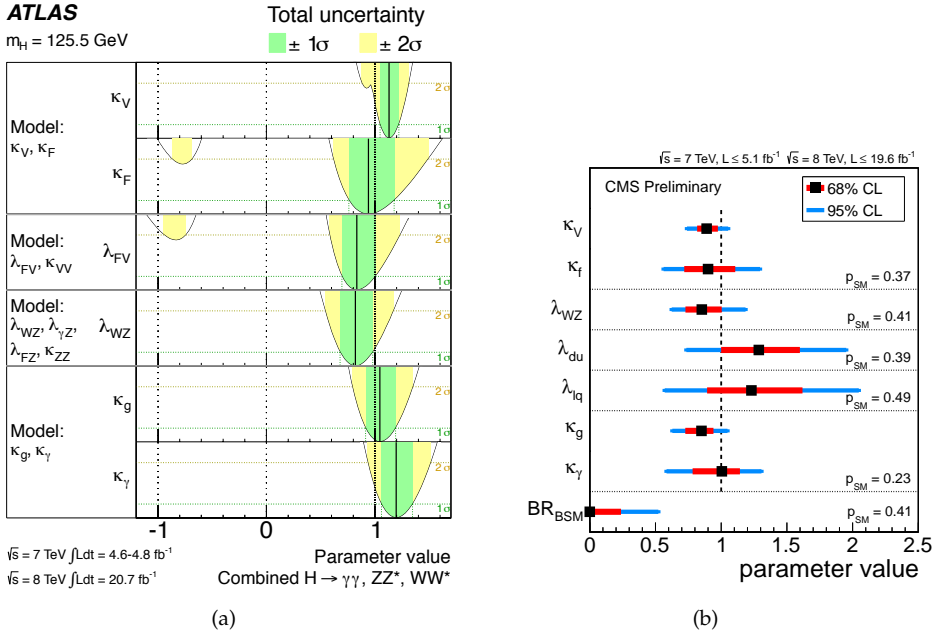

(a)

(b)

Figure 1.22: Summary of the fits for deviations in the couplings for the (a) ATLAS [60] and (b) CMS [71] experiments. More details on the meaning of the couplings listed are found in the text and in the references.

1.5.6 Quantum numbers

The Higgs boson is predicted to be a scalar, $J^{CP} = 0^+$. Determining the spin and parity of the observed state is therefore an important test of the SM.

A strong constraint comes from the sole observation in the $H \to \gamma\gamma$ decay channel. Thanks to the Landau-Yang theorem [72, 73] in fact, this allows to rule out $J = 1$ and forbids C-violating effects in the Higgs sector, fixing $C = +1$. In order to further constrain the spin and parity of the observed state, the fact that the kinematics of the Higgs boson production and decay depends on the spin and parity is exploited.

In the $H \to ZZ^* \to 4l$ the masses of the two Z bosons, the production and the decay angles in the Z rest frame carry information about the spin-parity of the decaying state. The full reconstruction of the final stare allows therefore to study such properties. In

the $H \rightarrow \gamma\gamma$ channel the sensitivity comes from the photons production angle $\cos(\theta^*)$ in the Collins-Soper frame. Finally, in the $H \rightarrow WW^* \rightarrow l\nu l\nu$ several variables, such as the transverse mass, the p_T and invariant mass of the two leptons system, and the two leptons azimuthal separation, are sensitive to spin-parity.

Typically the SM hypothesis was tested against one alternative at a time. Alternative model descriptions are based on [74], where the production and decay of a generic boson with various J^P quantum numbers are described by defining the most general amplitudes. A brief summary is given in Table 1.8, where the production modes considered are specified as well.

J^P	production	description
0^+	$gg \rightarrow X$	SM Higgs boson
0^-	$gg \rightarrow X$	pseudoscalar
0_h^+	$gg \rightarrow X$	BSM scalar with higher dimensional operators in the decay amplitude
2_{mgg}^+	$gg \rightarrow X$	Kaluza-Klein graviton like with minimal couplings
$2_{mq\bar{q}}^+$	$q\bar{q} \rightarrow X$	Kaluza-Klein graviton like with minimal couplings
1^-	$q\bar{q} \rightarrow X$	exotic vector
1^+	$q\bar{q} \rightarrow X$	exotic pseudovector

Table 1.8: Summary of scenarios considered for spin-parity testing. Details can be found in Ref. [74].

Results are shown in Figure 1.23 for the ATLAS [75] and in Table 1.9 for the CMS [64, 66, 76, 77] experiments. The results strongly favour the SM 0^+ hypothesis, and allow to exclude many alternative models at $> 95\%$ confidence level.

	$ZZ^* \rightarrow 4l$	$WW^* \rightarrow 2l2\nu$	$ZZ^* \rightarrow 4l$ and $WW^* \rightarrow 2l2\nu$ combination	$\gamma\gamma$
0^-	0.16%	-	-	-
1^-	$< 0.1\%$	-	-	-
1^+	$< 0.1\%$	-	-	-
$2_m^+ \, gg \rightarrow X$	1.5%	14%	0.6%	60.9%
$2_m^+ \, q\bar{q} \rightarrow X$	0.1%	-	-	16.9%

Table 1.9: Results of the CMS Higgs boson spin analysis [64, 66, 76, 77]. Confidence level of different hypotheses for the Higgs boson J^{CP} when compared with the SM hypothesis 0^+.
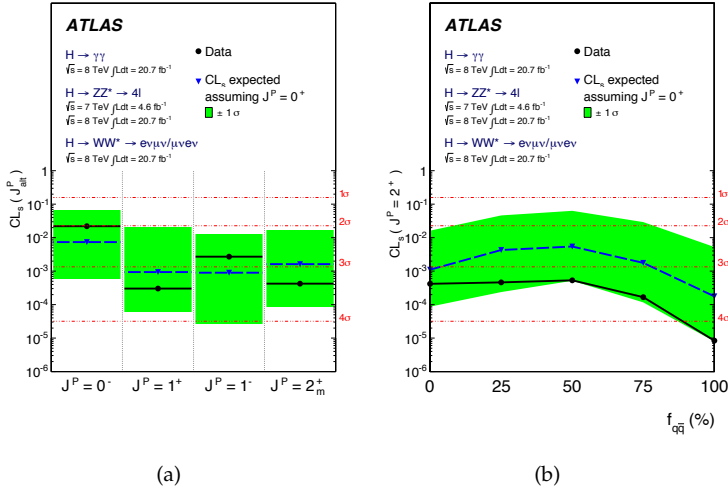
Figure 1.23: Results of the ATLAS Higgs boson spin analysis [75]. Expected (blue triangles/dashed lines) and observed (black circles/solid lines) confidence levels, assuming a $J^P = 0^+$ signal, for (a) alternative spin-parity hypotheses and (b) $J^P = 2^+$ hypothesis as a function of the production mode admixture $q\bar{q} \rightarrow X$ fraction for the spin-2 particle.

1.6 Tau leptons and the $H \rightarrow \tau^+\tau^-$ process

1.6.1 The tau lepton

The tau lepton belongs to the third family of fermions of the SM (see Table 1.1), which is characterized by the large mass of its components. Tau properties are summarised in Table 1.10. Due to this feature, the third family plays an essential role in the study of spontaneous symmetry breaking in the SM. The tau lepton does not make an exception, being the most massive lepton. Because of its mass the tau is the only lepton allowed to decay both in leptonic and hadronic channels, as shown in Table 1.11.

Spin	$\frac{1}{2}$
Mass	(1776.82 ± 0.16) MeV
Mean life	$(290.6 \pm 1.0) \times 10^{-15}$ s

Table 1.10: Tau lepton properties, figures are taken from Ref. [8].

This characteristic of the tau makes it a unique laboratory to make several precision measurements both regarding the electroweak and strong sector of the SM. These range from tau lepton properties measurements, weak coupling universality tests, α_s determination, strange quark mass measurement, evaluation of the V_{us} CKM matrix element to search for new physics beyond the SM by looking for rare decays. The very clean envi-

Decay modes	Branching ratio
$\tau \to e \, \nu_e \nu_\tau$	17.8%
$\tau \to \mu \, \nu_\mu \nu_\tau$	17.4%
$\tau \to h^\pm \text{neutr.} \nu_\tau$	49.5%
$\tau \to \pi^\pm \nu_\tau$	11.1%
$\tau \to \pi^0 \pi^\pm \nu_\tau$	25.4%
$\tau \to \pi^0 \pi^0 \pi^\pm \nu_\tau$	9.19%
$\tau \to \pi^0 \pi^0 \pi^0 \pi^\pm \nu_\tau$	1.08%
$\tau \to K^\pm \text{neutr.} \nu_\tau$	1.56%
$\tau \to h^\pm h^\pm h^\pm \text{neutr.} \nu_\tau$	14.57%
$\tau \to \pi^\pm \pi^\pm \pi^\pm \nu_\tau$	8.98%
$\tau \to \pi^0 \pi^\pm \pi^\pm \pi^\pm \nu_\tau$	4.30%
$\tau \to \pi^0 \pi^0 \pi^\pm \pi^\pm \pi^\pm \nu_\tau$	0.50%
$\tau \to \pi^0 \pi^0 \pi^0 \pi^\pm \pi^\pm \pi^\pm \nu_\tau$	0.11%
$\tau \to K_S^0 X^\pm \nu_\tau$	0.90%
$\tau \to (\pi^0) \pi^\pm \pi^\pm \pi^\pm \pi^\pm \pi^\pm \nu_\tau$	0.10%
other K modes	1.30%
others	0.03%

Table 1.11: Tau lepton decay modes and their branching ratios, figures are taken from Ref. [8].

ronment of $e^+ e^-$ colliders is particularly favorable with this respect. Machines running at the tau production threshold allow to make precision measurements such as the tau mass, and are very competitive, despite the low cross-section production at those energies, since systematics can be kept well under control. B-factories running on $\Upsilon(4S)$ are tau factories as well. They can rely on extremely high statistics, but have the disadvantage of being subject to a heavy background of hadron decays.

Running at the Z peak allows to have a much higher cross-section, 1.5 nb, than at other energies, and much smaller systematics than at a B-factory.
During the LEP I phase about 500000 tau pairs were collected by the four experiments, providing a unique environment for SM tests bases on tau leptons. Two such measurements are the measurement of the branching fractions of the decays $\tau \to \mu \nu \bar{\nu}$ and $\tau \to e \nu \bar{\nu}$ and that of the tau lifetime.

The first allowed to test the universality of the weak charged current, yielding a value for the ratio of the coupling to muons and to electrons [8, 78]

$$\frac{g_\mu}{g_e} = 0.9999 \pm 0.0021 \tag{1.41}$$

consistent with unity, and therefore confirming universality at the per mil level.

The determination of the tau lifetime, measured to be

$$\tau_\tau = 290.6 \pm 1.0 \text{ fs} \tag{1.42}$$

can be used together with the branching fractions to obtain the ratio of the couplings to electrons and muons

$$\frac{g_\tau}{g_\mu} = 1.0014 \pm 0.0022 \qquad \frac{g_\tau}{g_e} = 1.0015 \pm 0.0022 \tag{1.43}$$

which is again a stringent test to the universality of the couplings required by the SM description.

The LHC environment does not allow to make precision tests of tau properties. The importance of taus, as already stated, is rather as probes of the direct or chain decays of SM and BSM particles. Since at the LHC the cross-section for multi-jet production is overwhelming with respect to other type of processes, a priority for the physics with taus is to be able to identify hadronic systems from tau lepton decays from QCD jets. Being able to simulate properly hadronic tau decays is therefore of great importance. As it can be seen from Table 1.10, that lists tau decay modes with their branching ratios, the most important hadronic decay modes are

$$\tau \to \pi^\pm \nu_\tau$$
$$\tau \to \pi^0 \pi^\pm \nu_\tau$$
$$\tau \to \pi^0 \pi^0 \pi^\pm \nu_\tau$$
$$\tau \to \pi^\pm \pi^\pm \pi^\pm \nu_\tau$$

the last three are dominated by the decay through hadronic resonances

$$\tau \to \rho^\pm \nu_\tau \to \pi^0 \pi^\pm \nu_\tau$$
$$\tau \to a_1^\pm \nu_\tau \to \pi^0 \pi^0 \pi^\pm \nu_\tau$$
$$\tau \to a_1^\pm \nu_\tau \to \pi^\pm \pi^\pm \pi^\pm \nu_\tau$$

A proper description of the hadronic currents involved in these processes is fundamental for a good description of tau decays. Furthermore, energy and angular spectra of tau decays retain information about the spin of the parent tau lepton. Spin and spin correlations in tau pair production are therefore an important aspect to be covered for a proper tau simulation. A widespread used library for tau simulation, which has been extensively tested and tuned on available tau lepton data, is TAUOLA [79, 80]. TAUOLA is normally used in combination with PHOTOS [81], that provides generation of radiative corrections in cascade decays. The TauSpinner package dedicated to simulate and emulate spin correlations in tau decays has recently been developed [82].

1.6.2   Importance of the H $\to \tau^+\tau^-$ process observation

The $H \to \tau^+\tau^-$ process has a great importance, since it is one of the channels with largest BR in the low mass range, second only to $H \to b\bar{b}$, which is an experimentally very challenging channel at the LHC. Now that an observation has been made in the

decay channels to bosons, it is of uttermost importance to fully establish a direct observation of decays to fermions, and in particular to down-type fermions, and to perform measurements in these channels.

One of the important predictions of the SM is that the Higgs boson allows to give masses without spoiling the gauge invariance of the theory not only to gauge bosons, but to fermions as well. Deviations from the predicted couplings, as described in Section 1.4.2 could be an important hint for a Higgs sector more extended than the minimal version included in the SM or more generally for new physics beyond the SM.

An incompatibility between the masses observed in the channels would signal that the decaying state is not the same as the one for which boson decays are observed. Further Higgs states are predicted in simple extension of the SM Higgs sector, obtained introducing two Higgs doublets instead of one, each acquiring a vacuum expectation value different from zero. This results in the prediction of five physical states, three neutral, h, H, A and two charged $H^\pm$. In the absence of CP-violation two of the predicted states are CP-even (h, H) and the third one is CP-odd. Otherwise the physical states are CP-mixtures. Depending on how the fields introduced couple to fermions, the couplings of Higgs bosons are modified with respect to the SM ones. The most popular model is the one where one of the fields couple to up-type fermions, and the other to down-type fermions. This model is required by the Minimal Supersymmetric Standard Model, MSSM, one of the possible extensions of the SM. In this model and in certain regions of parameters space the coupling to tau leptons is greatly enhanced and the coupling to bosons suppressed.

Tau decays are especially suited to study the CP-properties in an extended Higgs sector, since spin correlations between the taus are sensitive to the CP-properties of the decaying resonance, and observables depending on the spin correlations can be built. Examples are the ϕ^* and ψ^*_{CP} variables defined in Ref. [83] and shown in Figure 1.24.
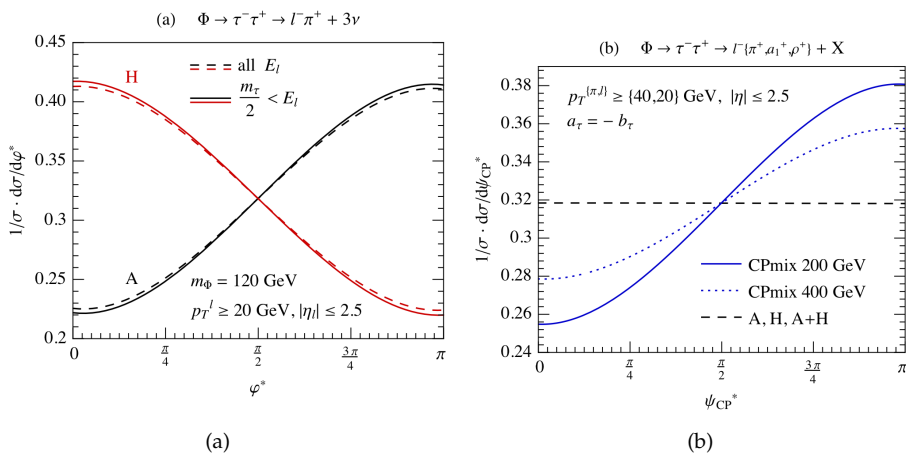

Figure 1.24: Distributions of the CP-sensitive ϕ^* and ψ^*_{CP} variables defined in Ref. [83].

The ATLAS detector at the LHC

ATLAS (A Toroidal Lhc ApparatuS) is one of the four main experiments at the Large Hadron Collider (LHC). In this chapter a brief introduction to the LHC collider and its physics environment is given, together with a description of the ATLAS detector. The methods for the reconstruction and identification of physics objects of interest for this work are reviewed, and some relevant performance results of the detector with pp collisions at $\sqrt{s} = 7$ TeV and $\sqrt{s} = 8$ TeV are presented.

2.1 The LHC collider

The LHC is designed to provide proton-proton collision at unprecedented high energy ($\sqrt{s}_{\text{design}} = 14$ TeV) and luminosity ($\mathcal{L}_{\text{peak}}^{\text{design}} = 10^{34} \text{cm}^{-2}\text{s}^{-1}$). It can also collide heavy ions (nucleon-nucleon centre-of-mass energy $\sqrt{s_{NN}} = 2.8$ TeV , $\mathcal{L}_{\text{HI,peak}}^{\text{design}} = 10^{27} \text{cm}^{-2}\text{s}^{-1}$). The LHC is built in a 27 km long tunnel. The proton beams are kept into their orbit by superconducting magnets operating at a temperature of 1.9 K and fields above 8 T and are accelerated and stored using a 400 MHz superconducting cavity system. The accelerator has both straight sections and arcs. In four of the straight sections there are interaction regions in which the beams share the same beam pipe and can be brought into collision. The four interaction points are surrounded by the LHC experiments: ATLAS and CMS are multipurpose experiments, designed to study high transverse momentum events for the search of the Higgs boson and phenomena beyond the SM, LHCb is an experiment devoted to the study of b-quark physics, while ALICE is optimised for the study of lead-ion collisions and the formation of a quark-gluon plasma. A schematic layout of the CERN accelerator complex, illustrating the LHC and its injection chain, is shown in Figure 2.1.

The LHC started operations on 10 September 2008, but immediately afterwards, during the commissioning phase, a major accident imposed a one year stop. During fall 2009 operations started again, culminating in the first 900 GeV collisions, recorded by the LHC experiments on 23 November 2009, and followed shortly after by collisions at 2.36 TeV, the highest energy ever reached before. For machine safety reasons it was decided to limit the maximum center of mass energy to 7 TeV, and the first collisions at this world record energy took place on 30th March 2010. In 2011 data were still taken at $\sqrt{s} = 7$ TeV, while the centre-of-mass energy was increased in 2012, reaching
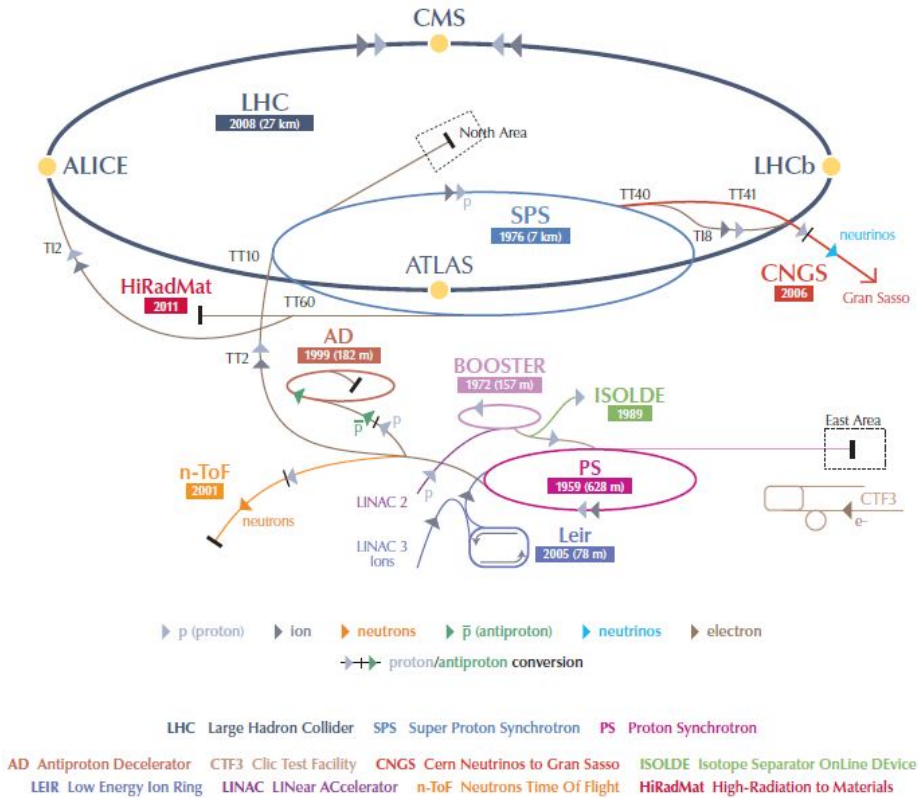
Figure 2.1: The CERN accelerator complex [84]. The injection of protons starts from the LINAC2, where protons receive a first acceleration. They are then further accelerated in the Booster, PS and SPS. They are injected in the LHC at an energy of 450 GeV, and then brought to the final beam energy.

$\sqrt{s} = 8$ TeV. Since 2010 the instantaneous and integrated luminosities of pp collisions have seen a huge increase, eventually reaching $\mathcal{L}_{\mathrm{peak}} = 7.73 \times 10^{33} \mathrm{cm}^{-2}\mathrm{s}^{-1}$ and $\int \mathcal{L} = 25$ fb in 2012. This high energy and luminosity has provided access to a number of rare SM processes, has pushed the search for new particles to the TeV scale and has culminated in the discovery of the Higgs Boson. Nominal energy and luminosity will be reached in 2015, after the Long Shutdown 1 phase, that is allowing for the consolidation of the LHC machine and experiment upgrades.

A direct consequence of the record luminosity reached by the LHC is a high level of pile-up. Pile-up is the effect of additional pp collisions in the same bunch-crossing as the hard scattering event or adjacent ones. Figure 2.2 shows the integrated luminosity delivered to ATLAS in 2010-2012 and the luminosity-weighted distribution of the mean number of interactions per bunch-crossing in 2011-2012.

During 2011 and 2012 runs of Pb-Pb and p-Pb collisions have been taken as well, but they are not discussed further since they are out of the scope of this work.
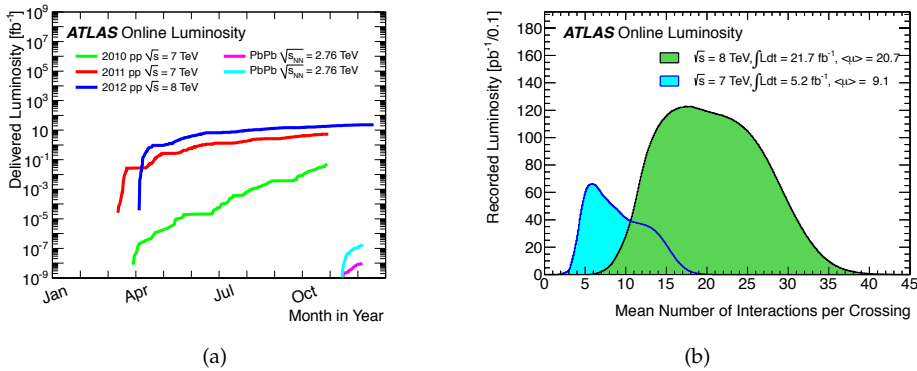
Figure 2.2: (a) Cumulative integrated luminosity versus day delivered to ATLAS during stable beams for p-p and Pb-Pb collisions. (b) luminosity-weighted distribution of the mean number of interactions per bunch-crossing for the ATLAS 2011 and 2012 data [3].

2.1.1 The physics program

The LHC physics program is very ambitious and covers a variety of topics in particle and nuclear physics. The main objectives are:

- The discovery of particles giving rise to spontaneous symmetry breaking in the SM.

- The test of the validity of the SM, with precision measurements of the W and top-quark masses and couplings and CP violation.

- The search for signatures beyond the SM.

- The study of properties of hadronic matter under extreme conditions. The transition to a state in which quarks and gluons are deconfined, called quark-gluon plasma, allows for insight in the behavior of matter at the dawn of time shortly after the Big Bang.

2.1.2 Detector requirements

The very high luminosity of the LHC is needed to pursue these objectives, since the cross-sections of the processes of interest are very low. Two main experimental difficulties then need to be met by experiments at the LHC: pile-up and the nature of proton-proton collisions itself. The second difficulty is related to the fact QCD processes dominate over the processes physicists are most interested in. This fact is illustrated in Figure 2.3, where the cross-sections for a few main QCD and electroweak processes are illustrated. Strong demands are therefore posed on the integrated luminosity needed and on the capability of the detectors of identifying experimental signatures characteristic of the processes under study.

The main requirements for detectors at the LHC are:

- **Fast response, high granularity and resistance to radiations.** The rates of events require a fast and sophisticated electronics, able to discriminate events, minimizing the effect of pile-up. A high granularity of the detector is necessary to handle the high particle fluxes. The detectors must be resistant to the high radiation doses, both in terms of operation and aging.

- **Trigger capabilities**. The output bandwidth of the detector is limited, and therefore the 40 MHz interaction rate must be reduced to ~ 400 Hz to be sent to permanent storage. The capability of triggering efficiently on interesting events with a very high background rejection is therefore crucial.

- **Full coverage**. The study of jets and of the energetic balance in the plane transverse to the beams is fundamental for the accomplishment of the physics goals. A fundamental requirement for this is a coverage over 2π in the azimuthal angle and $|\eta| < 5$ in pseudorapidity (for the definition of pseudorapidity see Section 2.2.1).

- **Particle identification**. The capability to reconstruct and identify electrons, muons, photons, tau leptons and jets is an essential requirement for the LHC experiments.
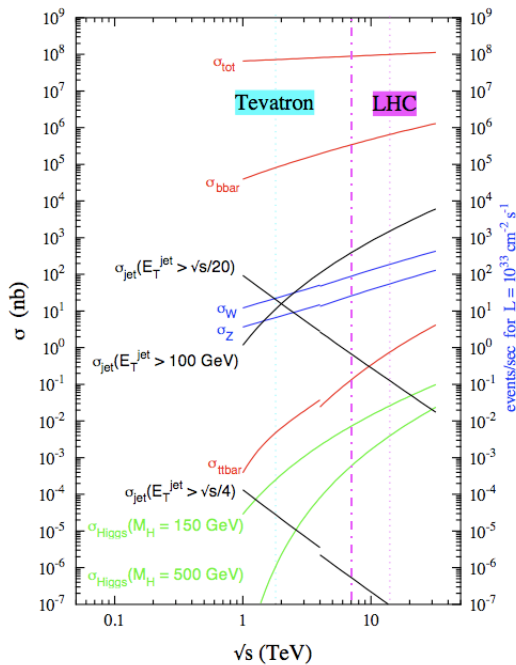

Figure 2.3: Production cross-sections for different SM processes at hadron colliders as a function of centre-of-mass energy. Operation points are marked: TEVATRON (dotted azure line) and LHC (the dotted magenta line indicates the nominal centre-of-mass energy $\sqrt{s} = 14$ TeV, the dotted dashed $\sqrt{s} = 7$ TeV). Discontinuities are due to the difference between $p\bar{p}$ collisions at the TEVATRON and pp at the LHC [85].

Further requirements for LHC experiments then are:

- **Simulation infrastructure**. In order to perform data analysis, signal and background predictions, including a detailed simulation of the detector response, need to be available.

- **Data storage and distribution infrastructure**. The amount of data recorded by LHC experiments is of the order of 15 petabytes per year. The capability of storing and providing access to data to analysts efficiently is fundamental for a successful physics program.

2.2 The ATLAS detector

The ATLAS detector surrounds the interaction region at point 1 of the LHC collider. It was completed in 2008 after five years of assembly works. ATLAS is a giant multi-purpose detector. Even though its performances are aimed at the Higgs search, it can cope with the study of a variety of phenomena. In the following the general layout and nominal performances are briefly reported, together with a description of the main subsystems. A complete description of the detector can be found in Ref. [86].

2.2.1 General layout

The general layout of ATLAS is shown in Figure 2.4. The detector has a cylindric symmetry. Its dimensions are 25 m in height and 44 m in length, while the overall weight is approximately 7000 tonnes.

The coordinate system used to describe the ATLAS detector originates from the nominal interaction point, at the centre of the detector. The beam direction defines the $z-$axis, and the x-y plane is transverse to the beams. The positive y-axis is defined as pointing upwards, whereas the x-axis points to the centre of the LHC. The azimuthal angle ϕ is measured around the z-axis, and θ is the polar angle from the beam axis. The pseudorapidity is defined as $\eta = -\ln\left(\tan\frac{\theta}{2}\right)$. Transverse quantities, such as the transverse three-momentum (p_T), the transverse energy (E_T) and the missing transverse momentum ($E_\mathrm{T}^\mathrm{miss}$), are defined in the x-y plane. The ΔR distance in the pseudorapidity-azimuth space is defined as $\Delta R = \sqrt{\Delta\eta^2 + \Delta\phi^2}$.

The main subsystems comprise the inner tracking detector (ID), the electromagnetic calorimeter, the hadronic calorimeter, the muon spectrometer (MS) and the luminosity detectors. They are described in the following sections together with the trigger system. The general requirements for the LHC experiments translate into nominal detector performance goals for the ATLAS detector as reported in Table 2.1.

2.2.2 Magnetic system

The ATLAS magnetic system is the most characteristic sub-system, and determines the structure of the ATLAS experiment itself, as it is shown in Figure 2.5. Its dimensions are 22 m in diameter and 26 m in length. The system comprises four large superconducting magnets, that provide an intense magnetic field over a volume of $\sim 12\,000\mathrm{m}^3$.
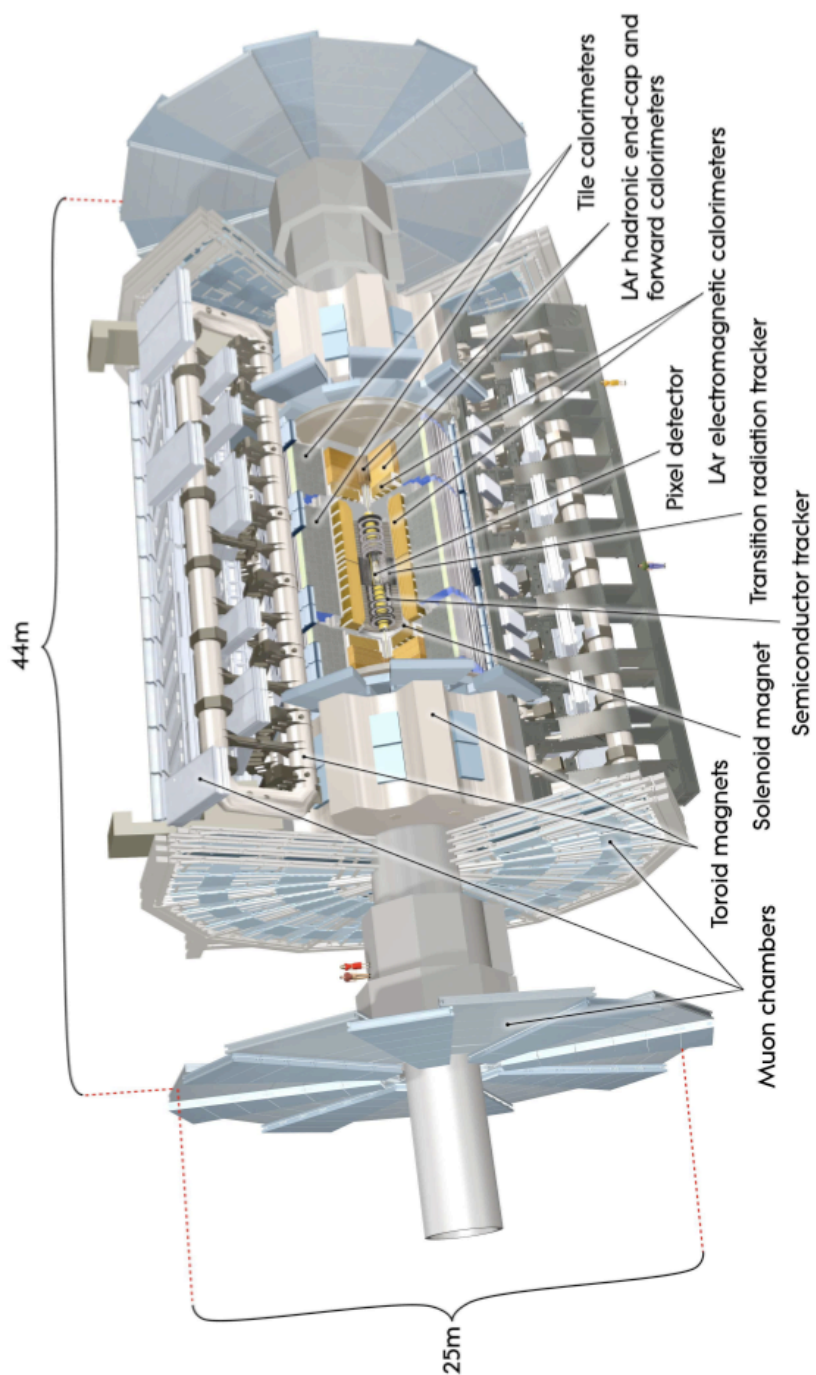
Tile calorimeters

LAr hadronic end-cap and
forward calorimeters

LAr electromagnetic calorimeters

Pixel detector

LAr electromagnetic calorimeters

Transition radiation tracker

Semiconductor tracker

Solenoid magnet

Toroid magnets

Muon chambers

44m

25m

Figure 2.4: General layout of the ATLAS detector [86].

Detector component	Required resolution	η coverage
Tracking	$\sigma_{p_T}/p_T = 0.05\% \, p_T \oplus 1\%$	$\pm\,2.5$
		($\pm\,2.0$ for the TRT)
EM calorimetry	$\sigma_E/E = 10\%/\sqrt{E} \oplus 0.7\%$	$\pm\,3.2$
		($\pm\,2.5$ for the trigger)
Hadronic calorimetry		
barrel and end-cap	$\sigma_E/E = 50\%/\sqrt{E} \oplus 3\%$	$\pm\,3.2$
forward	$\sigma_E/E = 100\%/\sqrt{E} \oplus 10\%$	$3.1 < |\eta| < 4.9$
Muon spectrometer	$\sigma_{p_T}/p_T = 10\%$ at $p_T = 1$ TeV	$\pm\,2.7$
		($\pm\,2.4$ for the trigger)

Table 2.1: Nominal detector performance goals and coverage for the ATLAS detector [86].
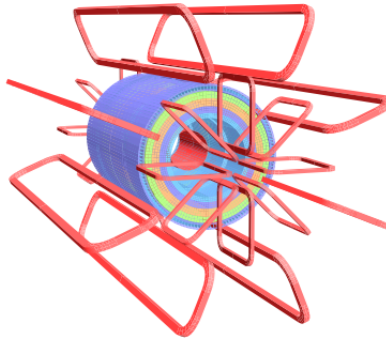
Figure 2.5: ATLAS magnetic system layout [86].

The central solenoid provides a 2 T magnetic field along the experiment z-axis. The ID is immersed in this field. The contribution of the solenoid to the material budget in front of the calorimeter is ~ 0.66 radiation lengths at normal incidence.

The magnetic system for the MS is generated by three large air-core toroids. The field is centred on the $z-$axis and perpendicular to the ID field. The barrel toroid has 9.4 m inner diameter, 20.1 m outer diameter and 25.3 m length. The two end-cap toroids, with 1.65 m inner diameter, 10.7 m outer diameter and 5.0 m length are inserted at each end of the barrel toroid, and line up with the solenoid. Each of three toroids consists of eight superconducting coils. The barrel toroid coils are housed in separate cryostats, with linking elements providing the overall mechanical stability. The end-cap toroids coils are assembled as a single cold mass and housed in the same cryostat. The end-cap toroid coil system is rotated by $22.5°$ with respect to the barrel toroid coil system to optimise the performance in the field overlap region.

The barrel toroid provides 1.5-5.5 Tm of bending power in the pseudorapidity range

$0 < |\eta| < 1.4$, and the end-cap toroids approximately 1-7.5 Tm in the region $1.6 < |\eta| < 2.7$. The bending power is lower in the transition regions where the two magnets overlap $(1.4 < |\eta| < 1.6)$.

2.2.3 Inner detector

The ID [87] is devoted to the measurements of charged particles tracks. This task is essential for the reconstruction of charged particles and their momentum measurement. The ID allows the reconstruction of primary and secondary vertices. The latter are signature of b-quark originated jets and tau leptons. Finally the ID provides fundamental particle identification information. Since the environment at the LHC is very busy, the granularity of the detector needs to be fine.

The ID is the system nearest to the beam pipe. Its overall dimensions are 2.1 m in diameter, 6.2 m in length. The system comprises three sub-detectors: the Pixel Detector, the Semiconductor Tracker (SCT) and the Transition Radiation Tracker (TRT), as shown in Figure 2.6.
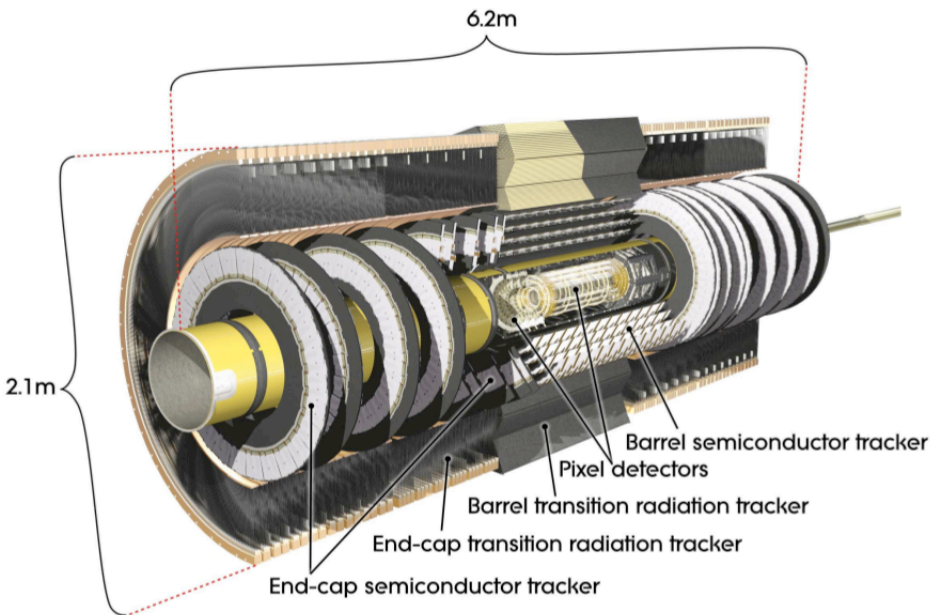

Figure 2.6: ATLAS ID layout [86].

The innermost sub-detector is the Pixel detector, which is made up by three cylindrical layers of silicon pixels in the barrel region and three disks in each end-cap. The granularity is very fine, with a pixel size in R-$\phi \times z$ of 50×400 μm^2, allowing for an intrinsic accuracy of better than 10 μm (R-ϕ) and 115 μm (η). This detector allows high precision measurements, with three expected hits per track, the inner layer one as close as ~ 2 cm to the beam pipe. The Pixel tracker allows as well for a time-over-threshold

measurement for the signal, that can be used for the measurement of the energy loss in the single detector elements. More details about the Pixel detector are given in Chapter 5. The pixel technology provides very high quality measurements, but its usage is limited to the most internal region, where a better track resolution is needed, by the cost and the enormous number of read-out channels, about 80.4 million.

Behind the Pixel detector the SCT completes the high precision tracking, with eight expected hits per track. The barrel comprises 4 cylindrical layers of modules of silicon microstrips, each made up by two sensors at a 40 mrad stereo angle in order to measure both coordinates. The pitch of the strip is about 80 μm. The end-cap is made up by 9 disks. The intrinsic accuracies of the SCT are 17 μm (R-ϕ) and 580 μm (η) and the total number of channels is approximately 6.3 million.

The TRT is made up by 4 mm straw tubes, arranged parallel to the beams in the barrel region and radially in the end-caps. The R-ϕ information only is provided, with an intrinsic accuracy of 130 μm per straw. A large number of hits per track is expected in this detector, about 36, and the total number of channels is about 351,000.
The TRT contributes both to tracking and particle identification. Its tubes are interleaved with layers of polypropylene fibres and foils: a charged particle that passes through the boundary region between materials with a different refraction index emits X-ray radiation whose intensity is proportional to the relativistic γ factor. The TRT works with two threshold levels, the ratio of the high threshold hits versus all the hits can be used to discriminate electrons and hadrons between them.

2.2.4 Calorimetry

The calorimeters purpose is to measure the energy of particles, together with their position, from their energy deposits. Moreover they limit the punch-through of particles towards the muon system and provide the η coverage crucial for the measurement of the transverse missing momentum. The calorimeter is divided into an electromagnetic compartment (EMCal), dedicated to the measurements of electrons and photons, and a hadronic compartment (HadCal), suited for jet reconstruction and missing tranverse momentum measurements.
The general layout of the calorimetric system is shown in Figure 2.7.

In order to cope with the demanding high luminosity environment, the EMCal [88] is realized as a lead-LAr (liquid argon) ionization chamber, that has good characteristics in terms of electronic noise, energy resolution, radiation resistance and possibility of reaching a high granularity. The EMCal is divided into two half-barrels (covering the $|\eta| < 1.4$ region) and two end-caps ($1.4 < |\eta| < 3.2$) each subdivided into two coaxial wheels. The region between the barrel and end-cap EMCal, $1.37 < |\eta| < 1.52$, is expected to have poorer performance because of the lack of instrumented material. It is often referred to as overlap region. To ensure the maximum azimuthal coverage the EMCal was designed with an accordion geometry: the read-out electrodes and lead absorbers are laid out radially and folded so that particles can not cross the calorimeter without being detected. The electrodes work as transmission lines as well, so that no dead regions must be introduced.
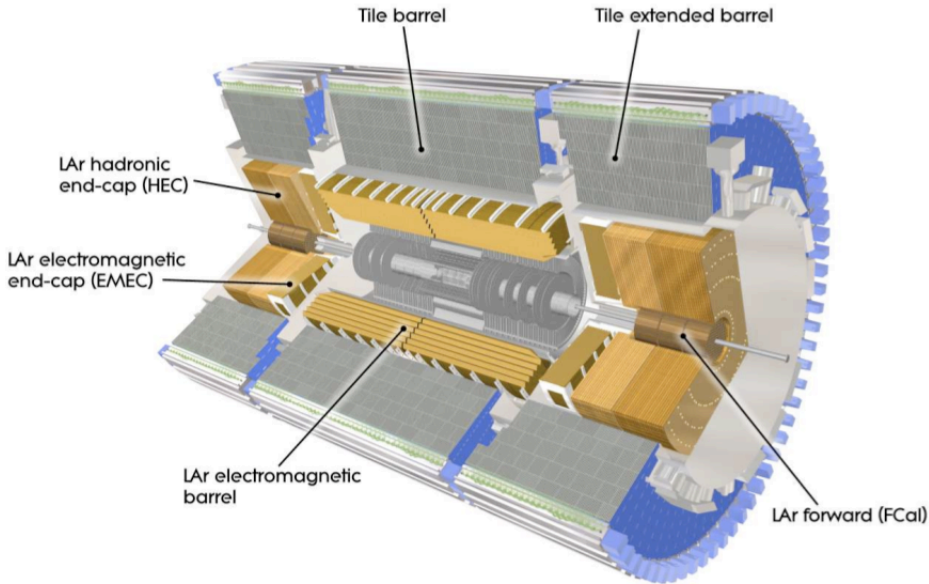
Figure 2.7: ATLAS calorimeters layout [86].

The barrel is segmented into three regions in depth (strips, middle and back) for a total depth of > 22 radiation lengths. Most of the energy of electrons and photons is collected in the middle. The fine granularity of the strips is necessary to improve the γ-π^0 discrimination. The back instead measures the tails of highly energetic electromagnetic showers and helps to distinguish electromagnetic and hadronic deposits. The end-cap inner wheel is segmented in just two regions, for a total depth of > 24 radiation lengths. The region $|\eta| < 1.8$ is equipped with a presampler, that allows to correct for the energy lost upstream in the tracker and in the calorimeter cryostat, that contains the solenoid coil.

The HadCal is realized with a variety of techniques depending on the region: central, end-cap and forward.

The central region is instrumented with the Tile Calorimeter (TileCal) [89], a sampling steel-scintillator detector. It is divided into a barrel ($|\eta| < 1.0$) and two extended barrels ($0.8 < \eta < 1.7$). There are three segmentations in depth, for a total depth of 9.7 interaction lengths (at $\eta = 0$). The read-out cells in pseudorapidity are pseudo-projective towers towards the interaction region.

The Hadronic End-cap Calorimeter (HEC) is a LAr-copper detector, and covers the region, $1.5 < |\eta| < 3.1$, overlapping both with the TileCal and the Forward Calorimeter.

The Forward Calorimeter (FCal) covers the $3.1 < |\eta| < 4.9$ region and is a LAr detector. The absorber material is copper, optimal for electromagnetic measurements, in the first segmentation in depth, and tungsten for the remnant two segmentations, which is more

suited to energy measurements of hadrons. Due to the high radiation dose expected in this region, a different electrode layout is preferred, consisting of a structure of concentric rods and tubes parallel to the beam axis. The total depth of this sub-detector is 10 interaction lengths, severely limited by the radiation doses that force to pull back the FCal with respect to the LAr.

2.2.5 Muon system

Ideally muons are the only charged particles that can traverse the calorimeters. They are measured by a large air-core muon spectrometer [90], whose layout is shown in Figure 2.8, in order to minimize the effect of multiple scattering.
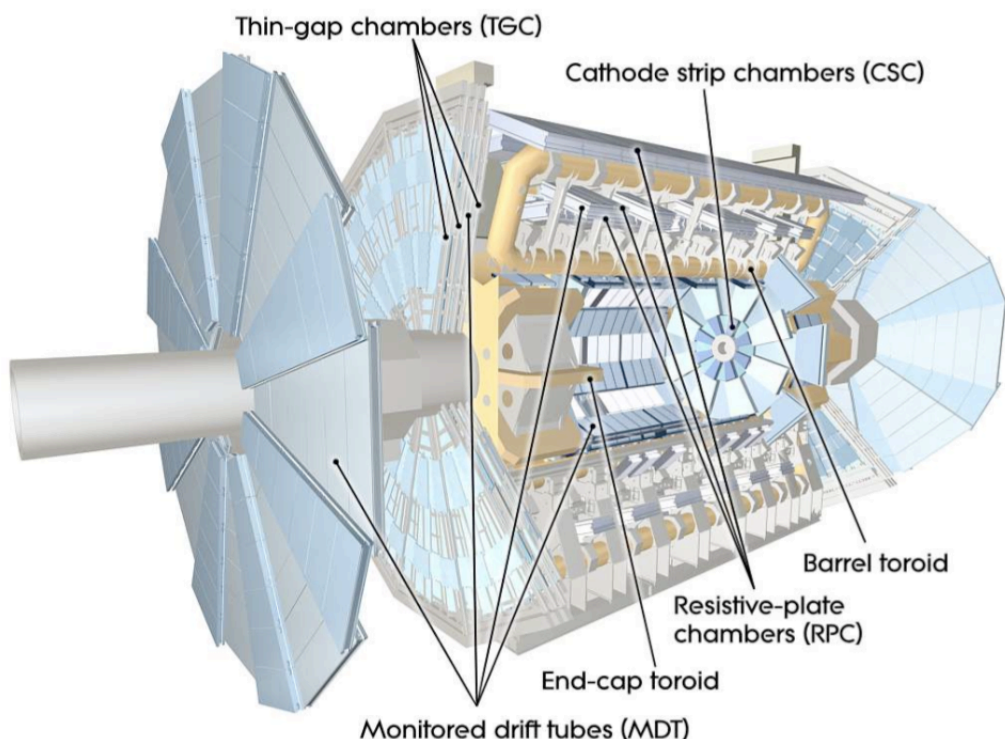
Figure 2.8: ATLAS muon system [86].

There are two different functions the muon chambers must accomplish: triggering and high precision tracking. The trigger system covers the region up to $|\eta| < 2.4$, and is composed by Resistive Plate Chambers (RPCs) in the barrel and Thin Gap Chamber (TGC) in the end-caps. The triggering system provides bunch-crossing identification (BCID), well-defined p_T thresholds and a measurement of the muon coordinate in the direction orthogonal to the chambers dedicated to precision tracking.

The tracking is performed by Monitored Drift Tubes (MDTs) in the central region and

Cathod Strips Chambers (CSCs) at large pseudorapidities. High precision mechanical assembly techniques and optical alignment systems provide the essential alignment of the chambers, while the magnetic field reconstruction relies on Hall sensors distributed throughout the spectrometer volume.

2.2.6   Luminosity detectors

An essential task for the detector is to determine precisely the luminosity recorded by the experiment. This is accomplished by redundant measurements, taken by three very forward detectors: the LUCID (LUminosity measurement using Cerenkov Integrating Detector), ALFA (Absolute Luminosity for ATLAS) and ZDC (Zero-Degree Calorimeter). In addition the Minimum Bias Trigger Scintillators (MBTS), mounted in front of the electromagnetic end-caps, have been used as luminosity detectors in early data analysis, beyond providing a minimum bias trigger signal. Information from the Bunch-Crossing Monitor (BCM) is used in luminosity measurements as well, in particular at high luminosity.

2.2.7   Trigger, read-out, data acquisition, and control systems

The ATLAS trigger system must be able to select interesting events while keeping the background rate low. The main difficulties are the high luminosity, corresponding to a rate of $\sim 10^9$ Hz pp interactions at nominal conditions, the low cross-sections of interesting processes and the bandwidth, that is nominally limited to 200 Hz. The system is implemented in three levels, each step providing a refinement of the decision by more sophisticated algorithms and lower rates. The first level (L1) is hardware-based and makes an initial decision based on timing from an electrostatic beam pick-up (BPTX), coarse detector information from muon trigger chambers and towers of calorimeter cells, together with multiplicity information from the MBTS and very forward detectors. The L1 provides regions of interest (RoIs) to the two further levels, that make up the high level trigger (HLT). The signatures the L1 looks for are high p_T electrons and photons, jets, hadronic tau decays and large values of missing transverse momentum. The L1 nominal output rate is ~ 100 kHz.

The L1 passes the RoI information to the HLT, which is composed by the second level trigger (L2) and the Event Filter (EF) and runs on a dedicated processor farm. The L2 examines the RoIs using more detector information than L1, and working in parallel on more RoIs and sub-detectors with more complete algorithms. The nominal output rate of L2 is about 1 kHz. The EF then has access to the complete event and uses reconstruction algorithms similar to the offline ones. At the EF the output rate is then reduced to approximately 200 Hz nominal rate. Several trigger chains that target different signatures are implemented. The set of trigger chains that are activated in a certain period takes the name of *trigger menu*. If a trigger output bandwidth is too large at any moment of the data taking run, it is possible either to deactivate it or *prescale* it, i.e. an established fraction of the events that fire a prescaled trigger are actually recorded.

After an event is accepted by the L1 trigger, the data are transferred off the detector to the Read Out Drivers (RODs), that are detector-specific functional elements of the front-

end systems. The first stage of the DAQ, the read-out system, receives and temporarily stores the data in local buffers. It is then solicited by the L2 trigger for the event data associated to RoIs. Those events selected by the L2 trigger are transferred to the event-building system and then to the event filter for final selection. Events selected by the event filter are moved to permanent storage at the CERN computer centre. In addition to the movement of data, the data acquisition also provides for the configuration, control and monitoring of the hardware and software components which together guarantee the data-taking functionality.

A scheme of the Trigger and Data Acquisition systems (TDAQ) is shown in Figure 2.9. Nominal values are shown, together with values for the 2012 operation in the gray blocks.
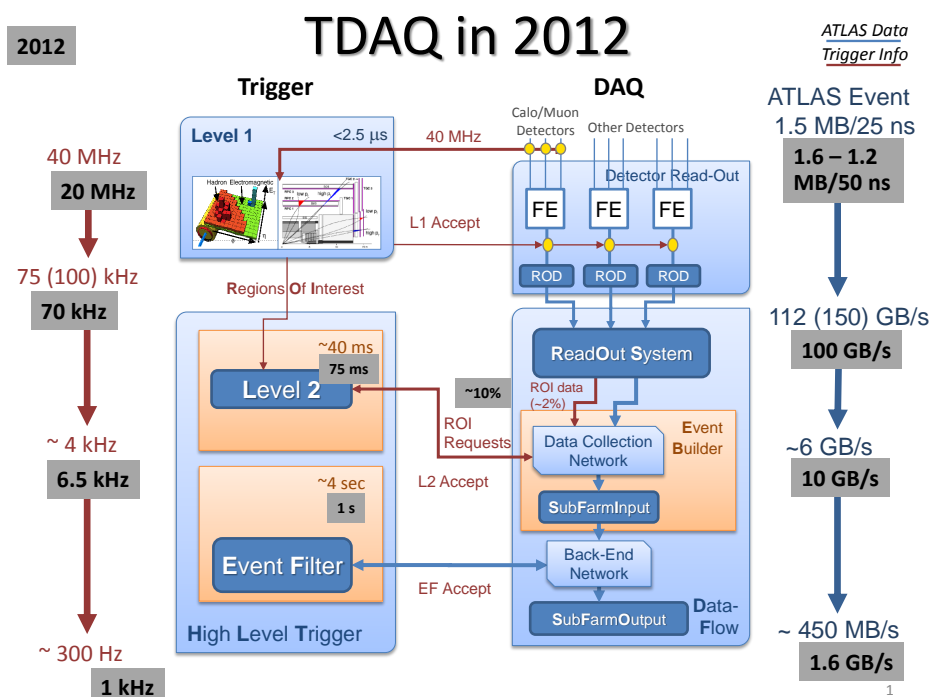
Figure 2.9: Overview of the ATLAS TDAQ system [3]. Details are given in the text.

The safe and coherent operation of the detector is ensured by the Detector Control System (DCS) that serves as a homogeneous interface to all sub-detectors and to the technical infrastructure of the experiment. The DCS puts the detector hardware into selected operational conditions, continuously monitors and archives its run-time parameters, signals any abnormal behaviour to operators and allows automatic or manual corrective actions to be taken. The DCS communicates with the TDAQ system in order to synchronise the state of the detector with data-taking. Moreover it handles the communication between the sub-detectors and other systems which are controlled independently.

2.2.8   Computing model

The amount of data collected by the ATLAS experiment is huge, so that simple distribution of large fractions of data to institutes worldwide would be impossible. The challenge of storing and processing data is met by the Grid paradigm and a high degree of decentralisation and sharing of computing resources.

There is a hierarchical structure where the primary event processing is carried out at the CERN Tier-0 facility. The raw data then are stored at CERN and copied to ten Tier-1 facilities, which are regional computing centres distributed around the world. These facilities can archive the data as well as provide reprocessing capabilities and data access. Derived datasets are copied to Tier-2 facilities, that allow for further analysis, and moreover provide simulation resources. Finally Tier-3 centers provide access to Grid resources and local storage for end-user data, as well as providing resources for simulation and analysis when possible. Calibrations based on processing raw data are produced at a CERN Analysis Facility, as well as at some Tier-2 centres. The ATLAS computing model is described in detail in Ref. [91]. Only a few particularly relevant aspects of the software infrastructure are detailed in the following Sections 2.2.9-2.2.11. Aspects relating to data quality information management are outlined in Section 2.2.12.

2.2.9   Reconstruction software

The global ATLAS software framework, Athena [91], has been optimised to be installed, configured and run on different types of computer facilities. It uses Python as on object-oriented scripting language to configure and load C++ packages. The Athena framework is based on GAUDI [92], originally developed by the LHCb experiment. Athena allows to process events delivered by the TDAQ system in different formats corresponding to the various reconstruction stages. Moreover it provides some tools for data analysis. The data formats are:

- *Byte-stream data*: a persistent representation of the data flow from the HLT.

- *Raw data object* (RDO): C++ object representation of the byte-stream data.

- *Event summary data* (ESD): full output of the detector reconstruction. It contains sufficient information to allow particle identification, track re-fitting, jet calibration, etc., thus allowing for the rapid tuning of reconstruction algorithms and calibrations.

- *Analysis object data* (AOD): summary of the reconstructed event. It contains sufficient information for all common analyses.

- *Derived tertiary physics datasets* (D3PD): flat ROOT ntuple format, customised for different combined performance and physics groups.

The goal of reconstruction is to build and calibrate objects in input to physics analysis, which are characterised by relatively few parameters. Example of these objects are photons, electrons, muons, hadronically decaying tau leptons, jets, missing transverse

momentum, interaction vertices. A typical reconstruction algorithm takes one or more collections as input, calls a set of modular tools, and outputs typically one collection of reconstructed objects.

2.2.10 Geometry and conditions databases

Relational databases are used to store detector information [93]. They can be accessed by ATHENA jobs to perform the various steps of the data reconstruction or simulation. The geometry database stores the description of the detector, that is all the fundamental constants for detector construction. These are for example volume dimensions, rotations, and positions and material properties. The conditions database stores information such as calibrations, dead channel maps and misalignments. This information can be indexed by intervals of validity. Both databases support versioning of the data.

2.2.11 Simulation

Simulation is widely used in the context of the ATLAS experiment, since it allows the assessment of the physics potential of the experiment, the test of algorithms and calibrations used in data analysis, and it is essential in the determination of detector acceptances and efficiencies. The simulation process happens in three steps: event generation, detector simulation and digitisation. After digitisation the simulation output can be reconstructed using the same algorithms that are used for data.

Generators provide the kinematic information of particles produced in the proton-proton collision final state, following the predictions of SM and BSM models, as discussed in Section 1.2.3. It is possible to use filters at the generation level, in order to reject events that are not interesting for the channel under study. Generators decay particles with a proper lifetime $c\tau \leq 10$ mm as well.

The final state event is then passed through a detailed detector simulation and digitization program [94] based on GEANT 4 [95, 96]. Each particle is propagated through the full ATLAS detector, whose configuration, including misalignments and distortions, is read from databases. The energies deposited in the sensitive portions of the detector are recorded as *hits*, containing the total energy deposition, position, and time. The interactions that particles can undergo include bremsstrahlung, ionization, hadronic interaction, decay and photon conversion. For each interaction a limit on the energy of the produced particles can be set, to decide whether it is propagated into the detector or it is accounted for together with the particle from which it originated. *Physics lists* include all numerical models that describe the interactions of particles in the GEANT4 simulation. Starting from 2008 the default GEANT4 physics list for the ATLAS detector simulation is QGSP_BERT [97, 98, 99], typical alternative lists are QSGP and FTFP_BERT [100].

The ATLAS digitization software converts the hits produced in the detector simulation into detector responses called digits. Typically, a digit is produced when the voltage or current on a particular read-out channel rises above a threshold within a particular time-window. During digitization, effects from pile-up interactions are taken into account as well, by overlaying hits from the hard scattering events to hits from the required number of additional pp interactions. Since effects from interactions in bunch-crossings

preceding or following the hard scattering one need to be simulated, these interactions can have a time offset as well. Effects due to beam-gas and beam-halo are treated in the same way as pile-up.

2.2.12   The LHC Run-I pp collision datasets

LHC Run-I spans from 2009 to 2013. The datasets of interest in this work are the pp collision runs taken at $\sqrt{s} = 7$ TeV and $\sqrt{s} = 8$ TeV in 2010, 2011 and 2012. Over this period ATLAS was able to collect data with high efficiency and with an excellent level of data quality. The operational conditions of the detector have been excellent, as it is shown in Table 2.2 showing the number of channels and approximate operational fraction per sub-detector. Data taking efficiencies over 2010, 2011 and 2012 are shown in Figure 2.10.

Subdetector	Number of Channels	Approximate Operational Fraction
Pixels	80 M	95.0%
SCT Silicon Strips	6.3 M	99.3%
TRT Transition Radiation Tracker	350 k	97.5%
LAr EM Calorimeter	170 k	99.9%
Tile calorimeter	9800	98.3%
Hadronic endcap LAr calorimeter	5600	99.6%
Forward LAr calorimeter	3500	99.8%
LVL1 Calo trigger	7160	100%
LVL1 Muon RPC trigger	370 k	100%
LVL1 Muon TGC trigger	320 k	100%
MDT Muon Drift Tubes	350 k	99.7%
CSC Cathode Strip Chambers	31 k	96.0%
RPC Barrel Muon Chambers	370 k	97.1%
TGC Endcap Muon Chambers	320 k	98.2%

Table 2.2: Number of channels and approximate operational fractions for the ATLAS detector in 2012 [3].

In order to compute the luminosity and assess data quality each run of data taking is divided into luminosity blocks (LB), each corresponding to about one minute of data taking. Figure 2.11 shows a summary of the data collected in 2011 and 2012 at $\sqrt{s} = 7$ TeV and $\sqrt{s} = 8$ TeV, with some basic information. Data-taking runs are grouped in periods of similar conditions. The dates, the number of run ranges and the total number of runs are given. The *StableLum* column indicates the luminosity calculated for periods when the LHC had declared the beams were stable, whereas *Ready lum* restricts to the LBs where ATLAS was effectively taking data. *MaxInstLum* refers to the maximum instantaneous luminosity reached during the data taking period indicated. The *μMax*
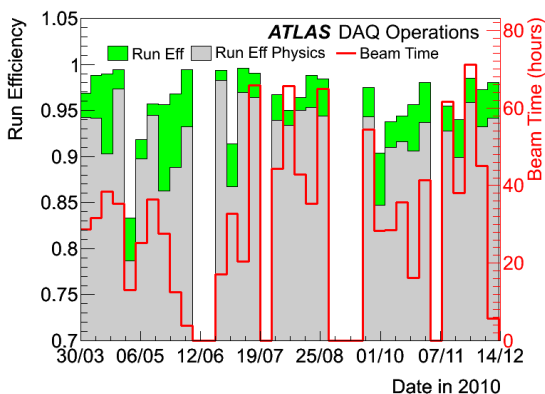
(a)
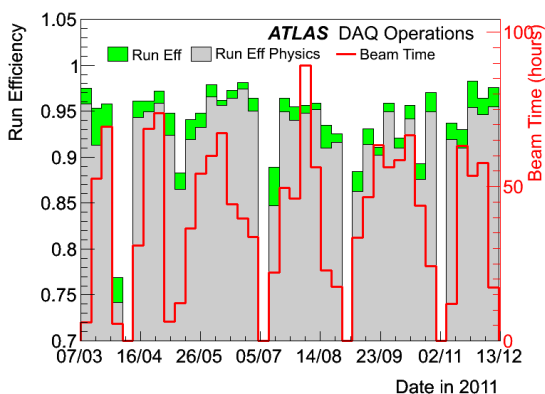
(b)
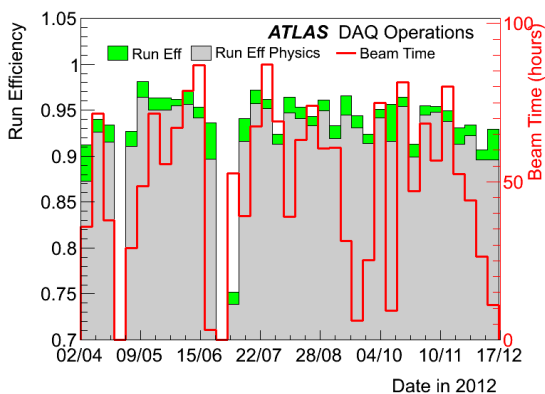
(c)

Figure 2.10: ATLAS data taking efficiencies in (a) 2010, (b) 2011 and (c) 2012 [3].

(Avg) column indicates the maximum number of interactions per bunch crossing averaged over all LBs. Finally some information about the LHC bunch-train structure over the periods of stable beams is given, namely the maximum number of colliding bunches *Bunch count* and the minimun bunch spacing *Bunch dt*.

Information about detector status and data quality is handled by a defect database system [101]. Defects are assigned by detector subsystems and combined performance groups based on automatic and human checks. Defects individuate specific detector and reconstruction problems. They are used to determine whether data is approved for use for physics analysis. The information on data quality decisions is made available to users through *good runs list* (GRL) files. An official tool is used to retrieve the luminosity corresponding to a specific GRL from a luminosity database. The luminosity weighted relative fraction of good quality data delivered by the various ATLAS subsystems during LHC fills with stable beams in *pp* collisions at $\sqrt{s} = 8$ TeV is shown in Figure 2.12.

Period	Date Range	Run Range	#	StableLum (pb^{-1})	Ready Lum	MaxInstLum (10^{30}cm^{-2}s^{-1})	μ Max (Avg)	Bunch dt (ns)
data10_7TeV **AllYear** *[A:I]*	10-Mar-30: 10-Oct-29	152166: 167844	126	46	44 (96%)	198	3.6	150 : 66825
A *[A1]*	10-Mar-30: 10-Apr-19	152166: 153200	19	4.3e-4	4.0e-4 (92%)	2.5e-3	1.6e-2	
B *[B1:B2]*	10-Apr-23: 10-May-17	153565: 155160	12	8.9e-3	8.7e-3 (98%)	6.5e-2	1.4e-1	5000 : 66825
C *[C1:C2]*	10-May-17: 10-Jun-05	155228: 156682	8	9.6e-3	8.8e-3 (92%)	2.2e-1	1.8e-1	2500 : 5000
D *[D1:D6]*	10-Jun-24: 10-Jul-19	158045: 159224	21	3.2e-1	3.1e-1 (97%)	1.5	2.1	2500 : 44625
E *[E1:E7]*	10-Jul-29: 10-Aug-18	160387: 161948	22	1.1	1.1 (97%)	3.8	1.5	2500
F *[F1:F2]*	10-Aug-19: 10-Aug-30	162347: 162882	10	2	1.9 (97%)	9.9	2	1000 : 1250
G *[G1:G6]*	10-Sep-22: 10-Oct-07	165591: 166383	18	9.4	9 (95%)	68	2.7	150
H *[H1:H2]*	10-Oct-07: 10-Oct-18	166466: 166964	9	9.1	8.6 (95%)	143	3.1	150 : 1250
I *[I1:I2]*	10-Oct-24: 10-Oct-29	167575: 167844	7	24	23 (96%)	198	3.6	150

(a)

Period	Date Range	Run Range	#	StableLum (pb^{-1})	Ready Lum	MaxInstLum (10^{30}cm^{-2}s^{-1})	μ Max (Avg)	Bunch Count	Bunch dt (ns)
data11_7TeV **AllYear** *[A:M]*	11-Mar-13: 11-Oct-30	177531: 191933	267	5434	5341 (98%)	3848	32	2 : 1842	25 : 8000
A *[A1:A2]*	11-Mar-13: 11-Mar-21	177531: 177965	12	9	8.7 (97%)	154	7.1	3 : 138	75 : 2500
B *[B1:B2]*	11-Mar-21: 11-Mar-24	177986: 178109	7	18	18 (97%)	247	9.2	138 : 194	75
D *[D1:D7]*	11-Apr-14: 11-Apr-29	179710: 180481	23	186	182 (98%)	659	7.3	214 : 598	50
E *[E1]*	11-Apr-30: 11-May-03	180614: 180776	5	53	52 (98%)	832	7.6	598 : 700	50
F *[F1:F3]*	11-May-15: 11-May-25	182013: 182519	17	160	156 (98%)	1100	8	14 : 874	50 : 1250
G *[G1:G6]*	11-May-27: 11-Jun-14	182726: 183462	28	572	566 (99%)	1263	7.9	874 : 1042	50
H *[H1:H4]*	11-Jun-16: 11-Jun-28	183544: 184169	13	287	283 (99%)	1264	6.8	1041 : 1318	50
I *[I1:I4]*	11-Jul-13: 11-Jul-29	185353: 186493	27	416	406 (97%)	1887	9.1	2 : 1331	50 : 2500
J *[J1:J2]*	11-Jul-30: 11-Aug-04	186516: 186755	9	240	237 (98%)	1995	9.6	1317	50
K *[K1:K6]*	11-Aug-04: 11-Aug-22	186873: 187815	19	685	676 (99%)	2328	11	1317	50
L *[L1:L7]*	11-Sep-07: 11-Oct-05	188902: 190343	59	1625	1599 (98%)	3252	16	250 : 1318	50
M *[M1:M10]*	11-Oct-06: 11-Oct-30	190503: 191933	48	1184	1160 (98%)	3848	32	2 : 1842	25 : 8000

(b)

Period	Date Range	Run Range	#	StableLum (pb^{-1})	Ready Lum	MaxInstLum (10^{30}cm^{-2}s^{-1})	μ Max (Avg)	Bunch Count	Bunch dt (ns)
data12_8TeV **AllYear** *[A:M]*	12-Apr-04: 12-Dec-16	200804: 216432	308	22754	22306 (98%)	7562	36	1 : 1380	25 : 44625
A *[A1:A8]*	12-Apr-04: 12-Apr-20	200804: 201556	29	910	892 (98%)	5363	30	2 : 1331	50 : 44625
B *[B1:B14]*	12-May-01: 12-Jun-18	202660: 205113	72	5594	5474 (98%)	6616	31	75 : 1380	50
C *[C1:C9]*	12-Jul-01: 12-Jul-24	206248: 207397	34	1643	1614 (98%)	6164	34	1 : 1368	25 : 24300
D *[D1:D8]*	12-Jul-24: 12-Aug-23	207447: 209025	48	3598	3532 (98%)	7265	34	32 : 1368	50
E *[E1:E5]*	12-Aug-23: 12-Sep-17	209074: 210308	29	2863	2808 (98%)	7562	36	1368	50
G *[G1:G5]*	12-Sep-26: 12-Oct-08	211522: 212272	18	1404	1380 (98%)	7205	34	72 : 1368	50
H *[H1:H6]*	12-Oct-13: 12-Oct-26	212619: 213359	22	1655	1617 (98%)	7450	35	72 : 1368	50
I *[I1:I3]*	12-Oct-26: 12-Nov-02	213431: 213819	14	1149	1126 (98%)	7237	34	1368	50
J *[J1:J8]*	12-Nov-02: 12-Nov-26	213900: 215091	29	2941	2890 (98%)	7367	35	29 : 1368	50 : 1000
L *[L1:L3]*	12-Nov-30: 12-Dec-06	215414: 215643	10	983	961 (98%)	7420	36	60 : 1368	50
M *[M1]*	12-Dec-15: 12-Dec-16	216399: 216432	3	14	13 (97%)	572	12	97 : 373	25

(c)

Figure 2.11: Summary of the (a) 2010, (b) 2011 and (c) 2012 datasets. More details are given in the text [102].

Inner Tracking Detectors			Calorimeters				Muon Detectors			
Pixel	SCT	TRT	LAr EM	LAr HAD	LAr FWD	Tile	MDT	RPC	CSC	TGC
99.1	99.9	100	90.7	96.6	97.8	100	99.9	99.8	96.2	99.8

Luminosity weighted relative detector uptime and good quality data delivery during 2010 stable beams in pp collisions at √s=7 TeV between March 30th and October 31st (in %). The inefficiencies in the LAr calorimeter will partially be recovered in the future.

(a)

ATLAS 2011 p–p run											
Inner Tracking			Calorimeters				Muon Detectors				Magnets
Pixel	SCT	TRT	LAr EM	LAr HAD	LAr FWD	Tile	MDT	RPC	CSC	TGC	Solenoid	Toroid
99.8	99.6	99.2	97.5	99.2	99.5	99.2	99.4	98.8	99.4	99.1	99.8	99.3

Luminosity weighted relative detector uptime and good quality data delivery during 2011 stable beams in pp collisions at √s=7 TeV between March 13th and October 30th (in %), after the summer 2011 reprocessing campaign

(b)

ATLAS p-p run: April-December 2012									
Inner Tracker			Calorimeters		Muon Spectrometer				Magnets
Pixel	SCT	TRT	LAr	Tile	MDT	RPC	CSC	TGC	Solenoid	Toroid
99.9	99.1	99.8	99.1	99.6	99.6	99.8	100.	99.6	99.8	99.5
All good for physics: 95.5%									

Luminosity weighted relative detector uptime and good quality data delivery during 2012 stable beams in pp collisions at √s=8 TeV between April 4th and December 6th (in %) – corresponding to 21.3 fb⁻¹ of recorded data.

(c)

Figure 2.12: Data quality for the (a) 2010, (b) 2011 and (c) 2012 datasets, more details are given in the text [3].

2.3 ATLAS reconstruction and performance

In this section a brief introduction to the ATLAS reconstruction of the physics objects of interest in this work is given. The performance of reconstruction, identification and calibration for various objects is reviewed.

In the following "tag-and-probe" method refers generically to a method where a sample of events from a specific process is selected by a tight selection on one or more of the objects in the event and a loose selection on the object of interest, on which measurements, for example of identification efficiencies, are performed.

2.3.1 Tracking and vertexing

The reconstruction of tracks is a key ingredient for the reconstruction algorithms of many physics objects of interest in this work. Track quality information, such as the number of hits in the various tracking layers, and track properties, such as the impact parameter, are used in various reconstruction and identification algorithms. Vertexing is fundamental in providing the position of the primary vertex in the event, that is used by reconstruction algorithms as well. Secondary vertices play an important role for objects originated from decays of tau leptons and b-quarks. These particles decay within the beam pipe but their lifetime is long enough to individuate the decay vertex. Finally the reconstruction of additional vertices is important in controlling the effects of pile-up.

Details on the tracking algorithms used in ATLAS can be found in Ref. [103]. The ATLAS tracking algorithms follow an inside-out sequence that starts from seed finding in the silicon layers. Seeds are then used to build roads, within which hits may be found while moving towards the outer edge of the silicon detector. Finally, the search is extended to the TRT and the collection of hits is fit to obtain the final track parameters.

Tracking efficiency is defined as the ratio between the number of matched tracks and the number of generated charged particles. As such, it must be inferred from simulation. Its reliability is based on the good agreement of simulation to data for the relevant tracking distributions, such as the number of hits on track for the three sub-detectors, that have been tested thoroughly with collisions and cosmic ray data. The tracking efficiency as a function of transverse momentum and pseudorapidity, obtained from a special simulation with no pile-up, is shown in Figure 2.13.

Vertices are found following an iterative vertex finding approach, that employs the adaptive vertex fitting algorithm [104]. Figure 2.14 shows the efficiency of reconstructing and selecting the primary vertex as a function of the average number of interactions per bunch-crossing. The efficiency depends on the event topology and on the selection, so $t\bar{t}$, $Z \to \mu^+\mu^-$ and $Z \to e^+e^-$ events are considered. Figure 2.15 shows the resolution on the x and z vertex coordinates as a function of the number of tracks. In this case data from a special low pile-up run is superimposed as well.
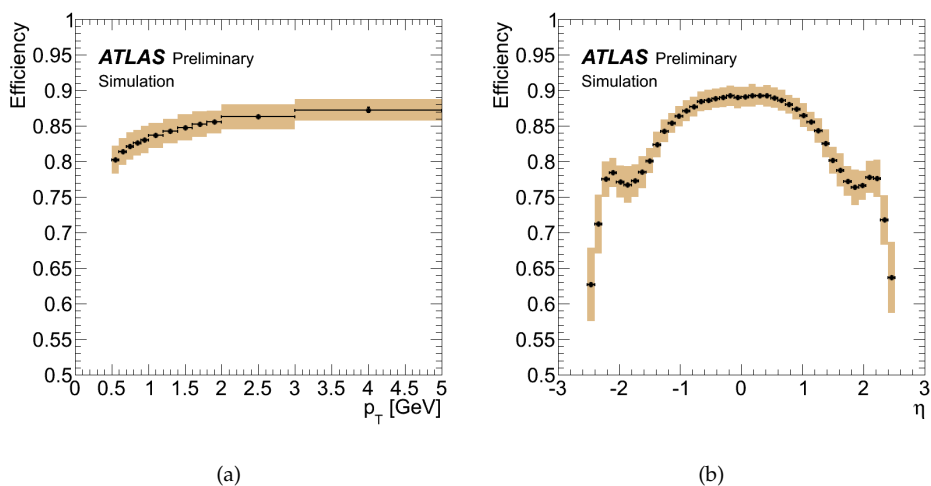
Figure 2.13: Track reconstruction efficiency (a) as a function of p_T, (b) as a function of η. The coloured band shows the effects of selection cuts and detector material on the efficiency.
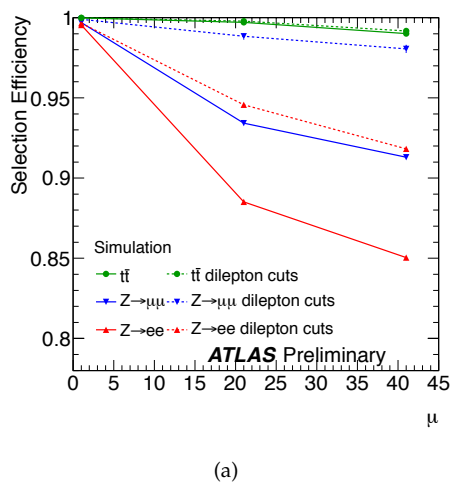
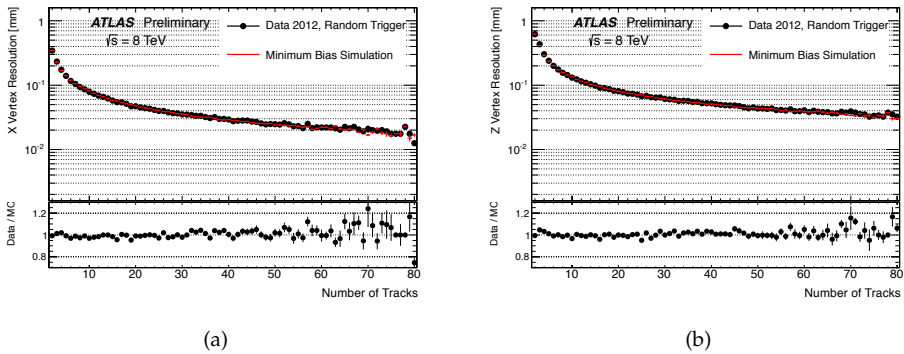**Figure 2.14:** Vertex reconstruction and selection efficiency as a function of μ [3].

Figure 2.15: Resolution on the (a) x (b) z vertex coordinates [3].

2.3.2 Electrons and photons

Electrons and photons are of great interest in ATLAS since they enter several analyses, both within the SM and beyond it. Inclusive electron measurements are necessary to evaluate the b-quark and c-quark production, are signature of W, Z, top and Higgs boson decays and possibly of decays of supersymmetric particles. In the context of this work in particular electrons play an important role, since tau leptons decay to electrons. Photons on the other hand are protagonists in direct photon measurements, that allow to test the gluon PDF, and in the measurement of the Higgs $H \to \gamma\gamma$ decay. Since photons are not used in the context of this work they will not be treated in detail.

The main signature of electrons and photons is the presence of a cluster in the EMCal. Electrons are then required to have a matching track in the ID, whereas photons are not allowed to have it. Electrons coming from conversions of photons in an e^+e^- pair in the detector material can be identified by missing hits in the tracker.

The electron and photon trigger, reconstruction and identification algorithms used in ATLAS are designed to achieve both a large background rejection and a high and uniform efficiency over the full acceptance of the detector, for transverse energies above 20 GeV [105, 106].

Electrons are triggered on using both information from the calorimeter and the tracker. At L1 electrons are searched for only in the calorimeter, and the trigger requirement is limited to a total transverse momentum threshold in adjacent calorimeter cell towers. At L2 fast calorimeter and tracking reconstruction algorithms are employed instead. The EF uses the same algorithms that are used offline. The expected trigger efficiencies for a few of the triggers used in the following are shown in Figure 2.16.

At the offline level, the search for electromagnetic objects starts using a sliding window algorithm, that looks for significant deposits in the EMCal. The size of these seed clusters corresponds to 3×5 cells in $\eta \times \phi$ in the middle (a cell has dimensions 0.025×0.025), and the transverse energy threshold is $E_T > 2.5$ GeV. Starting with 2012 data, tracks matched to clusters are refitted using a Gaussian Sum Filter-based model for

(a)   (b)
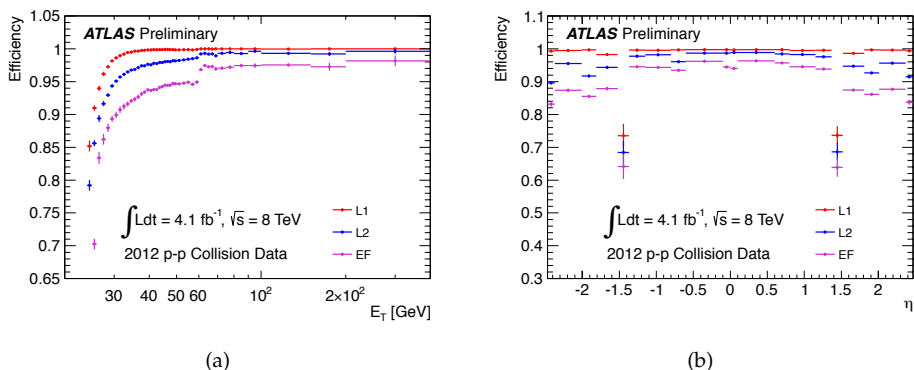
Figure 2.16: Trigger efficiencies at L1, L2 and EF as a function of (a) offline-reconstructed transverse energy and (b) offline reconstructed pseudorapidity for the standard single electron trigger in 2012 (`e24vhi_medium1 OR e60_medium1`) [3].

bremsstrahlung [107]. In the case of more matches the track closest in ΔR is considered. The electron cluster is then rebuilt using 3×7 longitudinal towers of cells. The cluster energy is determined considering contributions from the estimated energy deposit in the material in front of the EMCal, the measured energy deposit in the cluster, the estimated energy deposit outside the cluster, and the estimated energy deposit beyond the EMCal. The four terms are parametrised as a function of the measured cluster energies in the presampler detector (where it is present) and in the three EMCal longitudinal layers based on detailed simulation of energy deposition. The four-momentum is computed using the energy information of the final cluster and the direction of the best track matched to the original seed cluster. Requirements on the calorimeter operating conditions are applied at this point, that allow for the rejection of electrons reconstructed in badly functioning parts of the detector. Electron reconstruction efficiencies measured in data with a tag-and-probe method in $Z \rightarrow e^+ e^-$, $J/\Psi \rightarrow e^+ e^-$ and $W \rightarrow e\nu$ samples selected in data [106] and are shown in Figure 2.17.

The identification of electrons is based on cuts on calorimeter, tracking and combined variables. Three sets of cuts, *loose*, *medium* and *tight*, corresponding to approximate expected background rejection levels of 500, 5000 and 50000 respectively. The *loose* set of cuts includes requirements on EMCal middle layer and hadronic leakage variables, while the *medium* identification makes use in addition of information from the EMCal strip layer, from tracking and from track-cluster matching. Finally the *tight* set applies requirements on the particle E/p, identification information from the TRT detector, discrimination against photons using Pixel b-layer hit and reconstructed conversion vertices information. For all sets the cuts are optimised in 10 η bins. Identification efficiencies are measured exploiting a tag-and-probe method. Results are shown in Figure 2.18. Investigated sources of systematics uncertainty include the background level in the selected samples in data, the choice of discriminating variables used in the background estimation, and a possible bias in the background estimation method itself. The stability

of identification efficiencies with pile-up has been investigated for events with up to 30 primary vertices, and found to be robust within 3% in this range.

(a)

(b)
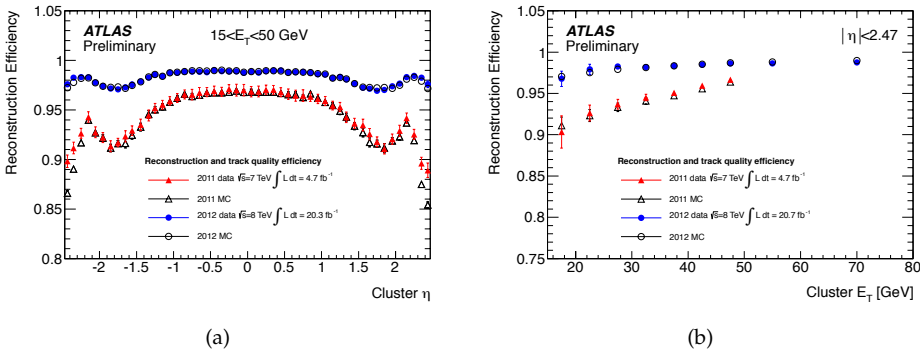
Figure 2.17: Electron reconstruction efficiencies as a function of (a) cluster η and (b) cluster E_T in 2011 and 2012 data [3].

(a)

(b)
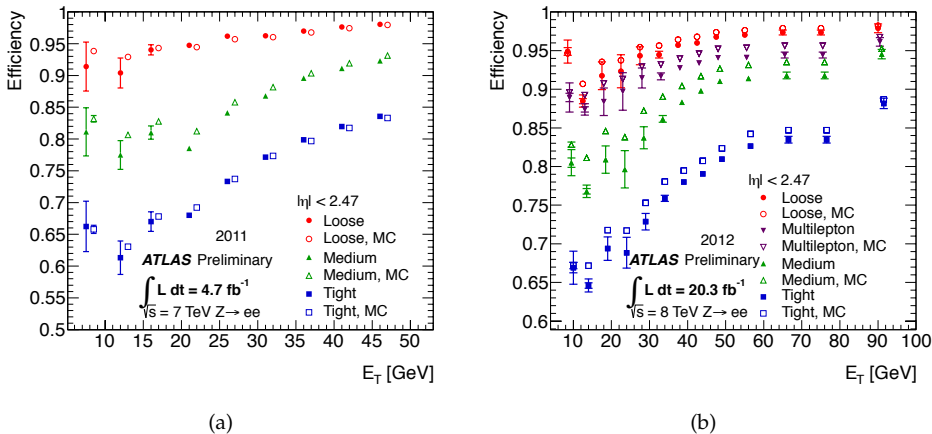
Figure 2.18: Electron identification efficiencies in data and simulation in (a) 2011 and (b) 2012 [3].

The energy scale of electrons is fixed by the calorimeter electromagnetic energy scale, which is determined from test-beam measurements. The knowledge of the electron energy scale is improved exploiting the known masses of the Z and J/Ψ particles. A strategy based on the ratio of the calorimeter energy measurements and tracker momentum measurement on a $W \rightarrow e\nu$ sample is employed as well. Sources of systematic uncertainties on the electron energy scale include the limited knowledge of the material budget in front of the calorimeter, the presampler detector energy scale, the calorimeter electronic calibration and cross-talk, non-linearities in the read-out electronics and the requirements on calorimeter operating conditions. The efficiency measurements using

$Z \rightarrow e^+e^-$, $J/\Psi \rightarrow e^+e^-$ and $W \rightarrow e\nu$ samples are affected by uncertainties due to background estimation methods, theoretical inputs and pile-up. Energy scale uncertainties as a function of the electron transverse momentum are shown in Figure 2.19 for two pseudorapidity regions.
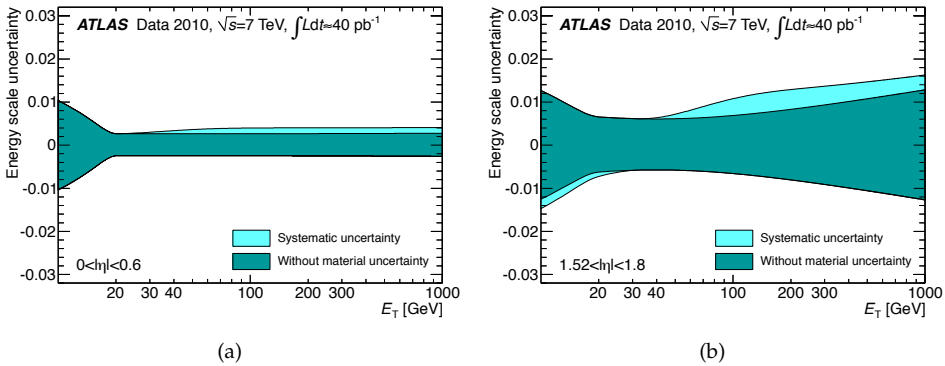
Figure 2.19: Electron total energy scale uncertainties as determined in 2010 data for the (a) $|\eta| < 0.6$ and (b) $1.52 < |\eta| < 1.8$ regions [106].

The fractional energy resolution is parametrised as

$$\frac{\sigma_E}{E} = \frac{a}{\sqrt{E}} \oplus \frac{b}{E} \oplus c \tag{2.1}$$

where the sampling term a, the noise term b and the constant term c are η-dependent parameters. The a parameter is very well known from studies of $J/\Psi \rightarrow e^+e^-$ events and is $a = 10\text{-}17\%$ as a function of η with a 10% uncertainty. The noise term is important only at low energies, and therefore the constant term c can be determined in $Z \rightarrow e^+e^-$ events as the term accounting for any residual resolution effects. Since great care was taken in the construction of the calorimeter to minimise all sources of response non uniformity, the constant term is $\sim 0.7\%$.

Electron isolation can be useful in many physics analysis to help separating prompt genuine electrons from b-quark and c-quark decays, or from fakes due to hadrons. Both calorimetric and tracking isolation can be employed. Calorimetric isolation variables in 2012 have been built in such a way as to be almost insensitive to pile-up.

2.3.3 Muons

Many physics processes at the LHC are accessible only through the detection of highly energetic muons, due to the overwhelming QCD background. The muon signature in particular is very clean.

The reconstruction of muons [108] is based on information from the MS, ID and calorimeters, and it ranges from transverse momenta of a few GeV up to a few TeV. Different kinds of muon candidates are built, depending on how the detector information is used in the reconstruction.

Stand-alone muons are reconstructed starting from MS hits, that are combined into segments to form then a track. The muon momentum measured using this track is corrected for the parametrized energy loss of the muon in the calorimeter, to obtain the muon momentum at the interaction point. The track is extrapolated back to the beam axis to obtain the η and ϕ coordinates of the muon and the impact parameter with respect to the interaction point.

Combined muons are built starting from tracks reconstructed independently in the MS and ID that are subsequently combined. This is the category with highest purity. It suffers from acceptance losses in the $|\eta| \sim 0$ region, only partially instrumented to provide space for calorimeter and ID services, and the region $1.1 < |\eta| < 1.3$, where a layer of chambers has not been installed yet.

Segment tagged muons are reconstructed using as seed an ID track. The reconstruction algorithms then search for track segments in the muon chambers that can be associated to the ID track extrapolated to the MS.

Calorimeter tagged muons are built starting from an ID track. The track is identified as a muon if energy depositions compatible with the minimum ionizing particle hypothesis can be associated to it. This is the category with lowest purity, and it is introduced only for analyses that need to recover acceptance in uninstrumented MS regions.

Muons are reconstructed using two different algorithm chains. Chain 1 performs a statistical combination of track parameters of the stand-alone and ID muon tracks. Chain 2 performs a global refit of muon tracks using hits from both the ID and MS. In the context of this work Chain 1 muons are used.

The muon reconstruction efficiency has been measured in data on selected $Z \rightarrow \mu^+\mu^-$ and $J/\Psi \rightarrow \mu^+\mu^-$ samples with a tag-and-probe method. The results with 2012 data are shown in Figure 2.20. The overall efficiency is > 0.98 and stable against the pile-up conditions.

The analysis of the di-muon mass spectrum in data, and in particular of the $Z \rightarrow \mu^+\mu^-$ decay, allows to correct the muon momentum resolution and scale in the simulation. Figure 2.21 shows the di-muon invariant mass spectrum in the Z boson window before and after corrections are applied. The main systematic uncertainty on the corrections arises from their extraction method. Corrections depend on the muon pseudorapidity and systematic uncertainties are introduced to cover a possible dependence on the transverse momentum. Possible dependencies on charge are found to be covered by systematic uncertainties.

ATLAS triggers on muons making use of fast information from RPC and TGC detectors at L1 and precision information from MDT and CSC at the HLT. Efficiencies for the standard muon triggers in 2012 are shown in Figure 2.22.

(a)

(b)

(c)
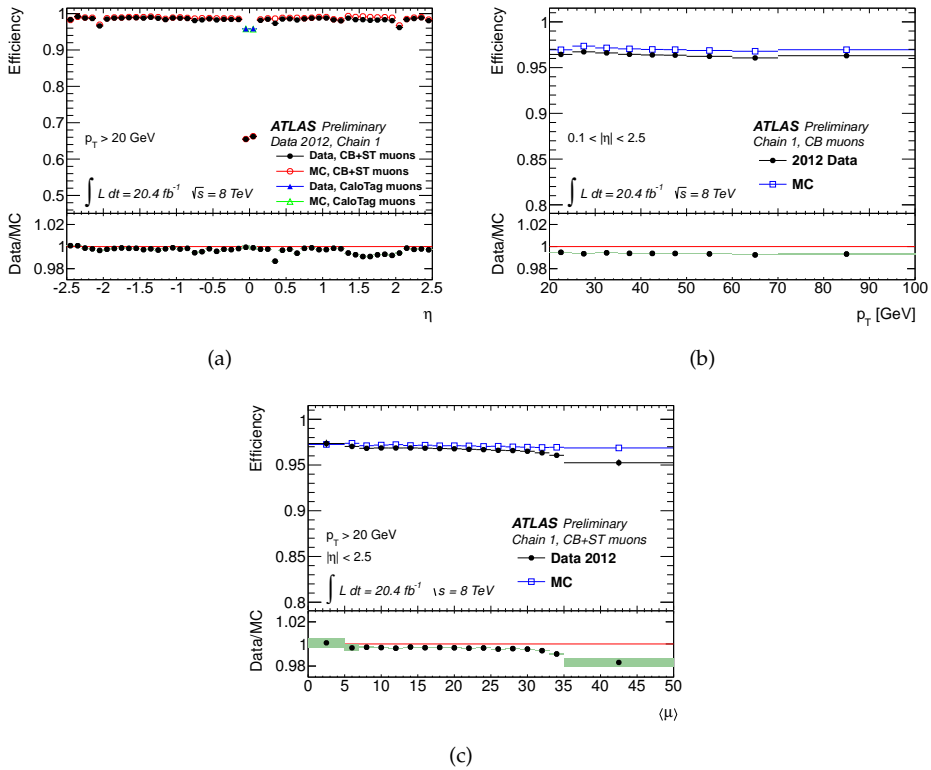
Figure 2.20: Muon reconstruction efficiency for Chain 1 in 2012 data, (a) as a function of η for different types of muons with $p_T > 20\,\text{GeV}$; (b) as a function of p_T for combined muons with $|\eta| < 2.5$ (c) as a function of the average number of interactions per bunch-crossing for combined muons with $|\eta| > 2.5$ [109].
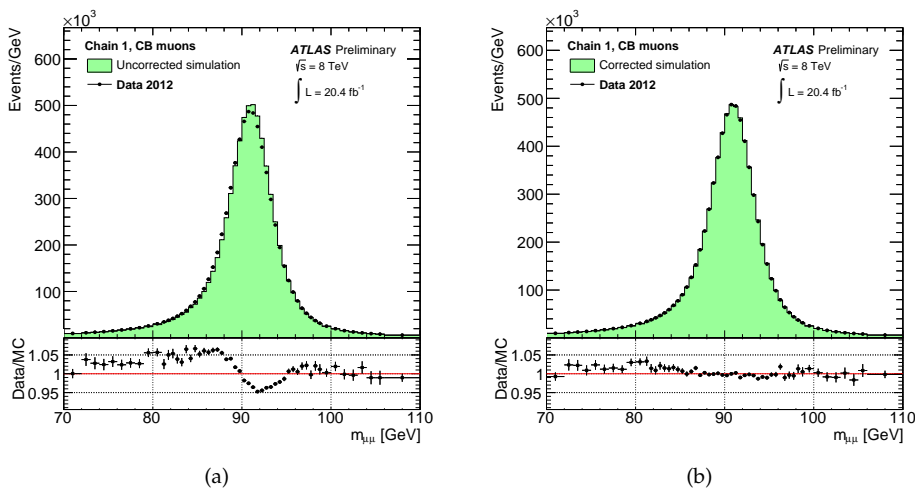
Figure 2.21: Di-muon invariant mass for Chain 1 combined muons, isolated and with $p_T > 25\,\text{GeV}$ in 2012 data. The solid histogram represents the simulation (POWHEG generator for $Z \rightarrow \mu^+\mu^-$ plus background modelling). In (a) the simulation has no corrections for resolution and energy scale applied. In (b) corrections are applied [109].
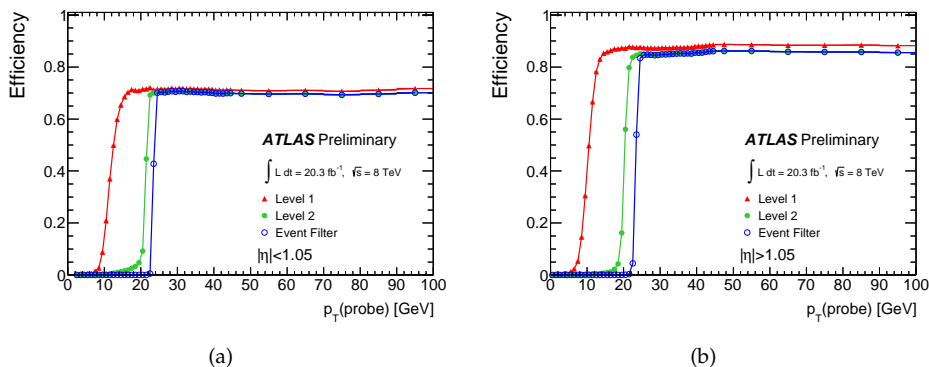
Figure 2.22: Efficiency of the standard single muon triggers used in 2012 (`mu24i_tight OR mu36_tight`) as a function of p_T in the (a) barrel and (b) endcap region [3].

2.3.4   Jets

Jets cover a fundamental role in the physics program of experiments at the LHC, as already introduced in Section 1.2.4. Jets are protagonists in SM QCD measurements, but cover an important role also in many search scenarios.

The ATLAS calorimeters are characterised by the high granularity (about 187000 cells independently read-out), high particle stopping power and large detector acceptance (9.8 rapidity units). These features allow for high quality jet reconstruction in the challenging LHC environment. In the following the jet reconstruction and calibration techniques at ATLAS are briefly described.

The most widely used jet algorithm in ATLAS is the anti-kt algorithm already introduced in Section 1.2.4, with $R = 0.4$ or $R = 0.6$ radius ($R = 0.4$ in the context of this work). Other radii for anti-kt and other recombination algorithms are used for specific purposes, such as performance and jet substructure studies. Since this type of jets are not used directly in the context of this work no details are given here.

A jet collection is not uniquely identified by the algorithm and its parameters: inputs and calibrations need to be specified as well.

Typical jet finder inputs are calorimeter cells, calorimeter towers and topological clusters. Generated particles are input to truth jet building instead. Calorimeter cell inputs offer a lot of information, but they are hard to handle, since, due to noise effects, signals can be negative. It is therefore convenient to collect cells into larger objects. In the tower representation cells are projected onto a fixed grid in (η, ϕ) space. Projective calorimeter cells which completely fit inside a tower contribute their total signal to the tower signal. Non-projective cells and projective cells larger than the tower bin size contribute a fraction of their signal to several towers, depending on the overlap fraction of the cell area with the towers. Even if the tower representation allows to deal with noise effects, it eventually introduces collinear and infrared unsafety, and therefore an alternative approach is preferred.

Topological cell clusters (topoclusters) are an attempt to reconstruct three-dimensional energy deposits in the calorimeter [110]. Topoclusters are formed from topologically connected ensembles of cells, built starting from seed cells with energy exceeding four times the gaussian width of the cell energy distribution measured in randomly triggered events ($E_{cell} > 4\sigma_{noise}$). To these cells neighbouring cells with an energy deposit exceeding $2\sigma_{noise}$ are added. Finally a contour of cells with no further requirements is included in the topocluster. A representation of the clustering process is displayed in Figure 2.23. After the initial clusters are formed, they are analysed for local signal maxima by a splitting algorithm, and split between those maxima if any are found.

ATLAS default jet collections use topological clusters as inputs.

Calorimeter cells and topoclusters by default are calibrated at the electromagnetic (EM) scale, that provides the correct calibration for electrons and photons. The interaction of electrons and photons in matter however is different with respect to that of hadrons. While the main interaction mode with matter for the first is electromagnetic,
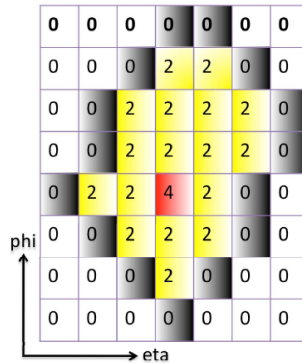
Figure 2.23: Schematic representation of topological clustering.

hadrons undergo more complex processes, such as nuclear interactions. The energy lost by particles producing the emission of neutrons or by causing fission of nuclei is not visible in typical non-compensating calorimeters, such as the ATLAS calorimeters. The calorimeters response to hadrons is therefore lower than that to electrons and photons.

Two global calibration schemes allow to calibrate topological clusters taking into account the different response to hadrons: the global cell energy-density weighting calibration scheme (GCW) and the local cluster weighting calibration scheme (LCW). In the LCW calibration, which is used in the context of this work, topoclusters are calibrated individually according to their characteristics (electromagnetic or hadronic) [111, 112]. Corrections are applied for the energy lost outside the topocluster as well. The weights for the calibration are determined from simulated jets, and compensate also for the energy lost in the dead materials. A scheme of jet reconstruction in ATLAS is shown in Figure 2.24. By default jets in ATLAS are built either from EM-scale or LCW-scale topoclusters.
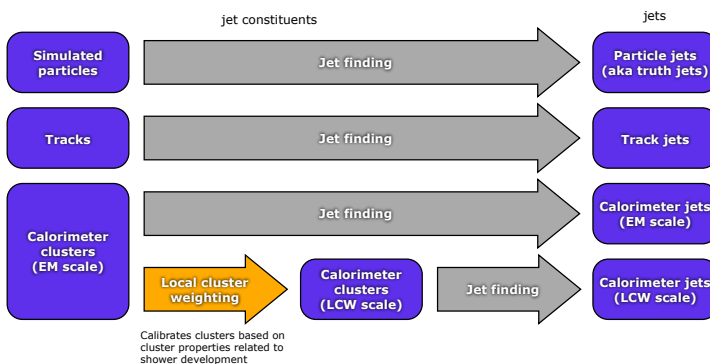
Figure 2.24: Schematic representation of jet reconstruction.

Both the EM and LCW energy scales do not account for further effects such as particles not totally contained in the calorimeter and particles that fall out of the reconstructed

jet but are included in the truth jet. The Jet Energy Scale (JES) is designed to be applied either on top of the EM-scale or the LCW-scale and correct for residual mis-calibration effects. The reference for the JES determination is the kinematics of the truth jet, that is built from generated stable particles before entering the detector, geometrically matched to the reconstructed jets.

The EM+JES calibration scheme includes a pile-up correction, a vertex correction and a jet energy and direction correction (see Figure 2.25).
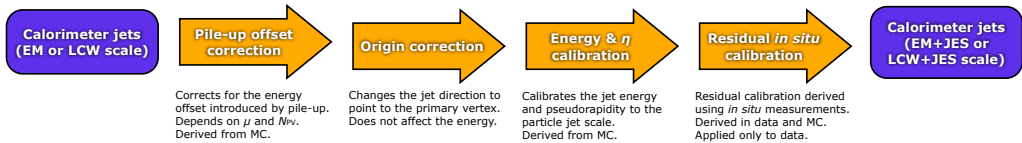
Figure 2.25: Schematic representation of the jet calibration procedure [113].

The pile-up correction is applied to EM scale jets, and corrects for contributions to the jet energy that do not originate from the hard scattering event. The correction can consist of an average offset correction derived from minimum-bias data as a function of the number of reconstructed vertices. Alternatively a correction based on the estimation of the pile-up contamination from the event energy density and measured jet areas has been used in 2012. The pile-up correction is validated using jets reconstructed using ID tracks as inputs. After the pile-up correction the jet origin is corrected to the primary interaction vertex. In order to do so, constituent clusters four-momenta are recomputed in a frame having as origin the primary vertex of the nominal interaction point. The recomputed four-momenta are then used for the calculation of the jet direction, while the energy is not affected. Subsequently the jet energy is corrected to restore the energy of the truth jet. Calibration constants are parametrised as a function of uncalibrated jet energy and pseudorapidity. Finally the jet pseudorapidity is corrected to account for a bias due to topoclusters reconstructed in poorly instrumented regions of the calorimeter. The LCW+JES calibration scheme is analogous to EM+JES, but the corrections are numerically smaller. Uncertainties on the EM+JES and LCW+JES calibrations arise from various sources. Uncertainties related to the JES calibration method include non-closure uncertainties, that affect only the absolute jet energy scale determination. Calorimeter response uncertainties can be assessed by propagating single particle uncertainties measured in-situ and from test-beam data. Uncertainties arising from detector simulation can be estimated using samples with modified calorimeter noise thresholds and different detector geometry description. Effects due to the physics model and parameters employed in Monte Carlo event generator are assessed using alternative generator configurations. The uniformity of the calorimeter response to jets is validated in-situ in events with di-jet topologies. The balance of jets in different calorimeter pseudorapidity regions can be exploited by different methods. The main uncertainty arises from the modelling of the relative jet response. Uncertainties on the pile-up corrections are derived by varying analysis choices applied in their derivation, and making use of track jets.

In-situ methods can be used to alternatively assess response, modelling and detector uncertainties. The same methods can be used to derive an additional correction to be applied to data. The methods include the comparison of the jet momentum with the momentum carried by its associated tracks, the p_T balance with photon or Z-boson and the balance between a high-p_T jet and a low-p_T jet system. The results of the various in-situ methods are combined taking correlations between methods into account. Relative uncertainties apply to the relative scale between data and simulation, whereas absolute uncertainties refer to the absolute energy calibration in data.

Additional uncertainties arise from the dependence of jet response on the flavour of the parton inducing the jet and the limited knowledge of the composition in the phase space regions considered in analyses. Flavour dependence for gluon and light quark initiated jets is studied in γ-jet and multi-jet samples.

An example summary of jet energy scale uncertainties as determined in 2012 data and simulation for LCW+JES jets with in-situ calibration is shown in Figure 2.26. The number of independent sources of systematic uncertainty is quite large. Reduction schemes that allow to preserve the information on correlations at best have been developed. In particular one of the proposed schemes concentrates on the typology of the sources, and is particularly suitable for combining different analyses and different experiments. This reduction scheme is summarised in Table 2.3.
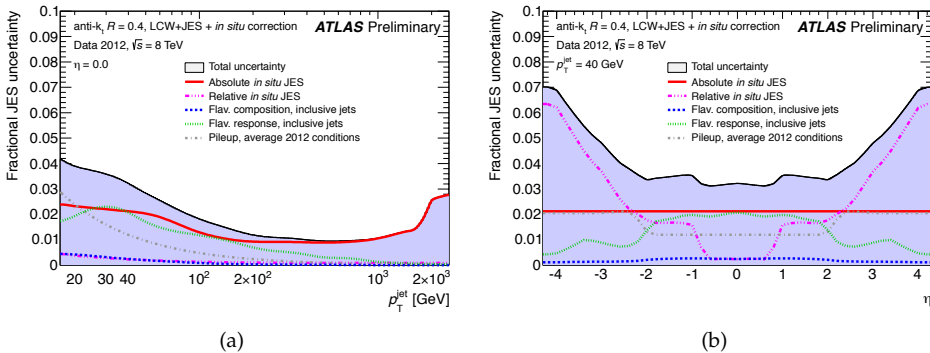
Figure 2.26: Fractional JES systematic uncertainty components in 2012 data as a function of p_T for anti-kt jets with $R = 0.4$ calibrated using the LCW+JES calibration scheme at (a) $|\eta| = 0.0$ as a function of p_T and (b) at $p_T = 40\,\text{GeV}$ as a function of η. The total uncertainty (all components summed in quadrature) is shown as a filled blue region topped by a solid black line. [3].

Recently a further global sequential calibration scheme (GS) has been deployed. This scheme starts from EM+JES jets and exploits the topology of energy depositions in order to characterise the content of the jet hadronic shower. This scheme leaves the mean jet energy unchanged but allows to improve the resolution. The uncertainties on the GS scale are given by the sum in quadrature of the EM+JES and uncertainties associated with GS corrections.

The resolution of the jet energy measurement was studied using in-situ techniques and was found to be well modeled by the simulation [114].

Category	2011 dataset	2012 dataset
	Complex correlation scheme across years.	
In-situ calibration	11 NP Components breakdown: 3 statistics and method `JES_Statistical` 4 modelling `JES_Modelling` 2 detector `JES_Detector` 2 mixed modelling and detector `JES_Mixed`	12 NP Components breakdown: 3 statistics and method `JES_Statistical` 4 modelling `JES_Modelling` 3 detector `JES_Detector` 2 mixed modelling and detector `JES_Mixed`
High-p_T jets	`SingleParticle_HighPt` correlated across all analyses and years	
Intercalibration	Modelling component `EtaIntercalibration.Modelling` correlated across all analyses and years Statistics and method component correlated across analyses `EtaIntercalibration_StatAndMethod`	Modelling component `EtaIntercalibration.Modelling` correlated across all analyses and years Statistics and method component correlated across analyses `EtaIntercalibration_TotalStat`
Pile-up	Out-of-time pile-up `Pileup_OffsetMu` correlated across all analyses and years	
	In-time pile-up `Pileup_OffsetNPV` correlated across all analyses and years	
	Residual pt dependent term `Pileup_PtTerm` correlated across all analyses	Non-existing
	Topology dependent term from jet area pile-up correction method `Pileup_RhoTopology` correlations depending on analysis	Non-existing
Non-closure	Non-closure term for non-standard Monte Carlo samples	Non-existing
Flavour	Flavour response to light-quark and gluon jets `JES_FlavourResponse`. Correlated across all analyses and years. Light-quark and gluon composition `JES_FlavourComposition`. Correlation depending on analysis. Bjet response uncertainty `JES_BJets`. Correlated across analyses and years, mutually exclusive with the two other flavour components.	

Table 2.3: Summary of JES uncertainty components and their correlations in 2011 and 2012.

In addition to affecting the measurement of the energy and direction of jets from the hard-scattering event, pile-up can give rise to additional jets prevalently formed by deposits due to additional pp interactions. In order to suppress this kind of jets, a jet vertex fraction variable is defined as

$$JVF = \frac{\sum_{\text{tracks}_{\text{jet}},\text{PV}} p_{\text{T}}}{\sum_{\text{tracks}_{\text{jet}}} p_{\text{T}}} \tag{2.2}$$

where the sums are taken over the tracks matched to the jet and PV denotes the tracks associated to the primary vertex. JVF is set to -1 for jets with no associated tracks. Jets within the tracking acceptance, and in phase space regions subject to the effects of pile-up are typically discarded if they do not satisfy specific JVF requirements (JVF above a certain threshold).

2.3.5 Hadronically decaying tau leptons

Tau leptons play a key role in many physics processes of interest at the LHC. Low energy taus are involved in SM analyses, in particular the study of the $W \to \tau\nu$ [115, 116], $Z \to \tau^+\tau^-$ [117] and top-quark decays [118], and for the search for Higgs bosons decaying to two taus. Moreover tau leptons are interesting for searches of heavy Higgs bosons decaying to two taus [119], Supersymmetry [120], exotic bosons $W^{'}$ and $Z^{'}$ [121] and leptoquarks [122].

The reconstruction and identification of tau leptons in ATLAS [123] focuses on hadronic decay channels, since it is impossible to distinguish muons and electrons from tau decays from prompt ones.

The visible part of the system of particles arising from hadronic tau decays is denoted in the following as $\tau_{\text{had-vis}}$. The reconstruction of $\tau_{\text{had-vis}}$ in ATLAS follows a top-down approach, starting from a very inclusive object and going into its details. As a consequence, reconstruction and identification are well separated procedures. The reconstruction has several different steps.

Seed selection

The seeds for reconstruction algorithms are anti-kt jets with $R = 0.4$, reconstructed from topological clusters calibrated with the LCW calibration already discussed in Section 2.3.4, with $p_{\text{T}} > 10\,\text{GeV}$ and $|\eta| < 2.5$.

Vertex selection

Since the primary vertex of the interaction, identified as the one having the largest $\sum p_{\text{T}}^2$ of associated tracks, is not necessarily the correct tau production vertex, in 2012 data a dedicated tool is used to associate the $\tau_{\text{had-vis}}$ to the best vertex hypothesis [124]. The $\tau_{\text{had-vis}}$ four-momentum and identification variables are calculated in a reference frame having the chosen vertex as origin. This vertex is referred to in the following as *tau vertex*.

Barycenter determination

The $\tau_{\text{had-vis}}$ barycenter is computed from the sum of the four-vectors of the seed jet constituents, assuming zero constituent mass.

Intermediate axis determination

Only the clusters in a $\Delta R < 0.2$ cone around the barycenter are considered. Their four-momenta are recalculated using the tau vertex coordinate system. The intermediate $\tau_{\text{had-vis}}$ axis is computed from the sum of these recalculated four-momenta.

Track association

Tracks satisfying the requirements in Table 2.4 are associated to the calorimetric $\tau_{\text{had-vis}}$. Tracks are associated as *core tracks* if their distance from the intermediate axis is $\Delta R \leq 0.2$ and as *isolation tracks* is they lay in $0.2 < \Delta R \leq 0.4$ of the intermediate axis.

Discriminating variables computation

Discriminating variables are computed from core tracks, isolation tracks and constituent calorimeter clusters. In order to mitigate the pile-up dependence in 2012 data only calorimeter clusters with $\Delta R < 0.2$ of the intermediate axis are considered.

Energy calibration and final four-momentum calculation

The $\tau_{\text{had-vis}}$ energy is determined from the clusters in a $\Delta R < 0.2$ cone of the barycenter. The final $\tau_{\text{had-vis}}$ direction is calculated after this energy calibration step, which is better detailed in the following.

Variable	Requirement
Transverse momentum	$p_{\text{T}} > 1\,\text{GeV}$
Number of Pixel hits	$n_{PIX} \geq 2$
Number of Pixel hits + number of SCT hits	$n_{\text{Si}} \geq 7$
Distance of closest approach to the tau vertex in the transverse	$|d_0| \leq 1.0\text{mm}$
Longitudinal distance of closest approach to the tau vertex	$|z_0 \leq \theta| \leq 1.5\text{mm}$

Table 2.4: Track quality requirements for tracks associated to $\tau_{\text{had-vis}}$ objects in 2012 [123].

Since $\tau_{\text{had-vis}}$ objects are a specific mix of charged and neutral hadrons, different from that of jets, a separate tau energy scale (TES) is determined [125]. The energy computed from clusters at the LCW-scale is already corrected for calorimeter non-compensation, but effects of material upstream of the calorimeter, underlying event and pile-up contributions and out-of-cone effects are not accounted for. Calibration constants are therefore derived to correct the LCW-scale momentum to the true visible tau momentum $p_{\text{vis}}^{\tau,\text{true}}$. The constants are derived separately for 1-prong and multi-prong $\tau_{\text{had-vis}}$ and in categories of $p_{\text{vis}}^{\tau,\text{true}}$ and reconstructed pseudorapidity $\eta_{\text{reco}}^{\tau}$. Response curves are shown in Figure 2.27.

The pseudorapidity of clusters is corrected to account for the bias due to clusters reconstructed in poorly instrumented calorimeter regions. The TES dependence on the pile-up conditions is reduced by means of a dedicated pile-up correction. TES uncertainties are
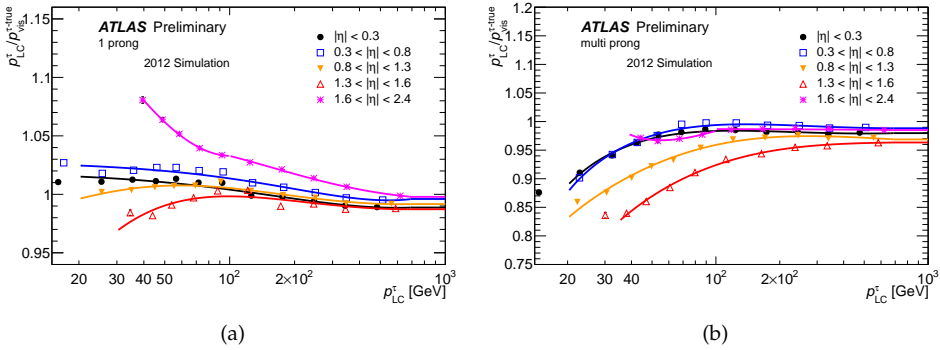
Figure 2.27: Response curves as a function of reconstructed $\tau_{\text{had-vis}}$ momentum at LCW-scale in bins of $\eta_{\text{reco}}^{\tau}$ for (a) 1-prong $\tau_{\text{had-vis}}$ and (b) multi-prong $\tau_{\text{had-vis}}$ in 2012 simulation [125].

derived propagating single particle uncertainties of the individual visible τ decay products to the tau energy scale. Single particle uncertainties are given by an in-situ measurement comparing calorimeter energy measurements to momenta measured in the ID (E/p method) and test-beam measurements, which are used to directly constrain the energy response to charged hadrons. Since test-beam measurements are available only for $|\eta| < 0.8$, for larger pseudorapidities uncertainty estimates obtained by comparing different shower models in simulated samples are used.

The TES determination is cross-checked by using the reconstruction of the mass of visible tau decay products in the $Z \to \tau_\mu \tau_{\text{had}}$ process as well. More details about TES and its uncertainty, and in particular of the cross-check method using $Z \to \tau^+\tau^-$ events are given in Chapter 6.

TES uncertainties as a function of the reconstructed transverse $\tau_{\text{had-vis}}$ momentum are shown in Figure 2.28.

The resolution of $\tau_{\text{had-vis}}$ momentum can be parametrised as

$$\frac{\sigma}{p} = \frac{a}{\sqrt{p}} \oplus b \tag{2.3}$$

The a and b parameters depend on the $\tau_{\text{had-vis}}$ pseudorapidity region and number of prongs. In 2012 simulation it is found that a ranges from ~ 0.7 in the $|\eta| < 0.3$ region, 1-prong $\tau_{\text{had-vis}}$, to ~ 1.30 in the most forward regions for 3-prong $\tau_{\text{had-vis}}$.

The reconstruction of $\tau_{\text{had-vis}}$ provides almost no identification against fakes, that can be due to hadronic jets originated by quarks and gluons, electrons and muons. A further identification step is therefore necessary to reduce the backgrounds in tau analyses. Several discriminating variables are used for identification, either exploiting a cut strategy or combined in multivariate discriminants.

The main variables that allow to separate genuine $\tau_{\text{had-vis}}$ from fakes due to quark- or gluon-induced jets are variables sensitive to shower width, track multiplicity and possible displacement of the decay vertex of the inducing particle. Genuine $\tau_{\text{had-vis}}$ tend to
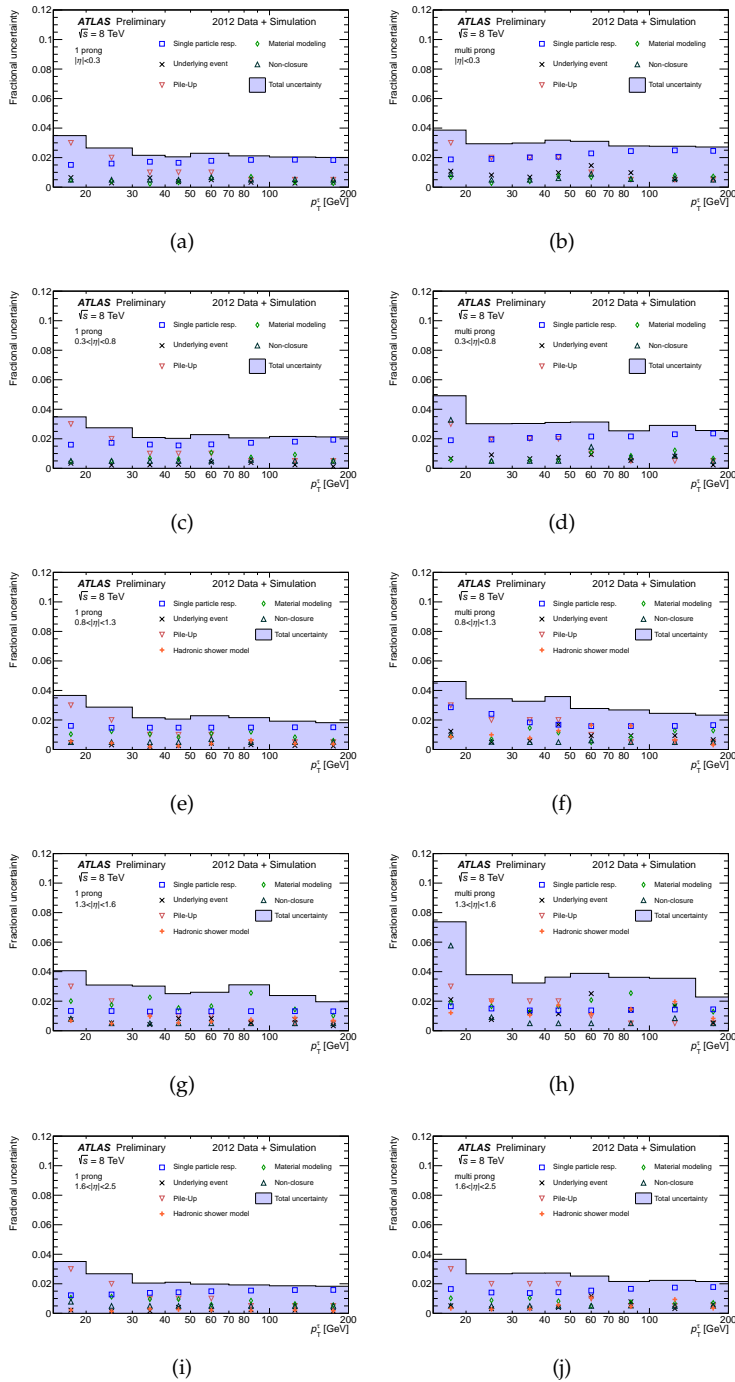
Figure 2.28: TES uncertainty for 1-prong (left) and multi-prong (right) $\tau_{\text{had-vis}}$ in η_τ bins in 2012 data and simulation [125].

be narrow: typically they are contained in a cone that shrinks with the Lorentz boost of the parent tau. QCD jets instead tend to shrink more slowly with the transverse momentum of the initiating parton. An important calorimeter shape variable is the fraction of the total tau energy contained in the centermost cone defined by $\Delta R < 0.1$, $f_{\text{corr}}^{\text{cone}}$, shown in Figure 2.29(a). On the tracking side relevant shape variables are the average p_{T}-weighted track distance from the tau axis R_{track} shown in Figure 2.29(b), and for multi-prong decays the distance to the track furthest from the tau axis ΔR_{max}, shown in Figure 2.29(c). As already introduced in Section 1.6.1 describing the basic properties of tau leptons, hadronic decays have typically 1 or 3 charged prongs. This translates in the small track multiplicity of $\tau_{\text{had-vis}}$. QCD jets tend to have typically more charged particles. Finally the fact the tau lepton has a decay length of the order of 1mm for taus from $H/W/Z$ decays can be exploited to distinguish $\tau_{\text{had-vis}}$ from light-quark and gluon jets, that originate from the primary vertex. A useful variable for 3-prong decays is the significance of a reconstructed secondary vertex $S_{\text{T}}^{\text{flight}}$, shown in Figure 2.29(d).
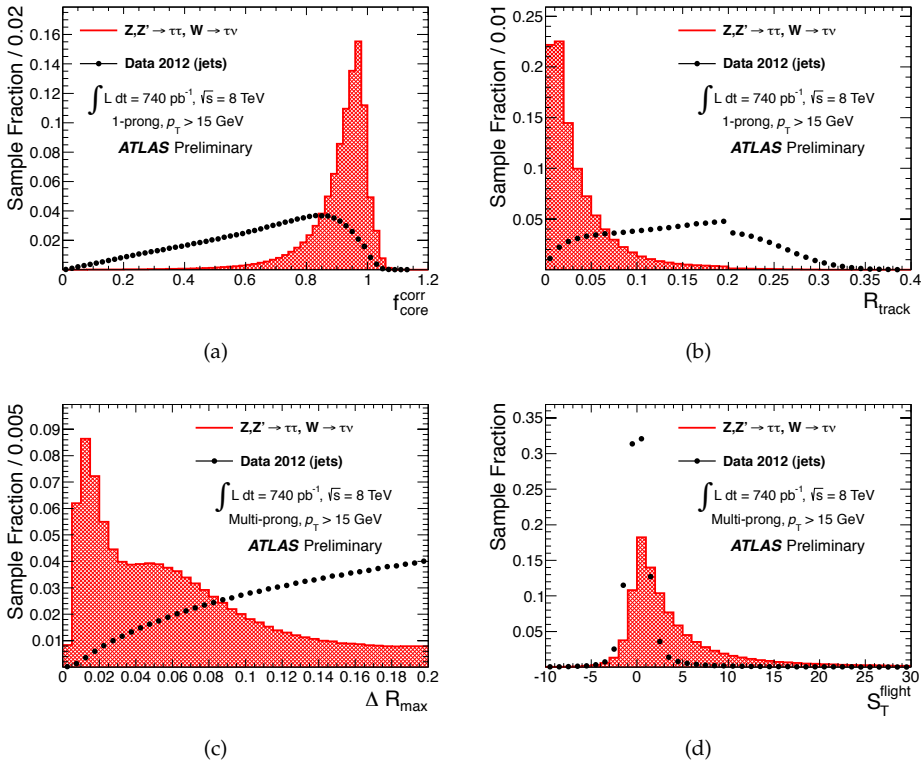
Figure 2.29: Examples of $\tau_{\text{had-vis}}$ identification variables in 2012 data and simulation, definitions are given in the text. (a) $f_{\text{corr}}^{\text{cone}}$, (b) R_{track}, (c) ΔR_{max}, (d) $S_{\text{T}}^{\text{flight}}$ [123].

The final discriminators that combine the information from various variables used in the context of this work are a cut-based discriminator for 2010 data and a BDT based dis-

criminator for 2011 and 2012 data. The performance of the 2012 discriminator is shown in Figure 2.30. Three working points, *loose*, *medium* and *tight* are defined by a cut on the BDT discriminant. The signal efficiency is determined from simulated $Z \to \tau^+\tau^-$, $W \to \tau\nu$ and $Z' \to \tau^+\tau^-$ samples. The background efficiency is determined from a data selected jet sample, and is only indicative since actual fake rates relevant for analyses depend on the detailed jet final state.
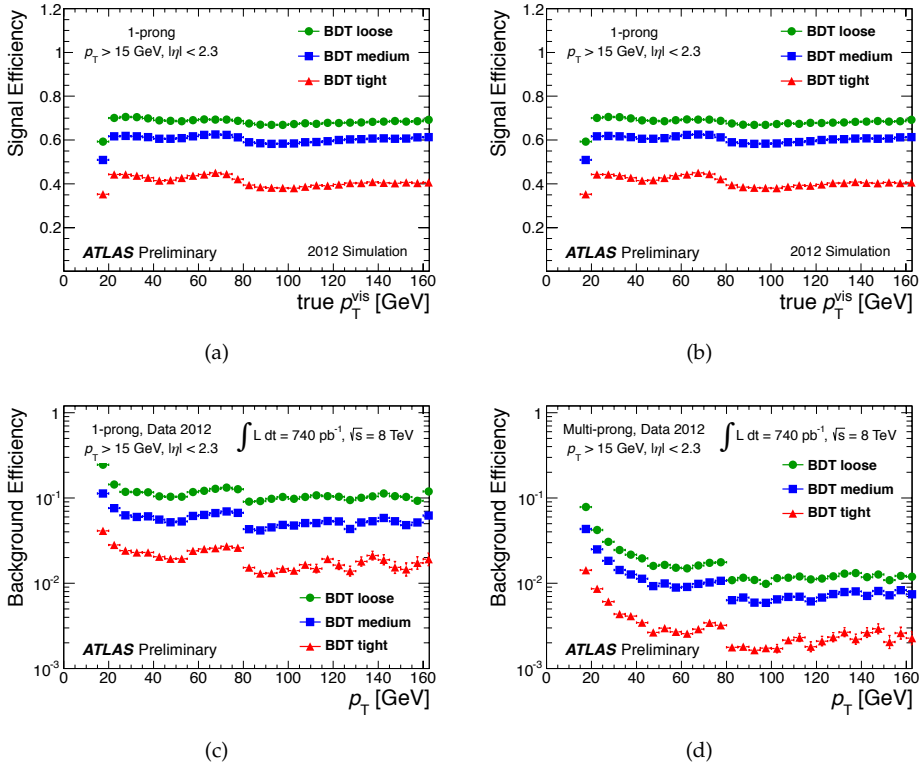
Figure 2.30: Performance of the BDT discriminator for $\tau_{\text{had-vis}}$ objects against QCD jets in 2012 simulation. (a) signal efficiency for 1-prong candidates, (b) signal efficiency for multi-prong candidates, (c) background efficiency for 1-prong candidates, (d) background efficiency for 3-prong candidates [123].

The performance is found to be stable against pile-up. Signal efficiencies are measured in data using a tag-and-probe method on selected $W \to \tau\nu$, $Z \to \tau^+\tau^-$ and $t\bar{t}$ samples. The application of the tag-and-probe method in the case of tau identification is particularly difficult due to the large contamination from backgrounds when identification is not applied. Scale factors for signal efficiencies are derived and shown in Figure 2.31. The main systematics on the knowledge of the $\tau_{\text{had-vis}}$ identification efficiencies arise from limited statistics and background estimation systematics in the tag-and-probe measurements, Monte Carlo generator and simulation physics list related uncertainties.

Electrons and muons can fake the signature of 1-prong $\tau_{\text{had-vis}}$ as well, and contribute
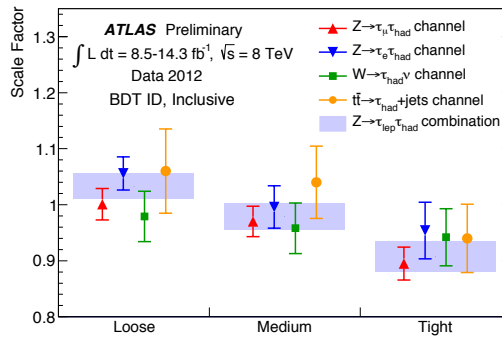
(a)

Figure 2.31: Summary of scale factors for $\tau_{\text{had-vis}}$ identification for the BDT discriminant in 2012 data [123].

significant backgrounds once the QCD jet backgrounds are suppressed.

A BDT-based discriminant is used against electrons. It exploits particle identification information from the TRT and longitudinal shower shapes in the calorimeter. Its performance is shown in Figure 2.32(a). Discrimination against muons can be achieved first of all by vetoing geometrically overlapping reconstructed muons. A few specific cases where muon reconstruction fails and a muon deposes enough energy in the calorimeter to be reconstructed as $\tau_{\text{had-vis}}$ are dealt with using a cut strategy on a few shower shape and tracking variables. An example of such variables is shown in Figure 2.32(b). A tag-and-probe method is used to measure the rate of electrons faking the $\tau_{\text{had-vis}}$ signature in a data selected $Z \to e^+e^-$ sample. The main systematic uncertainties on the fake rate arise from tag electron selection requirements.

The ATLAS detector has the capability to trigger on $\tau_{\text{had-vis}}$ objects as well. At the EF a BDT identification similar to the one used offline is employed in order to reduce inefficiencies in the offline selection. The trigger efficiency is measured with a tag-and-probe method using $Z \to \tau^+\tau^-$ events. The efficiency of the lowest threshold not prescaled trigger in 2012 is shown in Figure 2.33 both for data and Monte Carlo.

2.3.6 Jet flavour tagging

The knowledge of the flavour of the initiating parton of a jet can be very important in physics analyses. It is a requirement of multi-purpose detectors at the LHC to be able to efficiently tag jets containing heavy flavour hadrons. These jets are usually referred to as b-jets and the tagging procedure b-tagging. B-tagging information is heavily employed in top quark properties studies, searches such as $H \to b\bar{b}$ but other BSM searches and SM measurements as well. B-jets can be identified exploiting two characteristics of the b-quark: its long lifetime and large mass. The first characteristic implies the existence of a secondary vertex, with a typical displacement from the primary vertex that allows to

(a)   (b)
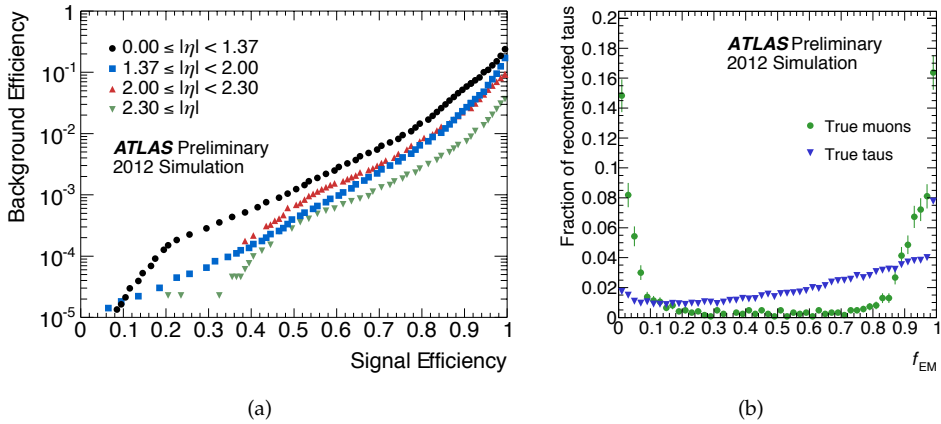
Figure 2.32: Discrimination of $\tau_{\text{had-vis}}$ against leptons in 2012. (a) performance of the electron BDT discriminant. (b) Electromagnetic fraction f_{EM} of $\tau_{\text{had-vis}}$ candidates matched to muons or true hadronically decaying taus [123].
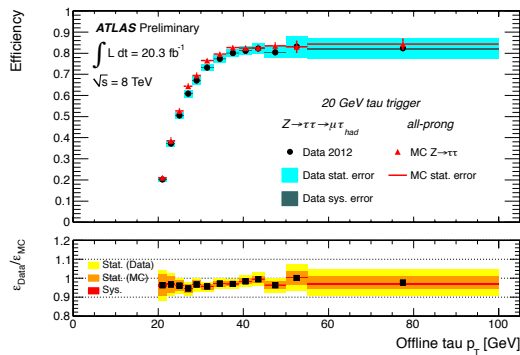
Figure 2.33: Efficiency with respect to offline $\tau_{\text{had-vis}}$ candidates for the `tau20_medium` trigger in 2012 as a function of p_{T}. Both the measurement in data and the prediction from simulation are shown [3].

reconstruct it separately in a significative number of cases. The large b-quark mass enables then the discrimination based on the invariant mass of the secondary vertex. These characteristics are exploited by three different algorithms: `SV1`, `IP3D` and `SV1`. The discriminant typically used in ATLAS, `MV1`, is a neural-newtwork based discriminant that uses the three algorithms results as input. Several methods are used to measure efficiencies and mis-tag rates in data. Efficiencies are measured in a sample of jets containing muons exploiting the dependence of the muons spectrum on the jet flavour [126]. Two different methods are used in this case to extract b-tagging efficiencies. Analogous measurements can be performed in samples containing $t\bar{t}$ pairs [127]. The combined results for the simulation correction factors derived from data with their uncertainties is shown in Figure 2.34(a). Mis-tag rates are measured both for light flavour and c-quark induced jets. The efficiency for light flavour jets is measured making use of the characteristics of the apperance of secondary vertices in such cases [128]. The efficiency for jets initiated by c-quarks is measured in the analysis of events with D^{**} mesons [129]. Results for 2011 data and simulation are shown in Figures 2.34(b) and 2.34(c). Similar results are obtained for the 2012 dataset.

(a)

(b)

(c)
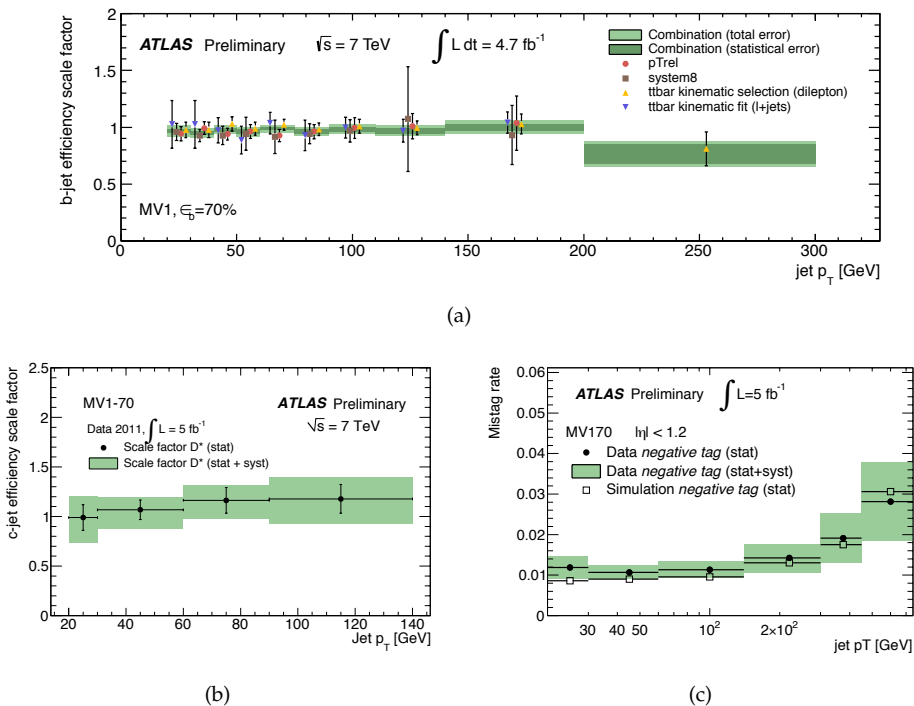
Figure 2.34: B-tagging simulation correction factor derived from 2012 data for (a) b-quark efficiencies, (b) c-quark efficiencies and (c) light flavour jet mistag rates with one of the determination methods used for jets with $|\eta| < 1.2$ [126, 128, 129].

2.3.7   Missing transverse momentum

Many interesting processes at the LHC are characterized by invisible final state particles, such as neutrinos or supersymmetric stable particles, that can not be detected since they are neutral and have very small interaction cross-sections. These processes include both SM processes, such as W decay, Z and Higgs boson decay to two taus, t-quark, and new physics signatures, such as the production of stable massive supersymmetric particles.

Since the interactions at the LHC have null total transverse momentum, it is possible to define the missing transverse momentum as

$$E_{\mathrm{T}}^{\mathrm{miss}} = \sqrt{(E_x^{\mathrm{miss}})^2 + (E_y^{\mathrm{miss}})^2} \quad \text{where} \quad E_x^{\mathrm{miss}}(E_y^{\mathrm{miss}}) = -\sum E_x(E_y) \qquad (2.4)$$

where $\sum E_x$ and $\sum E_y$ are sums over all of the energies measured in the detector. A true missing transverse momentum is a signature of processes with weakly interacting final state particles. Therefore it is a crucial requirement for ATLAS to be able to measure well the physics objects in an event, in order to avoid fake $E_{\mathrm{T}}^{\mathrm{miss}}$, and to obtain a high quality missing transverse momentum measurement for events where weakly interacting particles are actually produced.

The ATLAS $E_{\mathrm{T}}^{\mathrm{miss}}$ reconstruction is performed summing two terms:

$$E_{x(y)}^{\mathrm{miss}} = E_{x(y)}^{\mathrm{miss,\,calo}} + E_{x(y)}^{\mathrm{miss,\,muon}} \qquad (2.5)$$

The two terms are referred to as the calorimeter term and the muon term.

The $E_{x(y)}^{\mathrm{miss,\,calo}}$ term is the dominant one and it is calculated from the calorimeter cell energies over the range $|\eta| < 4.9$ (restricted to $|\eta| < 4.5$ in 2010 due to problems with the forward calorimeters). Only the cells belonging to topoclusters, already introduced in Section 2.3.4 are used to calculate the calorimeter term. The calibration can be further refined by considering to which physics object the topocluster cells belong to, so the best calibration can be used for the different reconstructed objects. In this case the $E_{\mathrm{T}}^{\mathrm{miss}}$ calorimeter term takes the form

$$E_{x(y)}^{\mathrm{miss,\,calo\,calib}} = E_{x(y)}^{\mathrm{miss,\,e}} + E_{x(y)}^{\mathrm{miss,\,\gamma}} + E_{x(y)}^{\mathrm{miss,\,\tau}} + E_{x(y)}^{\mathrm{miss,\,jets}} + E_{x(y)}^{\mathrm{miss,\,SoftTerm}} \qquad (2.6)$$

where each term is calculated from the negative sum of calibrated cell energies inside the corresponding objects. The $E_{x(y)}^{\mathrm{miss,\,SoftTerm}}$ is calculated from topoclusters and tracks which are not included in any physics object.

This refined calibration scheme improves the $E_{\mathrm{T}}^{\mathrm{miss}}$ performance in events containing high p_{T} physics objects, and the $E_{\mathrm{T}}^{\mathrm{miss}}$ calculated this way is referred to as `MET_RefFinal` in jargon. A scheme of the reconstruction of `MET_RefFinal` is displayed in Figure 2.35. The calorimeter term is particularly subject to the effects of pile-up. Terms corresponding to objects are the least affected, or, in the case of $E_{\mathrm{T}}^{\mathrm{miss,\,jets}}$, object reconstruction already provides for pile-up suppression. The $E_{\mathrm{T}}^{\mathrm{miss,\,SoftTerm}}$ term needs a dedicated pile-up suppression. Two different methods have been implemented in ATLAS
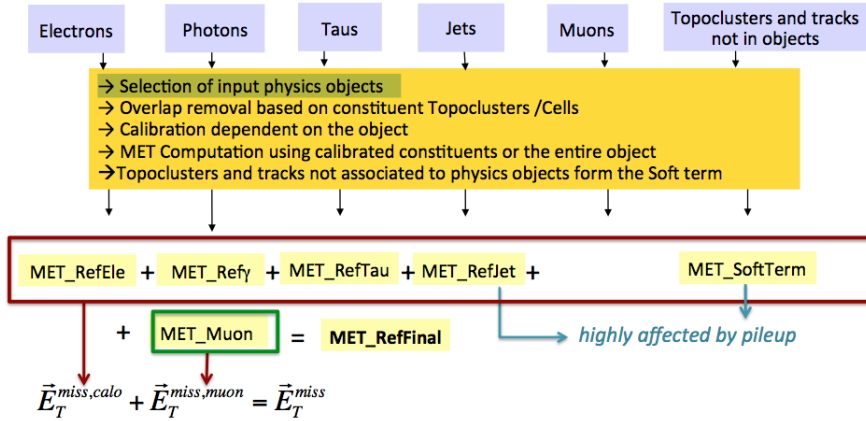
Figure 2.35: Scheme of `MET_RefFinal` reconstruction.

STVF suppression

A variable analogue to JVF, defined in Equation 2.2 is built

$$STVF = \frac{\sum_{\text{tracks}_{\text{SoftTerm}},\text{PV}} p_{\text{T}}}{\sum_{\text{tracks}_{\text{SoftTerm}}} p_{\text{T}}} \tag{2.7}$$

The $E_{\text{T}}^{\text{miss,SoftTerm}}$ is multiplied by the $STVF$ factor and the $E_{\text{T}}^{\text{miss}}$ calculated with the rescaled soft term takes the name of $STVF$.

JetArea suppression

The inputs to $E_{\text{T}}^{\text{miss, SoftTerm}}$ are fully reclustered using the k_t jet algorithm. The event energy density can be computed from selected k_t jets built from $E_{\text{T}}^{\text{miss, SoftTerm}}$ inputs. The event energy density is then used to subtract the contribution due to pile-up from k_t jets built from $E_{\text{T}}^{\text{miss, SoftTerm}}$ inputs, so that the corrected jet energy is $p_{\text{T corr}}^{\text{jet}} = p_{\text{T}}^{\text{jet}} - \rho \times A^{\text{jet}}$, where A^{jet} is the jet area. Different suppression variants are obtained according to how the event energy density is computed and if additional selections on the jets entering the $E_{\text{T}}^{\text{miss, jet}}$ term are performed [130]. In the `EJA` method (Extrapolated Jet Area) the event energy density is measured in the central detector region and extrapolated to the forward region. In the `EJAF` method (Extrapolated Jet Area Filtered) a JVF based selection for jets is used additionally. Finally in the `JAF` (Jet Area Filtered) the event energy density is measured over the full detector, and a JVF based selection for jets is used.

The $E_{\text{T}}^{\text{miss}}$ muon term, $E_{\text{T}}^{\text{miss,muon}}$, defined in Eq.2.4, accounts for the the momenta of muons measured by the muon detector. All the different reconstructed muons, described in Section 2.3.3, are used and special attention is paid to avoid double counting of the energy deposited in the calorimeters, already included in the calorimeter term.

Another important variable to be defined is the total transverse energy in the calorimeters, ΣE_T, defined as the scalar sum

$$\Sigma E_T = \Sigma E_T^e + \Sigma E_T^\gamma + \Sigma E_T^\tau + \Sigma E_T^{jets} + \Sigma E_T^{SoftTerm} \tag{2.8}$$

The performance of E_T^{miss} reconstruction is quantified in terms of resolution and linearity, and it has been studied in several event topologies. Figure 2.36 shows the E_T^{miss} resolution as a function of $\sum E_T(\text{event}) = \sum E_T + \sum p_T$. This choice is quite natural since the resolution would be expected to behave as $\sqrt{\sum E_T}$ if events had an isotrope energy flow. It can be seen how actually the dependence is more complicated than this, and the resolution depends on the event topology.
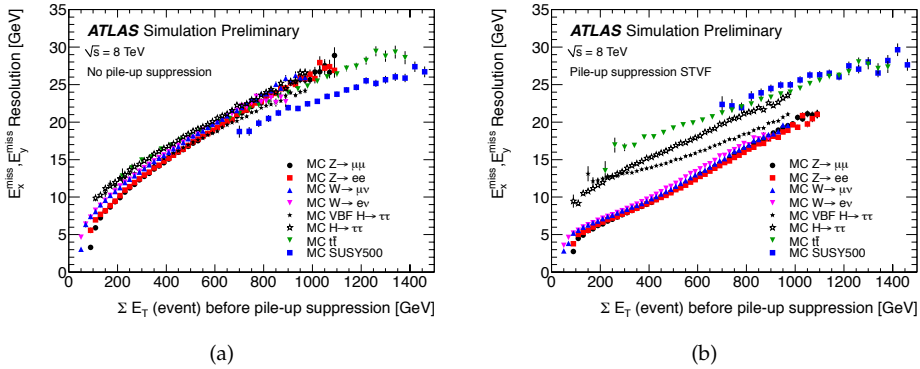
Figure 2.36: Combined E_x^{miss} and E_y^{miss} resolution as a function of $\sum E_T(\text{event})$ in different event topologies and (a) before (b) after STVF pile-up suppression [131].

Figure 2.37 instead shows the linearity of E_T^{miss}, that is the mean value of the ratio $(E_T^{miss} - E_T^{miss,\,true})/E_T^{miss,\,true}$. The mean value of the linearity has a positive bias in all event topologies, which is due to the fact that for small values of $E_T^{miss,\,true}$ resolution effects become dominant.

Typically pile-up suppression techniques allow to improve the resolution of E_T^{miss}, but in some case spoil the linearity.

Systematic uncertainties on the E_T^{miss} measurement are evaluated in terms of limited knowledge of the resolution and scale for all objects entering the E_T^{miss} reconstruction. In order to derive systematic uncertainties on the $E_{T\text{miss, Soft}}$ term, two different methods are employed, one based on the level of data/simulation agreement in $Z \rightarrow \mu^+\mu^-$ events with no jets and the other on the balance between hard objects and soft term in inclusive $Z \rightarrow \mu^+\mu^-$ events. In 2012 data and simulation the uncertainties derived with the second method are 3.6% on the scale and 2.3% on the resolution if no pile-up suppression is applied. If STVF pile-up suppression is used the the uncertainties rise to 7.9% and 4.8% respectively.
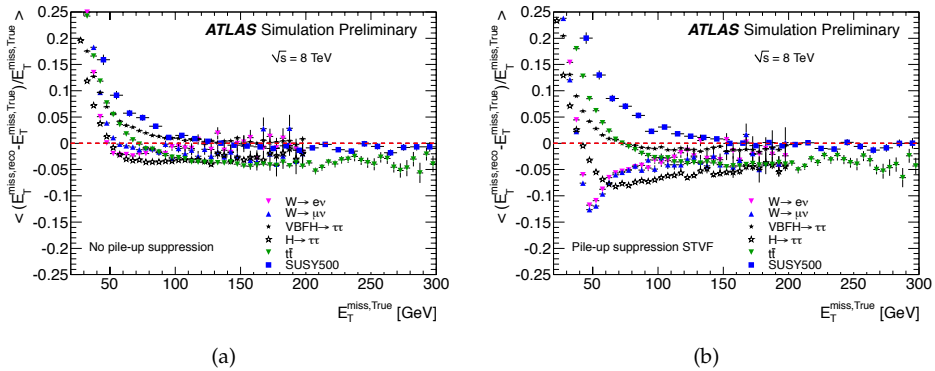
Figure 2.37: E_T^{miss} linearity as a function of $E_T^{miss,\,true}$ in different event topologies and (a) before (b) after STVF pile-up suppression [131].

2.3.8 Luminosity

Accuracy in the determination of the delivered luminosity covers an important role in cross-section measurements and searches. ATLAS uses several detectors providing redundant measurements in order to improve the confidence of the luminosity measurement [132]. The strategy for the luminosity determination is based on the relation

$$\mathcal{L} = \frac{\mu_{\mathrm{vis}} n_b f_r}{\sigma_{\mathrm{vis}}} \tag{2.9}$$

where μ_{vis} is the observed number of inelastic interactions in a bunch-crossing for a certain luminosity monitor, n_b is the number of bunch pairs colliding per revolution and f_r is the storage ring revolution frequency. The visible cross-section σ_{vis} is defined as the product of the inelastic pp cross-section and the efficiency of the detector employed. The σ_{vis} for the various luminosity monitors is measured in dedicated beam separation scans, also known as *Van der Meer* scans. These scans allow to infer the absolute luminosity from beam and machine parameters as

$$\mathcal{L} = \frac{n_b f_r n_1 n_2}{2\pi \Sigma_x \Sigma_y} \tag{2.10}$$

where n_1 and n_2 are the bunch populations, that can be measured externally, and Σ_x and Σ_y characterise the horizontal and vertical beam widths, that can be directly measured during beam-separation scans. Systematic uncertainties on the ATLAS luminosity measurement arise from the uncertainties in the absolute calibration and from additional uncertainties assessing the stability of the calibrated luminosity over time and varying operation conditions. Final uncertainties in the ATLAS luminosity scale are reported in Table 2.5. The results include corrections applied since July 2013, which account for beam-beam effects that had not been previously understood.

Dataset	Centre-of-mass energy	$\delta\mathcal{L}/\mathcal{L}$	Correction factor for publications prior to July 2013
2010	7 TeV	$\pm 3.5\%$	1.9%
2011	8 TeV	$\pm 1.8\%$	1.4%
2012	8 TeV	$\pm 2.8\%$	-

Table 2.5: Luminosity uncertainties and correction factors for publications prior to July 2013 for datasets used in the context of this work [132]

The H $\to \tau_{\text{lep}}\tau_{\text{had}}$ **process**

The SM $H \to \tau^+\tau^-$ process is of great interest for light Higgs boson masses (see Section 1.6.2). The branching ratio for this decay channel varies depending on the Higgs mass hypothesis. The latest prediction values can be found in Ref. [53].

The $H \to \tau^+\tau^-$ process can be studied in different channels, according to the decay modes of the tau leptons, as shown in Figure 3.1. The channel of interest in this study, $H \to \tau_{\text{lep}}\tau_{\text{had}}$ provides the largest sensitivity. Its characteristics are described in the following, together with a first brief description of the backgrounds, that are large and difficult to accurately predict. Another great experimental difficulty is related to the reconstruction of mass, which is shortly discussed giving some outlook on possible improvements of the present ATLAS strategy. Due to the experimental difficulty of this channel, in particular to the large irreducible $Z \to \tau^+\tau^-$ background and the limited mass resolution, it is necessary to exploit the characteristic signatures of production modes to extract the signal from the backgrounds. As a consequence, tagging the topology of production modes drives the analysis strategy. Production modes are described in this perspective in the second part of this chapter.

3.1 H $\to \tau^+\tau^-$ **signatures**

The tau lepton pairs produced by the Higgs boson decay provide different experimental signatures, depending on the tau decay channels. The $H \to \tau_{\text{lep}}\tau_{\text{lep}}$ channel is characterised by the very simple signature of two leptons in the final state. Its branching ratio however is small, $\sim 12\%$, and only the $H \to \tau_e\tau_\mu$ channel is actually clean, since same flavour channels suffer from huge backgrounds due to Drell-Yan lepton pairs. The $H \to \tau_{\text{had}}\tau_{\text{had}}$ channel has a large branching ratio, $\sim 40\%$, but since its signature involves only hadronic objects, it is very difficult to study in the harsh LHC environment. The $H \to \tau_{\text{lep}}\tau_{\text{had}}$ channel benefits both from the large branching ratio, $\sim 45\%$, and the clean signature offered by the final state lepton. The presence of a single isolated lepton is important even because it allows to trigger on leptons, which are simpler than hadronic object triggers. A schematic sketch of the basic signature of the inclusive $H \to \tau_{\text{lep}}\tau_{\text{had}}$ process is shown in Figure 3.2. It should be noted that the lepton and $\tau_{\text{had-vis}}$ carry opposite electric charges.
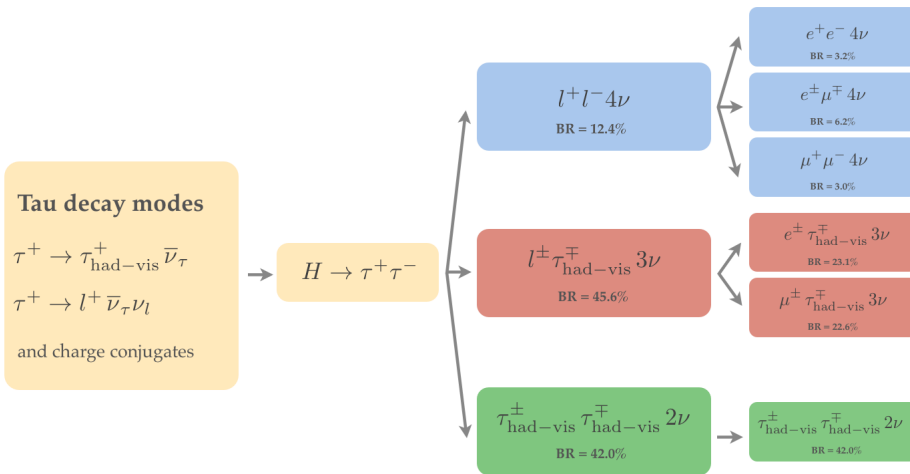
Figure 3.1: $H \to \tau^+\tau^-$ decay channels.
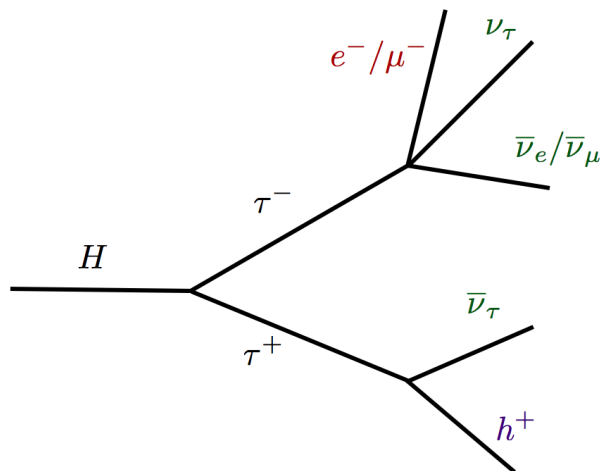
Figure 3.2: Basic signature of the inclusive $H \to \tau_{\mathrm{lep}}\tau_{\mathrm{had}}$ process.

3.2 Decay

The tau leptons from a $125\,\mathrm{GeV}$ Higgs are heavily boosted, $\gamma \sim 35$. Therefore the decay products are collimated around the parent tau momentum axis in the laboratory frame. At this energy all decay products are contained in a cone smaller than 0.2 in (η, ϕ) space.

The Higgs boson can be boosted in the plane transverse to the beams due to the underlying event activity, which leads to moderate boosts of a few tens GeV, or additional jet activity, that can result in boosts of a few hundred GeV. Decay products therefore are not always back-to-back, but can appear close to each other in the detector.

The rapidity of the Higgs boson is moderate, and therefore decay products tend to appear in the central detector region.

Electrons and muons in $H \to \tau_{\mathrm{lep}}\tau_{\mathrm{had}}$ have moderate transverse momentum spectra, due to neutrinos emitted in tau decays. This fact implies single lepton trigger thresholds and alternative combined triggers to recover acceptance at low momenta are critical. In ATLAS electrons and muons benefit from very good resolutions, and the energy and momentum scales, as well as identification efficiencies, are known to a high degree of accuracy (see Section 2.3.2 and 2.3.3). The hadronic system $\tau_{\mathrm{had\text{-}vis}}$ has slightly harder transverse momentum, since only one neutrino is emitted in this case. The reconstruction, identification and calibration of $\tau_{\mathrm{had\text{-}vis}}$ objects sets important experimental challenges, as shown in Section 2.3.5. Large fake rates of $\tau_{\mathrm{had\text{-}vis}}$ from jets and leptons require strong identification requirements in order to suppress the backgrounds. The control over tau identification efficiencies and fake rates has therefore a very important role in the context of this analysis. Moreover the effect of the limited knowledge of the tau energy scale is a dominant effect with respect to the scales of other visible decay products.

In the $H \to \tau_{\mathrm{lep}}\tau_{\mathrm{had}}$ process three neutrinos are emitted, that form two systems flying almost collinearly with visible decay products. Neutrinos can be detected only indirectly by measuring the missing transverse momentum, as described in Section 2.3.7. The momenta of the two neutrino systems partially compensate, and therefore the total $E_{\mathrm{T}}^{\mathrm{miss}}$ in the event is only moderate, peaking at less than 20 GeV. The direction of $E_{\mathrm{T}}^{\mathrm{miss}}$ typically points in between the visible decay products, and is more probably directed towards the lepton than to the $\tau_{\mathrm{had\text{-}vis}}$.

The proper invariant mass of the two taus system is defined as

$$m_{\mathrm{inv}\ \tau\tau} = \sqrt{(p_{\tau^+} + p_{\tau^-})^2} \tag{3.1}$$

where p_{τ^+} and p_{τ^-} are the four-momenta of the τ^+ and τ^- respectively. The invariant mass distribution is narrowly peaked at the generated Higgs mass. However the peak can not be fully reconstructed experimentally, since the neutrinos from the tau decays are not detected. A full mass reconstruction would require to solve equations for seven unknowns: the three-momenta of the neutrino systems associated to each τ lepton decay, that are described by the momentum magnitudes $p_{\nu\,1,2}$, and the polar and azimuthal angles $\theta_{\nu\,1,2}$ and $\phi_{\nu\,1,2}$, and the invariant mass $m_{\nu\,1}$ for the system associated to the leptonically decaying τ. The constraints available however are only four:

$$E_x^{\text{miss}} = p_{\nu\,1} \sin\theta_{\nu\,1} \cos\phi_{\nu\,1} + p_{\nu\,2} \sin\theta_{\nu\,2} \cos\phi_{\nu\,2} \qquad (3.2)$$

$$E_y^{\text{miss}} = p_{\nu\,1} \sin\theta_{\nu\,1} \sin\phi_{\nu\,1} + p_{\nu\,2} \sin\theta_{\nu\,2} \sin\phi_{\nu\,2} \qquad (3.3)$$

$$m_{\tau\,1}^2 = m_{\nu\,1}^2 + m_{\text{vis}\,1}^2 + 2\sqrt{p_{\text{vis}\,1}^2 + m_{\text{vis}\,1}^2}\sqrt{p_{\nu\,1}^2 + m_{\nu\,1}^2} - 2p_{\text{vis}\,1}p_{\nu\,1}\cos\Delta\theta_{\nu\,m1} \qquad (3.4)$$

$$m_{\tau\,2}^2 = m_{\text{vis}\,2}^2 + 2\sqrt{p_{\text{vis}\,2}^2 + m_{\text{vis}\,2}^2}\sqrt{p_{\nu\,2}^2 + m_{\nu\,2}^2} - 2p_{\text{vis}\,2}p_{\nu\,2}\cos\Delta\theta_{\nu\,m2} \qquad (3.5)$$

where the momenta, masses, polar and azimuthal angles of the visible decay products are indicated by $p_{\text{vis}\,1,2}$, $m_{\text{vis}\,1,2}$, $\theta_{\text{vis}\,1,2}$ and $\phi_{\text{vis}\,1,2}$ respectively. E_x^{miss} and E_y^{miss} indicate the two $E_{\text{T}}^{\text{miss}}$ components. The angles $\Delta\theta_{\nu\,m\,1,2}$ are then angles between the visible and respective invisible systems, and can be expressed in terms of the other variables. The $m_{\tau\,1,2}$ constraints are given by the tau lepton mass $m_\tau = 1.777\,\text{GeV}$.

Various reconstructed masses can therefore be defined depending on the assumptions applied to resolve this underconstrained system. The masses defined in the following are useful for different purposes, and are distinguished first of all by the treatment of the $E_{\text{T}}^{\text{miss}}$ in the event.

- **Visible mass**

  The simplest mass that can be reconstructed is a mass that makes use of the four-momenta of the visible decay products, that is of the lepton and $\tau_{\text{had-vis}}$ only. The visible mass is then defined as

  $$m_{\text{vis}} = \sqrt{(p_l + p_{\tau_{\text{had-vis}}})^2} \qquad (3.6)$$

  where p_l and $p_{\tau_{\text{had-vis}}}$ are the four-momenta of the lepton and $\tau_{\text{had-vis}}$ respectively. The visible mass does not peak at the H mass, but at lower values due to the missing energy of the neutrinos emitted in tau decays. The peak position moreover depends on the selection criteria applied. In the approximation of massless visible tau decay products the visible mass can be written as

  $$m_{\text{vis}} = \sqrt{2p_{\text{T}\,l}\,p_{\text{T}\,\tau_{\text{had-vis}}}\,(\cosh\Delta\eta - \cos\Delta\phi)} \qquad (3.7)$$

  where $\Delta\eta$ and $\Delta\phi$ are the pseudorapidity and azimuthal separation of the lepton and $\tau_{\text{had-vis}}$ respectively.

- **Transverse mass**

  The transverse mass is an invariant mass built just using transverse quantities

  $$m_{\text{T}} = \sqrt{(E_{\text{T}}^{\text{miss}} + E_{l,\text{T}})^2 - (E_x^{\text{miss}} + p_{l,x})^2 - (E_y^{\text{miss}} + p_{l,y})^2} \qquad (3.8)$$

  Since the lepton mass is negligible in this context, the transverse mass can be approximated by

  $$m_{\text{T}} = \sqrt{2p_{l,\text{T}} \cdot E_{\text{T}}^{\text{miss}} \cdot (1 - \cos\Delta\phi(l, E_{\text{T}}^{\text{miss}}))} \qquad (3.9)$$

where $\Delta\phi(l, E_{\mathrm{T}}^{\mathrm{miss}})$ is the angle between the lepton momentum vector in the transverse plane and the transverse missing momentum vector. When the angle $\Delta\phi(l, E_{\mathrm{T}}^{\mathrm{miss}})$ is small, the transverse mass is small as well. As a consequence $H \rightarrow \tau_{\mathrm{lep}}\tau_{\mathrm{had}}$ decays are characterised by a small transverse mass. The main use of the transverse mass in this context is as a discriminating variable, as explained in Section 3.4.

- **Composite particle mass**

  The simplest way to try to recover the energy lost by the three neutrinos in the final state in a full mass reconstruction is to treat the missing transverse momentum as if it were a particle with null longitudinal momentum, rather than due to two neutrino systems. It is possible then to define a composite particle mass by

  $$m_{\mathrm{comp}} = \sqrt{(p_l + p_{\tau_{\mathrm{had-vis}}} + p^{\mathrm{miss}})^2} \tag{3.10}$$

  where p_l and $p_{\tau_{\mathrm{had-vis}}}$ are the four-momenta of the lepton and $\tau_{\mathrm{had-vis}}$ respectively, and $p^{\mathrm{miss}} = (E_T^{\mathrm{miss}}, E_x^{\mathrm{miss}}, E_y^{\mathrm{miss}}, 0)$. Even in this case the peak position depends on the cuts applied for the event selection. Moreover the mass distribution displays a long tail that makes it unsuitable for a bump hunting analysis.

- **Invariant mass with the collinear approximation**

  A better invariant mass of the tau pair can be reconstructed from the decay products of the two taus under some assumptions:

  1. m_τ is negligible with respect to the typical energies involved in the process.

  2. The direction of the two neutrino systems produced in the tau decays are coincident with the measured decay products direction (collinear approximation).

  3. The tau decay products are not back to back ($\Delta\phi(l, \tau_{\mathrm{had-vis}}) \neq \pi$)

  Under these hypotheses the mass can be calculated as

  $$m_{\mathrm{coll}} = \sqrt{2(E_l + p_{\nu_1})(E_{\tau_{\mathrm{had-vis}}} + p_{\nu_2})(1 - \cos\theta)} \tag{3.11}$$

  where θ is the angle between the directions of the visible decay products of the taus (lepton and $\tau_{\mathrm{had-vis}}$). The only remaining unknowns are the energies of the two neutrino systems, that can be obtained solving the system given by Eq. 3.2 and 3.2. Mis-measurements of the $E_{\mathrm{T}}^{\mathrm{miss}}$ components or decays with the two taus nearly back to back can lead to unphysical solutions for p_{ν_1} and p_{ν_2} (negative energy). In these cases the invariant mass can not be reconstructed. The collinear approximation allows for the reconstruction of a mass that depends only mildly on the selection cuts and is peaked at the expected mass. However this happens at the cost of reconstruction inefficiencies, that depend both on the regime of azimuthal separation of the two visible decay products and the quality of reconstruction of $E_{\mathrm{T}}^{\mathrm{miss}}$.

- **Alternative mass reconstruction**
  The problem of the reconstruction of the invariant mass of a di-tau system can be addressed by an alternative strategy, known as Missing Mass Calculator, which is detailed in Section 3.3.

3.3 Invariant mass with the Missing Mass Calculator

The assumptions used for the reconstruction of the invariant mass with the collinear approximation are quite restrictive. The problem of missing degrees of freedom in the system of Eq. 3.2 can be addressed by an alternative strategy, first proposed in Ref. [133]. The mass reconstruction algorithm implementation takes the name of *Missing Mass Calculator* (MMC).

3.3.1 The concept

The basic idea behind the MMC method is the use of the information of the expected tau decay kinematics to choose a solution of the system of Eq. 3.2 in the kinematically allowed phase space of unconstrained variables. In the ATLAS implementation the phase space of the angles between the visible decay products and the respective neutrino systems is sampled using a Markov chain obtained with the Metropolis Hastings method [134]. The acceptance probability is built as an overall probability for the two angles between the visible and invisible decay products systems and the likelihood of the kinematics of a di-tau decay. The best mass estimator is computed from the sampled values as the one with highest probability.

Since the mass reconstruction performance is highly deteriorated by E_T^{miss} measurement resolution effects, the walk is performed in the phase space of E_T^{miss} as well. As a default an empirical two-parameters description of the resolution of the form $a + b\Sigma E_T$ (see Section 2.3.7) is used. The parameters of the E_T^{miss} scan are specifically tuned in simulated events.

Figure 3.3 shows the mass spectra for ggF $H \to \tau^+\tau^-$ events satisfying a basic selection (see Section 7.2.1) where the mass was reconstructed with the MMC algorithm. The information after full simulation was used, except for E_T^{miss}, which was considered at generator level (truth) and after full simulation. In this last case both the reconstruction with E_T^{miss} scan switched on and off are shown. The slightly lower reconstruction efficiency in the case where the generator level information was used is probably due to the fact the E_T^{miss} scan allows to partially compensate for the resolutions of the lepton and $\tau_{had\text{-}vis}$ in the event as well.

In the following some aspects relevant to the role of the E_T^{miss} measurement and usage in the MMC mass reconstruction are described.

3.3.2 E_T^{miss} measurement

The first important aspect to be considered is to provide the best possible measurement of E_T^{miss} to the mass reconstruction algorithm. In 2012 due to the harsh pile-up conditions mentioned in Section 2.1 several pile-up suppression algorithms were developed,
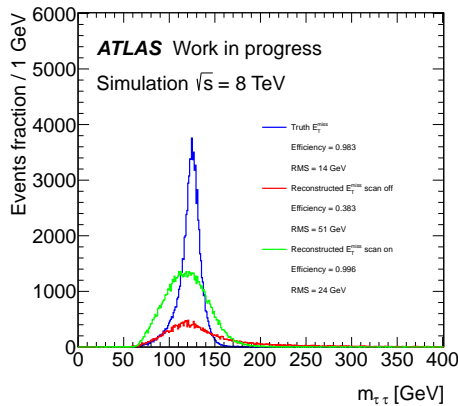
Figure 3.3: Mass reconstructed with MMC using different $E_{\mathrm{T}}^{\mathrm{miss}}$ inputs and switching the $E_{\mathrm{T}}^{\mathrm{miss}}$ scan on and off. More details are given in the text.

whose main principles are briefly summarised in Section 2.3.7. The $E_{\mathrm{T}}^{\mathrm{miss}}$ magnitude and angle resolutions, as well as the performance of mass reconstruction with the collinear approximation were considered to individuate the best performing reconstruction algorithm in the specific regime of the $H \to \tau_{\mathrm{lep}}\tau_{\mathrm{had}}$ analysis. The mass reconstructed with the collinear approximation was looked at rather than the MMC reconstruction directly to avoid dependencies on the specific $E_{\mathrm{T}}^{\mathrm{miss}}$ scan tune. As the pile-up affects especially the reconstruction of the $E_{\mathrm{T}}^{\mathrm{miss,\,SoftTerm}}$ term (see Section 2.3.7), the STVF and three variants of JetArea pile-up suppression [130] were considered. These variants differ in the procedure for the calculation of the event energy density and additional JVF requirements on the jets used in the computation of the $E_{\mathrm{T}}^{\mathrm{miss,\,soft}}$ term. Table 3.1 shows the performance in a sample of ggF $H \to \tau_{\mathrm{lep}}\tau_{\mathrm{had}}$ events with a basic event preselection and not in the category targeting VBF events. The magnitude and angle resolution are quoted, as well as the mean and width obtained for the collinear mass reconstruction and its efficiency. Table 3.2 shows the same figures but for VBF $H \to \tau_{\mathrm{lep}}\tau_{\mathrm{had}}$ events in the category targeting VBF events.

The STVF pile-up suppression in the $E_{\mathrm{T}}^{\mathrm{miss}}$ reconstruction provides a better resolution for ggF events than the Jet Area pile-up suppressions and a comparable resolution for VBF events . The Jet Area pile-up suppression provides a better angular resolution, which is probably the reason for the better reconstruction efficiency. Since the STVF pile-up suppression provides a smaller average bias in the $E_{\mathrm{T}}^{\mathrm{miss}}$ measurement, this is reflected in the mass reconstruction as well. Figure 3.4 shows spectra of invariant mass with the collinear approximation used. The distributions were fitted by a Crystal Ball function. It can be noted that the different resolution of the JetArea reconstruction variants leaves the core of the invariant mass distribution basically unaffected but leads to a much worse structure of the tails.

The topology of $H \to \tau^+\tau^-$ events offers interesting angular correlations between the expected $E_{\mathrm{T}}^{\mathrm{miss}}$ and visible decay products directions. The possibility of using these

Reconstruction	$\frac{E_T^{miss} - E_T^{miss,\ truth}}{E_T^{miss,\ truth}}$		$\Delta\phi(E_T^{miss}, E_T^{miss,\ truth})$	Collinear mass		
	Mean	Width	68% quantile	Mean	Width	Efficiency
STVF	0.54	1.43	1.16	155	63	0.371
EJA	0.71	1.54	1.05	165	68	0.489
EJAF	0.68	1.52	1.07	163	68	0.469
JAF	0.71	1.52	1.04	167	68	0.495

Table 3.1: E_T^{miss} and mass reconstruction with the collinear approximation performance for ggF $H \to \tau_{lep}\tau_{had}$ events ($m_H = 125\,\text{GeV}$) not in the VBF tagging category and for different E_T^{miss} pile-up suppression algorithms. The width is computed as the histogram RMS. Only statistically significant figures are shown.

Reconstruction	$\frac{E_T^{miss} - E_T^{miss,\ truth}}{E_T^{miss,\ truth}}$		$\Delta\phi(E_T^{miss}, E_T^{miss,\ truth})$	Collinear mass		
	Mean	Width	68% quantile	Mean	Width	Efficiency
STVF	0.21	0.79	0.27	127	25	0.758
EJA	0.26	0.76	0.27	130	31	0.738
EJAF	0.25	0.91	0.24	126	23	0.753
JAF	0.25	0.89	0.25	128	23	0.740

Table 3.2: E_T^{miss} and mass reconstruction with the collinear approximation performance in VBF $H \to \tau_{lep}\tau_{had}$ events ($m_H = 120\,\text{GeV}$) in the VBF tagging category and for different E_T^{miss} pile-up suppression algorithms. The width is computed as the histogram RMS. Only statistically significant figures are shown.

(a)

(b)

(c)

(d)
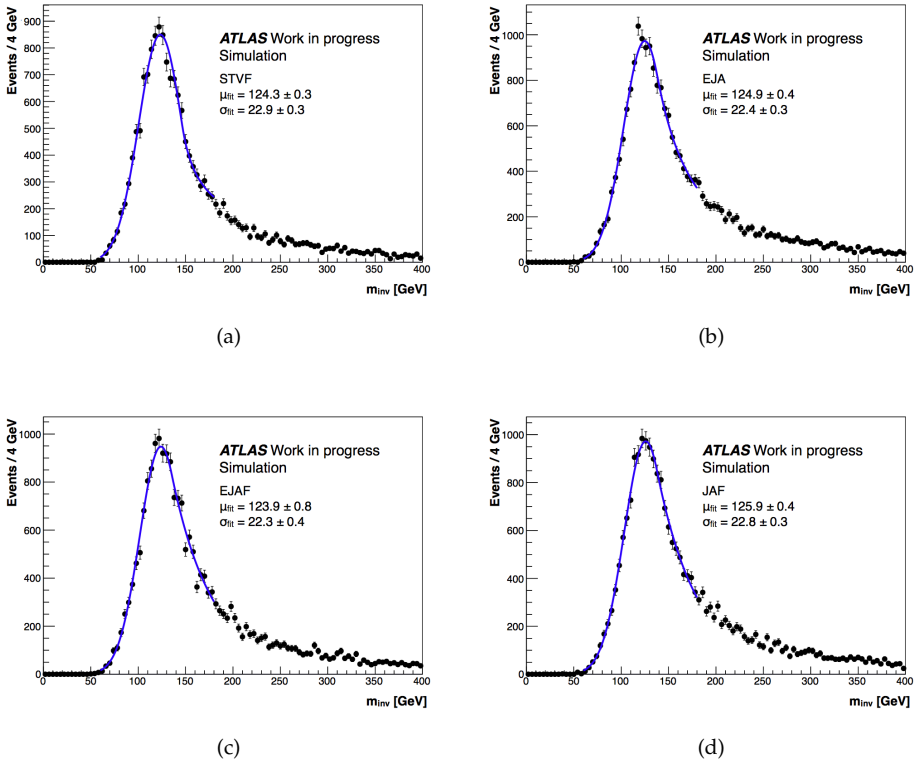
Figure 3.4: Invariant mass reconstructed with the collinear approximation for ggF $H \rightarrow \tau^+\tau^-$ events ($m_H = 125\,\text{GeV}$) with a basic preselection applied and for different $E_{\text{T}}^{\text{miss}}$ pile-up suppression algorithms.

correlations to contrast the deterioration of the measurement of $E_{\mathrm{T}}^{\mathrm{miss}}$ due to pile-up effects was investigated.

The $E_{\mathrm{T}}^{\mathrm{miss,\,SoftTerm}}$, which is largely affected by the pile-up, is generally corrected and retained as on average the resolution and bias with respect to the truth value are further deteriorated if it is dropped (this case is sometimes referred to as H_{T} $E_{\mathrm{T}}^{\mathrm{miss}}$ reconstruction), as shown in Figure 3.5 for ggF $H \to \tau^{+}\tau^{-}$ events satisfying a basic selection.
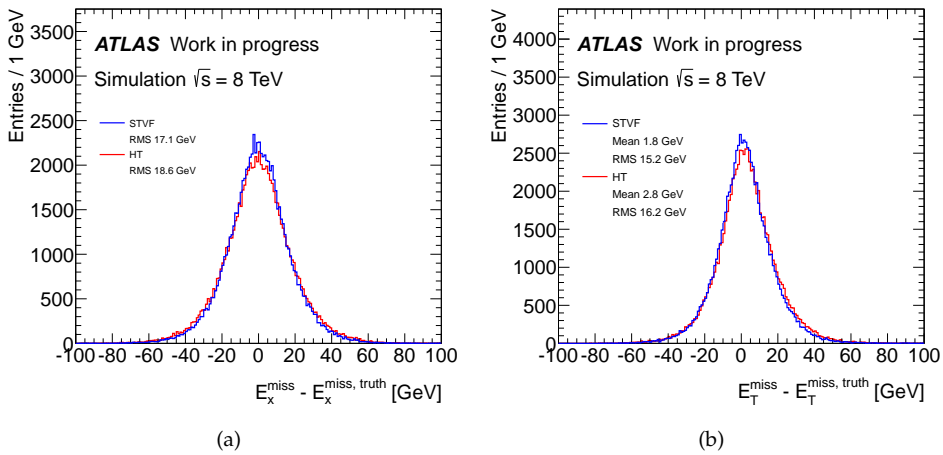
Figure 3.5: Resolution for the E_{x}^{miss} component and $E_{\mathrm{T}}^{\mathrm{miss}}$ for *STVF* and H_{T} $E_{\mathrm{T}}^{\mathrm{miss}}$ reconstruction in ggF $H \to \tau^{+}\tau^{-}$ events. More details are given in the text.

The fact that two neutrinos are emitted in a leptonic tau decay and only one in a hadronic decay enhance the probability that $E_{\mathrm{T}}^{\mathrm{miss}}$ points to the lepton direction rather than in the $\tau_{\mathrm{had\text{-}vis}}$ one. The possibility of dropping the $E_{\mathrm{T}}^{\mathrm{miss,\,SoftTerm}}$ term in the cases where the $E_{\mathrm{T}}^{\mathrm{miss}}$ points in the $\tau_{\mathrm{had\text{-}vis}}$ direction, assuming it is more probable that in these cases the $E_{\mathrm{T}}^{\mathrm{miss,\,SoftTerm}}$ term is badly reconstructed, was therefore investigated using the same sample described above. The choice of dropping the $E_{\mathrm{T}}^{\mathrm{miss,\,SoftTerm}}$ term was made in about $\sim 50\%$ of the cases. Figure 3.6 shows that choosing to drop the $E_{\mathrm{T}}^{\mathrm{miss,\,SoftTerm}}$ term when $E_{\mathrm{T}}^{\mathrm{miss}}$ points to the $\tau_{\mathrm{had\text{-}vis}}$ direction results in a slightly better $E_{\mathrm{T}}^{\mathrm{miss}}$ angular resolution. This is particularly evident when comparing to the choice of dropping the $E_{\mathrm{T}}^{\mathrm{miss,\,SoftTerm}}$ points in the lepton direction instead, indicating that the ansatz which was made was genuine. Improvements are however spoiled by the general worse performance of the H_{T} reconstruction. This is reflected in Figure 3.7 as well, where it can be seen that there is no improvement in the resolution of the $E_{\mathrm{T}}^{\mathrm{miss}}$ components.

3.3.3   Sanity and performance

The general sanity of the MMC algorithm was tested extensively in various other contexts, here only a few tests are presented.

A basic check was performed by using only the generator level information for events satisfying a basic selection (see Section 7.2.1) and a $E_{\mathrm{T}}^{\mathrm{miss}} > 20\,\mathrm{GeV}$ cut. The scan on $E_{\mathrm{T}}^{\mathrm{miss}}$
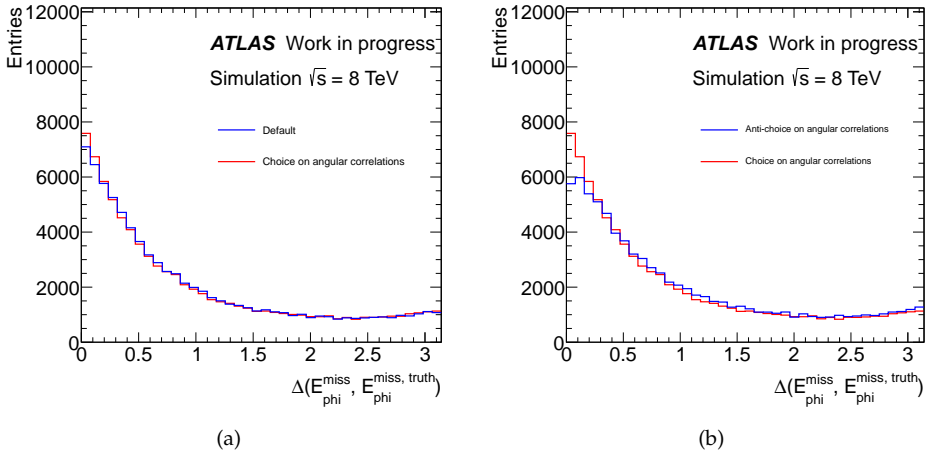
Figure 3.6: Angular $E_{\mathrm{T}}^{\mathrm{miss}}$ resolution dropping the $E_{\mathrm{T}}^{\mathrm{miss,\,SoftTerm}}$ term (red) compared to (a) the default *STVF* reconstruction (blue) and (b) to a reconstruction where the $E_{\mathrm{T}}^{\mathrm{miss,\,SoftTerm}}$ term is dropped when $E_{\mathrm{T}}^{\mathrm{miss}}$ points in the lepton direction instead (blue).
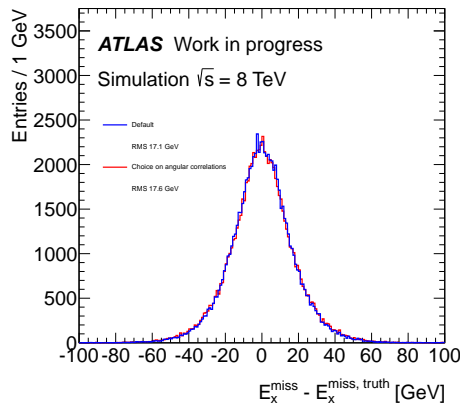
Figure 3.7: E_{x}^{miss} resolution dropping the $E_{\mathrm{T}}^{\mathrm{miss,\,SoftTerm}}$ term when $E_{\mathrm{T}}^{\mathrm{miss}}$ points to the $\tau_{\mathrm{had\text{-}vis}}$ direction compared to the default *STVF* reconstruction.

was switched off, and the performance of the MMC algorithm was compared to the mass reconstruction with the collinear approximation. Figure 3.8 shows mass spectra in the two cases, and it can be seen that the MMC algorithm allows for some improvement in the core of the distribution, which is narrower for the MMC algorithm. A large improvement was found for the tails of the mass distribution, which are mostly recovered by the MMC algorithm. In Table 3.3 the reconstruction efficiency and the peak width, computed as the histogram RMS, is shown in different regimes of the azimuthal separation of the lepton and $\tau_{\text{had-vis}}$. While in intermediate regimes the performance of the two algorithms is similar, MMC allows to recover the inefficiencies of the reconstruction with the collinear approximation when the lepton and $\tau_{\text{had-vis}}$ are back-to-back or very close in azimuth, which is the expected behaviour.

(a)   (b)
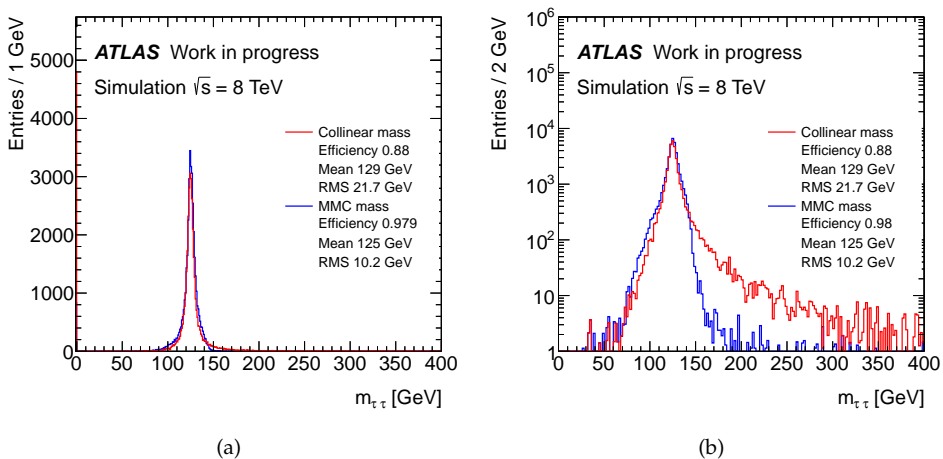
Figure 3.8: Mass reconstructed with the collinear approximation and the MMC algorithm for simulated ggF $H \rightarrow \tau^+\tau^-$ events with $m_H = 125\,\text{GeV}$ satisfying a basic selection and an $E_T^{\text{miss}} > 20\,\text{GeV}$ cut. Only generator level information was used in the mass reconstruction and the scan on E_T^{miss} was switched off in MMC. (a) linear scale, (b) logarithmic scale.

The general sanity of the scan on E_T^{miss} can be checked by comparing the E_T^{miss} used as input to the algorithm and the E_T^{miss} reconstructed from the solutions for the neutrino systems momenta obtained from the MMC algorithm to the generator level E_T^{miss} of the event. The comparison was performed on the same ggF $H \rightarrow \tau^+\tau^-$ sample used for the previous test. In this case however the components of the generator level E_T^{miss} were smeared with a gaussian resolution having as width the average resolution obtained for the simulated ggF sample used. The E_T^{miss} scan was tuned for the resolution used. Figure 3.9 shows the distributions of the E_x^{miss} and E_T^{miss} resolution in input and output of the MMC algorithm. The algorithm allows to reduce the resolution by $\sim 30\%$ and almost fully compensate for the average bias of E_T^{miss} induced by resolution effects, which is the desirable behaviour.

	Efficiency		Width [GeV]	
	Collinear	MMC	Collinear	MMC
$\Delta\phi < 0.5$	0.88 ± 0.01	0.94 ± 0.01	14.0 ± 0.4	14.2 ± 0.4
$0.5 < \Delta\phi < 1.0$	0.964 ± 0.005	0.962 ± 0.005	12.9 ± 0.3	13.8 ± 0.3
$1.0 < \Delta\phi < 1.5$	0.978 ± 0.003	0.972 ± 0.003	6.2 ± 0.1	6.6 ± 0.1
s $1.5 < \Delta\phi < 2.0$	0.973 ± 0.002	0.980 ± 0.002	6.06 ± 0.08	6.05 ± 0.08
$2.0 < \Delta\phi < 2.5$	0.969 ± 0.002	0.980 ± 0.002	5.23 ± 0.05	5.32 ± 0.05
$2.5 < \Delta\phi < 2.9$	0.912 ± 0.003	0.981 ± 0.001	9.13 ± 0.08	8.99 ± 0.08
$\Delta\phi > 2.9$	0.703 ± 0.004	0.984 ± 0.001	41.2 ± 0.4	14.3 ± 0.1

Table 3.3: Performance of mass reconstruction with the collinear mass approximation and MMC algorithm with the azimuthal separation of the lepton and $\tau_{\text{had-vis}}$. More details are given in the text.

(a)

(b)
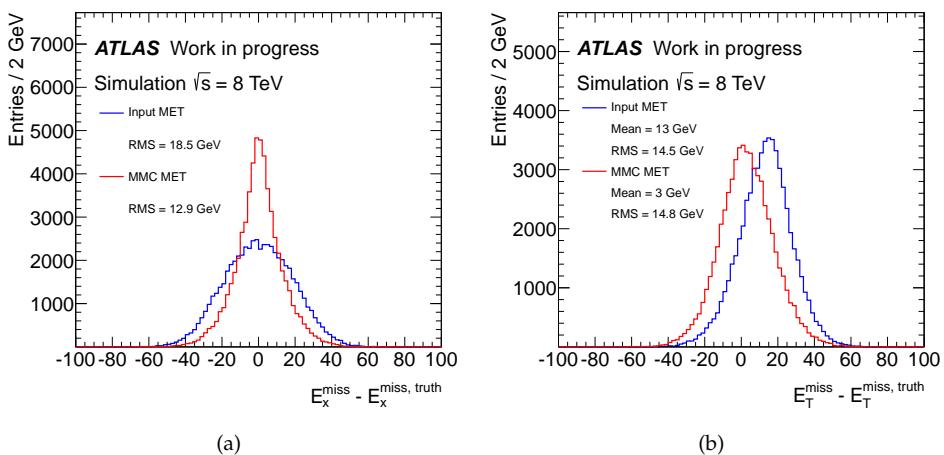
Figure 3.9: Resolutions of E_x^{miss} and E_T^{miss} in input to and output of the MMC algorithm. For the reconstruction of the mass the generator level information was used. The components of the generator level E_T^{miss} were smeared with the average resolution measured in the simulated sample used.

3.3.4 A few technicalities

The parametrisation of the E_T^{miss} resolution enters the algorithm both in the definition of the allowed phase space and in the acceptance probability used to build the Markov chain that allows to sample it. The role of the resolution was studied in ggF $H \to \tau^+\tau^-$ events satisfying a basic selection as described previously. The reconstruction of the mass was performed using truth information only, except for E_T^{miss}, where the truth information was smeared as already described in the previous section. The resolution used in the MMC algorithm was changed ranging from 0.25 to 5 times the resolution used in the E_T^{miss} smearing. Figure 3.10(a) and 3.10(b) show the efficiency of the MMC reconstruction by changing the resolution in the definition of the allowed E_T^{miss} phase space and in the acceptance probability used in building the Markov Chain respectively. Analogously Figure 3.10(c) and 3.10(d) show the width of the mass distribution, obtained as the histogram RMS. Finally Figure 3.10(e) and 3.10(f) show the m_{MMC} spectra corresponding to the different cases. The performance depends mostly on the resolution used in the definition of the allowed phase space, even if the mass spectrum, and especially its width, depends on the resolution used in the acceptance probability as well.

3.3.5 Towards an E_T^{miss} covariance matrix approach

From the previous studies it can be seen that the correctness of the information on the E_T^{miss} resolution in the algorithm is important for its performance. In the default MMC tune the only dependence of the E_T^{miss} resolution on the event kinematics is through the ΣE_T variable. For complex events like $H \to \tau^+\tau^-$, deposits in the calorimeter are not expected to be isotropic and therefore the actual event per event E_T^{miss} resolution is expected to be related to the event topology. For example in an event with a jet, a lepton and $\tau_{\text{had-vis}}$ and little other hadronic activity it would be more probable that a mismeasurement of E_T^{miss} makes it point towards the jet or $\tau_{\text{had-vis}}$, which are more difficult to measure precisely.

The resolution of E_T^{miss} can be described by

$$f(\mathbf{x}) = \frac{1}{2\pi\sqrt{|C|}} \exp -\frac{1}{2}\mathbf{x}^T C^{-1}\mathbf{x} \qquad \mathbf{x} = \begin{pmatrix} E_x^{\text{miss}} - E_x^{\text{miss, truth}} \\ E_y^{\text{miss}} - E_y^{\text{miss, truth}} \end{pmatrix} \qquad (3.12)$$

the covariance matrix is defined as

$$C = \begin{pmatrix} \text{varX} & \text{varXY} \\ \text{varXY} & \text{varY} \end{pmatrix} \qquad (3.13)$$

where $\text{var}X$, $\text{var}Y$ and $\text{var}XY$ are the variances and covariance for the $E_{x,y}^{\text{miss}}$ components. Figure 3.11 illustrates the difference between the approach of an isotropic E_T^{miss} resolution and the full covariance matrix approach. The MMC algorithm samples the phase space defined by the blue circle in the first case, and by the yellow ellipse in the second case. The capability of determining that an E_T^{miss} mismeasurement is more probable in a specific direction would allow MMC to sample a more realistic probability distribution and therefore to possibly obtain better results.
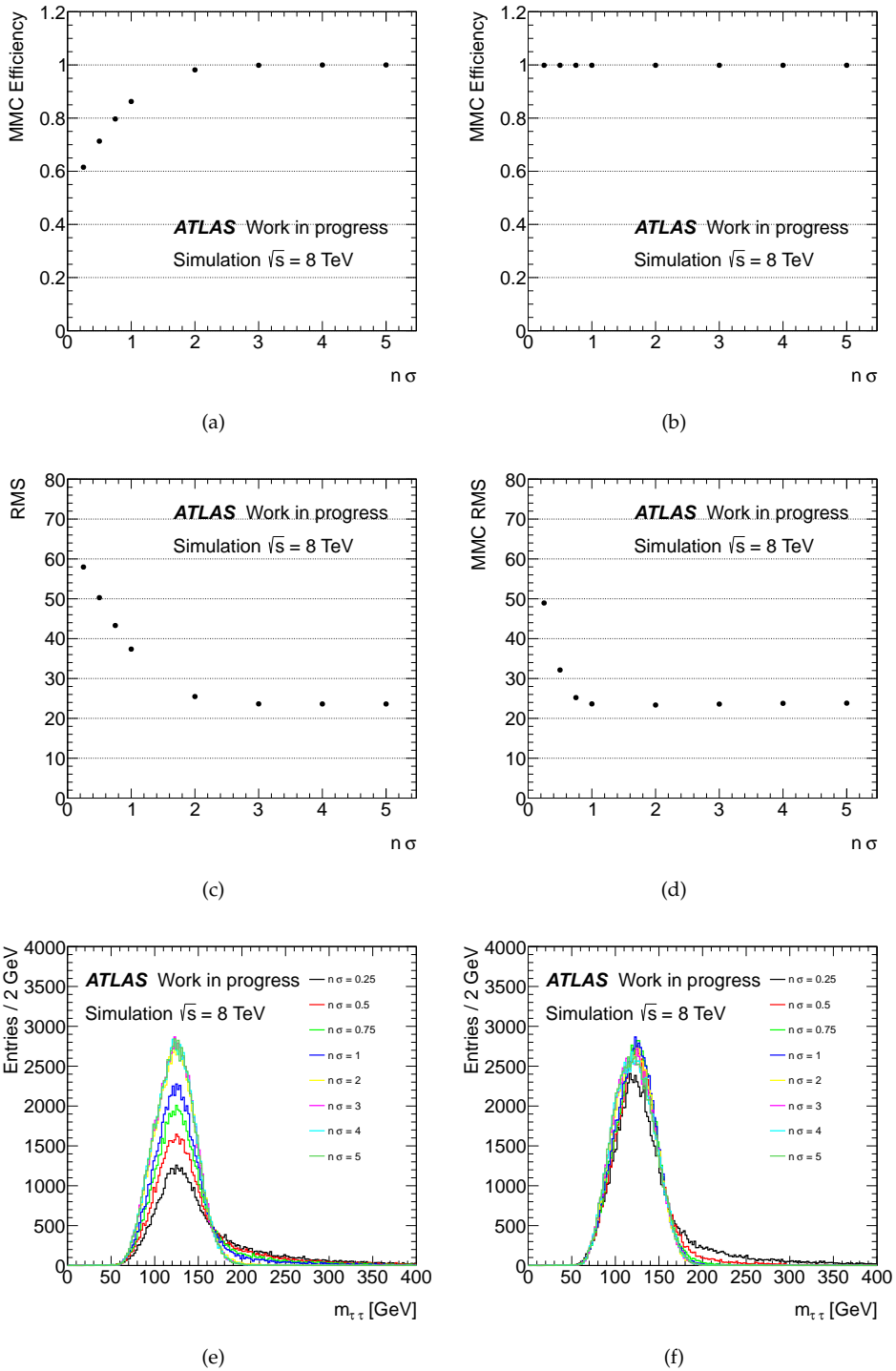
Figure 3.10: MMC (a-b) efficiency, (c-d) mass width and (e-f) mass spectra changing the E_T^{miss} resolution in the definition of (a-c-e) the allowed phase space for the E_T^{miss} scan and (b-d-f) the acceptance probability used to build the Markov Chain.
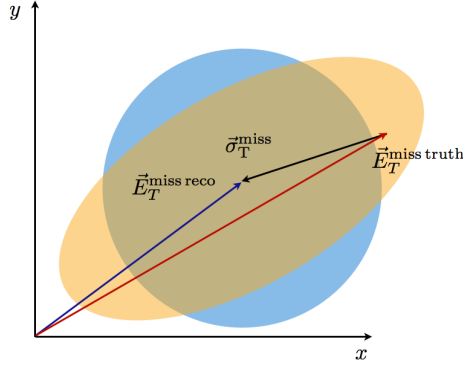
Figure 3.11: Sketch of possible approaches to the description of the $E_{\mathrm{T}}^{\mathrm{miss}}$ resolution in the MMC algorithm. More details are given in the text.

The characteristics of the ellipse are the lengths of the major and minor axes a and b and the angle between the major axis and the x axis θ

$$a, b = \frac{\mathrm{Tr}(C) \pm \sqrt{\mathrm{Tr}(C)^2 - 4\det(C)}}{2} \qquad \tan 2\theta = \frac{2\,\mathrm{var}XY}{\mathrm{var}X - \mathrm{var}Y} \qquad (3.14)$$

$$(3.15)$$

For a first test the same sample of ggF $H \to \tau^+\tau^-$ events used previously was considered. Only generator level information was used for the mass reconstruction, except for $E_{\mathrm{T}}^{\mathrm{miss}}$ for which it was smeared. The resolution for the E_x^{miss} and E_y^{miss} components was taken from a covariance matrix defined by

$$\mathrm{var}X = \left(\frac{\alpha\sigma}{(1 - \rho^2)^{\frac{1}{4}}} \right)^2 \qquad (3.16)$$

$$\mathrm{var}Y = \left(\frac{\frac{1}{\alpha}\sigma}{(1 - \rho^2)^{\frac{1}{4}}} \right)^2 \qquad (3.17)$$

$$\mathrm{var}XY = \rho\sqrt{\mathrm{var}X\,\mathrm{var}Y} \qquad (3.18)$$

where σ is the average resolution measured for the sample considered. For the specific test shown the values of the other two parameters were taken as $\alpha = 0.9$ and $\rho = 0.5$. Figure 3.12 shows the pulls obtained along the x and y axis when considering an isotrope covariance matrix, with $\mathrm{var}X = \mathrm{var}Y = \sigma^2$ and $\rho = 0$ and the covariance matrix corresponding to the smearing that was performed. As expected in this second case the pulls have a gaussian distribution with unitary width. In the previous case instead the pulls are narrower in the x axis direction and wider in the y axis direction.

(a)   (b)
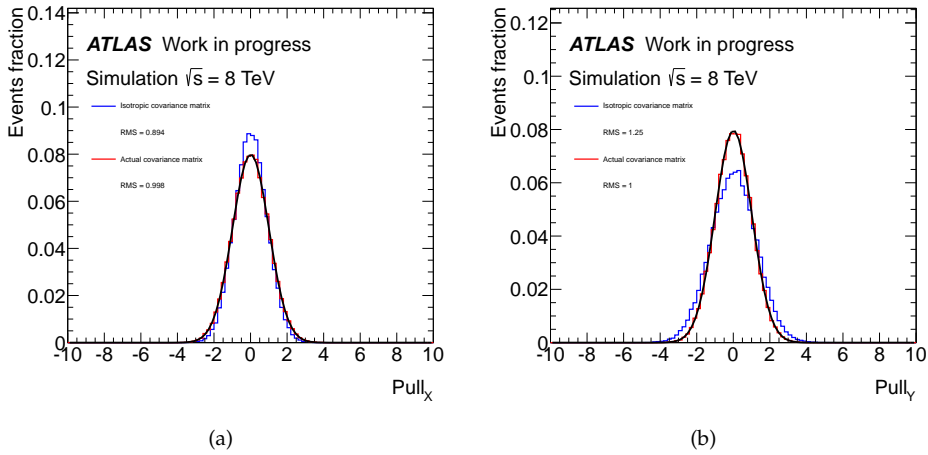
Figure 3.12: Pulls of (a) E_x^{miss} and (b) E_y^{miss} considering an isotrope covariance matrix and the matrix corresponding to the smearing performed. More details are given in the text.

Figure 3.13(a) shows the resolution of E_x^{miss} in output of MMC when using the isotrope covariance matrix and the matrix corresponding to the smearing in the algorithm. Some improvement can be seen, even if limited, especially when considering the large difference in pulls observed previously in Figure 3.12. Figure 3.13(b) shows the spectrum of m_{MMC} in the two cases. The efficiency, already very high, is marginally improved, while the resolution, computed as the histogram RMS, improves by about 5%. Therefore, even if it is clear that the constraint given by the tau lepton decay kinematics to the E_T^{miss} in the event is weak, using a E_T^{miss} covariance matrix is an approach that can be worthwhile to pursue.

A preliminary attempt to build a covariance matrix for E_T^{miss} with `MET_RefFinal` reconstruction and `STVF` pile-up suppression was made by considering the resolution only for the worse resolved objects, therefore only for the E_T^{miss} terms accounting for jets, $\tau_{\mathrm{had\text{-}vis}}$ and for calorimeter deposits not associated to any object.

The covariance matrix was obtained as a sum of the covariance matrices for the different E_T^{miss} terms. For terms accounting for objects the following was used

$$\mathrm{varX} = \sum_i \sigma_{p_{\mathrm{T}\,i}}^2 \cos^2 \phi_i \tag{3.19}$$

$$\mathrm{varY} = \sum_i \sigma_{p_{\mathrm{T}\,i}}^2 \sin^2 \phi_i \tag{3.20}$$

$$\mathrm{varXY} = \sum_i \sigma_{p_{\mathrm{T}\,i}}^2 \sin \phi_i \cos \phi_i \tag{3.21}$$

where the transverse momentum resolutions $\sigma_{p_{\mathrm{T}\,i}}$ were taken from appropriate parameterisation for the objects of interest.

(a)

(b)
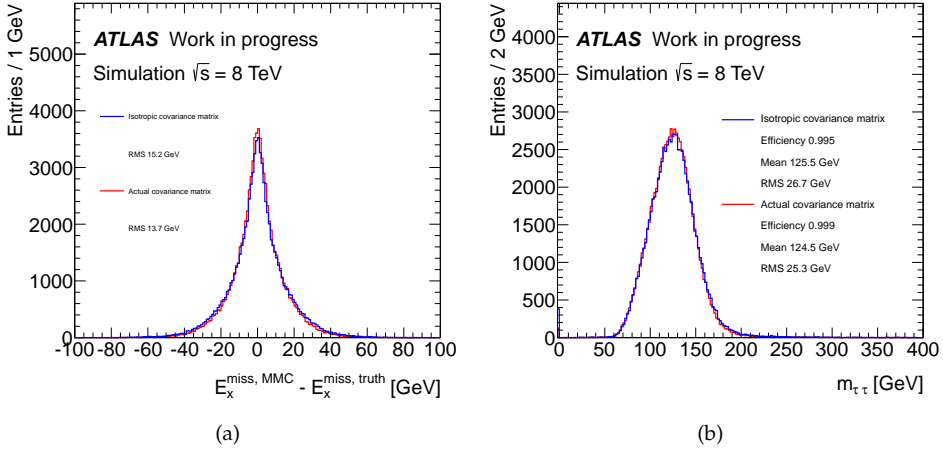
Figure 3.13: (a) resolution of E_x^{miss} in output of the MMC algorithm and (b) m_{MMC} mass spectrum using an isotropic covariance matrix in the reconstruction algorithm or the matrix used for the smearing. More details are given in the text.

For the $E_{\mathrm{T}}^{\mathrm{miss\ soft}}$ term instead

$$\mathrm{varX} = \mathrm{varY} = \alpha\sqrt{\sum E_{\mathrm{T}}^{\mathrm{soft}}} \tag{3.22}$$

$$\mathrm{varXY} = 0 \tag{3.23}$$

where the parametrisation was obtained from a sample of $Z \rightarrow \mu^+\mu^-$ events with no jets.

Assuming the correctness of the covariance matrices obtained this way, which will be further discussed in the following, the covariance matrices for $H \rightarrow \tau^+\tau^-$ ggF and VBF and $Z \rightarrow \tau^+\tau^-$ events were analysed. Considering Eq. 3.16-3.18 the values of α and ρ can be computed from the elements of the covariance matrix as

$$\rho = \frac{\mathrm{varXY}}{\sqrt{\mathrm{varXvarY}}} \tag{3.24}$$

$$\alpha = \sqrt[4]{r} \qquad r = \frac{\min(\mathrm{varX}, \mathrm{varY})}{\max(\mathrm{varX}, \mathrm{varY})} \tag{3.25}$$

The values of α and ρ in simulated $H \rightarrow \tau^+\tau^-$ and $Z \rightarrow \tau^+\tau^-$ events are shown in Figure 3.14 in order to provide a simple comparison to the test presented above.

Interestingly the values of α and ρ indicate that $H \rightarrow \tau^+\tau^-$ and $Z \rightarrow \tau^+\tau^-$ events can have quite anisotrope covariance matrices and that there can be marked differences depending on the topology.

Figure 3.15(a) and 3.15(b) show the major and minor axes of the ellipses corresponding to the same covariance matrices. Here the differences between topologies are particularly visible. VBF events tend to have a major axis of the ellipse markedly longer than
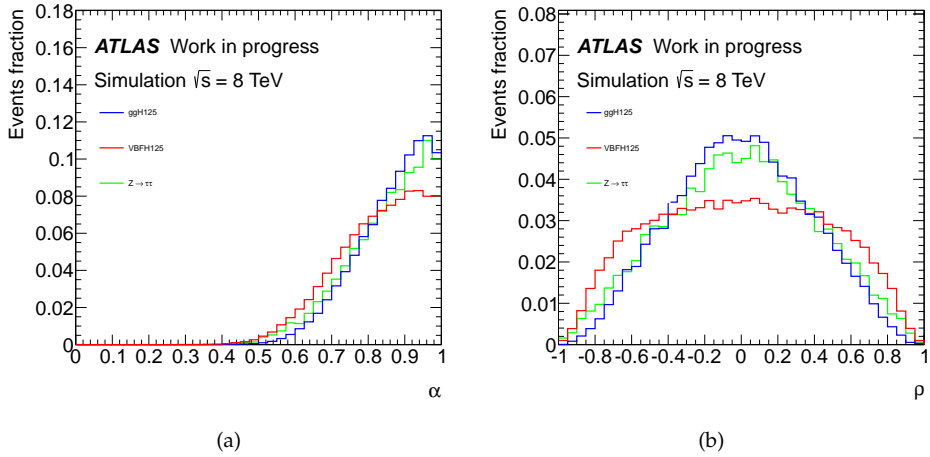
Figure 3.14: Values of α and ρ for ggF and VBF $H \to \tau^+\tau^-$ events as well as $Z \to \tau^+\tau^-$ events obtained with the covariance matrices described in the text.

the other samples. It was verified that it is typically aligned with one of the jets in the event. The two-peak structures visible for ggF $H \to \tau^+\tau^-$ and $Z \to \tau^+\tau^-$ events are due to populations of events with no jets and with jets.

Pulls along the major and minor axes were studied, as well as a pull for ρ, which was defined as $\text{Pull}_\rho = [(E_x^{\text{miss}} - E_x^{\text{miss truth}})(E_x^{\text{miss}} - E_x^{\text{miss truth}})]/\text{var}XY$. The pulls are typically better along the major axis and for ggF and $Z \to \tau^+\tau^-$ events, which indicates that the covariance matrix description is better for the topologies and in the aspects where the $E_T^{\text{miss, jet}}$ term is dominant with respect to the $E_T^{\text{miss, soft}}$ term. This could be expected since the description of the $E_T^{\text{miss, soft}}$ covariance matrix term is rather simplified, for example by the assumption that for this term the resolution is isotrope.

Aspects of the performance of the MMC algorithm and of its sanity have been studied. When using generator level information the resolution is of $\sim 14\,\text{GeV}$ for collinear events, but is greatly improved, down to $\sim 6\,\text{GeV}$ for events with intermediate azimuthal separation of the visible decay products. The largest improvements on the reconstruction with the collinear approximation are obtained in the reconstruction efficiency. It has been shown that there is some limited margin for the improvement of the MMC mass reconstruction with reconstructed objects when introducing a full covariance matrix description of E_T^{miss}. While there are indications that useful information is encoded in the covariance matrix for $H \to \tau^+\tau^-$ and $Z \to \tau^+\tau^-$ events, a proper description would require at least a better treatment of the covariance matrix term accounting for the $E_T^{\text{miss, soft}}$ term.
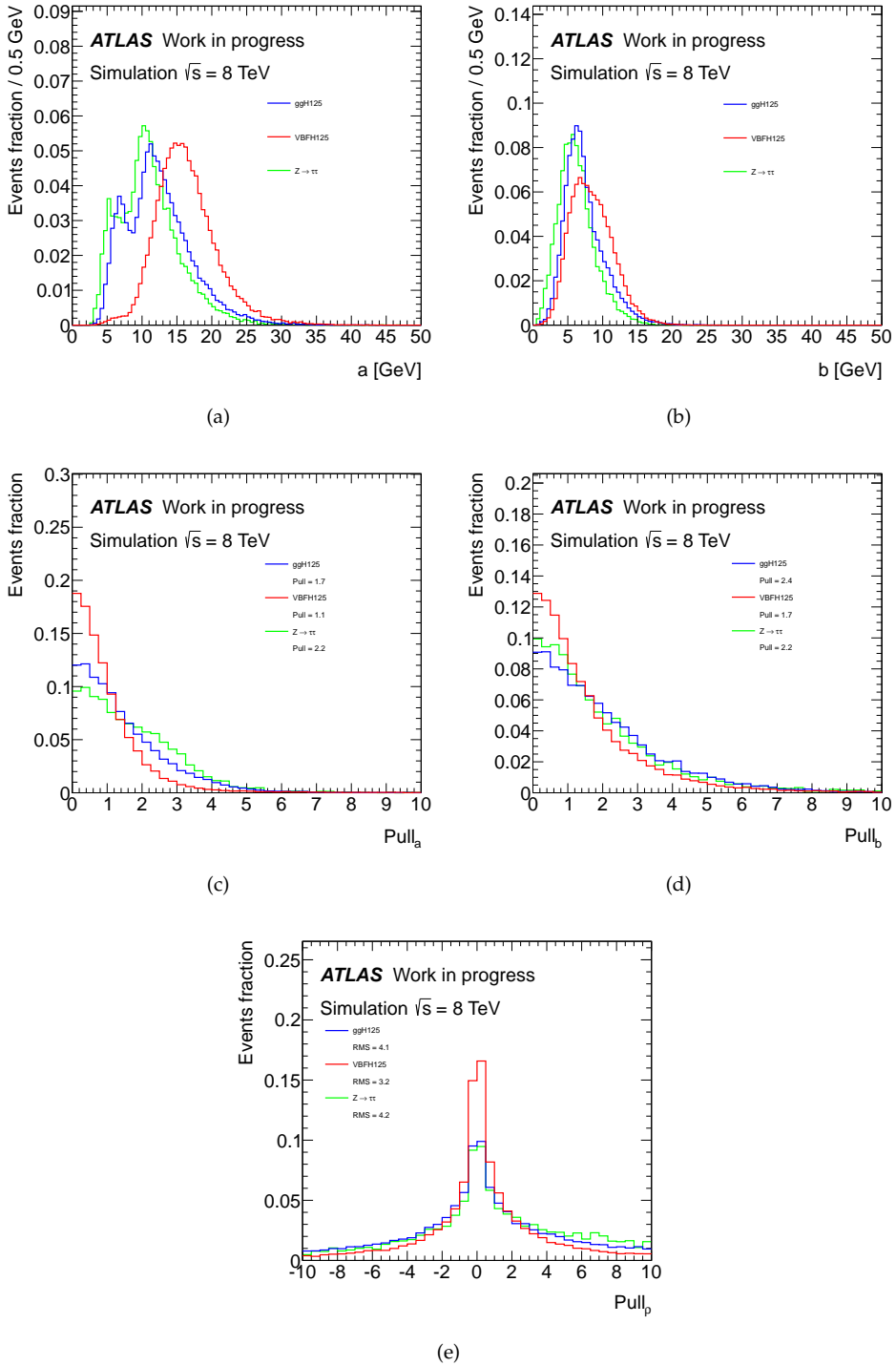
Figure 3.15: (a) ellipse major axis and (b) minor axis for $H \to \tau^+\tau^-$ ggF and VBF events and $Z \to \tau^+\tau^-$ events. (c) pull along the major axis direction, (b) pull along the minor axis direction and (c) pull for ρ. More details are given in the text.

3.4 Backgrounds

The study of the $H \to \tau_{\text{lep}}\tau_{\text{had}}$ process suffers from many background processes. These can be divided into reducible and irreducible backgrounds. While the negative effect of reducible backgrounds can be mitigated by a strategy of object identification and event topology cuts, in principle the signal can be extracted from the irreducible backgrounds only by means of mass spectroscopy. Actually however exclusive characteristics of the production modes help to limit the impact of these backgrounds. A schematic representation of the mechanism by which the backgrounds mimic the $H \to \tau_{\text{lep}}\tau_{\text{had}}$ signature is given in Figure 3.16.
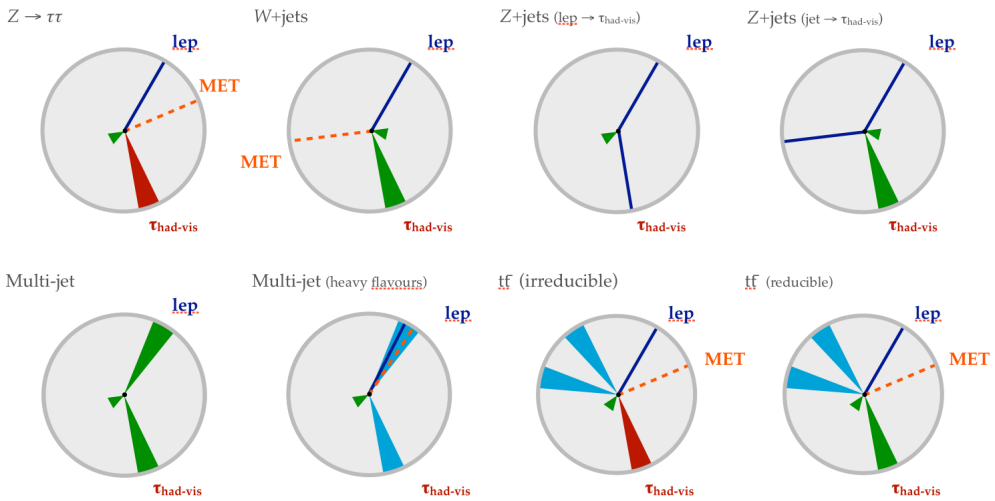
Figure 3.16: Schematic representation of the main backgrounds to $H \to \tau_{\text{lep}}\tau_{\text{had}}$. The colours in the figure indicate the actual object in the event: blue lines are leptons (e/μ), red cones $\tau_{\text{had-vis}}$, yellow dotted line $E_{\text{T}}^{\text{miss}}$ and green cones QCD jets. Small green cones indicate either additional jets or soft hadronic activity. The labels indicate the interpreted signature.

3.4.1 $Z \to \tau^+\tau^-$

The largest background to the $H \to \tau^+\tau^-$ process is irreducible $Z \to \tau^+\tau^-$. The modelling of the $Z \to \tau^+\tau^-$ background in the details of the final state is a crucial aspect of $H \to \tau^+\tau^-$ studies. Since this background is irreducible and mass resolution is limited, it is practically impossible to define a representative control region, free from other backgrounds and that does not overlap with the signal region. A partially data driven approach to the estimation of this background can nevertheless be pursued. The basic idea is to use selected $Z \to \mu^+\mu^-$ data events to accurately model the kinematics of the Z boson production, which is affected by large theory and modelling uncertainties, including the pile-up conditions. Even the kinematics of the decay, apart from the difference

between the muon and τ lepton masses, is identical. Since the coupling of the Higgs boson to muons is small, a data selected $Z \to \mu^+\mu^-$ sample is virtually signal free. The method takes the name of *embedding*. The starting point is the selection of $Z \to \mu^+\mu^-$ events, that requires two high transverse momentum muons, isolation and a di-muon invariant mass window. For every event in the selected sample then the $Z \to \mu^+\mu^-$ kinematics is extracted, Muons are replaced by tau leptons on truth level, with the same kinematics (except the mass difference is considered). The tau leptons are then decayed with TAUOLA and PHOTOS, taking the spin correlations into account. The decay event is then processed by the full ATLAS detector simulation, digitisation and reconstruction, leading to a Monte Carlo mini-event. Muon tracks and calorimeter energy deposits estimated from simulation are subtracted from the original event. The $Z \to \tau^+\tau^-$ mini-event is finally merged. Only after the embedding full reconstruction is run. A scheme of the complete embedding procedure is shown in Figure 3.17. Since trigger efficiencies can not be emulated properly embedding samples need some dedicated procedure to derive the overall normalisation. Corrections for specific detector effects have been derived as well depending on the analysis. Systematic uncertainties on the embedding procedure arise from the dependence of results on the isolation requirements applied for the selection of $Z \to \mu^+\mu^-$ events in data, and on the procedure of subtraction of the muon energy deposits in the calorimeter.
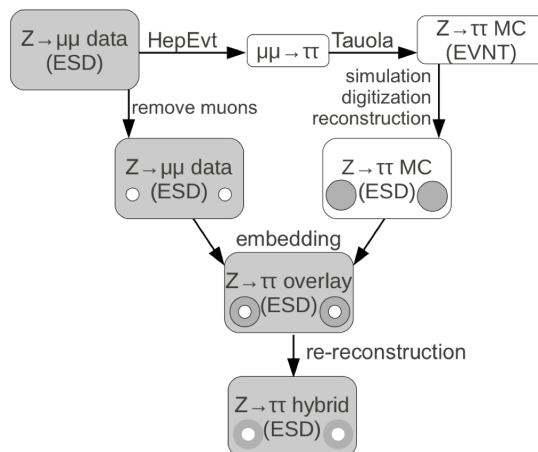
Figure 3.17: Flowchart of the embedding procedure described in the text [135].

The modelling of $Z \to \tau^+\tau^-$ events can be obtained from Monte Carlo simulation as well, especially in cases where the embedding sample statistics is not sufficient or for cross-checking purposes. Typically the ALPGEN generator is used to accurately model additional jet multiplicity and kinematics. The matched shower is typically Herwig+Jimmy, since it is found to model jet multiplicities better. PYTHIA8 is used in some specific cases, described when relevant.

3.4.2 Multi-jet

Di-jet and multi-jet events can easily fake the $H \rightarrow \tau^+\tau^-$ signature, either with both the lepton and $\tau_{\text{had-vis}}$ faked by QCD jets or with a true lepton, *eg* from semileptonic *b*-quark decays, and a fake $\tau_{\text{had-vis}}$. The charge correlation between the object interpreted as lepton and the one interpreted as $\tau_{\text{had-vis}}$ is, as a first approximation, absent. Ideally there would be no $E_{\text{T}}^{\text{miss}}$ in the event, but mismeasurement of the jets can lead to fake $E_{\text{T}}^{\text{miss}}$, typically aligned with one of the two objects faking the $H \rightarrow \tau^+\tau^-$ signature. Multi-jet events can be strongly suppressed using lepton isolation cuts and $\tau_{\text{had-vis}}$ identification. In principle they would not have a peaking mass distribution, but this can be partially induced by cuts. The description of multi-jet events is subject to several theory and modelling uncertainties. Moreover, since the cross-section for such processes is large, the statistics of Monte Carlo events needed would exceed the ATLAS simulation capabilities. It is therefore preferred to model multi-jet events in a fully data-driven way with different techniques depending on the analysis.

3.4.3 W + jets

The production of a W boson in association with jets occurs according to diagrams analogous to those for Z + jets production shown in Figure 1.4. The $H \rightarrow \tau^+\tau^-$ signature can be faked by the presence of a genuine lepton and a fake $\tau_{\text{had-vis}}$ mimicked by an additional jet in the final state. Fakes from fully hadronic W boson decays are negligible. Since the charge of the incoming and outgoing quarks is the same, W + jets events that contaminate the signal selection display some significative charge anti-correlation. The $E_{\text{T}}^{\text{miss}}$ in this type of events is genuine, since it originates from the neutrino from the W boson leptonic decay. As a consequence, the transverse mass of the lepton and $E_{\text{T}}^{\text{miss}}$ displays a Jacobian peak at the W boson mass. This fact is typically exploited to suppress the W + jets background with a moderate tranverse mass cut. Contrary to $H \rightarrow \tau^+\tau^-$ events the $E_{\text{T}}^{\text{miss}}$ in the event points away from the objects interpreted as the visible tau decay products. This fact is used in order to obtain some additional background suppression using angular correlation variables depending on the analysis. Similarly to multi-jet events the mass spectrum of W + jets events is non-resonant, but some shaping of the spectrum can be induced by selection cuts. W + jets events are typically simulated using the ALPGEN generator in order to reproduce the kinematics of associated jets accurately. The parton shower is either Herwig+Jimmy or PYTHIA8, depending on the analysis. A delicate point in the description of the background from W + jets is the modelling of the rate at which a jet induced by a quark or gluon fakes the $\tau_{\text{had-vis}}$ signature, which is typically not correctly simulated. Due to this reason the contribution of the W + jets background is estimated with data-driven or partially data-driven techniques depending on the analysis. This is possible since it is relatively simple to select pure W + jets control regions reverting the transverse mass cut.

3.4.4 $Z + \text{jets}$

Events where a Z boson decays leptonically, $Z \to e^+ e^-$ and $Z \to \mu^+ \mu^-$, can fake the $H \to \tau^+ \tau^-$ signature with a lepton that fakes the $\tau_{\text{had-vis}}$. No genuine $E_{\text{T}}^{\text{miss}}$ is present in these events, but it can easily be faked, especially in harsh pile-up conditions. This background is insidious since it displays a peak in the mass spectrum. The visible mass peaks at about the Z mass, but once the information from fake $E_{\text{T}}^{\text{miss}}$ is added in the mass reconstruction, the peak is pushed to higher values, possibly overlapping with a light Higgs boson signal. $Z + \text{jets}$ events can be modelled using Monte Carlo samples from the ALPGEN generator, showered either by Herwig+Jimmy or PYTHIA8. Similarly to the case of $W + \text{jets}$ events the modelling of the rate at which electrons and muons fake the $\tau_{\text{had-vis}}$ signature is crucial. For electrons in particular mis-modellings have been observed and needed to be corrected as described in Section 2.3.5 making use of a $Z \to e^+ e^-$ control region. Another mechanism by which $Z + \text{jets}$ events can fake the $H \to \tau^+ \tau^-$ signature is analogous to the mechanism explained for $W + \text{jets}$ events, that is with a QCD jet faking the $\tau_{\text{had-vis}}$ signature. This background can be suppressed by vetoing the presence of additional leptons in the final state. Any residual background is modeled using Monte Carlo simulation.

3.4.5   Top

Backgrounds from t-quark are dominated by $t\bar{t}$ pair production. Depending on the region of phase space this background can have a non-negligible irreducible component from decays of the type

$$t\bar{t} \to W^+ b \, W^- \bar{b} \to \tau^+ \nu_\tau b \, \tau^- \bar{\nu}_\tau \bar{b} \to l^+ \nu_l \bar{\nu}_\tau \nu_\tau b \, \tau_{\text{had-vis}}^- \nu_\tau \bar{\nu}_\tau \bar{b}. \tag{3.26}$$

The reducible component originates from similar decay chains, but where the lepton signature may come from a leptonic W decay, other than $W \to \tau\nu$. The fake $\tau_{\text{had-vis}}$ may be due to a jet, which is typically from W hadronic decays rather than from b-jets. Top backgrounds may originate from single-top production as well, but this occurrence is much rarer. Production in s- and t-channel as well as Wt production are considered. Single-top contamination is typically estimated only with Monte Carlo simulation using the AcerMC generator [136]. Top backgrounds are suppressed by the same cuts used against $W + \text{jets}$. Moreover a simple handle to reduce the contamination from top events in the selected sample is to veto the presence of b-tagged jets in the event.

3.4.6   Diboson

Diboson production gives typically small contributions to the total background. Similarly to backgrounds from $t\bar{t}$ pair production it can have both a reducible and an irreducible component. This background is typically estimated simply from Monte Carlo simulation. The generators used include Herwig and ALPGEN for $q\bar{q}$ production, and $gg2WW$ [137] for loop induced gg production. Samples are typically showered by Herwig+Jimmy.

3.5 Production

Production processes play a crucial role in the analysis strategy of the $H \to \tau^+\tau^-$ process. As noted in the previous section in fact, the selection of $H \to \tau_{\text{lep}}\tau_{\text{had}}$ events is experimentally challenging, and the contamination from backgrounds is large. Production processes offer characteristic signatures that can be exploited to better separate the signal from backgrounds. Two production modes are relevant in the context of this work: the ggF and VBF modes already introduced in Section 1.4.3. The VH and t$\bar{\text{t}}$H processes have small cross-sections, that make these processes less relevant for a discovery analysis. The cross-sections for the various production processes at $\sqrt{s} = 7$ TeV and $\sqrt{s} = 8$ TeV are listed in Appendix **??**. A scheme of the priorities in the categorisation strategy is shown in Figure 3.18. This scheme is peculiar to the $H \to \tau^+\tau^-$ channel. The actual implementation of the categorisation scheme is presented in Chapter 7.

3.5.1 VBF tagging

The peculiar topology of the VBF production mode is the one that can best be used to suppress backgrounds in this channel. Therefore it is the first target of an event categorisation strategy. Since cuts have to be placed to select the topology of interest, the study of differential distributions covers an important role. In particular the distributions of jet multiplicity and leading two jet spectra are of great interest. Typically in experiments the two leading p_{T} jets are chosen as the tagging jets. It should be noted however that this choice is not obvious, and rather the most natural one from a theory point of view would be to select the jets with largest rapidity separation. The first choice of the tagging jets partially acts as a veto on additional jet activity in the event. Relevant variables of the two tagging jets system include their rapidity separation and the di-jet mass. The presence of additional radiation in the event is usually studied by the presence of a third jet in the rapidity gap between the two tagging jets, even if in analyses different variables that select similar phase space regions can be used. Ref. [138] includes studies of the dependence of relevant differential distributions for different NLO calculations and the results obtained matching the NLO prediction with parton shower with the POWHEG method. In Ref. [53] the effect of the parton-shower matching scheme is investigated comparing results from POWHEG and aMC@NLO [139, 140]. In principle in a discovery analysis, that does not aim as a first goal to the study of different production modes, it is not necessary to suppress ggF events in VBF-tagging categories. Actually however theory uncertainties on the predictions of the ggF contribution in VBF-like phase space are very large. Events from ggF can display characteristics similar to VBF ones. The contribution to the di-jet selection is already subject to uncertainties in the inclusive $H + 2\,\text{jets}$ selection. Moreover cuts on variables sensitive additional hadronic activity in the event effectively divide the sample into an exclusive 2-jet bin and an inclusive $\geq$3-jet bins. Great care therefore has to be taken in determining the VBF tagging criteria not to let theory uncertainties in the ggF contamination explode. This topic is treated in Section 8.3 of Ref. [53].

3.5.2 Making the most of ggF production

Also the ggF production mode offers some characteristics that allow to distinguish $H \rightarrow \tau^+\tau^-$ from the main irreducible $Z \rightarrow \tau^+\tau^-$ background. The first of these characteristics is the Higgs boson transverse momentum p_T^H, that tends to be harder than the Z boson p_T. Requiring a moderate boost of the di-tau system allows to improve the mass reconstruction for genuine resonant $\tau\tau$ events as well. This fact can be used in the analysis especially to suppress fakes. For this type of events in fact the collinear approximation often does not allow to obtain physical solutions for the neutrino four-momenta. It is therefore convenient to define a *Boosted* category that exploits the better sensitivity that can be achieved in this particular region of phase space. Such a category allows to include in the analysis VBF events that do not pass the tagging requirements as well. The prediction of the shape of the transverse momentum of the Higgs boson for ggF events is not trivial. The best prediction available presently is the NNLO+NNLL prediction provided by the HqT program [141, 142, 143]. In POWHEG the contribution of the real-emission cross-section that is treated with shower Monte Carlo is governed by a reduction factor of the form $1 - \texttt{hfact}^2/(p_T^{H\,2} + \texttt{hfact}^2)$. The value of the damping factor $\texttt{hfact}$ can be set by the user and following the recommendations of Ref. [138] can be set to $\texttt{hfact} = m_H/1.2$ to reproduce the HqT prediction. Presently the implementation of ggF in POWHEG includes the treatment of the finite top and bottom quark mass effect, that affects the Higgs transverse momentum distribution [144]. A treatment of the issues related to the prediction of p_T^H and its uncertainties can be found in Ref. [138] and [53].

After the selection of *VBF* and *Boosted* categories, the signal sensitivity can still be enhanced by selecting a category of events where at least one jet is present. Naively this can be understood by the larger probability of a gluon emission off the gluon line in the ggF leading order diagram with respect to the $q\bar{q}$ initiated Z boson production. Remaining events are grouped in a dedicated zero jet category.
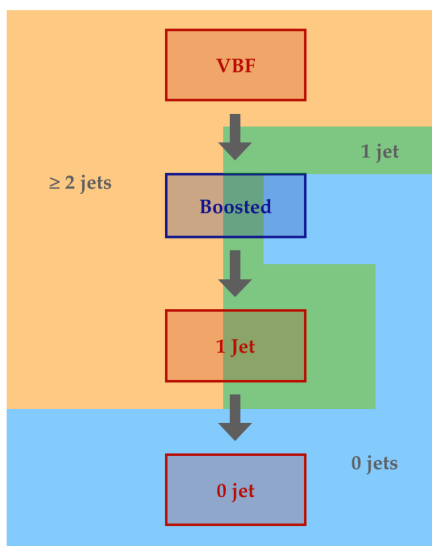
Figure 3.18: Scheme of the $H \to \tau^+\tau^-$ categorisation strategy based on production mode tagging. Categories in the red blocks are defined based mostly on the jet properties in the event. In blue the *Boosted* category is defined mainly through the Higgs boson transverse momentum. The categorisation priorities, typical ot the $H \to \tau^+\tau^-$ channel analysis, are indicated by the gray arrows. Coloured areas naively illustrate jet multiplicity bins.

Warming up: $Z \to \tau^+\tau^-$ cross-section measurement

The search for $H \to \tau^+\tau^-$ is experimentally very challenging at a hadron collider as the LHC. Its signature can easily be mimicked by several other processes, as described in Section 3.4. The $Z \to \tau^+\tau^-$ process in particular is the largest background to $H \to \tau^+\tau^-$, and its study is therefore very important to pursue a search for this Higgs boson decay channel. Demonstrating the feasibility of a $Z \to \tau^+\tau^-$ analysis is a crucial step in gaining control over all of the other backgrounds as well. Moreover $Z \to \tau^+\tau^-$ is a source of true hadronically decaying τ leptons, and being able to select a well controlled sample of $Z \to \tau^+\tau^-$ events is fundamental for the study of $\tau_{\text{had-vis}}$ reconstruction and identification performance.

The measurement of the $Z \to \tau^+\tau^-$ inclusive cross-section is the simplest complete measurement that can be performed, and was therefore carried out on 2010 data collected at $\sqrt{s} = 7$ TeV [117], and afterwards repeated on the 2011 dataset [145]. In a cross-section measurement, besides the control over the background, a crucial role is played by the definition of the methodology.

In this Chapter the measurement of the cross-section in the $Z \to \tau_{\text{lep}}\tau_{\text{had}}$ channel, both in the $\tau_\mu\tau_{\text{had}}$ and $\tau_e\tau_{\text{had}}$ channels, on 2010 data is described, with a few highlights on the measurement in the other channels and on 2011 data.

Throughout the following $Z \to \tau^+\tau^-$ will indicate the Drell-Yan $pp \to Z/\gamma^* \to \tau^+\tau^-$ process, which in the kinematical region considered is dominated by the Z peak contribution. An analogous convention is used for $Z \to l^+l^-$ (with $l = e/\mu$).

4.1 Data and Monte Carlo samples

The data sample used in this analysis corresponds to a total integrated luminosity of about 36 pb^{-1}, recorded with stable beam conditions and a fully operational detector in 2010 (see Section 2.2.12).

Events are selected using single lepton triggers. For the $\tau_\mu\tau_{\text{had}}$ final state, single muon triggers requiring $p_{\text{T}} > 10 - 13$ GeV, depending on the run period, are used. For the $\tau_e\tau_{\text{had}}$ final state, a single electron trigger requiring $E_{\text{T}} > 15$ GeV is used. The efficiencies of the triggers are determined from data using a tag-and-probe method, applied to $Z \to \mu^+\mu^-$, $Z \to e^+e^-$ and $W \to e\nu$ events respectively.

At the time this analysis was performed the Monte Carlo generators mentioned in Section 3.4 were not yet of common use. The samples used in this analysis are generated at $\sqrt{s} = 7$ TeV with less refined Monte Carlo generators. In particular Z and W samples were generated with PYTHIA6 and diboson samples with HERWIG. The default ATLAS MC10 tune [146] was used. For the default signal sample the MRSTLO* modified LO PDF set was used [147]. For the determination of signal acceptances and related uncertainties a high statistics (2M events) generator only sample was used. For the estimation of acceptance theory uncertainties alternative samples were used as better described in Section 4.5.3.

4.2 Event selection

The event selection includes the selection of good quality events with the $Z \to \tau_{\mathrm{lep}} \tau_{\mathrm{had}}$ signature and further selections that are then applied to suppress the backgrounds.

4.2.1 Event preselection and object selection

The selection of $Z \to \tau^+ \tau^-$ events is based first of all on an event preselection, which allows to select events with a well reconstructed primary vertex and to reject events with jets or $\tau_{\mathrm{had\text{-}vis}}$ candidates caused by out-of-time cosmic-rays, beam-halo events or known noise effects in the calorimeters [148].

Then the presence of a lepton (e/μ) and a $\tau_{\mathrm{had\text{-}vis}}$ fulfilling the following requirements is required.

Muons

Muons are required to

- be combined (see Section 2.3.3),
- have a p_{T} greater than $15\,\mathrm{GeV}$,
- have $|\eta| < 2.4$ in order to match the trigger acceptance,
- have a longitudinal impact parameter of less than 10 mm with respect to the primary vertex, to mitigate the impact of fakes,
- pass the ID track quality criteria described in [149]

Electrons

Electrons are required to

- have transverse energy $E_{\mathrm{T}} > 16\,\mathrm{GeV}$,
- be within the rapidity range $|\eta| < 2.47$, excluding the overlap region between the barrel and end-cap calorimeters $1.37 < |\eta| < 1.52$,
- pass *tight* identification criteria (see Section 2.3.2 and Ref. [150]).

$\tau_{\mathrm{had\text{-}vis}}$

Reconstructed $\tau_{\mathrm{had\text{-}vis}}$ objects are required to

- have a transverse momentum $p_\mathrm{T} > 20\,\mathrm{GeV}$,

- lie within the pseudorapidity range $|\eta| < 2.47$, excluding the region $1.37 < |\eta| < 1.52$,

- pass *medium* identification cuts,

- pass a dedicated cut-based selection to reject fake $\tau_\mathrm{had\text{-}vis}$ from electrons (see Section 2.3.5 and Ref. [151]).

The $\tau_\mathrm{had\text{-}vis}$ identification methods (see Section 2.3.5) were in the commissioning phase at the time the analysis was performed, therefore identification requirements were based only on three robust variables describing the energy-weighted transverse width of the $\tau_\mathrm{had\text{-}vis}$ candidate in the electromagnetic calorimeter (R_EM), its p_T-weighted track width (R_track), and the fraction of the transverse momentum carried by the leading track. In order to account for the increasing collimation of the $\tau_\mathrm{had\text{-}vis}$ candidates with increasing p_T, the cuts on the quantities R_EM and R_track were parametrized as a function of the candidate p_T. The identification was optimized separately for candidates with one or multiple tracks.

The $\tau_\mathrm{had\text{-}vis}$ identification and electron fake rejection requirements applied led to an efficiency of $\sim 40\%$ ($\sim 30\%$) for real 1-prong (3-prong) τ candidates as determined from signal Monte Carlo simulated samples.

Isolation requirements were applied to both electron and muon candidates using the following variables.

- $I_{PT}^{\Delta R}$ was defined as the ratio between the total transverse momentum of charged particles in the ID in a cone of size ΔR centered around the lepton direction and the transverse momentum (energy) of the muon (electron) candidate.

- $I_{ET}^{\Delta R}$ was defined as the ratio between the total transverse energy measured in the calorimeters in a cone ΔR around the lepton direction and the transverse momentum (energy) of the muon (electron) candidate.

In the reconstruction of all the isolation variables, the lepton p_T or E_T was subtracted. The selections applied were:

Muons $I_{PT}^{0.4}/p_\mathrm{T} < 0.06$ and $I_{ET}^{0.4}/p_\mathrm{T} < 0.06$,

Electrons $I_{PT}^{0.4}/E_\mathrm{T} < 0.06$ and $I_{ET}^{0.3}/E_\mathrm{T} < 0.1$.

The efficiencies for these isolation requirements were measured in data using $Z \to \mu^+\mu^-$ and $Z \to e^+e^-$ events. Figure 4.1 shows the distribution of the $I_{ET}^{0.4}/p_\mathrm{T}$ variable for muon and $I_{ET}^{0.3}/E_\mathrm{T}$ variable for electron candidates.

Correction factors, to account for measured differences in the identification and isolation efficiencies in data and simulation, were applied to Monte Carlo simulated samples as a function of η and ϕ of muon candidates and η and p_T of the electron candidates.

As multiple electron, muon, or $\tau_\mathrm{had\text{-}vis}$ candidates may be reconstructed from the same localized response in the ATLAS detector, an overlap removal procedure was performed to ensure a unique hypothesis for each object. Since muons and electrons can

(a)   (b)
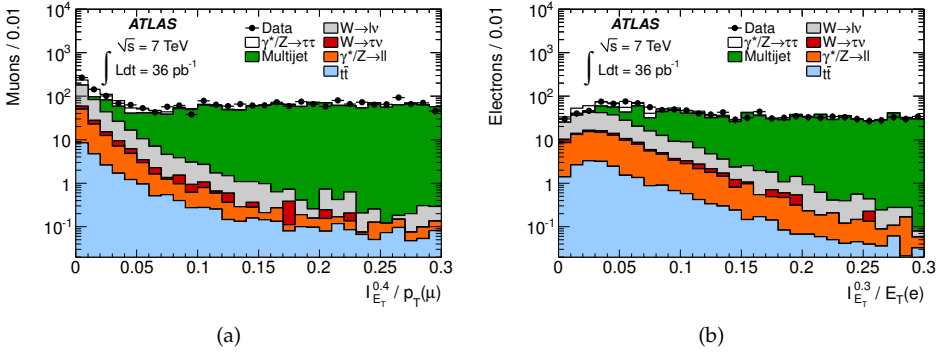
Figure 4.1: Isolation variables (a) $I_{ET}^{0.4}/p_T$ for muon and (b) $I_{ET}^{0.3}/E_T$ for electron candidates, after selecting one $\tau_{\text{had-vis}}$ candidate and one lepton with opposite signs in the $\tau_\mu\tau_{\text{had}}$ and $\tau_e\tau_{\text{had}}$ channels respectively. The multijet background is estimated from data according to the method described in Section 4.3; all other processes are estimated using Monte Carlo simulation.

be selected with a higher purity than hadronic τ decays, any preselected $\tau_{\text{had-vis}}$ was not considered if it laid within $\Delta R < 0.4$ of any preselected lepton. Electron candidates were removed if they overlapped with muon candidates within $\Delta R < 0.2$. Finally electron and muon candidates were removed if they laid within $\Delta R < 0.2$ from a harder reconstructed lepton of the same kind.

Since the `MET_RefFinal` E_T^{miss} reconstruction was in the commissioning phase when the analysis was performed, a simplified E_T^{miss} calculation where the calorimeter term $E_T^{\text{miss, calo}}$ was reconstructed from LCW calibrated topological clusters only was used (see Section 2.3.7 and Ref. [152]).

In the analysis of the $Z \to \tau_{\text{lep}}\tau_{\text{had}}$ channel the $\tau_\mu\tau_{\text{had}}$ and $\tau_e\tau_{\text{had}}$ channels were considered separately up to the combination, where correlations among systematic uncertainties were taken into account.

4.2.2 Background suppression

The event preselection and object selection requirements described in the previous section allowed to select a sample which however was still highly contaminated by backgrounds. Cuts were therefore applied in order to suppress events faking the $Z \to \tau_{\text{lep}}\tau_{\text{had}}$ signature. The main characteristics of backgrounds that were typically exploited to suppress them are summarised in Section 3.4, the specific implementation chosen for this analysis is detailed in the following.

Lepton isolation
Lepton isolation is the main handle for the suppression of multi-jet backgrounds. Since it entered lepton selection has already been discussed in the previous section.

Additional $\tau_{\text{had-vis}}$ cuts The chosen $\tau_{\text{had-vis}}$ was required to have exactly 1 or 3 associated tracks and a reconstructed charge of unit magnitude. These characteristics discriminate genuine $\tau_{\text{had-vis}}$ from QCD jets.

Charge correlations The chosen $\tau_{\text{had-vis}}$ and the chosen lepton were required to have opposite charges as expected from $Z \to \tau^+\tau^-$ decays (OS).

Transverse mass

The main suppression of the $W +$ jets background was achieved by requiring a low transverse mass of the lepton and $E_{\text{T}}^{\text{miss}}$ in the event (defined in Section 3.2). Distributions of m_{T} are shown in Figure 4.2 (a-b). The cut chosen for this analysis is $m_{\text{T}} < 50\,\text{GeV}$.

Angular correlations

Additional suppression of the $W +$ jets background was obtained by requiring that $E_{\text{T}}^{\text{miss}}$ pointed in between the lepton and $\tau_{\text{had-vis}}$. The variable $\Sigma \cos \Delta\phi$ was defined as the sum of the angles between the lepton and $E_{\text{T}}^{\text{miss}}$ and $\tau_{\text{had-vis}}$ and $E_{\text{T}}^{\text{miss}}$ respectively:

$$\Sigma \cos \Delta\phi = \cos(\Delta\phi(l, E_{\text{T}}^{\text{miss}})) + \cos(\Delta\phi(\tau_{\text{had-vis}}, E_{\text{T}}^{\text{miss}})). \tag{4.1}$$

Distributions of $\Sigma \cos \Delta\phi$ are shown in Figure 4.2 (c-d). $W +$ jets backgrounds accumulate at negative $\Sigma \cos \Delta\phi$, since the neutrino recoils against the lepton and jet system, whereas the $Z \to \tau^+\tau^-$ distribution has an asymmetric tail extending into positive $\Sigma \cos \Delta\phi$ values, that correspond to topologies where the $E_{\text{T}}^{\text{miss}}$ points between the lepton and $\tau_{\text{had-vis}}$, as expected for the $E_{\text{T}}^{\text{miss}}$ originating from two tau leptons decays. High $\Sigma \cos \Delta\phi$ are typical of events where the Z boson has higher p_{T}. Events were therefore selected by requiring $\Sigma \cos \Delta\phi > -0.15$. The chosen cut is inclusive of the bulk of events with nearly back-to-back visible decay products. Even though the resolution of the $\phi(E_{\text{T}}^{\text{miss}})$ direction is degraded for low values of $E_{\text{T}}^{\text{miss}}$, this had no adverse effect on the impact of this cut, as such events correspond to $\Sigma \cos \Delta\phi \sim 0$ and hence pass the selection.

Dilepton veto

Any event with more than one muon or electron candidate was vetoed, which strongly suppressed background from $Z \to l^+l^-$ events. To increase the background rejection, the selection criteria for the second lepton were relaxed with respect to those described in Section 4.2.1: the ID track quality requirements were dropped for muons, while electrons were required only to pass the *medium* selection and have $E_{\text{T}} > 15\,\text{GeV}$.

Visible mass window

Selected events were required to have a visible mass in the range $35 < m_{\text{vis}} < 75\,\text{GeV}$. This window was chosen to include the bulk of the signal, while avoiding background contamination from $Z \to l^+l^-$ decays. For $Z \to \mu^+\mu^-$ events the peak is at slightly lower values than for $Z \to e^+e^-$ events for two reasons: muons misidentified as $\tau_{\text{had-vis}}$ leave less energy in the calorimeter compared to misidentified electrons, and the proportion of events where the $\tau_{\text{had-vis}}$ arises from a misidentified jet, as opposed to a misidentified lepton, is higher in $Z \to \mu^+\mu^-$ events.
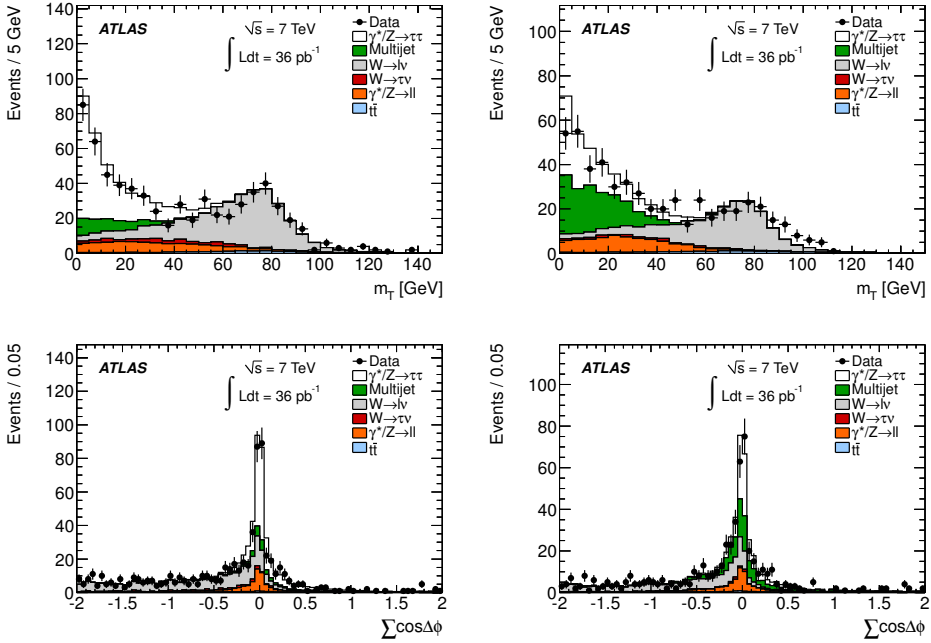
Figure 4.2: The distributions of the transverse mass, m_T, are shown for the (a) $\tau_\mu \tau_{had}$ and (b) $\tau_e \tau_{had}$ channels. The distributions of $\Sigma \cos \Delta \phi$ are shown for the (c) $\tau_\mu \tau_{had}$ and (d) $\tau_e \tau_{had}$ final states. All distributions are shown after the object selection for the given final state and after requiring exactly one electron or muon candidate. A requirement on the charge of the $\tau_{had\text{-}vis}$ candidate to be of opposite sign to that of the lepton is also applied. The background is estimated as described in Section 4.3.
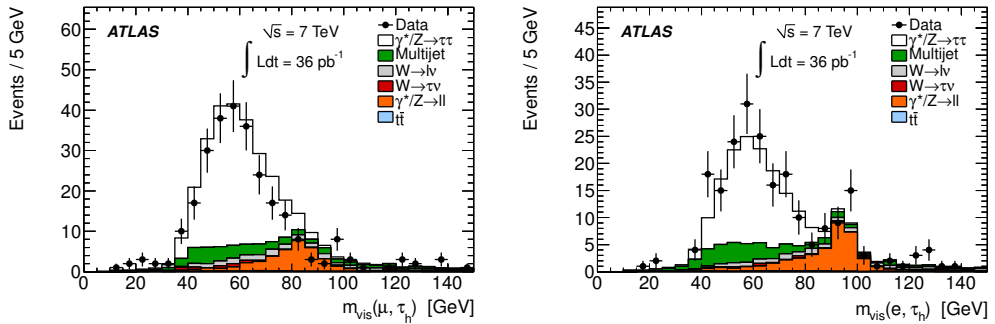
Figure 4.3: The distributions of the visible mass of the $\tau_{had\text{-}vis}$ candidate and the lepton are shown for the (a) $\tau_\mu \tau_{had}$ and (b) $\tau_e \tau_{had}$ channels. These distributions are shown after the full event selection, except for the visible mass cut. The background is estimated as described in Section 4.3.
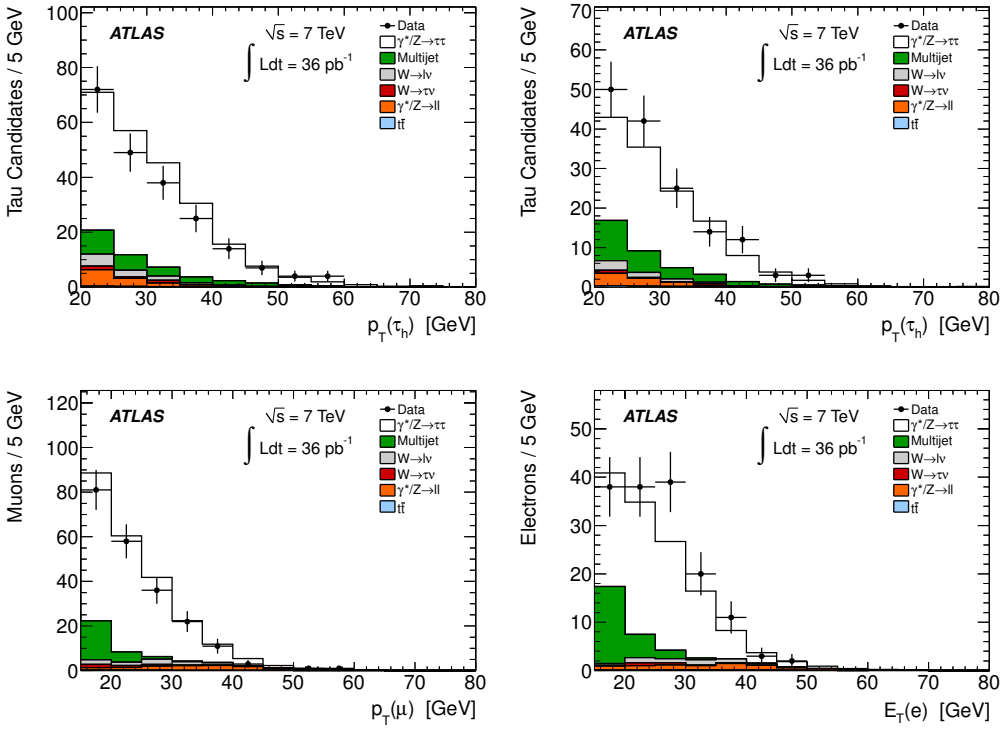
Figure 4.4: Distributions of (a-b) the p_T of the $\tau_{\text{had-vis}}$ candidate (c-d) of the muon and (d) E_T of the electron, for events passing all signal selections for the (a-c) $\tau_\mu\tau_{\text{had}}$ and (b-d) $\tau_e\tau_{\text{had}}$ final states.
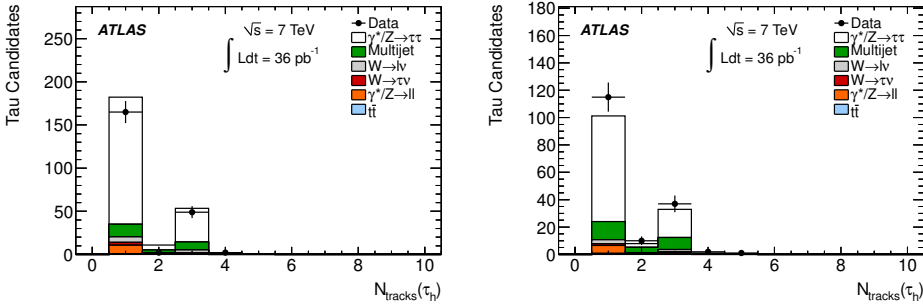
Figure 4.5: Distribution of the number of tracks associated to the chosen $\tau_{\text{had-vis}}$ after the full selection, including the opposite-charge requirement for the $\tau_{\text{had-vis}}$ and the lepton, except the requirement on the number of tracks and on the magnitude of the $\tau_{\text{had-vis}}$ charge. (a) for the $\tau_\mu \tau_{\text{had}}$ and (b) for the $\tau_e \tau_{\text{had}}$ channel. The background is estimated as described in Section 4.3.

The distribution of the visible mass after the full selection except the visible mass cut is shown in Fig. 4.3. The distributions of the lepton and $\tau_{\text{had-vis}}$ candidate p_{T}, for events passing all signal selections, are shown in Fig. 4.4. The distribution of the number of tracks associated to the $\tau_{\text{had-vis}}$ candidate after the full selection except the requirements on the number of associated tracks and on the magnitude of the $\tau_{\text{had-vis}}$ charge is shown in Fig. 4.5. This last figure is particularly important since it evidences clearly the presence of genuine $\tau_{\text{had-vis}}$ in the selected sample, characterised by having one of three associated tracks.

4.3 Background estimation

For the measurement of the $Z \to \tau^+ \tau^-$ production cross-section it is crucial to be able to estimate the number of background events in the selected sample. The largest background contributions, expected to arise from multi-jet and $W + \text{jets}$ events, were estimated with fully data-driven and partially data-driven methods.

$W + \text{jets}$ **background**

The $W + \text{jets}$ background is known to be poorly predicted by the simulation, due to a mismodelling of the rate of jets faking the $\tau_{\text{had-vis}}$ signature. Its normalisation was therefore taken from a $W + \text{jets}$ enriched control region, defined to contain events that pass all selection cuts except the m_{T} and $\Sigma \cos \Delta\phi$ cuts. The resulting region provides a highly pure $W + \text{jets}$ sample. Residual backgrounds from $Z + \text{jets}$ and $t\bar{t}$ in this region were estimated using Monte Carlo simulated samples and subtracted before deriving the normalisation factor. The multijet background contamination in this region was expected to be negligible. The obtained normalisation factors are

$\tau_\mu \tau_{\text{had}}$ channel $0.73 \pm 0.06 \, (\text{stat})$

$\tau_e \tau_{\text{had}}$ channel $0.63 \pm 0.07 \, (\text{stat})$

Multi-jet background

The multi-jet background was estimated in a fully data-driven way, using a 2D-sidebands method. Three control regions were defined requiring the two candidate τ lepton decay products to have same sign charge (SS) and/or the lepton to fail the isolation requirement. The method is illustrated in Figure 4.6. The pair of regions with non-isolated lepton was used to determine a transfer factor, $R_{OS/SS}$, from the OS to the SS region as

$$R_{OS/SS} = \frac{N_{OS}^{\text{non iso}} - N_{OS\,\text{ew}}^{\text{non iso}}}{N_{SS}^{\text{non iso}} - N_{SS\,\text{ew}}^{\text{non iso}}} \qquad (4.2)$$

Non multijet backgrounds were subtracted in all three control regions using Monte Carlo simulation (N_{ew}). For the SS control regions the $W +$ jets normalisation factor was recomputed using a new $W +$ jets control region identical to that described above, except for having the SS requirement applied. Charge correlation requirements change in fact the relative population of quark- and gluon-induced jets faking the $\tau_{\text{had-vis}}$ signature, leading to different $\tau_{\text{had-vis}}$ misidentification probabilities. The following values of $R_{OS/SS}$ were obtained:

$\tau_\mu \tau_{\text{had}}$ channel $1.07 \pm 0.04\,(\text{stat}) \pm 0.04\,(\text{syst})$

$\tau_e \tau_{\text{had}}$ channel $1.07 \pm 0.07\,(\text{stat}) \pm 0.07\,(\text{syst})$

The multijet background was estimated after the full selection as

$$N_{\text{Multi-jet}} = R_{OS/SS} \left(N_{SS}^{\text{iso}} - N_{SS\,\text{ew}}^{\text{iso}} \right) \qquad (4.3)$$

This method assumes that the transfer factor $R_{OS/SS}$ is independent of lepton isolation.
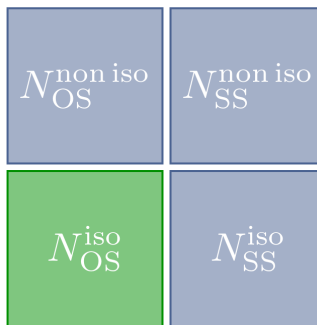
Figure 4.6: Scheme of the 2D-sidebands method used for the estimation of the multi-jet background. The green box is the signal region, the blue ones are the three control regions.

Other backgrounds

The contributions from $Z + \text{jets}$, $t\bar{t}$ and diboson backgrounds were estimated using Monte Carlo simulated samples.

4.4   Methodology for cross-section calculation

The measurement of the cross-section was performed using the formula

$$\sigma_{Z \to \tau\tau}^{m_{\text{inv}}66-116\,\text{GeV}} \times BR = \frac{N_{\text{obs}} - N_{\text{bkg}}}{A_Z \cdot C_Z \cdot \mathcal{L}} \tag{4.4}$$

where

- BR is the branching ratio for the channel of interest

- N_{obs} is the number of observed events in data

- N_{bkg} is the number of estimated background events

- A_Z denotes the kinematic and geometric acceptance for the signal process. It was determined from generator level Monte Carlo as

$$A_Z = \frac{N_{\text{dressed}}^{\text{gen kin}}}{N_{\text{ME}}^{\text{gen}\,m_{\text{inv}}66-116\,\text{GeV}}} \tag{4.5}$$

where

   - $N_{\text{ME}}^{\text{gen}\,m_{\text{inv}}66-116\,\text{GeV}}$ denotes the number of events at generator level whose invariant mass at matrix element level lies within mass window [66, 116] GeV.

   - $N_{\text{dressed}}^{\text{gen kin}}$ instead is the number of events at generator level that fall within the fiducial regions defined below. In this case the bare τ lepton decay products were dressed with photons radiated both from the τ leptons and by the decay products themselves, within a $\Delta R < 0.1$ cone in the case of electrons and muons and $\Delta R < 0.4$ cone in the case of hadronic decay products. An illustration of the dressing procedure is shown in Figure 4.7. Dressing the τ lepton decay products allows to perform a partial QED final state radiation correction back to the matrix element level, that however excludes the radiation at wide angle. Using a dedicated sample where the QED final state radiation was switched off it was checked that the impact of the radiation at wide angle on the acceptance is -1.2% for the $\tau_\mu \tau_{\text{had}}$ channel and -1.4% for the $\tau_e \tau_{\text{had}}$ channel.

The A_Z factor by construction includes a correction for events that migrate from outside the invariant mass window in the fiducial cuts. The central values for the A_Z factor were determined using the PYTHIA Monte Carlo sample described in Section 4.1. The lower bound on the invariant mass of the default sample was
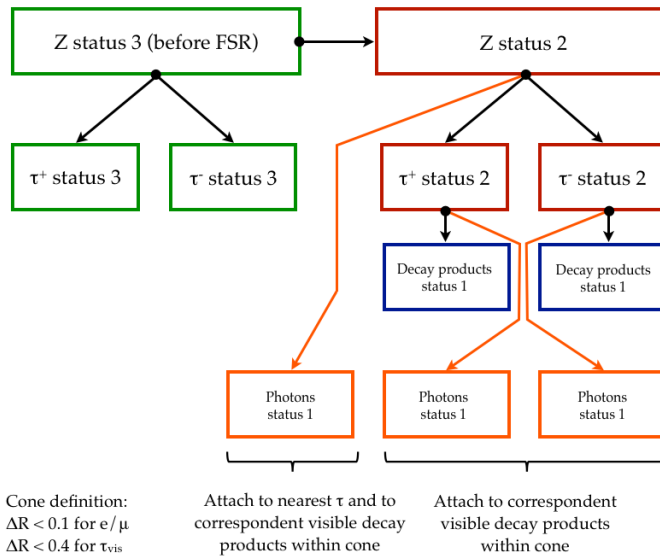
Figure 4.7: Simplified scheme of the PYTHIA event record for $Z \to \tau^+\tau^-$ events illustrating the dressing procedure. The particle status code is defined according to the HEPEVT scheme [153]: status 1 particle are not decayed or fragmented, and represent the final state as given by the generator, status 2 particles are decayed or fragmented entries, status 3 particles are intermediate resonances for documentation.

10 GeV and therefore the sample included a tail of low-mass γ^*/Z events from outside the Z peak that could possibly migrate within the fiducial cuts. The obtained central values are reported in Table 4.1. The difference in A_Z values between $\tau_\mu\tau_{\mathrm{had}}$ and $\tau_e\tau_{\mathrm{had}}$ channel is essentially due to the exclusion of the calorimeter overlap region from the fiducial region for the selection of electrons. The statistical uncertainty on the A_Z correction factors was found to be at the 2‰ level for both channels.

- C_Z is the correction factor that accounts for the efficiency of triggering, reconstructing and identifying decays within the geometrical acceptance. It is defined as

$$C_Z = \frac{N^{\mathrm{reco\,pass}}}{N^{\mathrm{gen\,kin}}_{\mathrm{dressed}}} \tag{4.6}$$

where

  – $N^{\mathrm{reco\,pass}}$ is the number of signal events that pass the analysis cuts after full simulation corrected with data-driven factors as mentioned in Section 4.2
  – $N^{\mathrm{gen\,kin}}_{\mathrm{dressed}}$ is defined in the same way as the A_Z numerator.

By construction C_Z includes a correction for migrations from outside of the acceptance. The statistical uncertainty on the C_Z correction factors is 1.5% for the $\tau_e\tau_{\mathrm{had}}$ channel and 1.2% for the $\tau_\mu\tau_{\mathrm{had}}$ channel.

- $\mathcal{L}$ denotes the integrated luminosity for the channel of interest.

	$\tau_\mu\tau_{\mathrm{had}}$ channel	$\tau_e\tau_{\mathrm{had}}$ channel
A_Z	$0.11691 \pm 0.00023\,\mathrm{(stat.)}$	$0.10073 \pm 0.00021\,\mathrm{(stat.)}$
C_Z	$0.2045 \pm 0.0024\,\mathrm{(stat.)}$	$0.1197 \pm 0.0017\,\mathrm{(stat.)}$

Table 4.1: Central values for the A_Z acceptance factor defined by Eq. 4.5 from PYTHIA ATLAS MC10 Monte Carlo generated with MRSTLO* PDF at generator level and C_Z correction factor defined by Eq. 4.6 determined using the same sample at generator level and after full detector simulation.

The cross-sections defined by Eq. 4.4 are total inclusive cross-sections and depend on an extrapolation from the observed region defined by the kinematical cuts to the full phase-space in the denominator of A_Z This extrapolation depends on the theoretical model used for Z production. In order to provide a measurement independent from theoretical extrapolation, fiducial regions based uniquely on observables, for which A_Z is unity, were defined. This results in a fiducial cross-section measurement

$$\sigma^{\mathrm{fid}}_{Z\to\tau\tau} \times BR = \frac{N_{\mathrm{obs}} - N_{\mathrm{bkg}}}{C_Z \cdot \mathcal{L}} \tag{4.7}$$

The fiducial regions were defined by the following cuts:

$\tau_\mu\tau_{\text{had}}$ **channel**

- Muon: $p_{\text{T}} > 15$ GeV, $|\eta| < 2.4$

- $\tau_{\text{had-vis}}$: $E_{\text{T}} > 20$ GeV, $|\eta| < 2.47$, excluding $1.37 < |\eta| < 1.52$

- Event: $\Sigma \cos \Delta\phi > -0.15$, $m_{\text{T}} < 50$ GeV, m_{vis} within $[35, 75]$ GeV

$\tau_e\tau_{\text{had}}$ **channel**

- Electron: $E_{\text{T}} > 16$ GeV, $|\eta| < 2.47$, excluding $1.37 < |\eta| < 1.52$

- $\tau_{\text{had-vis}}$: $E_{\text{T}} > 20$ GeV, $|\eta| < 2.47$, excluding $1.37 < |\eta| < 1.52$

- Event: $\Sigma \cos \Delta\phi > -0.15$, $m_{\text{T}} < 50$ GeV, m_{vis} within $[35, 75]$ GeV

Only stable particles were used in the definition of the denominator of C_Z. Since the invariant mass of the di-tau system was not observed in this analysis context, the invariant mass window for the cross-section measurement was not considered in the definition of the fiducial region. The visible mass window was not assigned any role of mass estimator, but was treated exactly the same way as other cuts, due to its weak relationship with the invariant mass (see Figure **??**).
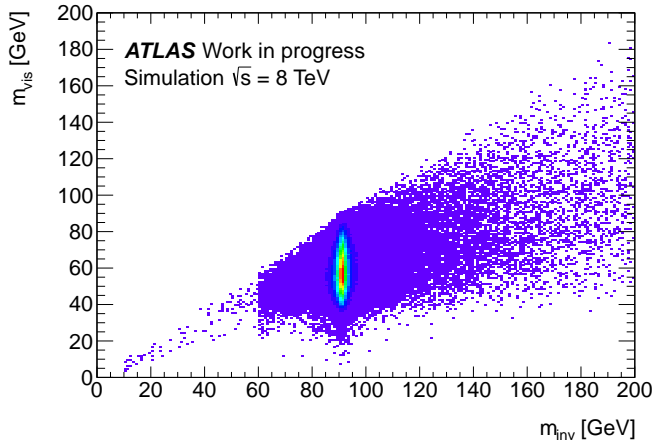
Figure 4.8: Visible mass m_{vis} versus invariant mass m_{inv} for the $Z \to \tau^+\tau^-$ signal sample used for A_Z determination in the $\tau_\mu\tau_{\text{had}}$ channel. The visible mass has an upper bound given by the invariant mass as expected, but other than this the relationship between the two is weak. The discontinuity in the distribution at 60 GeVis due to the sample being made up by two invariant mass slices with different statistical power.

A_Z is defined in order to extrapolate the cross-section measured in the fiducial region to an inclusive region more immediately comparable to theory predictions. The choice of correcting back to matrix element level was taken mainly for compatibility with the $Z \to l^+l^-$ and $W \to l\nu$ cross-section measurements in other channels [150].

4.5   Systematic uncertainties

Systematic uncertainties affect all of the terms of Equation 4.4, with the exception of the number of observed events. Uncertainties in C_Z arise from the limited knowledge of the actual efficiencies for the reconstruction and selection of objects from the simulation. Similar sources of uncertainties affect the estimation of the number of background events, even indirectly through background subtraction. Moreover, uncertainties introduced by the background estimation procedure are considered for the N_{bkg} term.

Further sources of systematic uncertainty affect the A_Z extrapolation factor. The uncertainty on the luminosity was taken to be 3.4%, as determined in [154].

A summary of all the uncertainties detailed below is given in Table 4.3.

4.5.1   Systematic uncertainties affecting the simulation

The limited knowledge of the following efficiencies, fake factors and energy scales affect the accuracy of predictions that make use of simulated samples.

Efficiency of lepton trigger, identification, and isolation

   Uncertainties on the data-driven corrections to the lepton trigger, identification and isolation efficiency in the Monte Carlo simulation arise both from statistical and systematic uncertainties on the efficiency measurements.

Efficiency of $\tau_{\mathrm{had\text{-}vis}}$ identification

   The uncertainties on the hadronic $\tau_{\mathrm{had\text{-}vis}}$ reconstruction and identification efficiencies were evaluated by varying simulation conditions, such as the underlying event model, the amount of detector material, the hadronic shower model and the noise thresholds of the calorimeter cells in the cluster reconstruction.

Electron and jet misidentification as $\tau_{\mathrm{had\text{-}vis}}$

   The probability for an electron or a QCD jet to be misidentified as a $\tau_{\mathrm{had\text{-}vis}}$ was measured in data using an identified $Z \rightarrow ee$ sample where $\tau_{\mathrm{had\text{-}vis}}$ identification was applied to one of the electrons. Correction factors were derived for the Monte Carlo misidentification probability for electrons. The QCD jet misidentification probability was measured in $Z \rightarrow \ell\ell$+jet events. The difference to the Monte Carlo prediction for the same selection, added in quadrature with the statistical and systematic uncertainties of the measurement, was taken as the systematic uncertainty. Correction factors and uncertainties were applied considering the $\tau_{\mathrm{had\text{-}vis}}$ truth match. The $\tau_{\mathrm{had\text{-}vis}}$ candidate misidentification systematic uncertainties are not applied to the W Monte Carlo samples, where the uncertainty on the data-driven normalization was applied instead.

Energy scales

   The $\tau_{\mathrm{had\text{-}vis}}$ energy scale uncertainty was estimated by varying the detector geometry, hadronic showering model, underlying event model as well as the noise thresholds of the calorimeter cells in the cluster reconstruction in the simulation, and comparing to the nominal results [151]. The electron energy scale was determined from data as described in Section 2.3.2. Additionally, the calorimetric

component of the E_T^miss is sensitive to the energy scale, and this uncertainty was evaluated by propagating first the electron energy scale uncertainty into the E_T^miss calculation and then shifting all topological clusters not associated to electrons according to their uncertainties [152].

The electron and $\tau_\text{had-vis}$ energy scales, as well as the scale of the calorimetric component of the E_T^miss, were treated as correlated. The muon momentum scale, and the correlated effect on the E_T^miss, was also evaluated but found to be negligible in comparison with other uncertainties.

Other sources

A number of other sources, such as the uncertainty due to the object quality requirements on $\tau_\text{had-vis}$ candidates and E_T^miss, the uncertainty on the reweighting procedure used to model the actual data pile-up conditions in the simulation, lepton resolution and charge identification uncertainties and theoretical uncertainties on the cross-sections used for the background prediction were also evaluated but found to have a small impact on the total uncertainty.

4.5.2 Systematic uncertainties on the background estimation methods

Besides the uncertainties due to the subtraction of residual backgrounds in the control regions, the $W + \text{jets}$ and multijet background predictions are affected by uncertainties inherent to the estimation methods.

$W + \text{jets}$ background

The uncertainty on the W+jets background estimation method is dominated by the statistical uncertainty on the calculation of the normalization factor in the control region, as described in Section 4.3.

Multi-jet background

The accuracy of the prediction of the multi-jet background relies on the validity of the assumption that the transfer factor $R_{OS/SS}$ is independent of the lepton isolation. Systematic uncertainties were therefore derived by studying the dependence of $R_{OS/SS}$ on the isolation variables cuts. The statistical uncertainty on the number of data events in the various control regions is a further source of uncertainty.

4.5.3 Systematic uncertainties on the acceptance

The theoretical uncertainty on the geometric and kinematic acceptance factor A_Z defined by Eq.4.5 is dominated by the limited knowledge of the proton PDFs and the modelling of the Z-boson production at the LHC. These uncertainties were assessed considering three components:

- **Uncertainty within one PDF set**

  This uncertainty was determined for the CTEQ6.6 NLO PDF by using the 22 PDF error eigenvectors available [155] using the LHAPDF tool [156, 157]. The variations were obtained by reweighting the default sample to the relevant CTEQ6.6

error eigenvector. For each eigenvector i then the acceptances A_Z^{i+} and A_Z^{i-} were calculated from the up and down eigenvector excursion, and the uncertainty was derived using the standard prescription

$$\Delta A_Z = \frac{1}{2}\sqrt{\Sigma_i \left(A_Z^{i+} - A_Z^{i-}\right)^2} \qquad (4.8)$$

- **Deviations between different PDF sets**

  This uncertainty was evaluated by considering the maximal deviation between the acceptance obtained using the default sample and the values obtained reweighting this sample to the CTEQ6.6 and HERAPDF1.0 [158] PDF sets with the LHAPDF tool.

- **General modelling uncertainty**

  A general modelling uncertainty was estimated using a MC@NLO combined with HERWIG parton shower sample. This uncertainty includes higher order and parton shower effects. The alternative sample was generated with the CTEQ6.6 PDF set and ATLAS MC10 tune and a lower bound on the invariant mass of 60 GeV. Since Herwig in association with external generators did not handle tau polarisations correctly at the time, the acceptance obtained from the MC@NLO sample was corrected for this effect. The correction factor was derived by dedicated samples generated switching on and off the polarisation effects. The applied correction factor is 0.9917 ± 0.0002 for the $\tau_\mu\tau_{\text{had}}$ channel and 0.9904 ± 0.0002 for the $\tau_e\tau_{\text{had}}$ channel, where the quoted uncertainties are statistical. This correction procedure led to a more conservative estimate of the systematics. The deviation with respect to the A_Z factor obtained using the default sample reweighted to the CTEQ6.6 PDF set central value and with an applied lower bound on the invariant mass of 60 GeV was taken as uncertainty.

A summary of the geometric and kinematic acceptances obtained with the different PDF and model variations and of the correspondent estimated relative uncertainties is given in Table 4.2.

Two further sources of systematic uncertainty in the determination of the A_Z acceptance factor are the modelling of the QED radiation and the modelling of tau lepton decays.

In the default sample the QED radiation is modeled by PHOTOS which has an accuracy better than 0.2%, that is therefore negligible with respect to uncertainties due to PDFs. The modelling of the tau lepton decay branching ratios in the hadronic modes can affect the p_{T} spectrum of hadronically decaying taus. As a cross-check a signal sample generated with Sherpa, which includes its own library to decay tau leptons, was used to investigate possible differences in the fraction of energy taken up by the hadronic system from the tau decay with respect to TAUOLA.

Considering a sum in quadrature of the different sources of uncertainty a theoretical uncertainty on A_Z of 3% is assigned for both channels.

	$\tau_\mu\tau_{\text{had}}$ channel	$\tau_e\tau_{\text{had}}$ channel
PYTHIA MRSTLO* $m_{Z/\gamma^*} > 10$ GeV	0.1169	0.1007
PYTHIA CTEQ6.6 $m_{Z/\gamma^*} > 10$ GeV	0.1191	0.1026
PYTHIA HERAPDF1.0 $m_{Z/\gamma^*} > 10$ GeV	0.1185	0.1020
PYTHIA CTEQ6.6 $m_{Z/\gamma^*} > 60$ GeV	0.1185	0.1022
MC@NLO CTEQ6.6 $m_{Z/\gamma^*} > 60$ GeV	0.1174	0.1016
MC@NLO CTEQ6.6 $m_{Z/\gamma^*} > 60$ GeV spin effect correction	0.1165	0.1006

(a)

	$\tau_\mu\tau_{\text{had}}$ channel	$\tau_e\tau_{\text{had}}$ channel
CTEQ 6.6 eigenvector set	1.2%	1.2%
Different PDF sets	1.9%	1.9%
Model dependence	1.8%	1.6%
Total uncertainty	2.9%	2.8%

(b)

Table 4.2: (a) Central values of the A_Z geometric and kinematic acceptance factor obtained with PYTHIA MRSTLO* and variations (PYTHIA CTEQ6.6, PYTHIA HERAPDF1.0, MC@NLO CTEQ6.6). (b) Relative uncertainties on the A_Z factors, calculated as described in the text.

4.6   Cross-section measurement

Combining the numbers from the previous sections, collected for reference in Table 4.4 and following the method described in Section 4.4, the calculation of the cross-section could be performed, yielding the results described below. The correlations between $N_{\text{obs}} - N_{\text{bkg}}$ and C_Z were taken into account.

4.6.1   Measured fiducial cross-section

The fiducial cross-section was calculated, as defined in 4.7, to be

$$\sigma_{Z\to\tau^+\tau^-}^{\text{fid}} \times BR(\tau_\mu\tau_{\text{had}}) = 23 \pm 2\,(\text{stat}) \pm 3\,(\text{syst}) \pm 1\,(\text{lumi})\ \text{pb} \qquad (4.9)$$

for the $\tau_\mu\tau_{\text{had}}$ channel and

$$\sigma_{Z\to\tau^+\tau^-}^{\text{fid}} \times BR(\tau_e\tau_{\text{had}}) = 27 \pm 3\,(\text{stat}) \pm 5\,(\text{syst}) \pm 1\,(\text{lumi})\ \text{pb} \qquad (4.10)$$

for the $\tau_e\tau_{\text{had}}$ channel.

4.6.2   Measured total cross-section

The total cross-section, as defined in 4.4, after correction of the total cross-section for the $(\tau_l\tau_{\text{had}})$ branching ratio, 0.22495 ± 0.00074 for the $\tau_\mu\tau_{\text{had}}$ channel and 0.23130 ± 0.00074 for the $\tau_e\tau_{\text{had}}$ channel [8], the following value for the inclusive cross-section was obtained:

$$\sigma_{Z\to\tau^+\tau^-}^{m_{\text{inv}}\,66-116\,\text{GeV}} = 0.86 \pm 0.08\,(\text{stat}) \pm 0.12\,(\text{syst}) \pm 0.03\,(\text{lumi})\ \text{nb} \qquad (4.11)$$

Systematic uncertainty	$\tau_\mu\tau_{\mathrm{had}}$	$\tau_e\tau_{\mathrm{had}}$
Muon efficiency	3.8%	–
Muon resolution and momentum scale	0.2%	–
Electron efficiency, resolution and charge misidentification	–	9.6%
$\tau_{\mathrm{had\text{-}vis}}$ identification efficiency	8.6%	8.6%
$\tau_{\mathrm{had\text{-}vis}}$ misidentification	1.1%	0.7%
Energy scale (e/$\tau_{\mathrm{had\text{-}vis}}$/jets/$E_{\mathrm{T}}^{\mathrm{miss}}$)	10%	11%
Multi-jet estimate method	0.8%	2%
W normalization factor	0.1%	0.2%
Object quality cuts	1.9%	1.9%
Pile-up description in simulation	0.4%	0.4%
Theoretical cross-section	0.2%	0.1%
A_Z systematics	3%	3%
Total Systematic uncertainty	15%	17%
Statistical uncertainty	9.8%	12%
Luminosity	3.4%	3.4%

Table 4.3: Relative statistical and systematic uncertainties in % on the total cross-section measurement. The electron and muon efficiency terms include the lepton trigger, reconstruction, identification and isolation uncertainties, as described in the text.

for the $\tau_\mu\tau_{\mathrm{had}}$ channel and

$$\sigma_{Z\rightarrow\tau^+\tau^-}^{m_{\mathrm{inv}}\,66-116\,\mathrm{GeV}} = 1.14 \pm 0.14\,(\mathrm{stat}) \pm 0.20\,(\mathrm{syst}) \pm 0.04\,(\mathrm{lumi})\ \mathrm{nb} \qquad (4.12)$$

for the $\tau_e\tau_{\mathrm{had}}$ channel.

4.7 Results for the $Z \rightarrow \tau_{\mathrm{lep}}\tau_{\mathrm{lep}}$ channels, combination and comparisons

The measurement of the $Z \rightarrow \tau^+\tau^-$ cross-section using the 2010 dataset was also performed in the fully leptonic channel (Section 4.7.1). The cross-section measurement was repeated with data at $\sqrt{s} = 7$ TeV collected in 2011 as well, both in the semileptonic and fully-leptonic channels.

4.7.1 Leptonic channels results

The leptonic channels studied were $Z \rightarrow \tau_e\tau_\mu$ and $Z \rightarrow \tau_\mu\tau_\mu$. The background suppression and estimation for these two channels used different techniques described in Ref. [117], but the general methodology for the cross-section computation was the same. The components for the cross-section calculation are shown in Table 4.5.
The fiducial cross-sections were defined in the regions:

$\tau_e\tau_\mu$ channel

	$\tau_\mu\tau_{\mathrm{had}}$	$\tau_e\tau_{\mathrm{had}}$
N_{obs}	213 ± 15	151 ± 12
$N_{\mathrm{obs}} - N_{\mathrm{bkg}}$	$164 \pm 16 \pm 4$	$114 \pm 14 \pm 3$
A_Z	$0.11691 \pm 0.00023 \pm 0.00351$	$0.10073 \pm 0.00021 \pm 0.00302$
C_Z	$0.2045 \pm 0.0024 \pm 0.0262$	$0.1197 \pm 0.0017 \pm 0.0189$
$\mathcal{L}$	35.51 ± 1.21	35.75 ± 1.22

Table 4.4: The components of the $Z \to \tau^+\tau^-$ cross-section calculation. The first uncertainty is statistical and the second systematic.

	$\tau_e\tau_\mu$	$\tau_\mu\tau_\mu$
N_{obs}	85	90
$N_{\mathrm{obs}} - N_{\mathrm{bkg}}$	$76 \pm 10 \pm 1$	$43 \pm 10 \pm 3$
A_Z	0.114 ± 0.003	0.156 ± 0.006
C_Z	0.29 ± 0.02	0.27 ± 0.02
$\mathcal{L}$	$35.5 \pm 1.2 \, \mathrm{pb}^{-1}$	$35.5 \pm 1.2 \, \mathrm{pb}^{-1}$

Table 4.5: The components of the $Z \to \tau^+\tau^-$ cross-section calculation for the leptonic channels. For $N_{\mathrm{obs}} - N_{\mathrm{bkg}}$ the first uncertainty is statistical and the second systematic. For all other values the total uncertainty is given.

- Electron: $E_{\mathrm{T}} > 16\,\mathrm{GeV}$, $|\eta| < 2.47$, excluding $1.37 < |\eta| < 1.52$

- Muon: $p_{\mathrm{T}} > 10\,\mathrm{GeV}$, $|\eta| < 2.4$
- Event: $\Sigma \cos \Delta\phi > -0.15$, m_{vis} within $[25, 80]\,\mathrm{GeV}$

$\tau_\mu\tau_\mu$ channel

- Leading muon: $p_{\mathrm{T}} > 15\,\mathrm{GeV}$, $|\eta| < 2.4$
- Subleading muon: $p_{\mathrm{T}} > 10\,\mathrm{GeV}$, $|\eta| < 2.4$
- Event: m_{vis} within $[25, 65]\,\mathrm{GeV}$

Theoretical uncertainties on the A_Z acceptances were calculated using the same method described in Sec. 4.5.3, resulting in uncertainties of 3% for the $\tau_e\tau_\mu$ and 4% for the $\tau_\mu\tau_\mu$. Fiducial and total cross-sections obtained obtained are

$$\sigma^{\mathrm{fid}}_{Z\to\tau^+\tau^-} \times BR(\tau_e\tau_\mu) = 7.5 \pm 1.0\,(\mathrm{stat}) \pm 0.5\,(\mathrm{syst}) \pm 0.3\,(\mathrm{lumi})\,\mathrm{pb} \tag{4.13}$$

$$\sigma^{m_{\mathrm{inv}}66-116\,\mathrm{GeV}}_{Z\to\tau^+\tau^-}(\tau_e\tau_\mu\mathrm{channel}) = 1.06 \pm 0.14\,(\mathrm{stat}) \pm 0.08\,(\mathrm{syst}) \pm 0.04\,(\mathrm{lumi})\,\mathrm{nb} \tag{4.14}$$

for the $\tau_e\tau_\mu$ and

$$\sigma^{\mathrm{fid}}_{Z\to\tau^+\tau^-} \times BR(\tau_\mu\tau_\mu) = 4.5 \pm 1.1\,(\mathrm{stat}) \pm 0.6\,(\mathrm{syst}) \pm 0.2\,(\mathrm{lumi})\,\mathrm{pb} \tag{4.15}$$

$$\sigma_{Z \to \tau^+\tau^-}^{m_{\text{inv}} 66-116\,\text{GeV}}(\tau_\mu\tau_\mu\text{channel}) = 0.96 \pm 0.22\,(\text{stat}) \pm 0.12\,(\text{syst}) \pm 0.03\,(\text{lumi})\,\text{nb} \quad (4.16)$$

for the $\tau_\mu\tau_\mu$.

4.7.2 Combination of channels and comparisons

The combination of the semi-leptonic and leptonic channels was performed using the the Best Linear Unbiased Estimate (BLUE) method, described in [159, 160]. A basic description of the method and on the assumption on which the combination was based can be found in Ref. [117]. A combined cross-section measurement

$$\sigma_{Z \to \tau^+\tau^-}^{66 < m_{\text{inv}} < 116\,\text{GeV}} = 0.97 \pm 0.07\,(\text{stat}) \pm 0.06\,(\text{syst}) \pm 0.03\,(\text{lumi})\,\text{nb} \quad (4.17)$$

is obtained from the four final states, $\tau_\mu\tau_{\text{had}}$, $\tau_e\tau_{\text{had}}$, $\tau_e\tau_\mu$ and $\tau_\mu\tau_\mu$.

The results are graphically shown in Figure 4.9, both for the single channels and the combination. All results compare well with the theoretical expectation of 0.96 ± 0.05 nb for the invariant mass window $[66, 116]$ GeV. The result published by the CMS collaboration, $1.00 \pm 0.05\,(\text{stat}) \pm 0.08\,(\text{syst}) \pm 0.04\,(\text{lumi})$ nb, refers to a different mass window, $[60, 120]$ GeV, and is therefore not directly comparable [161].

The measurement was repeated using part of the 2011 dataset and a similar procedure, documented in Ref [145]. The main differences are that the $\tau_\mu\tau_\mu$ channel was dropped and that combined lepton-$\tau_{\text{had-vis}}$ triggers were used. The resulting cross-section is $0.92 \pm 0.02\,(\text{stat}) \pm 0.08\,(\text{syst}) \pm 0.03\,(\text{lumi})$ nb in the $[66, 116]$ GeV mass window, to be compared with the result obtained in 2010 reported in Eq. 4.17.
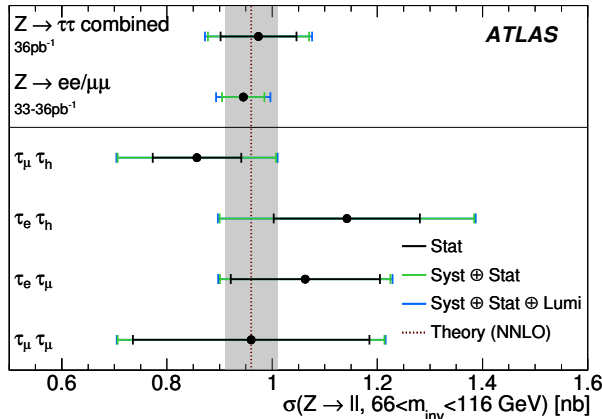
Figure 4.9: The individual cross-section measurements by final state, and the combined 2010 result. The $Z \to l^+l^-$ combined cross-section measured by ATLAS in the $Z \to \mu^+\mu^-$ and $Z \to e^+e^-$ final states is also shown for comparison. The gray band indicates the uncertainty on the NNLO cross-section prediction.

4.8   Summary

The first measurement performed at ATLAS in a genuine di-tau final state has been presented. The measurement of the cross-section of the $Z \to \tau^+\tau^-$ process has demonstrated the feasibility of analyses involving hadronically decaying tau leptons. A particular emphasis has been given to the methodology aspects of this measurement and to the determination of theory uncertainties, that have resulted to be well under control when compared to the dominant experimental uncertainties.

On the tracking side: Pixel clusterisation

For the study of the $H \to \tau^+\tau^-$ process the performance of the reconstruction and identification of hadronic τ lepton decays is crucial. This performance depends both on the tracking and calorimeter measurement capabilities of ATLAS.

On the tracking side a relevant aspect is the tracking efficiency. The presence of tracks associated to a calorimeter jet allows in fact to build identification variables and to roughly characterise the τ lepton decay mode (1-prong or 3-prong). The precision of the measurement of the track impact parameter and the reconstruction of secondary vertices plays an important role in tau identification as well. Aspects relevant to $\tau_{\text{had-vis}}$ reconstruction and identification have already been outlined in Section 2.2.3. The Pixel detector plays an important role in providing efficient and high quality track reconstruction and vertexing. The main purpose of the Pixel detector is in fact to provide precision measurements of the positions of charged particles emerging from collisions at a few centimeters from the interaction point. In this Chapter aspects of this topic are presented.

5.1 The Pixel detector

The main components of the Pixel detector are the active region the internal services (power, monitoring, optical input/output and cooling) and their mechanical support structures and the external services. The active region, illustrated in Figure 5.1, consists of three barrel layers (starting from the inside *Layer0* or *b-Layer*, *Layer1* and *Layer2*) and two end-caps, each with three disks.

The basic building block of the active region is the *module*. In the barrel modules are arranged parallel to the beam axis on support structures that take the name of staves. In the disks instead the modules are arranged radially in the plane transverse to the beams on disk sectors. Basic parameters of the Pixel detector active region are shown in Table 5.1.

5.1.1 Pixel modules

The 1744 Pixel modules cover the sensitive $\sim 1.7\,\text{m}^2$ area of the Pixel detector. All modules are almost identical and assembled from the following parts:

- **Sensor tile**. Described into more detail in the following, the tile contains 47,232 pixel sensor cells.
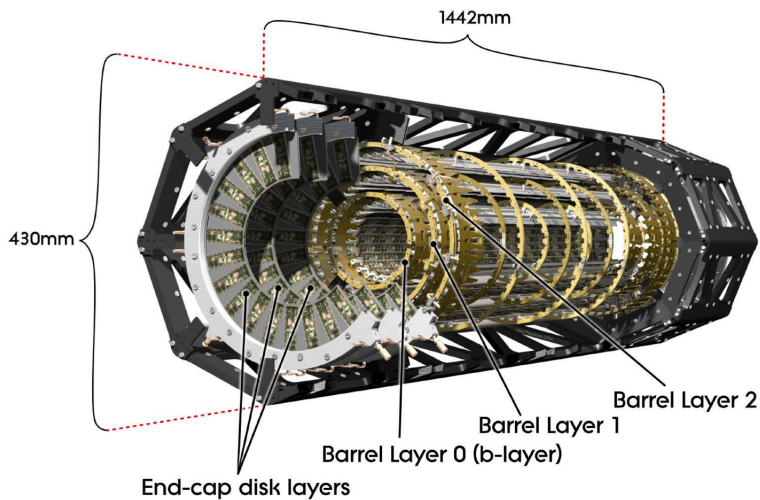
Figure 5.1: Schematic view of the Pixel detector active region [162].

Barrel					
Layer	Mean radius [mm]	Number of staves	Number of modules	Number of channels	Active Area [m^2]
0	50.5	22	286	13,178,880	0.28
1	88.5	38	494	22,763,520	0.49
2	122.5	52	676	31,150,080	0.67
Total		112	1456	67,092,480	1.45
End-caps					
Disk	Mean z [mm]	Number of sectors	Number of modules	Number of channels	Active Area [m^2]
0	495	8	48	2,211,840	0.0475
1	580	8	48	2,211,840	0.0475
2	650	8	48	2,211,840	0.0475
Total one endcap		24	144	6,635,520	0.14
Total two endcaps		48	288	13,271,040	0.28

Table 5.1: Basic Pixel detector parameters [162].

- **Front-end electronics**. Sixteen front-end electronics chips (FE) are connected by means of fine-pitch bump-bonding to the sensor pixel cells (see Section 5.1.2).

- **Flex-hybrid**. A fine-pitched, double-sided flexible printed circuit to route signals and power.

- **Modules control chip (MCC).** Situated on the flex-hybrid, receives and transmits signal data out of the modules.

- **Pigtail connection.** Flexible foil that provides connection to the electrical services via a micro-cable. In the disks micro-cables are attached without the pigtail.

The elements of a pixel barrel module are shown in Figure 5.2.
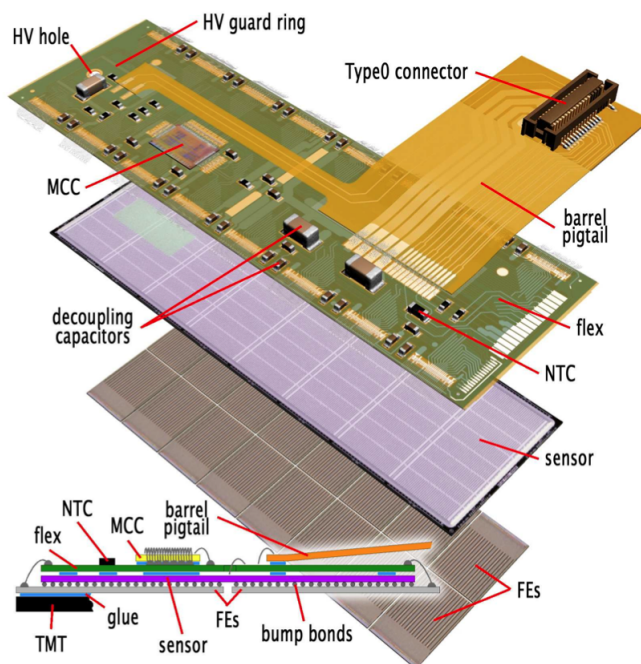
Figure 5.2: Pixel barrel module elements [162].

Pixel sensors function as solid-state ionization chambers. Each sensor tile is made by an array of bipolar diodes placed on a high-resistivity n-type bulk, $256\pm3\,\mu$m thick. High positive (p) and negative (n) dose regions are implanted on each side of the silicon wafer. While the n-side of the wafer is segmented into pixels to obtain the single diodes, the p side is common to all. A depletion region at the pn junction operates in reverse bias and extends over the whole bulk sensor volume. Charged particles traversing this volume excite electrons form the valence band to the conduction band, creating electron-hole pairs in the medium. The generated charge carriers can be collected at the terminals. The

read-out happens on the opposite side with respect to the *pn* junction, which is located at the back. The 47,232 pixel implants present on each sensor tile are arranged in 144 *columns* and 328 *rows*. In 128 columns the pixel pitch is $400 \times 50\,\mu\mathrm{m}^2$. In the remaining 16 columns the pitch is $600 \times 500\,\mu\mathrm{m}^2$ (*long pixels*). In each column eight pairs of pixel implants near the center lines are ganged to a common read-out channel (*ganged pixels*).

The long side of the pixel implants defines the *local-y* coordinate, and is parallel to the beam axis in the barrel and to the radial direction in the disks. The short side instead defines the *local-x* coordinate, which is used for the momentum measurement, as it is orthogonal to the magnetic field.

5.1.2   Readout electronics

Each read-out cell in the FEs contains an analogue block where the sensor charge signal is amplified and compared to a programmable discriminator threshold. The digital read-out then transfers the hit pixel address, a hit time stamp and a digitised amplitude, the time over threshold (ToT), to buffers at the chip periphery. The 16 FE chips in each pixel module are arranged in two rows of eight chips and are read out by the MCC. Each module is then connected to the off-detector RODs through optical fiber links. A detailed description of the Pixel detector electronics is given elsewhere [162].

5.2   Cluster properties in the Pixel detector

When a charged particle traverses a layer of matter it undergoes interactions that can cause ionisation and atomic excitation in the material. The mean particle energy loss is described by the Bethe-Bloch equation (see Ref. [8]), and is calculated to be $388\mathrm{eV}/\mu\mathrm{m}$ for silicon detectors. The stochastic single particle behaviour is instead described by a straggling function that, in the case of the thick Pixel sensors, can not be approximated by a Landau function but is rather computed numerically. The ionisation process can result in high energy knock-out electrons as well, that take the name of δ-rays.

In silicon, where the average energy to produce a electron-hole pair can be taken as $W = 3.68\,\mathrm{eV}$, the expected charge release for a minimum ionising particle is 19 ke. Electrons and hole drift in the detector in opposite directions towards the electrodes, with a velocity determined by the electric field and charge mobility. In the Pixel detector the drift velocity at a 300 K temperature is calculated to be $5.29 \times 10^6\mathrm{cm/s}$. During their drift charges experiment lateral spread as well. The spread has a gaussian distribution whose width is proportional to the squared root of the drift time and diffusivity coefficient. At ATLAS this parameter is computed to be equal to $25\,\mathrm{cm}^2\,\mathrm{s}^{-1}$. The read-out cell of the Pixel detector is based on a fast charge preamplifier with constant current feedback, followed by a tunable discriminator. The total pulse height is measured using the ToT, the period of time during which the signal remains above the discriminator threshold, that is nearly proportional to the collected charge. The detector is tuned so that all channels have the same ToT response to an injected charge of 20 ke in each pixel. The discriminator threshold can be tuned to provided dispersion below 40 e. At the beginning of data taking a threshold of 4000 e was used. Later it was lowered to 3500 e. In both cases the

electronic noise is about 150 e for normal size pixels, providing an extremely favourable threshold over noise ratio.

The passage of a particle usually causes the generation of charge carriers in a few neighbouring pixels. The set of pixels for which the charge is over threshold and that share at least one corner takes the name of *cluster*. The position of the cluster together with the distance of the module mid-plane from the beam axis form space-points that are the input to tracking algorithms. The determination of the position is the topic of the following section. The total charge of a cluster is given by the sum of the charges collected by the individual pixels.

The charge distribution within the cluster carries information about the path of the particle in the detector. This can be understood by a simple geometrical model developed during test-beam studies [163, 164], and illustrated in Figure 5.3. The charge is proportional to the path-length of the particle under a given pixel. The threshold of the front-end electronics corresponds to a minimal path-length, below which no signal is recorded. This simple model does not consider the effects due to fluctuations in the energy loss, δ-rays, diffusion, cross-talk between the pixels and electronic inefficiencies, but it is sufficient to qualitatively describe some of the general properties of clusters.
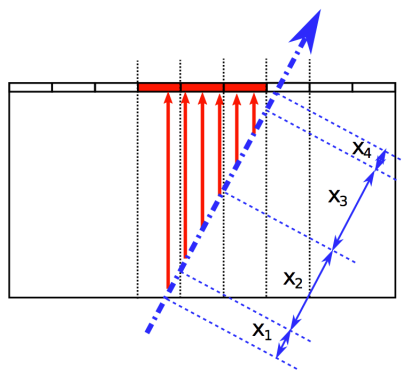
Figure 5.3: A simple geometrical model allows to compute the charge released in each read-out channel, by considering the path-length of the particle under each pixel [165].

A very relevant property of clusters is their size, that is defined by the number of pixels over threshold in the *local-x* and *local-y* directions respectively. If no magnetic field is present charges drift perpendicular to the module surface. According to the simple geometrical model introduced the cluster size therefore depends on the particle incidence angle, that determines the path-length in the detector. The cluster size is minimum when the particle hits the detector perpendicularly. In this case the cluster size can be larger than one due to the effects of charge diffusion. Increasing the incidence angle the typical cluster size increases as well. If a magnetic field is present, the incidence angle needs to be corrected for the effects of the magnetic field on the charge drift. In the barrel modules in fact, where the electric and magnetic field are perpendicular, the charges are subject to a non-null Lorentz force, that makes them drift along a direction that forms

an angle α_L with the magnetic field. The angle α_L takes the name of Lorentz angle [163, 166, 167, 168, 169] and depends on the magnetic field as

$$\tan\alpha = \mu_H B \qquad (5.1)$$

where μ_H is the Hall mobility, which is related to the charge carriers mobility through a factor dependent on temperature. As a consequence, α_L depends on the magnetic and electric field and on the sensors temperatures. The Lorentz angle has been measured in 2010 ATLAS data at $\sqrt{s} = 7$ TeV as $\alpha_L = 211.3 \pm 1.6$.

Figure 5.5 shows the incidence angle distribution for various cluster sizes in data and Monte Carlo. The pseudorapidity variable $\eta_i = -\log(\tan(\theta_i/2))$ is defined by the projection of the particle incidence angle on the module θ_i along the *local-y* direction. The projection along the *local-x* direction is instead called ϕ_i. The histograms in these figures are stacked, and the ϕ_i angle is corrected for the Lorentz angle. The data sample is from a mix of jet, $\tau_{\text{had-vis}}$ and missing transverse momentum triggers while the Monte Carlo sample is from a di-jet sample. A description of the track and cluster selection can be found in Section 5.4.1. The ϕ_i distribution displays a peak at 0 that corresponds to the clusters in the end-cap disks, that populate the two peaks in the η_i distribution as well. The bulk of the ϕ_i distribution is found at positive ϕ_i values up to $20°$, and this is due to the tilt of the Pixel modules in the detector. The distribution does not model the data well. This is due to several reasons. First of all the kinematics of the events in the two samples is not fully comparable. This can be seen in Figure 5.5, that shows a comparison between the two samples of the ϕ_i and η_i distributions. From the ϕ_i distribution it can be noted that the relative populations in the barrel and in the disks are different between data and the simulation. This fact points to a substantial difference between the two samples. The differences in the η_i distribution is instead sensitive to the beam-spot modelling. Figure 5.4 shows a comparison between the average cluster sizes in data and simulation, restricted to the bulk of the clusters. The η_i cluster size distribution shows a better agreement than the ϕ_i one. While the previous is mostly determined by the detector geometry, the second is more sensitive to effects such as diffusion, cross-talk between pixels and Lorentz angle modelling. Finally Figure 5.7 shows the same histograms of Figure 5.4, but normalised bin-by-bin to the total number of clusters. From Figure 5.6 one can see that the minimum of the cluster size along the *local-x* direction occurs for a corrected incidence angle of 0 as expected. At larger incidence angles the population of two-row clusters takes a larger fraction of the total events. From $\phi_i \sim 10°$ 3-row clusters start to be significant. At large ϕ_i the relative population of 1-row clusters increases again: this fact points to the presence of split clusters. These clusters originate by the passage of only one particle but, due to the charge being shared by a large number of clusters, can be split into more than one cluster when the deposition in one of the intermediate pixels fluctuates under threshold.

The charge spatial distribution in the cluster carries information about the passage point of the particle in the detector. According to the geometrical model described, the information is carried mainly by the charge collected in the first and last pixel of the cluster in each direction. It is convenient to define the charge sharing variables in the
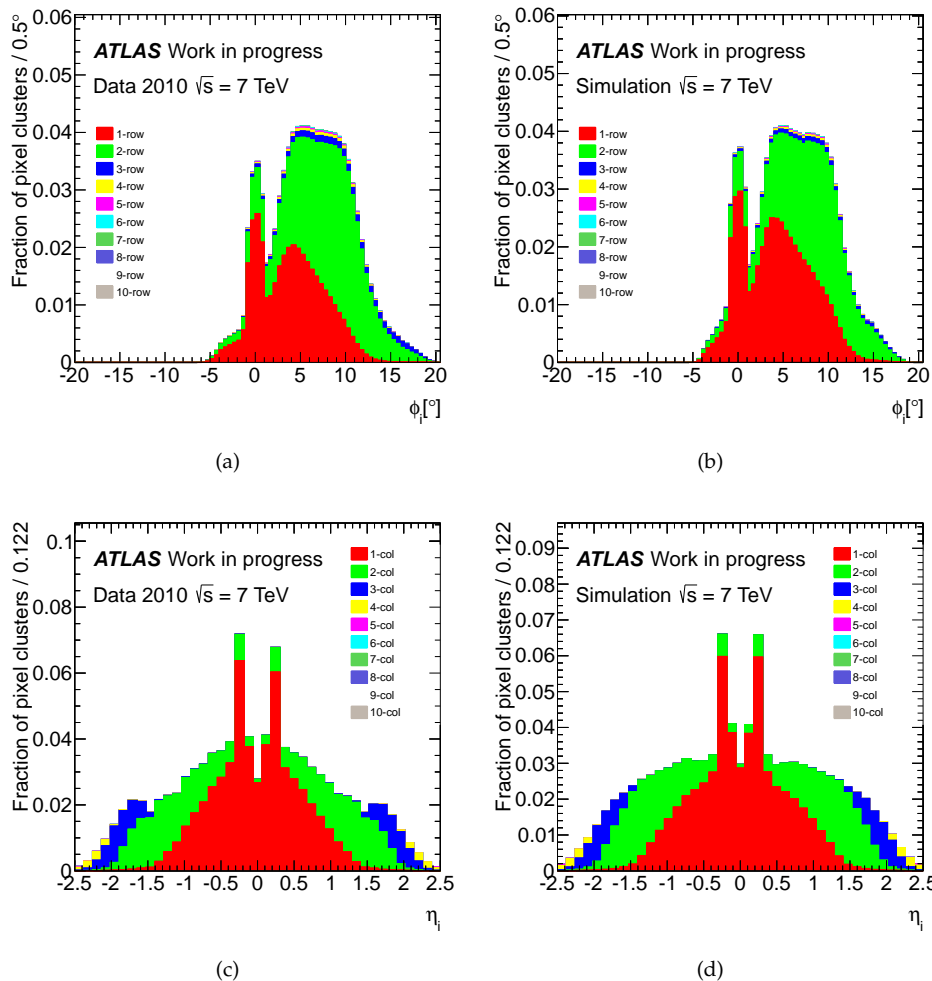
Figure 5.4: Cluster size in the *local-x* (a-b) and *local-y* (c-d) directions as a function of the track incidence angle in a sample of $\sqrt{s} = 7$ TeV data taken in 2010 by jet, tau and missing transverse momentum triggers and a Monte Carlo simulated sample of di-jet events.

(a)   (b)
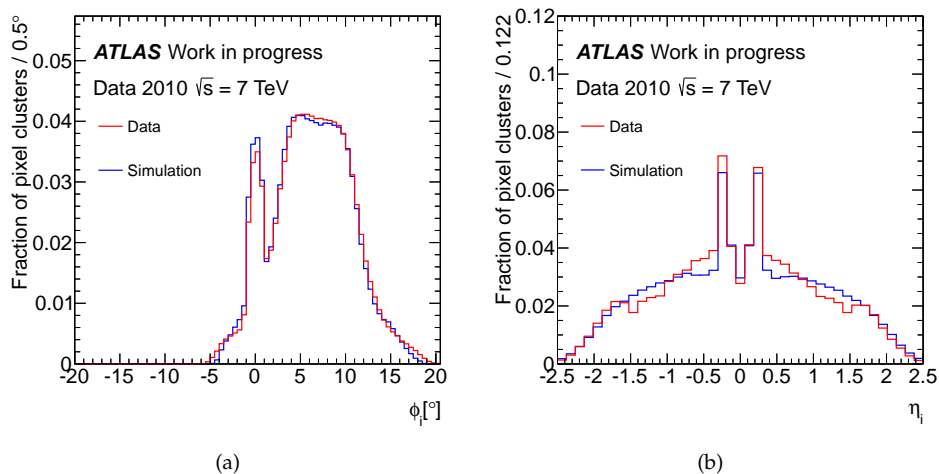
Figure 5.5: Distributions of incidence angle in data and Monte Carlo simulation. More details are given in the text.

(a)   (b)
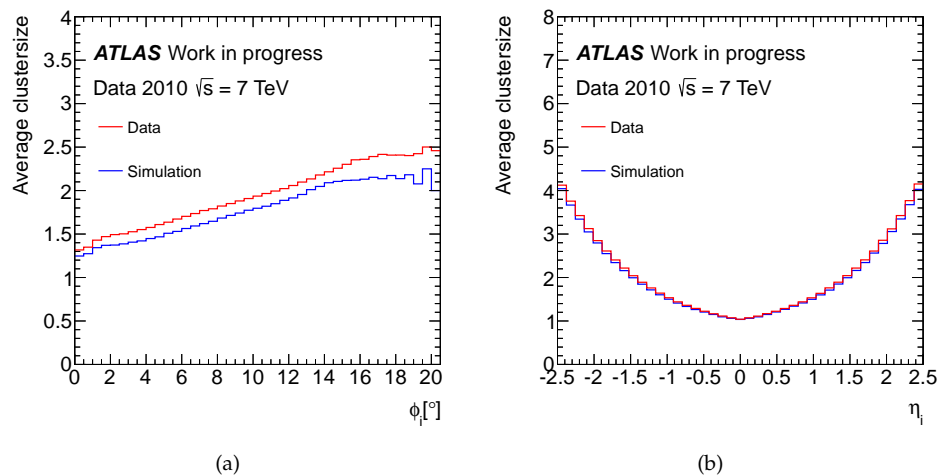
Figure 5.6: Distributions for the average cluster size in data and Monte Carlo simulation. The ϕ_i distribution is restricted to the bulk of clusters. More details are given in the text.
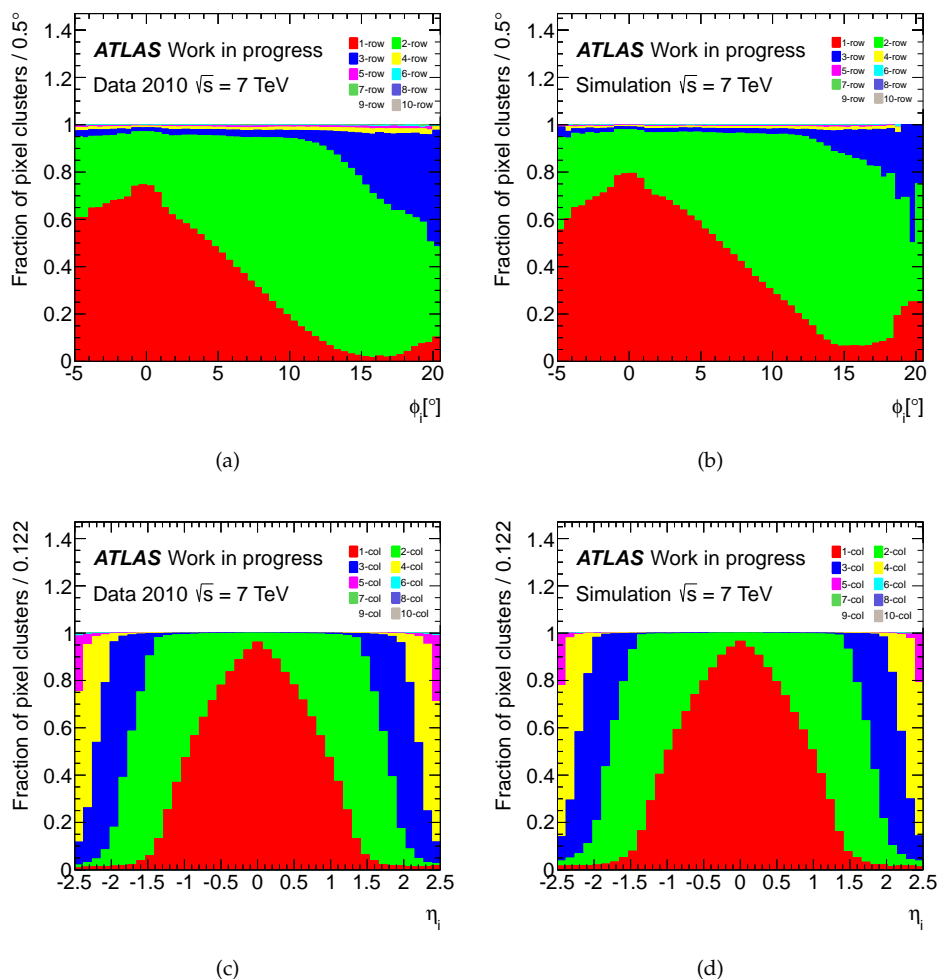
Figure 5.7: Cluster size in the *local-x* (a-b) and *local-y* (c-d) directions as a function of the track incidence angle in a sample of $\sqrt{s} = 7$ TeV data taken in 2010 by jet, tau and missing transverse momentum triggers and a Monte Carlo simulated sample of di-jet events. In this case the fraction of clusters for every cluster size in each bin is normalised to the total clusters fraction for that bin.

local-x and *local-y* directions as

$$\Omega_{x(y)} = \frac{q_{\text{last row (col)}}}{q_{\text{first row (col)}} + q_{\text{last row (col)}}} \tag{5.2}$$

where $q_{\text{first row (col)}}$ and $q_{\text{last row (col)}}$ are the charge of the first and last row or column respectively. The distributions of Ω_x and Ω_y are shown in Figure 5.8. The $\Omega_{x,y}$ variables take value $1/2$ if the cluster is completely symmetric, and values that tend to 0 or 1 for highly asymmetric clusters. The position of the edges of the distribution depends on the the incident angle, number of pixels and thresholds. The Ω_y distribution is pretty flat in the central region. The Ω_x distribution exhibits a slope that is due to 2-row clusters probably originating from δ-rays and the effect of the Lorentz angle. The structures around the 0 value are probably due to effects of the ToT quantization.

(a)   (b)
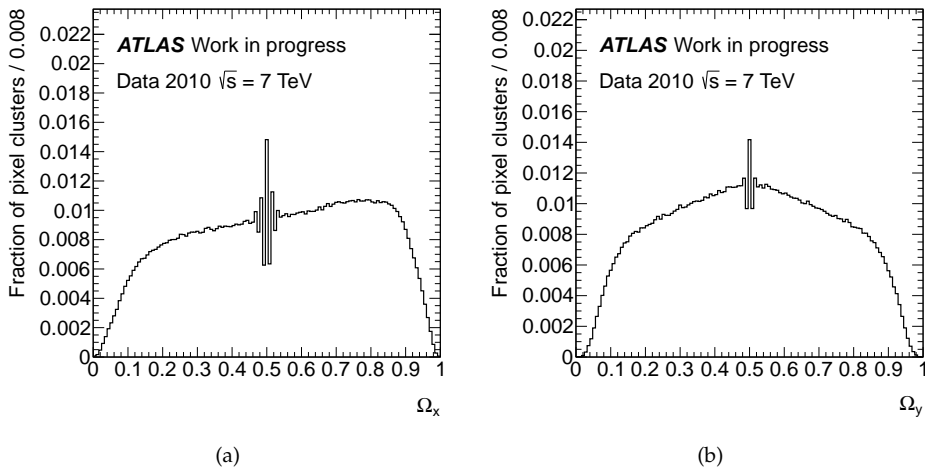
Figure 5.8: Distributions of (a) Ω_x and (b) Ω_y in 2010 data at $\sqrt{s} = 7$ TeV for clusters with size > 1.

5.3 Position reconstruction

As already mentioned the reconstruction of the position of the charged particles when they traverse the detector is the main task of this tracking system, and the achievement of a good resolution is fundamental for the good performance of the reconstruction of physics objects in the detector. The resolution depends on the pixel size and on the incidence angle of particles, and can be improved using the information of charge deposition within the cluster.

The position of a charged particle crossing-point can be estimated using several algorithms.

Centre of the cluster algorithm

The simplest way to reconstruct the position of the particle crossing-point in the detector is to consider the geometrical centre of the cluster

$$x_{\text{centre}} = \frac{x_{\text{first row}} + x_{\text{last row}}}{2} \tag{5.3}$$

$$y_{\text{centre}} = \frac{y_{\text{first col}} + y_{\text{last col}}}{2} \tag{5.4}$$

where x_{row} and y_{col} are the coordinates of the centre of the row or column considered respectively. This algorithm is very simple and does not make use of any information on the spatial distribution of the charge in the cluster and does not require a track to be reconstructed beforehand.

Digital algorithm

Some information on the shape of the cluster can be taken into account by considering a possible geometrical asymmetry of the cluster. This can be accomplished by computing weights for every row and column as

$$w_i^{\text{row (col)}} = \frac{n_i^{\text{row (col)}}}{\sum_i n_i^{\text{row (col)}}} \tag{5.5}$$

where n_i is the number of pixels in the cluster for row (column) i. The position of the cluster is then computed as the weighted mean

$$x_{\text{dig}} = \sum_i w_i^{\text{row}} x_i \tag{5.6}$$

$$y_{\text{dig}} = \sum_i w_i^{\text{col}} y_i \tag{5.7}$$

The digital algorithm takes into account the two-dimensional cluster shape but does not make an explicit use of the charge distribution within the cluster and does not require tracks to be reconstructed beforehand.

Charge sharing algorithm

The charge sharing algorithm makes explicit use of the information of the collected charge in the single cluster pixels. As seen in Section 5.2, only the charge collected in the first and last rows or columns is actually sensitive to the particle crossing-point in the detector. The position can therefore be computed correcting the coordinates of the centre of the cluster, as defined in Equations 5.3 and 5.4, with an additional factor based on the charge sharing variables defined in Equation 5.2. The charge sharing coordinates are computed as

$$x_{\text{charge sharing}} = x_{\text{centre}} + \Delta_x \left(\Omega_x - \frac{1}{2} \right) \tag{5.8}$$

$$y_{\text{charge sharing}} = y_{\text{centre}} + \Delta_y \left(\Omega_y - \frac{1}{2} \right) \tag{5.9}$$

where the $\Delta_{x,y}$ parameters relate the cluster asymmetry along each direction with the position correction. The values of the $\Delta_{x,y}$ parameters depend both on the cluster size and on the incidence angle of the track. Figure 5.10 shows the mean difference between the x_{centre} and y_{centre} position and the truth particle crossing-points in the simulation. The relationship is at first order linear. It can be seen that, especially in the *local-y* direction, deviations from linearity occur. Since these deviations are not too large, they are only expected to deteriorate the algorithm performance with respect to the optimum. It will be shown in Section 5.4.1 how the charge sharing algorithm can be calibrated making use of real data. Since the $\Delta_{x,y}$ correction factors strongly depend on the incident angle, this algorithm requires track parameters to be known beforehand. Alternatively, the incidence angle can be approximately determined using the beam spot position information.

5.4   Charge sharing clustering

The concept of the charge sharing determination of the cluster position has already been introduced in Section 5.3. In the following the procedure and results of the calibration on real data are shown, together with results for the validation of the calibration used by ATLAS during part of the 2011 data taking.

5.4.1   Calibration

The charge sharing algorithm can be calibrated using real data. The residual between the cluster position computed with the centre of the cluster algorithm and the position from track extrapolation can in fact be used to determine the correction factors $\Delta_{x,y}$ as the slope of the straight line represented by the equation

$$x_{\text{centre}} - x_{\text{extr}} = -\Delta \left(\Omega_x - \frac{1}{2} \right) \tag{5.10}$$

The relationship between the residuals and the charge sharing is illustrated in Figure 5.10 for a few examples.

In 2010 data were taken and reconstructed with a preliminary calibration based on early data and tagged with the name `PixelOfflineReco-7TeV-000-04`. The main motivations for a recalibration were to get a better calibration from the increased available statistics and to benefit from the improved ID alignment included in the 2010 data reprocessing campaign. The data considered for the calibration had been taken during 2010 with a mix of jet, $\tau_{\text{had-vis}}$ and missing transverse momentum triggers. The selection of tracks and clusters include the following requirements:

- Track $p_{\text{T}} > 5\,\text{GeV}$

- $5\,n_{\text{SCT Hits}} + n_{\text{TRT Hits}} \geq 30$, where $n_{\text{SCT Hits}}$ and $n_{\text{TRT Hits}}$ are the number of hits in the SCT and TRT respectively

- $\sqrt{(1000(\mu\text{m/GeV})/p_{\text{T}})^2 + \text{Res}_{\text{Cut}}^2} \geq \text{Res}_{\text{dig}}$, where p_{T} is the track p_{T}, Res_{dig} is the residual between the position computed with the digital algorithm and the track

(a)

(b)

(c)

(d)
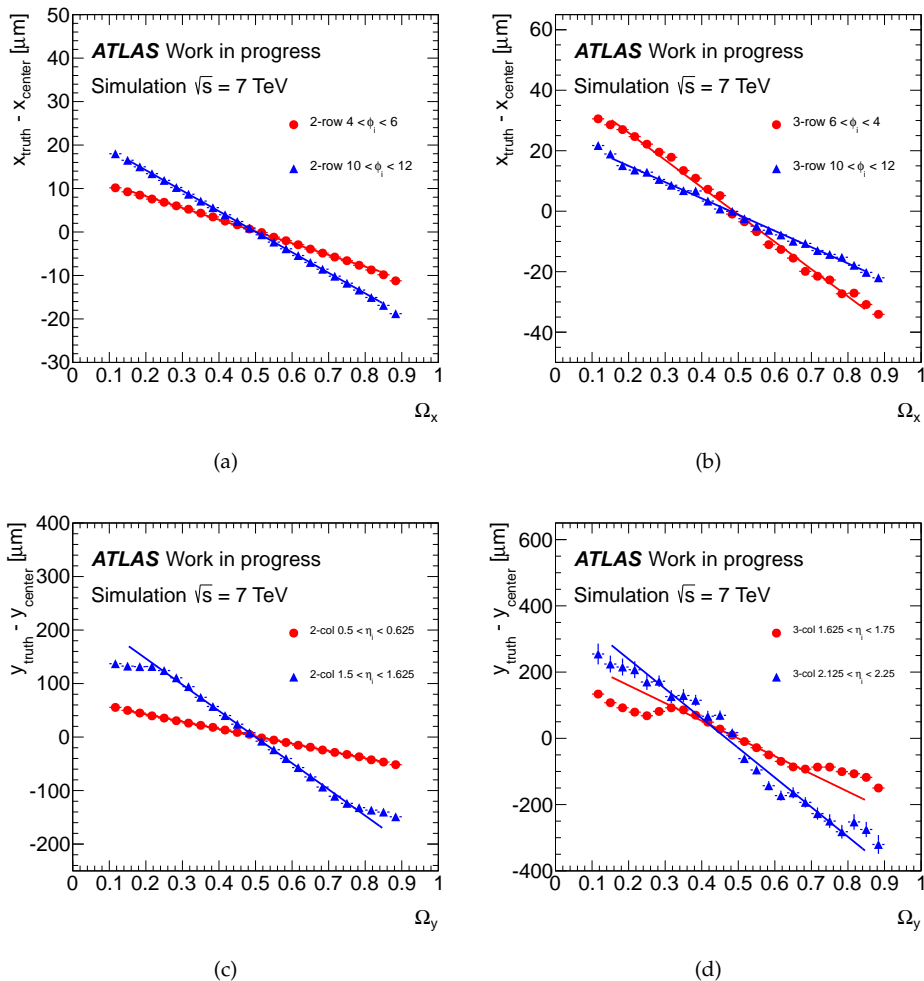
Figure 5.9: Dependence of the mean difference between the reconstructed and truth particle crossing-point in the detector on the charge sharing $\Omega_{x,y}$ along the (a-b) *local-x* and (c-d) *local-y* coordinates and (a-c) 2 rows (columns) clusters and (b-d) 3 rows (columns) clusters.
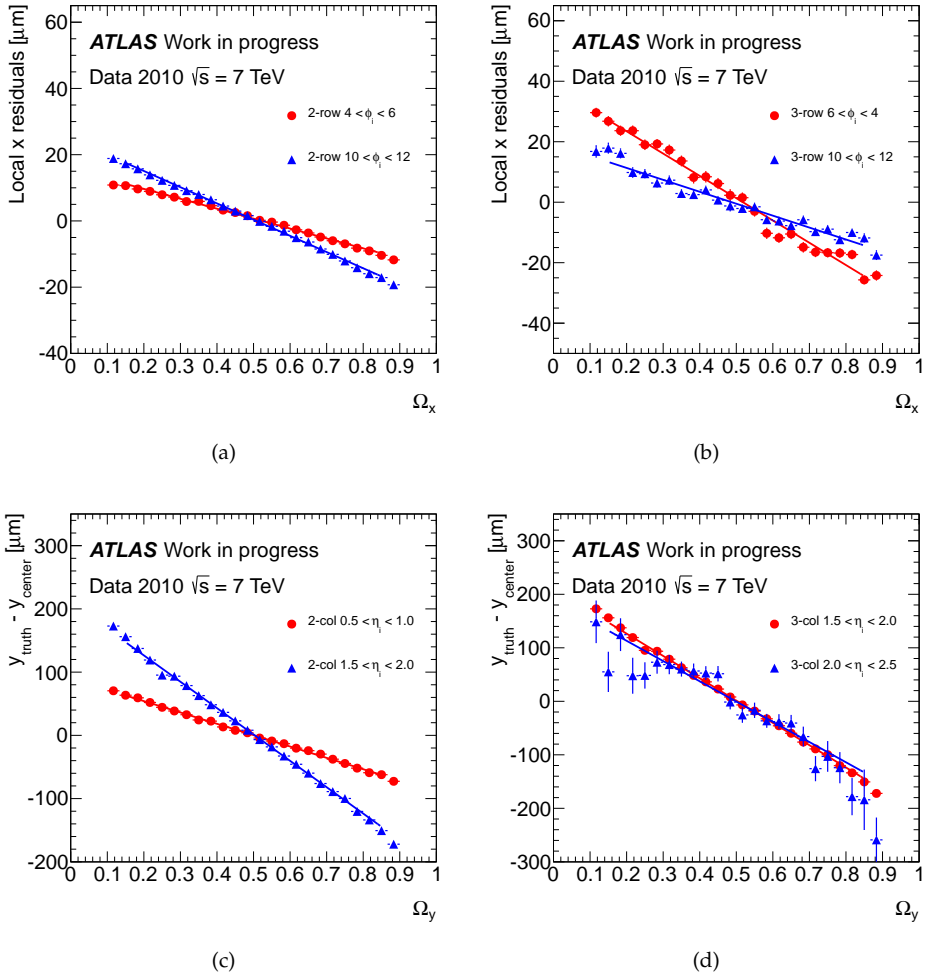
Figure 5.10: Dependence of residuals on the charge sharing $\Omega_{x,y}$ along the (a-b) *local-x* and (c-d) *local-y* coordinates and (a-c) 2 rows (columns) clusters and (b-d) 3 rows (columns) clusters in 2010 data (see the text for further details).

extrapolation, and $\mathrm{Res}_{\mathrm{Cut}}$ is a cut that takes the value $\mathrm{Res}_{\mathrm{Cut}} = 80\mu\mathrm{m}$ in the *local-y* direction and $\mathrm{Res}_{\mathrm{Cut}} = 400\mu\mathrm{m}$ in the *local-y* direction. The purpose of this cut is to consider only the bulk of well resolved clusters.

The selection had been previously optimised in Ref. [165]. Calibration constants were determined in the following binnings

- 32 ϕ_i bins from $[-60, 60]$

- 10 η_i bins from $[-2.5, 2.5]$

- 3 cluster size bins: 2, 3, 4 rows/columns

- 2 bins for barrel and end-caps

The range of the ϕ_i distribution is larger than the range for collision data because the database can accommodate cosmic data as well. In order to derive the constants, sets of histograms of the residuals of the cluster position with respect to the extrapolated track position are prepared for every bin of cluster size, incident angle and detector region. Each set is composed of thirty histograms, corresponding to equal width charge sharing bins. Histograms have 100 bins and range $[-150, 150]\,\mu\mathrm{m}$ for residuals in the *local-x* direction and $[-400, 400]\,\mu\mathrm{m}$ in the *local-y* direction. For each histogram with more than 50 entries the RMS of the distribution is extracted, considering only bins within $[\mu - 3\mathrm{RMS}_0, \mu + 3\mathrm{RMS}_0]$, where μ is the histogram mean and RMS_0 is a first calculation of the RMS for which the full histogram is considered.

The RMS as a function of the charge sharing is fit with a straight line over the range $[0.15 - 0.85]$. This range is chosen in order to avoid the edges of the charge sharing distributions.

The result of the fit was rejected if:

- the fit had not converged,

- the probability for the fit χ^2 was < 0.05,

- the slope of the straight line resulted to be negative,

- the absolute value of the slope of the straight line was smaller than two times its error from the fit.

Part of the fit results failing these requirements were recovered following manual inspection. The results for the calibration constants are shown in Figure 5.11, where they are indicated by the tag name `PixelOfflineReco-7TeV-000-05`. The constants of `Pixel OfflineReco-7TeV-000-04` are shown as well. With respect to the `PixelOffline Reco-7TeV-000-04` tag, the new Δ_y corrections are quite similar for 2-column clusters and larger at large η_i incidence angles for 3-column clusters. Constants were determined for 4-column clusters at large η_i as well. The new Δ_x corrections are very similar to the previous tag for 2- and 3-row clusters. Constants for 4-row clusters were computed as well.
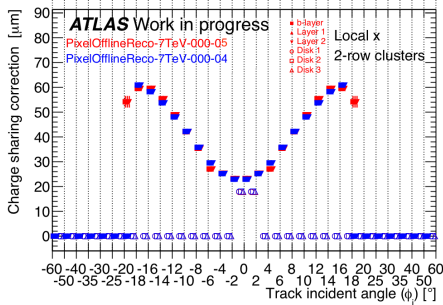
(a)
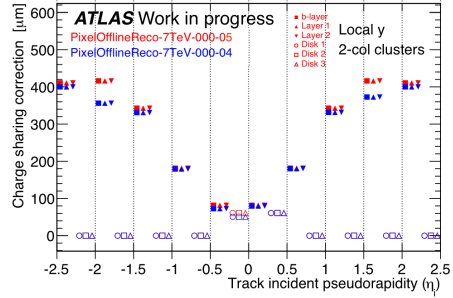
(b)
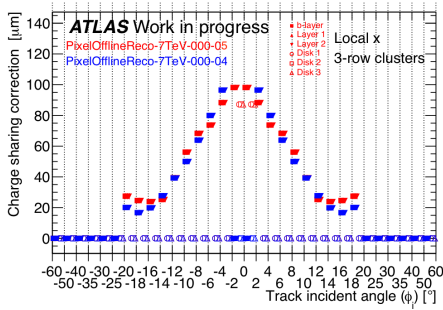
(c)
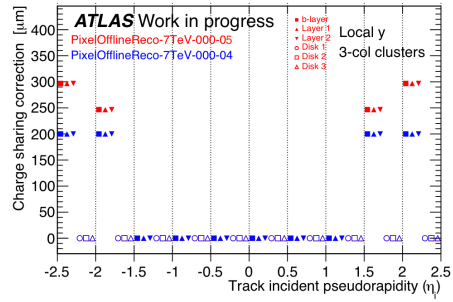
(d)
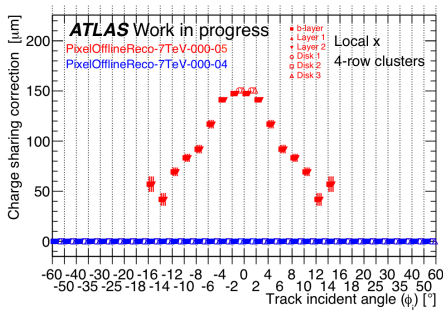
(e)
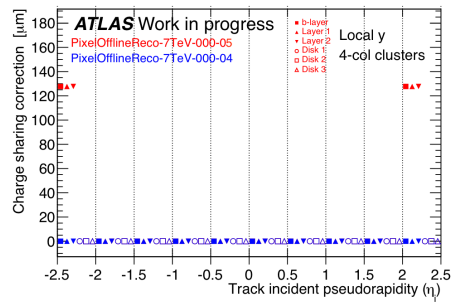
(f)

Figure 5.11: Charge sharing calibration constants in `PixelOfflineReco-7TeV-000-04` and `PixelOfflineReco-7TeV-000-05` as a function of (a-c-e) ϕ_i and (b-d-f) η_i for cluster size (a-b) two, (c-d) three and (e-f) four.

5.4.2 Performance and validation

The performance of the charge sharing calibration can be assessed by looking at the position resolution in the Monte Carlo simulation. Figure 5.12 shows the resolution for a $t\bar{t}$ Monte Carlo sample reconstructed with `PixelOfflineReco-7TeV-000-05`. The charge sharing algorithm allows for a large improvement of the resolution with respect to the centre of cluster algorithm. The shoulders in the distributions are better understood looking at the different cluster sizes separately, as shown in Figure 5.13 for the resolutions along the *local-x* direction and Figure 5.14 for the *local-y* one. The resolution for clusters with only one pixel over threshold is by definition unaffected by the choice of the algorithm. A large improvement is seen both for two-row and two-column clusters. The charge sharing algorithm allows for a slightly better resolution in 3-row clusters, while most of the improvement in 4-row clusters is due essentially to partial recovery of tails in the distribution. Clusters with 3 or 4 rows are in fact mostly due to δ-rays, and in these cases the linear approximation does not hold. Along the *local-y* direction the resolution is largely improved for 3-column and 4-column clusters as well. The resolution with respect to the truth position is used in order to assign an uncertainty to the cluster position. This uncertainty is used as an input to tracking algorithms too.

(a)

(b)
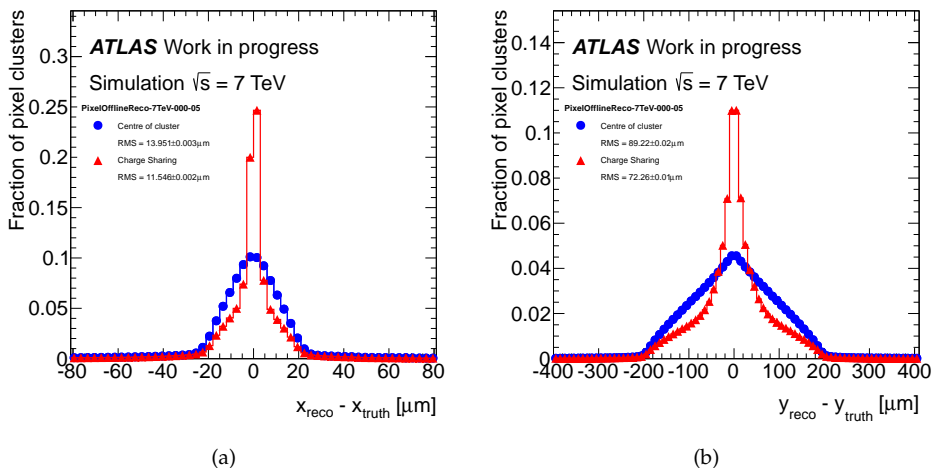
Figure 5.12: Resolution in the (a) *local-x* and (b) *local-y* direction for the centre of cluster algorithm and charge sharing clustering algorithm with `PixelOfflineReco-7TeV-000-05` in a $\sqrt{s} = 7$ TeV $t\bar{t}$ Monte Carlo sample.
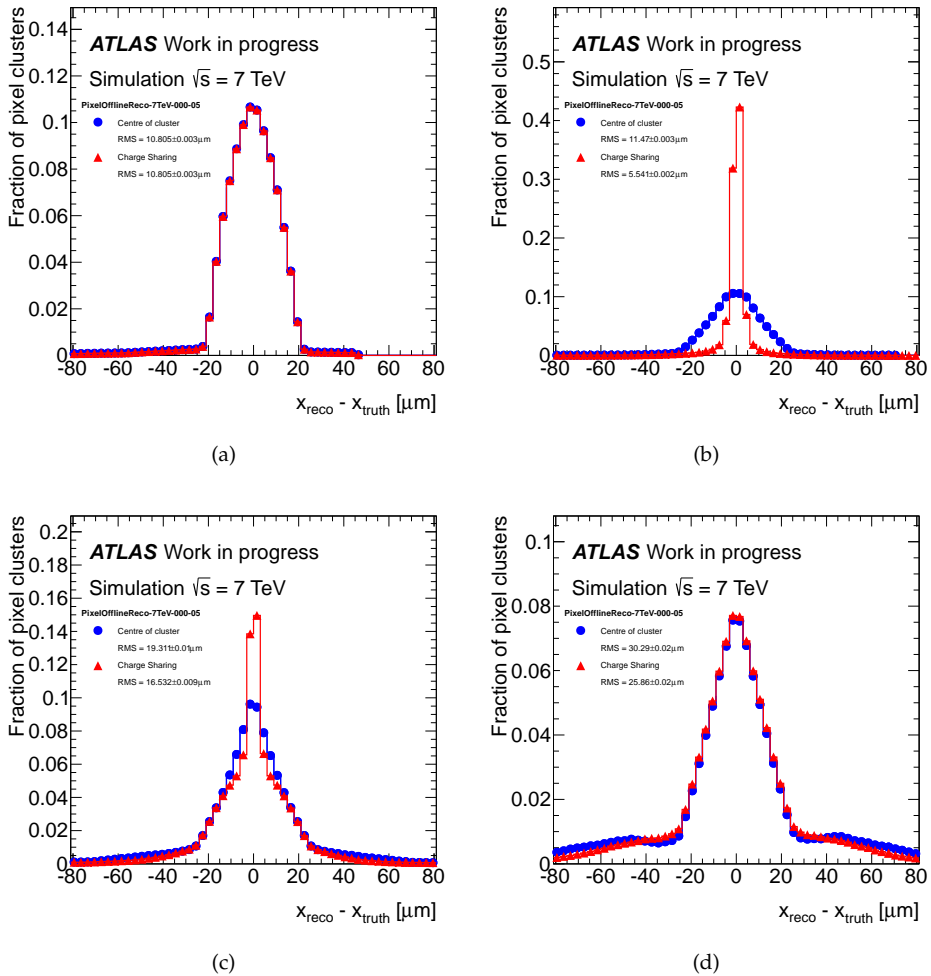
Figure 5.13: Resolution in the *local-x* direction for the centre of cluster algorithm and charge sharing algorithm with `PixelOfflineReco-7TeV-000-05` in a $\sqrt{s} = 7$ TeV $t\bar{t}$ Monte Carlo sample for cluster size (a) one, (b) two, (c) three and (d) four.
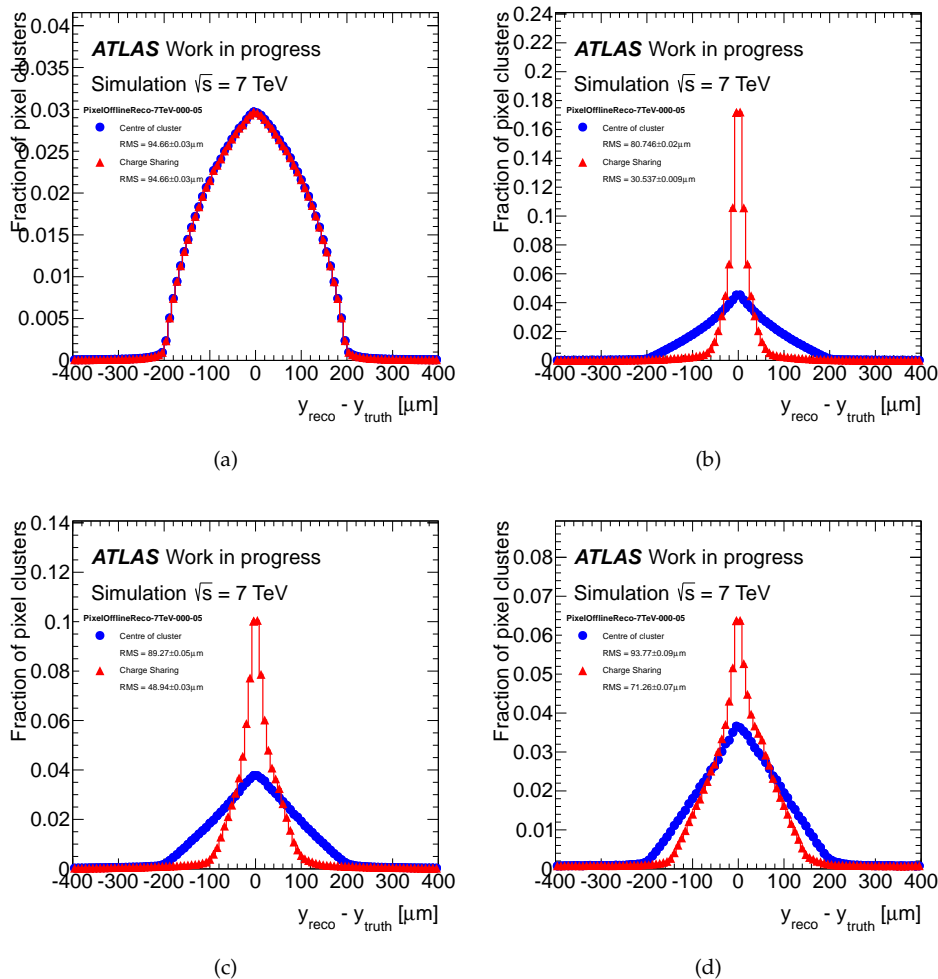
Figure 5.14: Resolution in the *local-y* direction for the centre of cluster algorithm and charge sharing algorithm with `PixelOfflineReco-7TeV-000-05` in a $\sqrt{s} = 7$ TeV $t\bar{t}$ Monte Carlo sample for cluster size (a) one, (b) two, (c) three and (d) four.

The distributions for the residuals between the cluster position and the track extrapolation were studied in a few cases representing the bulk the distribution. A subset of the same data sample used for the derivation of the calibration was privately re-reconstructed using `PixelOfflineReco-7TeV-000-05`. The results were compared to the position reconstruction with the charge sharing algorithm using `PixelOffline Reco-7TeV-000-04`. Figure 5.15 and 5.16 show distributions of the residuals for the bulk of the interesting clusters, that is for clusters with two rows for residuals in the *local-x* direction and with two columns for residuals in the *local-y* direction. From these distributions it is clear that the performance for the bulk of the clusters is similar for the two tags. The distributions of the pulls, that is the ratios of the residuals divided by the uncertainties assigned to the cluster position, are shown as well. These distributions have width ~ 1, which suggests a correct assignment of the uncertainties. Figure 5.17 shows the residuals and pulls in the *local-x* direction for 4-row clusters. This is an example of a particular case: with the `PixelOfflineReco-7TeV-000-04` tag, no charge sharing calibration constants are determined for 4-row clusters. The position reconstructed with the charge sharing algorithm reduces therefore to the centre of the cluster one. The residuals display a double peak, most probably due to δ-rays. With `Pixel OfflineReco-7TeV-000-05` constants are determined for the 4-row case as well, as shown in Figure 5.11(e). This allows for a partial recovery of a single-peak structure, as shown in Figure 5.17 (c) and (d), where the structures visible in (a) and (b) are definitely smoothed.

The distributions for the residuals are finally shown in Figure 5.18 as a function of ϕ_i for residuals in the *local-x* direction and η_i for residuals in the *local-y* one. The distributions are shown for data and Monte Carlo simulation for `PixelOfflineReco-7TeV-000-04` and for a sample of data taken in early 2011 for `PixelOfflineReco-7TeV-000-05`. It can be seen that the agreement between data and the simulation is fair for `PixelOfflineReco-7TeV-000-04` and that a similar performance is achieved with `PixelOfflineReco-7TeV-000-05` in 2011 data. The sample of 2011 data is from a mix of triggers from all signatures that is used for prompt reconstruction.
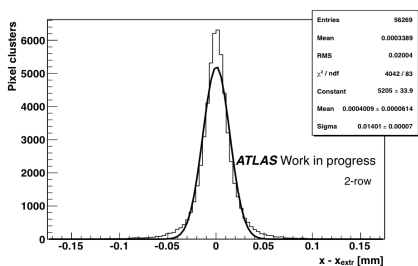
(a)
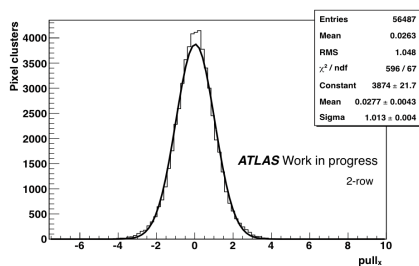
(b)
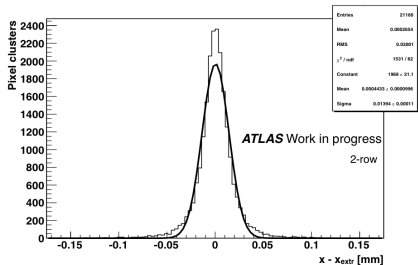
(c)
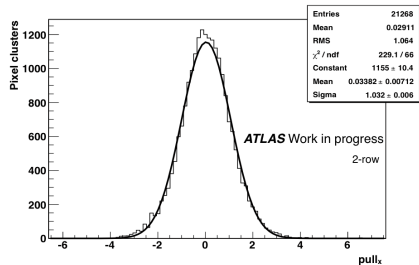
(d)

Figure 5.15: Distributions of residuals and pulls for the charge sharing position reconstruction along the *local-x* direction with calibration tag (a,b) `PixelOfflineReco-7TeV-000-05` and (c,d) `PixelOfflineReco-7TeV-000-04` for the bulk of clusters. More details are given in the text.
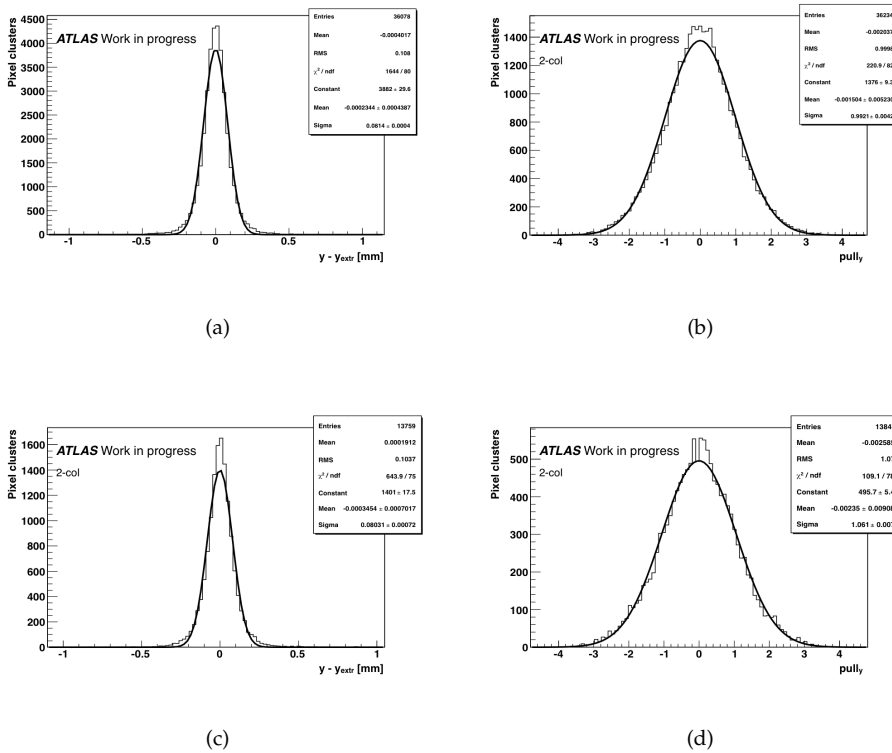
Figure 5.16: Distributions of residuals and pulls for the charge sharing position reconstruction along the *local-y* direction with calibration tag (a,b) `PixelOfflineReco-7TeV-000-05` and (c,d) `PixelOfflineReco-7TeV-000-04` for the bulk of clusters. More details are given in the text.
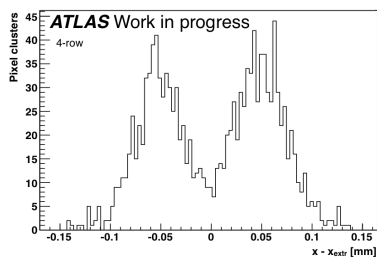
(a)
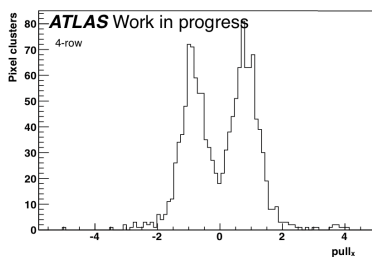
(b)
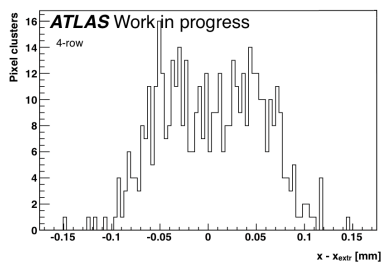
(c)
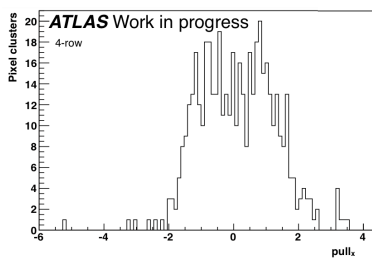
(d)

Figure 5.17: Distributions of residuals and pulls for the charge sharing position reconstruction with calibration tag (a,b) `PixelOfflineReco-7TeV-000-05` and (c,d) `PixelOfflineReco-7TeV-000-04` for the 4-row clusters. More details are given in the text.
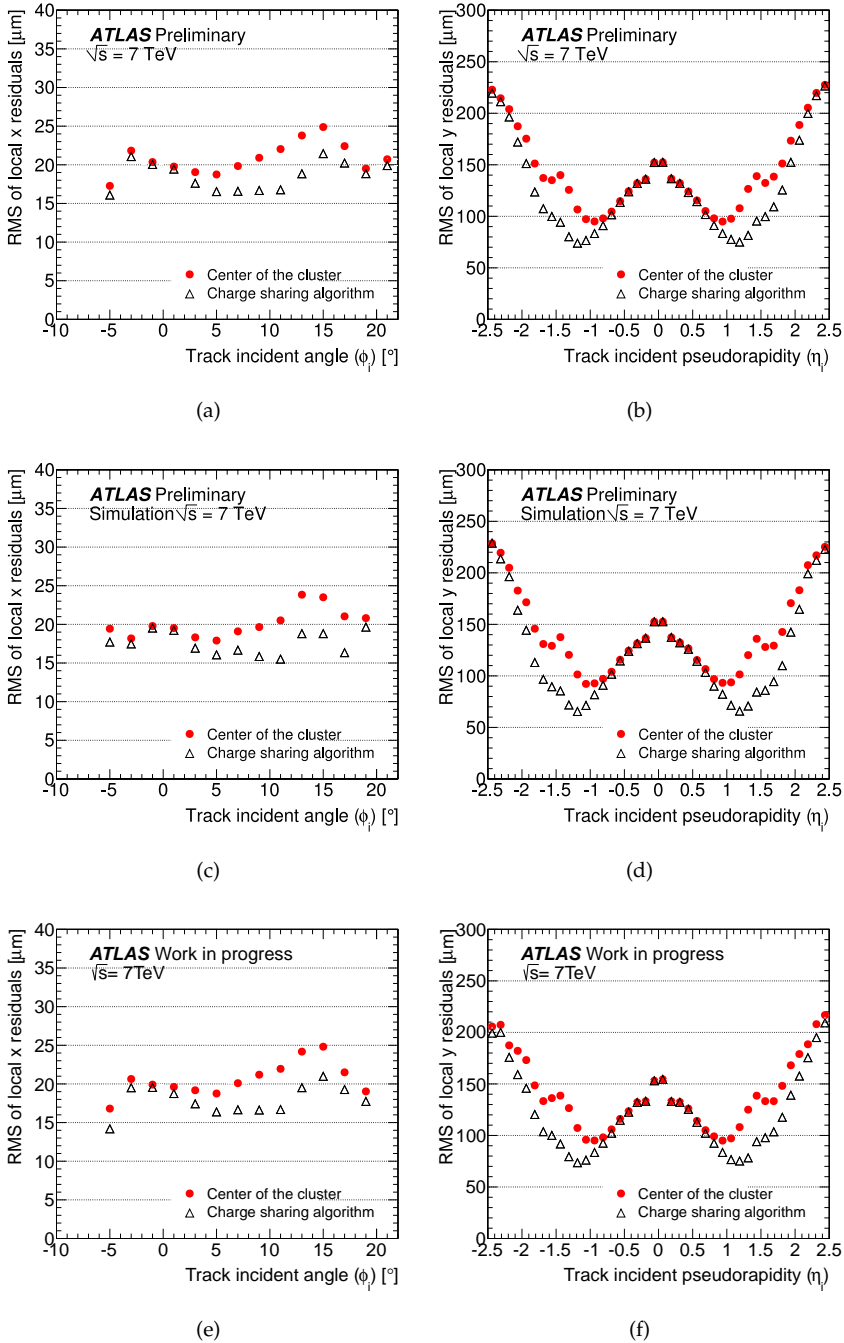
Figure 5.18: Distributions of the residuals between cluster position and track extrapolation as a function of (a-c-e) ϕ_i and (b-d-f) η_i. The results for charge sharing calibration tag `PixelOffline Reco-7TeV-000-04` are shown for (a-b) data collected in 2010, (c-d) Monte Carlo simulation. Results are shown for tag `PixelOfflineReco-7TeV-000-05` for data collected in 2011 (e-f).

5.5   Neural network clustering

Hadronically decaying tau leptons and high p_T jets are characterised by highly colli-mated particles. In these environments the track density is high, and it results often in merged measurements in the Pixel detector. Charge can in fact be deposited in neigh-bouring pixels, and clusters be shared between particles, as illustrated in Figure 5.19. Due to the importance of tracking in the $\tau_{\text{had-vis}}$ and in jet flavour tagging it is desirable to be able to resolve measurements due to more than one particle. The charge sharing algorithm is limited with this respect, because it implicitly assumes that a cluster is due to the passage of one particle only. Moreover by definition it considers the cluster char-acteristics along one direction at a time only. Using the information from the full cluster can allow not only to resolve multiple particles in a cluster, but to improve the resolution for one particle clusters too. Neural networks allow to handle non-linear correlations be-tween input variables, and are therefore chosen for this application.
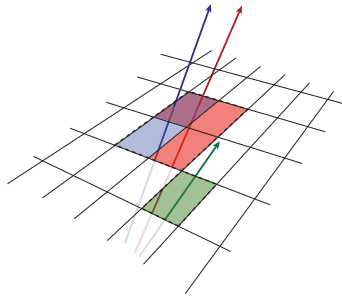
Figure 5.19: Illustration of charge deposition in a layer of the Pixel detector by multiple particles in a dense environment.

5.5.1   The algorithm

Multiple feed-forward multilayer perceptron neural networks (NN) are used to estimate the number of particles traversing the cluster, the position of the crossing-points and their errors. The network for a single intermediate layer corresponds to the function

$$F_i(\vec{x}) = h\left(\sum_j w_{ij} g\left(\sum_k w_{jk} x_k + \theta_j\right) + \theta_i\right) \tag{5.11}$$

where $\vec{x}$ is the vector of input nodes (variables) and F_i are the output nodes. The network parameters w and θ are adjusted during the training process, and $g(x)$ and $h(x)$ are activation functions. The g function is conventionally chosen to be

$$g(x) = \left(1 + e^{-2x}\right)^{-1} \tag{5.12}$$

while the choice of the h function is application dependent. A NN can be used for classi-fication or interpolation problems. In classification the number of output nodes is equal

to the number of possible choices, with the i-th choice having as target $\{00...1_{i-\text{th}}...00\}$. In interpolation linear functions are chosen for the h functions, which allows to set the targets to the desired values.

The input variables are the same for all the NNs:

- 7×7 matrix of the charge deposited in each pixel of the candidate cluster. The matrix is centred on the cluster position determined by the charge weighted centroid of the cluster,

- a vector with the longitudinal size of the pixels in the charge matrix,

- the direction of the candidate charged particles traversing the cluster.

The NNs used include two intermediate layers. They are trained on $t\bar{t}$ events generated with MC@NLO matched to HERWIG and di-jet events generated using PYTHIA with the JetNet package [170]. The estimation of the parameters of interest happens as follows:

Number of particles per cluster
> The number of particles per cluster N is estimated using a NN dedicated to classification. Three output nodes corresponding to one, two or three particles traversing the cluster are considered.

Cluster position
> Different NNs are used depending on the number of particles traversing the cluster. The $2 \times N$ output nodes are trained to represent an estimate of the position of the crossing-point.

Cluster position uncertainty
> Separate NNs are used to estimate the uncertainties on the estimated positions in the *local-x* and *local-y* directions.

5.5.2 Cluster performance

The cluster performance of the algorithm can be assessed by studying the residuals of the estimated position with respect to the track extrapolation, as already done for the charge sharing clustering in Section 5.4. The selection criteria on tracks and clusters are the same listed in Section 5.4.1, with the exception of the transverse momentum cut that is raised to $p_T \geq 10\,\text{GeV}$. The samples used are a $t\bar{t}$ simulated sample, generated with MC@NLO matched to HERWIG, and a sample of high-p_T multi-jet events selected in 2011 data. Figure 5.20 shows the residuals for the position estimated with the charge sharing or neural network algorithms with respect to the track extrapolation. From these global plots is is clear that the neural network clustering allows for some improvement in the performance of the reconstruction of the particle crossing-point in the detector. This improvement is not so large, as expected for the bulk of the clusters. It can be observed looking at the logarithmic plots that the improvement in the *local-y* direction is
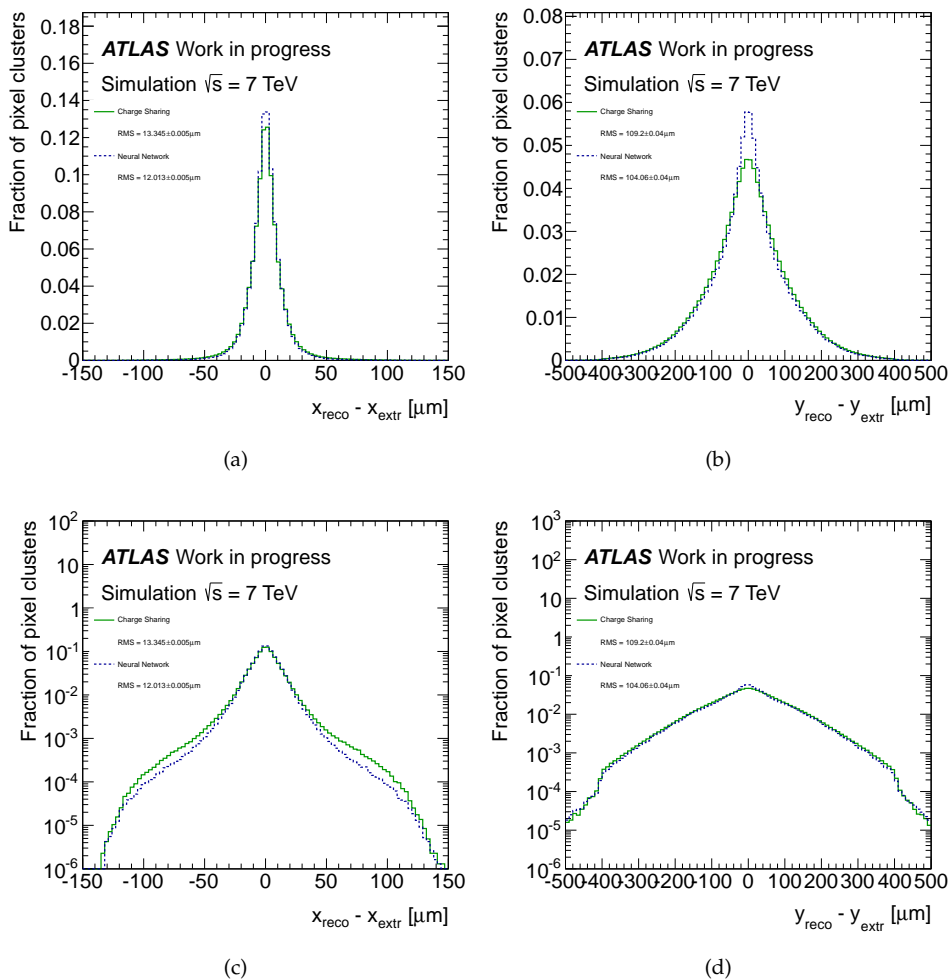
Figure 5.20: Residuals along the (a-c) *local-x* and (b-d) *local-y* directions for the charge sharing algorithm and the neural network clustering. The scale is linear in the top row and logarithmic in the bottom row.

mostly due to the recovery of tails, whereas in the *local-y* direction the improvement is concentrated in the core of the distribution.

The residuals are shown as a function of a few relevant variables in Figure 5.21 and 5.22. Residuals along the *local-x* direction show a larger improvement for the neural network clustering especially in the ϕ_i region populated by 2-row clusters. Some dependence on η_i is visible for both algorithms, but the improvement is pretty flat in this variable, suggesting a correlation due to geometrical reasons only. As expected the largest improvement is observed for 3-row and 4-row clusters, and for clusters in the barrel, especially in the *b-layer*. Some discrepancy is observed between the data and simulation distributions as a function of ϕ_i, while a much better agreement is observed for the distribution as a function of the cluster size. These two facts point to the observed poor modelling of the cluster size as a function of ϕ_i as the source of the discrepancy. The distribution of *local-y* residuals displays the best improvement in the η_i region populated by 2-column and 3-column clusters. Also in this case the distribution as a function of ϕ_i displays no preferred region for the improvement. Contrary to the case of *local-x* residuals, the distribution of *local-y* residuals as a function of the cluster size shows the largest disagreement between data and simulation for the regions of largest improvement. This points to the fact the neural network clustering may be overperforming in the simulation, since it was trained on a simulated sample. The fact that the residual distribution for the charge sharing algorithm shows similar discrepancies, and that the largest discrepancy is observed for barrel layers, especially the *b-layer*, may rather suggest a geometrical source of the discrepancy.
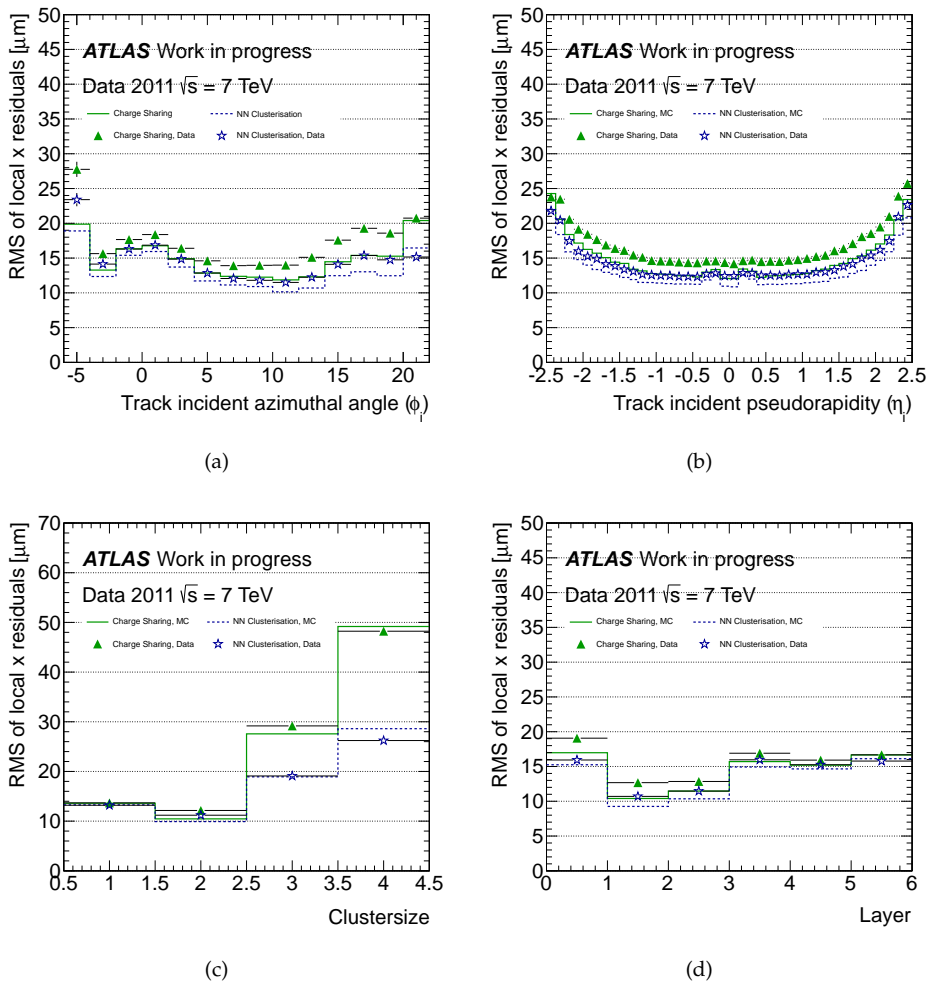
Figure 5.21: Residuals along the *local-x* direction as a function of (a) ϕ_i, (b) η_i, (c) cluster size and (d) layer for the charge sharing algorithm and the neural network clustering in both data and simulation.
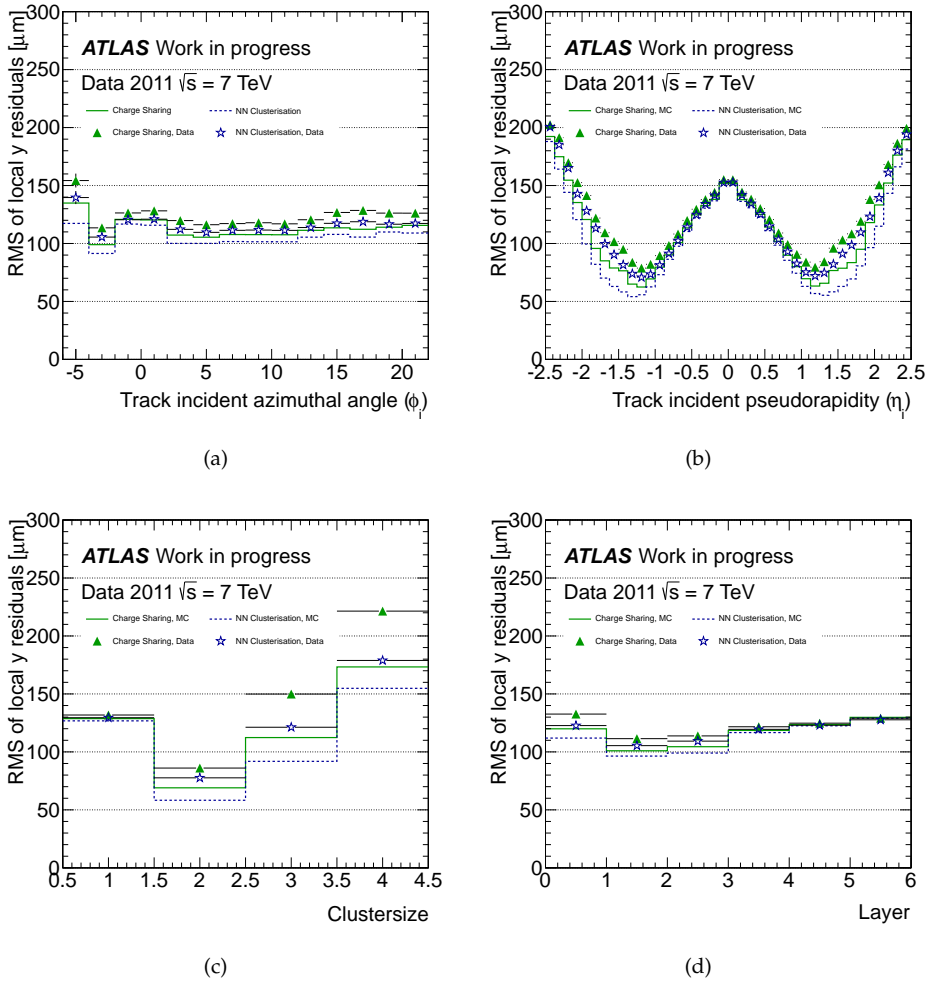
Figure 5.22: Residuals along the *local-y* direction as a function of (a) ϕ_i, (b) η_i, (c) cluster size and (d) layer for the charge sharing algorithm and the neural network clustering in both data and simulation.

The distributions of *local-x* residuals for the best-improvement cases is shown in Figure 5.23. Three-row clusters show a distribution affected by tails with the charge sharing clustering. The neural network clustering recovers these tails. For 4-row clusters instead the charge sharing clustering can clearly not resolve the double peak structure, most probably due to multiple particles traversing the cluster and δ-rays.

(a)   (b)
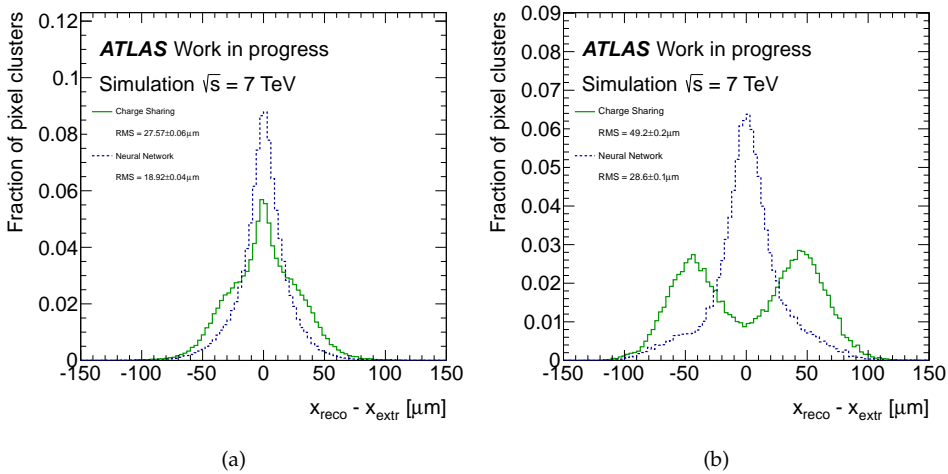
Figure 5.23: Residuals along the *local-x* direction for (a) 3-row and (b) 4-row clusters for the charge sharing algorithm and the neural network clustering.

Figure 5.24 shows the uncertainties assigned for the cluster position reconstructed with the charge sharing and neural network algorithms. Only a marginally smaller uncertainty is assigned to the *local-x* position by the neural network. The largest improvement is in the region where it is expected as shown in Figure 5.21(a). These features are in agreement with what observed for the global residuals distributions of Figure 5.20. The uncertainty in the *local-y* direction position reconstruction is much smaller in the region of best improvement of the neural network clustering. Distributions of the pulls for the crossing-point position reconstructions are shown in Figure 5.25. The *local-x* pull distribution displays some disagreement between data and simulation for both the charge sharing and neural network clustering. The poor modelling of the cluster size distribution is even in this case a good candidate source. The *local-y* pull distributions shows a good agreement in the central region, where a slight underestimation of the uncertainties for the neural network clustering can be observed as well. A large disagreement is present in the regions where both the charge sharing and neural network clustering have the largest improvement over the centre of the cluster algorithm and the neural network gains most over the charge sharing clustering. The largest discrepancy observed for the neural network clustering may be explained either by an overperformance in the simulated samples reconstruction or a more marked underestimation of the uncertainty in specific regions.

(a)   (b)
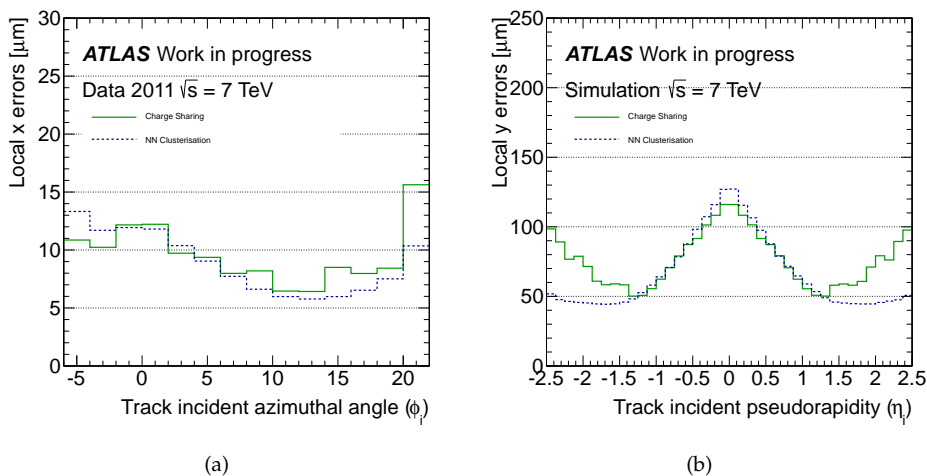
Figure 5.24: Uncertainty assigned for the cluster position in the (a) *local-x* and (b) *local-y* directions for the charge sharing algorithm and the neural network clustering.

(a)   (b)
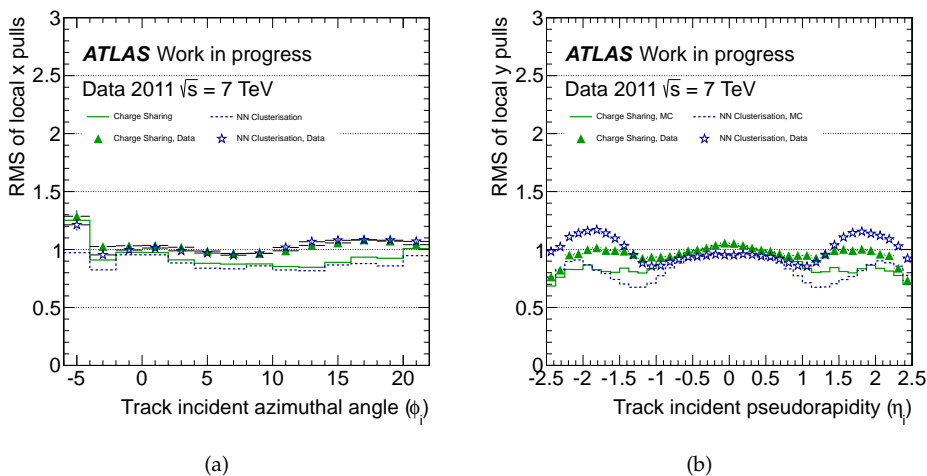
Figure 5.25: Pulls for the cluster position in the (a) *local-x* and (b) *local-y* directions for the charge sharing algorithm and the neural network clustering in both data and simulation.

5.6   Outlook on $\tau_{\text{had-vis}}$ identification

The performance of the reconstruction of the particle crossing-point in the detector is very important to ensure a high level performance of the ATLAS tracking.

It has already been mentioned in Section 2.3.5 that this tracking information is heavily used in $\tau_{\text{had-vis}}$ reconstruction and identification. A high track reconstruction efficiency, even in busy environments, is essential to correctly associate tracks to $\tau_{\text{had-vis}}$ candidates, allowing to classify them correctly and to compute sound tracking related identification variables. An excellent reconstruction of primary vertices is important to correctly define the reference frame for the reconstruction of the $\tau_{\text{had-vis}}$ four-momentum and identification variables. A summary of the variables used for $\tau_{\text{had-vis}}$ identification in 2012 data and simulation is given for convenience in Table 5.2, more details can be found in Ref. [123]. It should be noted that most of the identification variables rely directly on tracking information. Two interesting variables are the impact parameter significance of the leading track, $S_{\text{lead track}}$ and the significance of the transverse flight path before decay S_{Tflight}, that exploit the relatively long lifetime of τ leptons. These variables rely on the performance of measurement of tracks impact parameter and secondary vertices reconstruction.

The performance of the Pixel detector contributes decisively to the excellent track impact parameter resolution achieved by ATLAS, shown in Figure 5.26 and vertex reconstruction, shown in Figure 5.27.

(a)   (b)
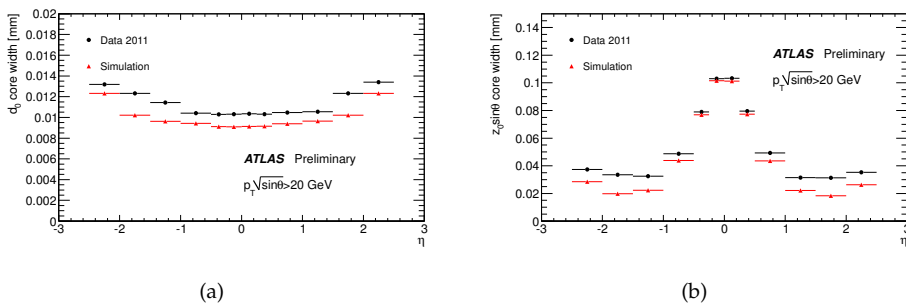
Figure 5.26: (a) transverse impact parameter d_0 core width and (b) longitudinal impact parameter $z_0 \sin \theta$ core width for data (black) and simulation (red) as a function of pseudorapidity η for tracks with $p_T/\sqrt{\sin \theta} > 20 \, \text{GeV}$, one hit in the Pixel b-layer and 0 shared hits in the silicon detectors. The core width is computed from a gaussian fit to central 2 sigma region of the distribution [3].

The impact of the improvements introduced by the neural network clustering is illustrated in Figure 5.28, that shows the track impact parameter resolution with the charge sharing and neural network clustering obtained from a simulated $t\bar{t}$ sample. For this sample ideal simulation and reconstruction were used, with no detector misalignment and error adaption to data applied.

Variable	Description	TR	IP	SV	Usage
$f_{\text{core}}^{\text{corr}}$	Fraction of transverse energy in the central region corrected for the number of vertices	•			ID1, ID3, EV
f_{track}	Fraction of the leading track p_{T} with respect to the EM scale energy of cells in a core cone	•			EV, MV
$f_{\text{track}}^{\text{corr}}$	Leading track momentum fraction corrected for the number of vertices	•			ID1, ID3, EV
R_{track}	p_{T}-weighted track width from core and isolation tracks	•			ID1, ID3, EV
$S_{\text{lead track}}$	Impact parameter significance of the leading track in the core region	•	•		ID1
$N_{\text{track}}^{\text{iso}}$	Number of tracks in isolation annulus	•			ID1
ΔR_{max}	Maximal ΔR between an associated track and the intermediate axis	•			ID3
$S_{\text{T}}^{\text{flight}}$	Transverse flight path before decay significance	•		•	ID3
m_{tracks}	Invariant mass of all associated tracks	•			ID3
f_{EM}	Electromagnetic energy fraction				EV, MV
f_{HT}	TRT High threshold hits fraction	•			EV
$E_{\text{T,strip}}^{\text{max}}$	Secondary energy deposits in the strip compartment				EV
$f_{\text{HCAL}}^{\text{leadtrk}}$	Ratio between energy in the HadCal and leading track momentum	•			EV
$f_{\text{ECAL}}^{\text{leadtrk}}$	Ratio between energy in the EMCal and leading track momentum	•			EV
f_{PS}	Presampler strip energy fraction				EV
$f_{\text{EM}}^{\pi^{\pm}}$	Electromagnetic energy of charged pions over calorimetric electromagnetic energy	•			EV
f_{iso}	Calorimetric ring isolation				EV
R_{Had}	Transverse energy weighted width in the HadCal				EV

Table 5.2: Synthetic definition of the variables used in 2012 $\tau_{\text{had-vis}}$ identification. The columns TR, IP and SV are marked if the variable uses tracking, impact parameter or secondary vertex information respectively. More details about identification variables can be found in Appendix A of [123]. In the usage column the identification algorithms for which the variable is used are indicated: identification for 1-prong $\tau_{\text{had-vis}}$ (ID1), identification for 3-prong $\tau_{\text{had-vis}}$ (ID3), electron veto (EV) and muon veto (MV).
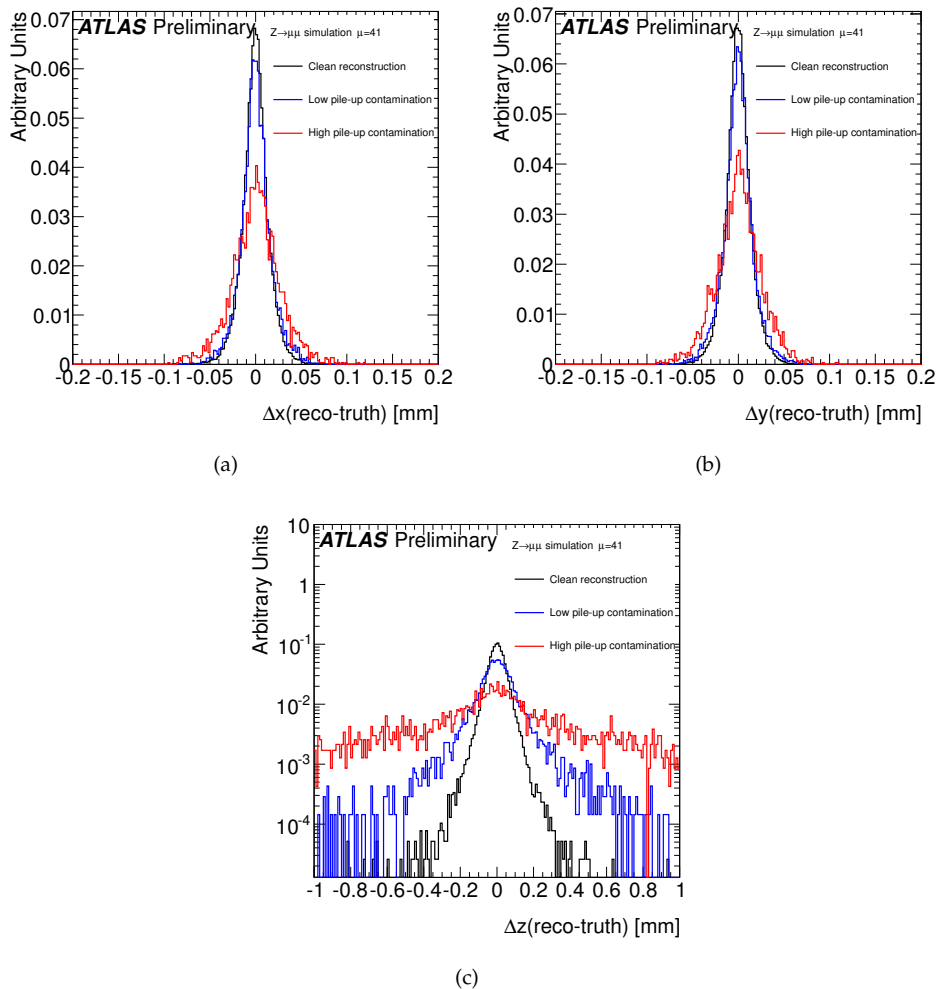
Figure 5.27: Residuals of the reconstructed primary vertex coordinates, (a) x, (b) y, (c) z, for $Z \to \mu^+\mu^-$ simulated interactions overlayed with 40 pile-up interactions. The three categories of clean reconstruction, low pile-up contamination, and high pile-up contamination show progressively degrading resolution [3].
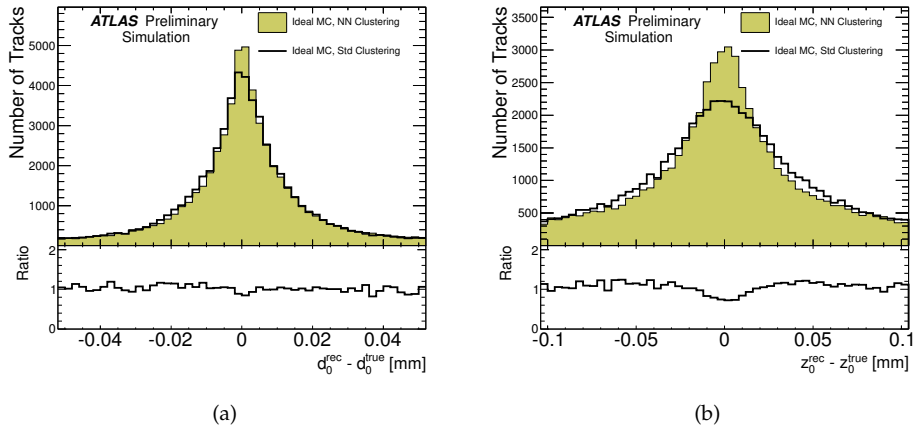
Figure 5.28: (a)transverse and (b) longitudinal impact parameter resolution for tracks with at least 1 B-layer hit and $p_{\mathrm{T}} > 10\,\mathrm{GeV}$ in an ideally reconstructed $t\bar{t}$ Monte Carlo sample. Detector misalignment and error adaption to data have not been applied. The distributions compare tracks reconstructed with the charge sharing and NN clustering algorithms [3].

5.7   Summary

The Pixel detector main purpose it to provide measurements of the crossing-points of charged particles in the detector with high precision. These measurements are crucial in achieving highly efficient and precise tracking and vertexing, that play an important role in the reconstruction and identification of hadronically decaying tau leptons. In this Chapter the main characteristics of the Pixel detector have been reviewed. The characteristics of clusters in the Pixel detector have been described, together with the methods for the determination of the detector crossing-point position from the variables describing the cluster. In particular the method and results for the calibration of the charge sharing algorithm used for the first part of the 2011 data taking have been described. The motivations for a new Pixel detector neural network clustering and its concept have been reviewed, and the results of the cluster performance validation of this new method on 2011 data and simulation have been shown.

On the calorimeter side: in-situ tau energy scale

The reconstruction of hadronically decaying tau leptons plays a crucial role in the $H \rightarrow \tau^+\tau^-$ analysis. One of the most important aspects is the measurement of the energy. As already discussed in Section 2.3.5, this measurement is based on the calibrated energies of clusters associated to the reconstructed $\tau_{\text{had-vis}}$ object. On top of this energy determination an additional calibration is needed to restore the correct $\tau_{\text{had-vis}}$ energy scale (TES). This calibration accounts for effects due to particles lost in front of the calorimeter, out of cone energy losses and imperfections in the LCW calibration of clusters (see Section 2.3.4). In this Chapter, after a brief description of the TES calibration as applied for the 2011 dataset and of the baseline determination of scale uncertainties, a method to cross-check the scale in real data is presented. This method is based on the sensitivity of the $Z \rightarrow \tau^+\tau^-$ visible mass peak to the TES.

Throughout this Chapter the notation $< \pm x$ indicates that the module of some quantity is smaller than x.

6.1 TES calibration summary

In 2011 data and simulation TES corrections were applied in the following order: pile-up correction, application of calibration constants and finally pseudorapidity correction. A detailed description of the 2011 TES calibration can be found in Ref. [171]. For the determination of all corrections and calibration constants a mixed sample of simulated $W \rightarrow \tau\nu$, $Z \rightarrow \tau^+\tau^-$, $Z' \rightarrow \tau^+\tau^-$ ($M = 250, 500, 750, 1000 \, \text{GeV}$) events was used. The selection of $\tau_{\text{had-vis}}$ objects included *loose* identification cuts, an isolation requirement ($\Delta R > 0.5$ from any reconstructed jet with $p_{\text{T}} > 15 \, \text{GeV}$) and a geometric match with a true $\tau_{\text{had-vis}}$ with energy $> 10 \, \text{GeV}$ within $\Delta R < 0.2$.

Pile-up correction

The purpose of the pile-up correction is to equalize the $\tau_{\text{had-vis}}$ response as a function of the pile-up conditions, in particular of the number of primary vertices N_{PV} (the dependence on the number of interactions per bunch-crossing was found to be much weaker). The pile-up correction was performed by the subtraction of an offset of the form

$$E_{\text{pile-up}} = A\left(|\eta_{\text{reco}}|, n_p\right)\left(N_{PV} - < N_{PV} >\right) \tag{6.1}$$

where $< N_{PV} >$ is the average number of interactions per bunch-crossing for the sample used to derive the calibrations ($< N_{PV} >= 5.2$). The A parameters were determined as a function of the reconstructed pseudorapidity η_{reco} and number of prongs n_p. The distribution of the difference between the $\tau_{\text{had-vis}}$ energy at the LCW scale and the true energy was fitted with a gaussian in bins of true energy, η_{reco}, n_p and N_{PV}. A two-step procedure was used, involving a fit without range restrictions and a further fit within $[\mu - 2\sigma, \mu + 2\sigma]$, where μ and σ parameters were obtained from the first fit. The dependence of the mean values of the gaussian as a function of N_{PV} was fitted with a linear function, and the slope defined the A parameters.

Calibration constants

The $\tau_{\text{had-vis}}$ response was defined as

$$R = \frac{E_{\text{LCW}}}{E_{\text{truth}}} \tag{6.2}$$

where E_{truth} is the true $\tau_{\text{had-vis}}$ energy and E_{LCW} the energy at the LCW scale. The response was fitted with a gaussian in bins of E_{truth} and $|\eta_{\text{reco}}|$. The fit was performed with the same two-step procedure described for pile-up corrections. The mean values of the fit were used to construct response functions for each $(|\eta_{\text{reco}}|, n_p)$ bin, as a function of E_{LCW}. These curves were fitted with the empirical function

$$f_{(|\eta_{\text{reco}}|, n_p)}(E_{\text{LCW}}) = a \frac{(b E_{\text{LCW}} + c)^d}{\log{(E_{\text{LCW}+e})}} \tag{6.3}$$

with five parameters a, b, c, d and e. The functions were extrapolated with a constant equal to the function last point value at low and high energy. Figure 6.1 shows the response functions for one-prong and multi-prong tau decays for different pseudorapidity points.

Pseudorapidity correction

Due to clusters reconstructed in not well instrumented calorimeter regions, even if the energy is well calibrated the reconstructed pseudorapidity showed biases. It was therefore corrected to obtain the final pseudorapidity as

$$|\eta_F| = |\eta_{\text{reco}}| - \eta_{\text{bias}} \tag{6.4}$$

where the η_{bias} correction was derived as the average difference between $|\eta_{\text{reco}}|$ and the absolute value of the true $\tau_{\text{had-vis}}$ psudorapidity.

The final energy and transverse momentum were derived using

$$E_F = \frac{E_{\text{LCW}} - E_{\text{pile-up}}}{f_{(|\eta_{\text{reco}}|, n_p)}(E_{\text{LCW}})} \tag{6.5}$$

and the final pseudorapidity given by Eq 6.4. The final energy and transverse momentum were found to agree with the true values within $\sim 1\%$.
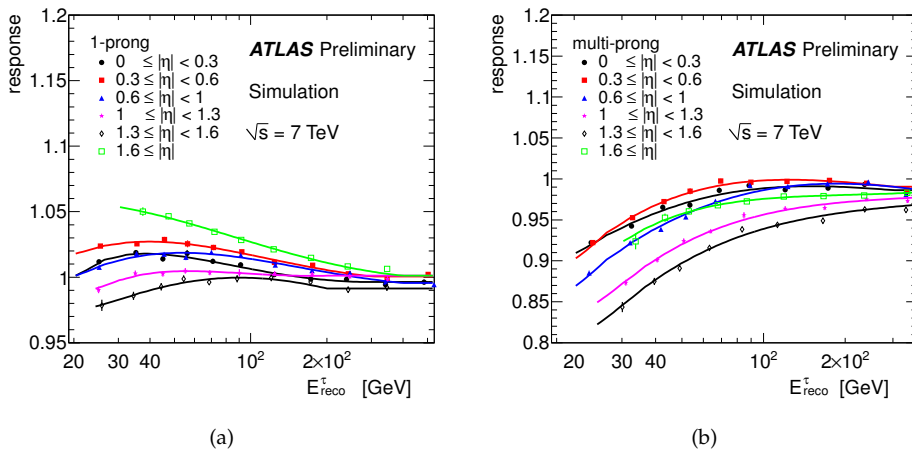
Figure 6.1: Response curves as a function of the reconstructed $\tau_{\text{had-vis}}$ energy at LCW scale for (a) one-prong and (b) multi-prong tau decays for different pseudorapidity points. Uncertainties are statistical only [171].

6.2 TES baseline uncertainty summary

The baseline uncertainty for the TES was obtained for 2011 data and simulation considering contributions from several sources. More details can be found in Ref. [171].

Single particle calorimeter response

The calorimeter response uncertainty at the LCW scale was evaluated from simulated samples of $Z \to \tau^+\tau^-$ and $Z' \to \tau^+\tau^-$ events. Single particle response uncertainties were convoluted with the $\tau_{\text{had-vis}}$ particle composition to determine the contribution of calorimeter response uncertainties to the TES uncertainty. Each particle contributing to clusters associated to the $\tau_{\text{had-vis}}$ object was classified, and to each category different types of uncertainty applied.

- *Low momentum charged hadrons.* The response was determined in-situ using energy depositions of particles associated to isolated tracks (E/p).

- *High momentum charged hadrons.* The pion response was determined from the analysis of data from the combined test-beam (CTB) performed in 2004, where a full slice of the ATLAS detector was exposed to a pion beam. These results were only used for the barrel calorimeter up to $|\eta| < 0.8$ and complement E/p measurements at high momenta.

- *Particles depositing electromagnetic energy.* An example is neutral pions. The electromagnetic energy response was studied using electrons from Z boson decays and minimal ionizing muons in the TileCal.

A pseudo-experiment approach was used for the propagation. Additional uncertainties were applied to account for different hadronic shower models in the simu-

lation in the region not covered by the CTB analysis ($0.8 < |\eta| < 2.5$).

Other uncertainties

Other sources of uncertainty include the underlying event model choice, the description of the material in front of the calorimeters, non-closure of the calibration method and pile-up. These uncertainties were weighted by the energy fraction carried by particles outside the range of the E/p measurement, that partially accounts for these uncertainties.

Figure 6.2 shows a summary of the TES uncertainties in 2011.

6.3   TES uncertainty from $Z \to \tau^+\tau^-$: motivation and concept

The TES baseline uncertainty determination is based on a detailed study of several sources of uncertainty, propagating the impact of these sources to the reconstructed $\tau_{\text{had-vis}}$ energy. This approach can allow, under appropriate assumptions, a correct treatment of uncertainty correlations. On the other hand the TES baseline determination is limited by the fact in-situ measurements, the E/p and CTB analyses, provide information mainly in the low-pt and centermost detector region respectively. It is therefore desirable to pursue a different type of approach, that, although providing information only in an inclusive way, can complement the in-situ information especially in the $0.8 < |\eta| < 2.5$ detector region.

The concept for an in-situ determination of the tau energy scale had been first proposed in Ref. [108, 172] and it has been further developed in Ref. [173]. A revised methodology and first application in real data is presented in the following sections.

The basic idea is to use the dependence of the visible mass peak position for $Z \to \tau^+\tau^-$ events to constrain the TES. In particular $Z \to \tau_\mu \tau_{\text{had}}$ events were used to obtain a clean sample without the need of using $\tau_{\text{had-vis}}$ triggers, that could have introduced biases in the measurement. The visible mass is defined in Eq. 3.7. If a rescaling factor for the $\tau_{\text{had-vis}}$ transverse momentum is allowed, such that

$$p_{\text{T}}^{'\,\tau_{\text{had-vis}}} = (1 + \alpha)\, p_{\text{T}}^{\tau_{\text{had-vis}}} \tag{6.6}$$

at first order the mass takes the form

$$m_{\text{vis}}(\alpha) \sim \left(1 + \frac{1}{2}\alpha\right) \sqrt{2 p_{\text{T}\,l}\, p_{\text{T}\,\tau_{\text{had-vis}}} \left(\cosh \Delta\eta - \cos \Delta\phi\right)} = \left(1 + \frac{1}{2}\alpha\right) m_{\text{vis}}\left(\alpha = 0\right) \tag{6.7}$$

This simple dependence becomes more complicated once selection cuts are applied.

The concept can in principle be used to determine an absolute energy scale. As a first analysis however, it was preferred to first test the concept by determining a possibly non-null α scale-factor to match the simulation and the data. In particular possible differences of α scale-factors in different detector regions were tested. With the available statistics in 2011 it was in fact estimated that results not better than the baseline uncertainty determination could have been obtained. Efforts were therefore concentrated
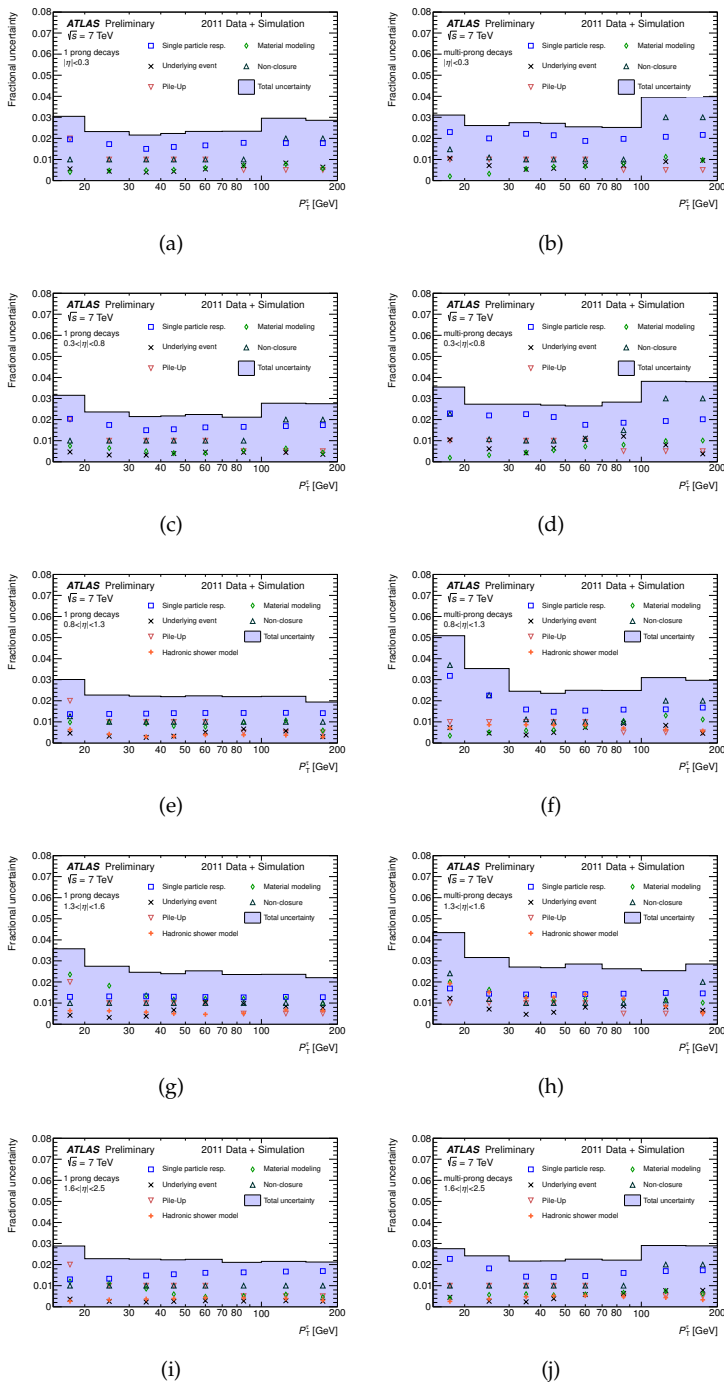
Figure 6.2: TES uncertainty for 1-prong (left) and multi-prong (right) $\tau_{\text{had-vis}}$ in η_τ bins in 2011 data and simulation [171].

in providing a cross-check for the detector regions where little in-situ information was available for the baseline determination.

As an estimator of the peak position the median of the distribution was chosen. Figure 6.3 shows the dependence of the median of the m_{vis} distribution for $Z \rightarrow \tau^+\tau^-$ events from the embedding sample with the selection described in Section 6.5.2.
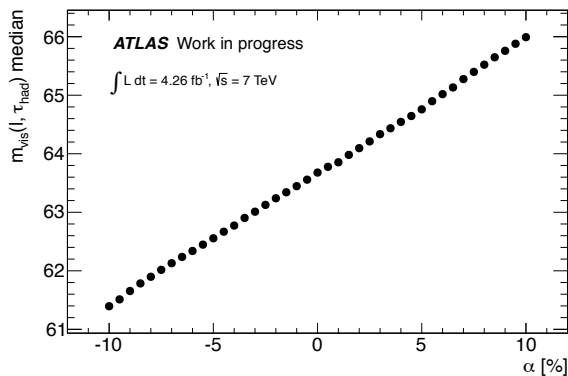
Figure 6.3: Median of the visible mass distribution as a function of the $\tau_{\mathrm{had\text{-}vis}}$ transverse momentum rescaling parameter α for $Z \rightarrow \tau^+\tau^-$ embedding events with the selection described in Section 6.5.

6.4 Data and Monte Carlo Samples

This analysis was performed on the 2011 dataset collected at $\sqrt{s} = 7$ TeV (see Section 2.2.12). The integrated luminosity of the dataset for which all relevant subsystems of the ATLAS detector were fully operational corresponds to 4.26 fb^{-1}. Events were selected by triggering on a muon candidate with $p_{\mathrm{T}} > 18$ GeV. For later data taking periods the muon trigger contained additional muon quality requirements in order to keep a low p_{T} threshold and avoid prescaling.

The signal and background Monte Carlo samples used in this study were generated at $\sqrt{s} = 7$ TeV and passed through a full detector simulation as described in Section 2.2.11 and Chapter 3.

To model $Z \rightarrow \tau^+\tau^-$ events an embedding sample (see Section 3.4.1) was used. The $Z \rightarrow \mu^+\mu^-$ events for the embedding procedure were selected in data by requiring exactly two muons with $p_{\mathrm{T}} > 20$ GeV and requiring that the sum of the momenta of all tracks in a $\Delta R < 0.2$ cone around a muon did not exceed 20% of the muon p_{T}. Additionally the two muons were required to have a common primary vertex and to have invariant mass > 55 GeV. The overlap between the data used to generate the embedding sample and the data used for this analysis is negligible, as a veto on any events that did not contain exactly one lepton was included. The normalisation of the embedding sample was obtained from an Alpgen fully simulated $Z \rightarrow \tau^+\tau^-$ Monte Carlo sample after the full selections detailed below.

6.5 Object and Event Selection

6.5.1 Physics Objects

Muon candidates (see Section 2.3.3) were required to be `Combined`, to have $|\eta| < 2.4$ and $p_\mathrm{T} > 22\,\mathrm{GeV}$, to ensure that they were in the plateau of the trigger efficiency curve. The candidate track was also required to have a minimum distance from the primary vertex in the z direction of less than 10 mm, to suppress events in which the muons did not originate from the hard scattering event, and also to satisfy track quality criteria. Correction factors were applied to the simulation prediction to account for measured discrepancies between simulation and data in the muon p_T resolution [174] and the muon identification efficiency [175]. Calorimeter isolation was imposed for muon candidates by requiring the energy deposited in the EMCal and HadCal which was not associated to the muon in a cone of $\Delta R < 0.2$ was less than 4% of the muon p_T. Additionally track isolation was imposed by requiring that the number of tracks not associated to the muon in a cone of $\Delta R < 0.4$ was 0.

Hadronically decaying tau lepton candidates were required to have $p_\mathrm{T} > 20\,\mathrm{GeV}$ and to be in the η region considered for the analysis. Moreover $\tau_\mathrm{had\text{-}vis}$ candidates were required to have one or three associated tracks, to have unitary charge and to be satisfy *medium* BDT discriminant based identification (see Section 2.3.5). To reduce contamination from electrons and muons, tau candidates were required to pass a loose BDT-based electron veto and a muon veto. To account for problems in the optical read-out electronics in the LAr calorimeter, which caused a portion of the EMCal to be unusable for part of the dataset, $\tau_\mathrm{had\text{-}vis}$ candidates with a leading track p_T within $-0.1 < \eta < 1.55$ and $-0.9 < \phi < -0.5$ were rejected for the relevant portion of data and simulated samples.

Electron candidates were required to have $p_\mathrm{T} > 15\,\mathrm{GeV}$ and to be in the fiducial volume of the barrel or endcaps ($|\eta| < 1.37$ or $1.52 < |\eta| < 2.47$). They were also required to pass *tight* identification requirements.

Jet candidates were required to have $p_\mathrm{T} > 20\,\mathrm{GeV}$ and $|\eta| < 5$. Jets were only used for event cleaning and therefore were not required to pass rigourous selection criteria.

The measurement of the missing transverse momentum was used only for selection cuts. The `MET_RefFinal` reconstruction was used (see Section 2.3.7 and [176]).

As multiple electron, muon, or $\tau_\mathrm{had\text{-}vis}$ candidates may be reconstructed from the same localized response in the ATLAS detector, an overlap removal procedure was performed to ensure a unique hypothesis for each object. Since muons and electrons can be selected with a higher purity than $\tau_\mathrm{had\text{-}vis}$, any $\tau_\mathrm{had\text{-}vis}$ candidate was not considered if it laid within $\Delta R < 0.4$ of any lepton. Electron candidates were removed if they overlapped with muon candidates within $\Delta R < 0.2$. Electron and muon candidates were removed if they laid within $\Delta R < 0.2$ from a harder reconstructed lepton of the same kind. For this procedure some of the requirements on the selected objects were dropped. Muons also included objects reconstructed from ID tracks matched to MS track segments, while $\tau_\mathrm{had\text{-}vis}$ were not required to pass BDT identification.

6.5.2   Event Selection

Collision events that passed the trigger conditions discussed in Section 6.4 were further required to have a reconstructed primary vertex with at least four associated tracks. Quality criteria were applied to reject events which had jet or $\tau_{\text{had-vis}}$ candidates that originated from non-collision backgrounds, cosmic ray background or known sources of calorimeter noise [177].

The presence of one isolated muon and one $\tau_{\text{had-vis}}$ was required. When more than one $\tau_{\text{had-vis}}$ passed the selection and overlap removal criteria, the leading p_{T} candidate was chosen as the $\tau_{\text{had-vis}}$ characterising the event signature.

Events with additional loosely selected leptons were vetoed as well as events where the selected $\tau_{\text{had-vis}}$ did not pass a *loose* BDT-based electron veto and a muon veto (see Section 2.3.5 and Ref. [178]. Additionally, $\tau_{\text{had-vis}}$ candidates matching muons reconstructed with an ID track plus a segment track in the MS in a $\Delta R < 0.2$ cone were rejected.

To reject background events due to $W +$ jets the following cuts were applied.

$$\cos \Delta\phi(\tau_{\text{had-vis}}, E_{\text{T}}^{\text{miss}}) + \cos \Delta\phi(l, E_{\text{T}}^{\text{miss}}) > -0.15 \tag{6.8}$$

$$m_T = \sqrt{2p_{\text{T}}^l \cdot E_{\text{T}}^{\text{miss}}(1 - \cos \Delta\phi(l, E_{\text{T}}^{\text{miss}}))} < 50\,\text{GeV} \tag{6.9}$$

More detail on these variables can be found in Section 4.2.2 and 3.2 respectively. Finally to further reduce the multi-jet background the selected muon and hadronic tau were required to have opposite charge (OS).

6.6   Background estimation

Backgrounds in the selected sample were estimated using different techniques. The backgrounds due to the $Z \rightarrow \mu^+\mu^-$ and $t\bar{t}$ pair production processes were fully estimated from the Monte Carlo simulated samples, a mixed technique was used for the $W \rightarrow \mu\nu$ background and an almost fully data driven method was used for the multi-jet background.

W + jets background estimate

The $W +$jets background was estimated from the Monte Carlo simulated samples. However, since $W +$ jets events typically enter the selected sample due to an additional jet faking the $\tau_{\text{had-vis}}$ signature and the rate of jets faking $\tau_{\text{had-vis}}$ was known to be mismodelled in simulation, the normalisation of the Monte Carlo prediction was corrected with factors obtained from data.

A region dominated by W decays was obtained by reversing the $W +$jets suppression cuts described in 6.5.2. The factors were obtained after the charge correlation selection by

subtracting the small non-W contribution (estimated from Monte Carlo) from the data events and then dividing by the number of events found in the W Monte Carlo:

$$k_W = \frac{n_{\text{data}}\left(W_{\text{control}}\right) - n_{\text{rest MC}}\left(W_{\text{control}}\right)}{n_{W\ MC}\left(W_{\text{control}}\right)}.$$
(6.10)

The normalisation factors, evaluated from the W+jets control region separately for each $\tau_{\text{had-vis}}$ η region considered in the analysis, are shown in Table 6.1.

Region	k_W
$\lvert\eta\rvert < 2.5$	0.587 ± 0.008
$\lvert\eta\rvert < 0.8$	0.615 ± 0.013
$0.8 < \lvert\eta\rvert < 1.3$	0.601 ± 0.020
$1.3 < \lvert\eta\rvert < 1.6$	0.557 ± 0.027
$1.6 < \lvert\eta\rvert < 2.5$	0.545 ± 0.015
$0.8 < \lvert\eta\rvert < 2.5$	0.565 ± 0.011

Table 6.1: Scale factors k_W of the $W +$ jets normalisation. Uncertainties are purely statistical.

Multi-jet background estimate

The background due to multi-jet events was estimated by a data driven method. A multi-jet enriched control region was constructed by requiring the two candidate τ decay products, one hadronic and the other leptonic, to have the same sign (SS). The ratios of events where the candidates have opposite sign charge to those where they have the same sign $R_{OS/SS}$ was then measured in an additional separate pair of control regions where the lepton isolation requirement was inverted. Electroweak backgrounds in all three control regions were subtracted using Monte Carlo simulation. The visible mass distribution shape was taken from the SS, lepton isolated region and scaled with the normalisation factor $R_{OS/SS}$. This method assumes that the shape of the distribution in the SS region is compatible with the shape in the OS region and that the lepton isolation is uncorrelated with the charge product of the tau decay product candidates.

This estimation was performed in each η region separately, and Table 6.2 shows the normalisation factors used.

6.7 Fitting Method

Since the visible mass distribution can not be trivially described by an analytic function, fits were made to templates. Templates were produced including both signal and background events using the samples described in Section 6.4 and the multi-jet background prediction as described in Section 6.6. The full analysis described in Section 6.5.2, with the exception of the multi-jet background estimation, was repeated scaling the $\tau_{\text{had-vis}}$ p_{T} according to Eq. 6.6, with α varied between -10% and 10% in 0.5% steps, leading to 41 different templates.

Region	$R_{OS/SS}$
$|\eta| < 2.5$	1.102 ± 0.024
$|\eta| < 0.8$	1.154 ± 0.041
$0.8 < |\eta| < 1.3$	1.093 ± 0.057
$1.3 < |\eta| < 1.6$	1.056 ± 0.074
$1.6 < |\eta| < 2.5$	1.062 ± 0.041
$0.8 < |\eta| < 2.5$	1.070 ± 0.030

Table 6.2: $R_{OS/SS}$ ratios, computed as described in the text, and their statistical uncertainties for the different $\tau_{\text{had-vis}}$ η regions.

The $\tau_{\text{had-vis}}$ p_T was also scaled for the background contributions, as the energy scale of a fake $\tau_{\text{had-vis}}$ which passes all selection criteria was expected to be strongly correlated to energy scale of genuine $\tau_{\text{had-vis}}$. The $\tau_{\text{had-vis}}$ p_T scaling was not applied to the multi-jet contribution, since it was taken directly from data. Figures 6.4, 6.5 and 6.6 show a selection of the templates, with data superimposed as well, for the chosen $\tau_{\text{had-vis}}$ η regions that were considered. Figure 6.4(d) highlights a normalisation issue with the simulation, which was related to differences in the modelling of $\tau_{\text{had-vis}}$ identification efficiency in the simulation for the $\tau_{\text{had-vis}}$ identification employed for this analysis.

In order to assess which template best fitted the observed data, a test statistic intended to quantify the distance between the peaks of the two distributions was evaluated. The template that minimised the test statistic was chosen as best. The performance of the following test statistics was investigated:

- The Kolmogorov-Smirnov distance

- The χ^2 distance between the two distributions

- The difference between the medians of the distributions

- The difference in the mean values from a gaussian fit to the distributions.

Of these the median of the visible mass distribution was found to provide results that are most stable with respect to statistical fluctuations. Table 6.3 shows the value of α obtained for the chosen tau η regions and the observed difference in α between the $|\eta| < 0.8$ region and other regions, which are the quantities of interest for this analysis. Here α can be understood as the percentage shift in the TES applied to the simulation such that the simulation matches the data.

The uncertainties due to limited statistics of the data sample was assessed by generating 1000 toy experiments for each $\tau_{\text{had-vis}}$ η region considered. The visible mass distribution was generated by fluctuating each bin separately according to a Poisson distribution with the bin content as mean. The fitting procedure was repeated for each of these toy experiments, leading to distributions of preferred templates as shown in Figure 6.7. Table 6.4 shows the statistical uncertainties, computed from the RMS of the distributions of preferred templates for the chosen $\tau_{\text{had-vis}}$ η regions.

(a) $|\eta| < 2.5$, $\alpha = -10\%$

(b) $|\eta| < 0.8$, $\alpha = -10\%$

(c) $|\eta| < 2.5$, $\alpha = 0.5\%$

(d) $|\eta| < 0.8$, $\alpha = -1.5\%$

(e) $|\eta| < 2.5$, $\alpha = 10\%$

(f) $|\eta| < 0.8$, $\alpha = 10\%$
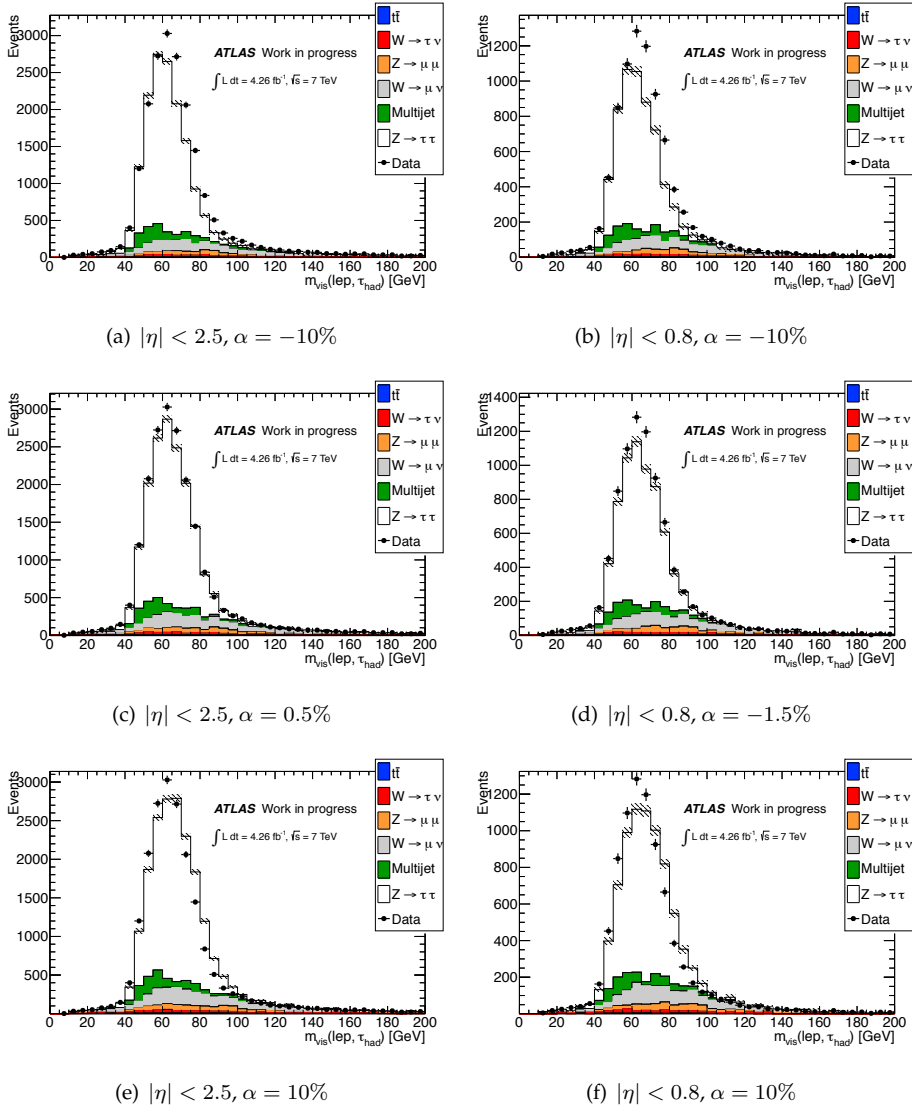
Figure 6.4: Selection of templates, obtained as described in Section 6.7 for the inclusive sample (left column) and central barrel $|\eta| < 0.8$ region (right column) for values of α of -10% (top row), +10% (bottom row) and the values chosen as best fitting the data (middle row).

(a) $0.8 < |\eta| < 1.3$, $\alpha = -10\%$

(b) $1.3 < |\eta| < 1.6$, $\alpha = -10\%$

(c) $0.8 < |\eta| < 1.3$, $\alpha = 1.0\%$

(d) $1.3 < |\eta| < 1.6$, $\alpha = 3.0\%$

(e) $0.8 < |\eta| < 1.3$, $\alpha = 10\%$

(f) $1.3 < |\eta| < 1.6$, $\alpha = 10\%$
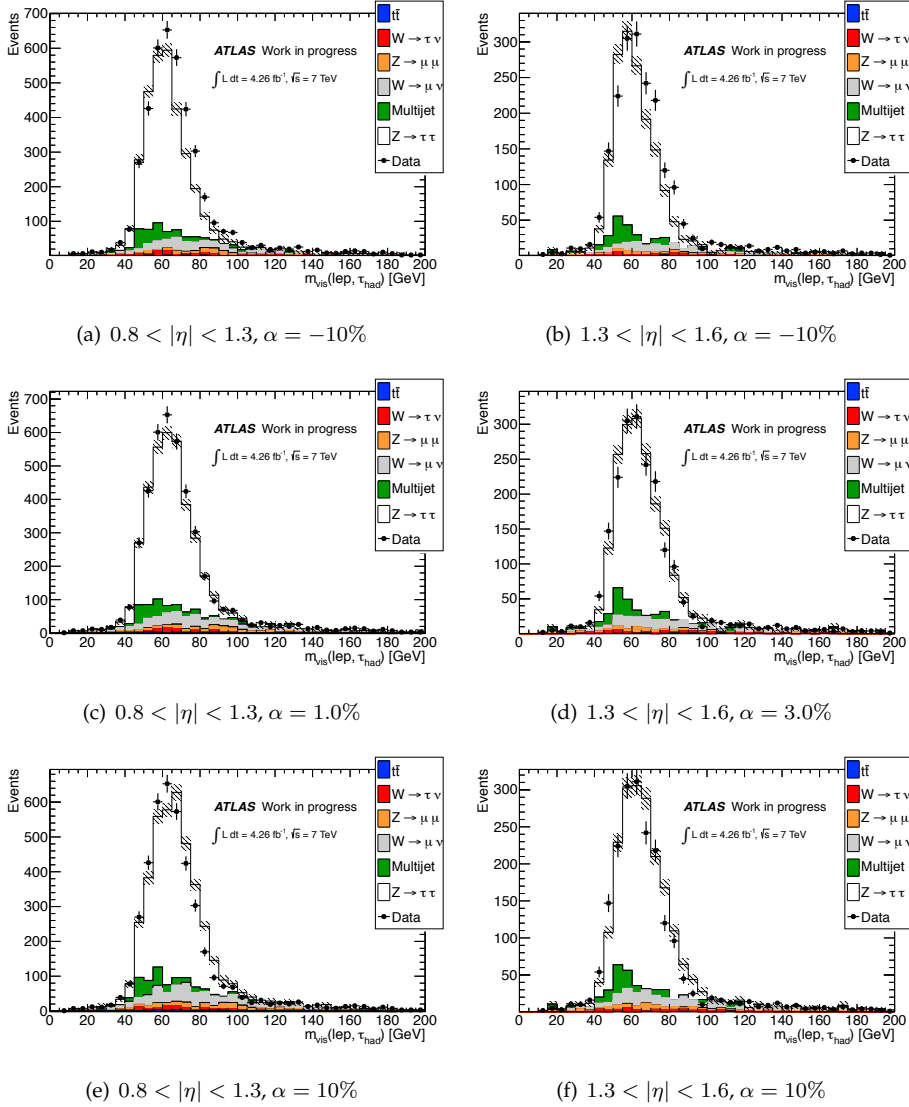
Figure 6.5: Selection of templates, obtained as described in Section 6.7 for the forward barrel $0.8 < |\eta| < 1.3$ (left column) and overlap region $1.3 < |\eta| < 1.6$ (right column) for values of α of -10% (top row), +10% (bottom row) and the values chosen as best fitting the data (middle row).

(a) $1.6 < |\eta| < 2.5$, $\alpha = -10\%$

(b) $0.8 < |\eta| < 2.5$, $\alpha = -10\%$

(c) $1.6 < |\eta| < 2.5$, $\alpha = 0.5\%$

(d) $0.8 < |\eta| < 2.5$, $\alpha = 1.5\%$

(e) $1.6 < |\eta| < 2.5$, $\alpha = 10\%$

(f) $0.8 < |\eta| < 2.5$, $\alpha = 10\%$
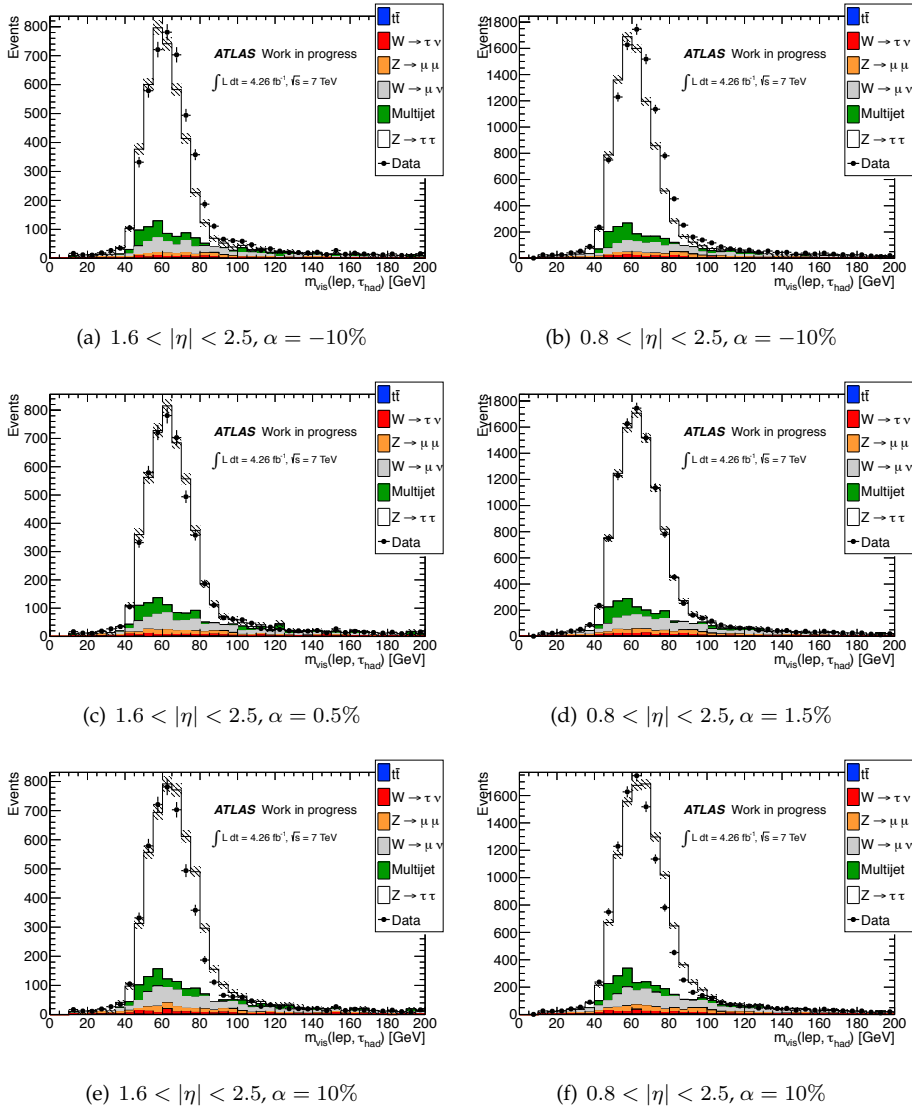
Figure 6.6: Selection of templates, obtained as described in Section 6.7 for the end-cap region $1.6 < |\eta| < 2.5$ (left column) and integrated forward region $0.8 < |\eta| < 2.5$ (right column) for values of α of -10% (top row), +10% (bottom row) and the values chosen as best fitting the data (middle row).

Region	Preferred α value	Shift with respect to the $|\eta| < 0.8$ region
$|\eta| < 2.5$	0.5%	-
$|\eta| < 0.8$	-1.5%	-
$0.8 < |\eta| < 1.3$	1.0%	2.5%
$1.3 < |\eta| < 1.6$	3.0%	4.5%
$1.6 < |\eta| < 2.5$	0.5%	2.0%
$0.8 < |\eta| < 2.5$	1.5%	3.0%

Table 6.3: Preferred α values for the data visible mass distributions for the embedding signal samples in $\tau_{\text{had-vis}}$ η regions and deviations of the α values preferred in the forward region with respect to the central barrel.
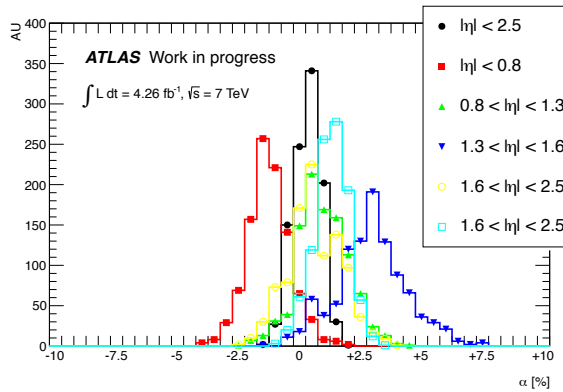
Figure 6.7: Distributions of the preferred α values for toy experiments generated from the data visible mass distribution as described in Section 6.7.

6.8 Systematic Uncertainties

Several sources of systematic uncertainty that could affect the measurement were assessed. In order to quantify the impact of each source of uncertainty the templates derived from the nominal distribution were fitted to a distribution where each sample was systematically varied in a consistent manner. The value of α which provided the best fit provided then a measure of the shift between the nominal templates and those that would have been derived from a systematically varied sample. Each source described in this section was considered separately.

6.8.1 Model samples statistics

The uncertainty due to the limited statistics in the model used to make the templates was assessed using the same procedure described in Section 6.7 for data, but considering fluctuations of the template which had no scaling of the $\tau_{\text{had-vis}}$ p_{T}. As each event in the model was weighted due to corrections for known discrepancies between simulation and data, each bin was fluctuated separately according to a gaussian distribution with

	Data statistical uncertainty
$|\eta| < 2.5$	0.6%
$|\eta| < 0.8$	0.9%
$0.8 < |\eta| < 1.3$	1.0%
$1.3 < |\eta| < 1.6$	1.4%
$1.6 < |\eta| < 2.5$	1.1%
$0.8 < |\eta| < 2.5$	0.7%

Table 6.4: Statistical uncertainties on the preferred α values from toy experiments generated from the data visible mass distribution as described in Section 6.7.
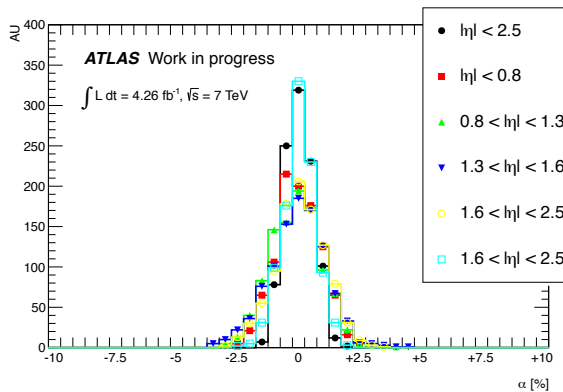
Figure 6.8: Distributions of the preferred α values for toy experiments generated from the model visible mass distribution as described in Section 6.8.1.

as mean the bin content and as variance the sum of the squares of the event weights in the bin. This way the actual bin statistical uncertainty could be used. The distributions of the preferred templates for 1000 generated toy experiments are shown in Figure 6.8 and the corresponding uncertainties are shown in Table 6.5.

6.8.2 Systematics related to the embedding procedure

Signal samples produced with the embedding procedure described in Section 3.4.1 are subject to systematic effects due to the procedure itself. In order to evaluate the effects of the muon isolation requirement used to select $Z \to \mu^+\mu^-$ events in data, embedding samples were generated with varied muon isolation requirements:

Tight isolation The energy deposited in the EMCal and HadCal not associated to the muon in a cone of $\Delta R = 0.2$ was required to be less than 4% of the muon p_{T}. Additionally the sum of the momenta of the tracks in a $\Delta R = 0.4$ from the muon was required to be less than 6% of the muon p_{T}.

No isolation No isolation requirements applied.

	Model statistical uncertainties
$|\eta| < 2.5$	0.6%
$|\eta| < 0.8$	1.0 %
$0.8 < |\eta| < 1.3$	1.0%
$1.3 < |\eta| < 1.6$	1.2%
$1.6 < |\eta| < 2.5$	1.0%
$0.8 < |\eta| < 2.5$	0.7%

Table 6.5: Systematic uncertainties on the preferred α values from toy experiments generated from the model visible mass distribution as described in Section 6.8.1.

The analysis isolation cuts described in Section 6.5.2 were left unchanged.

Any systematic effect due to the procedure of calorimeter cell subtraction during the replacement of muons with tau leptons in the embedding procedure was evaluated conservatively by scaling up and down the energy of each cell by 30% before subtraction as was performed in Ref. [135]. Table 6.6 shows the preferred α values for models with variations on the embedding procedure when compared to the nominal model.

	Tight isolation	No isolation	Cell energy up	Cell energy down
$|\eta| < 2.5$	0.5%	0.5%	-1.5%	2.0%
$|\eta| < 0.8$	$< \pm 0.5\%$	$< \pm 0.5\%$	-1.5%	2.5%
$0.8 < |\eta| < 1.3$	$< \pm 0.5\%$	0.5%	-2.0%	1.5%
$1.3 < |\eta| < 1.6$	2.5%	2.5 %	-1.0%	2.0%
$1.6 < |\eta| < 2.5$	$< \pm 0.5\%$	$< \pm 0.5\%$	-1.0%	1.0%
$0.8 < |\eta| < 2.5$	0.5%	1.0%	-1.5%	1.5%

Table 6.6: Preferred α values for the variations in the embedding procedure described in Section 6.8.2 when fitted with nominal templates.

6.8.3   Muon systematics

In order to account for the uncertainties in the description of the muon momentum resolution and reconstruction and identification efficiency in the simulation [175, 179], visible mass distributions were produced in which these quantities had been fluctuated up and down separately. Table 6.7 shows the observed shifts in the preferred value of α for the modified models.

6.8.4 $\tau_{\mathrm{had\text{-}vis}}$ identification efficiency

The effect of the uncertainties in the $\tau_{\mathrm{had\text{-}vis}}$ identification efficiencies was evaluated similarly to the muon correction factors described in Section 6.8.3. The identification efficiency was fluctuated up and down by 4% for tau $p_{\mathrm{T}} > 22$ GeV and 8% for tau p_{T} in [20,

	MS resolution up	MS resolution down	ID resolution up	ID resolution down	Efficiency up	Efficiency down
$|\eta| < 2.5$	$< \pm 0.5\%$	$< \pm 0.5\%$	$< \pm 0.5\%$	$< \pm 0.5\%$	$< \pm 0.5\%$	$< \pm 0.5\%$
$|\eta| < 0.8$	$< \pm 0.5\%$	$< \pm 0.5\%$	$< \pm 0.5\%$	$< \pm 0.5\%$	$< \pm 0.5\%$	$< \pm 0.5\%$
$0.8 < |\eta| < 1.3$	$< \pm 0.5\%$	$< \pm 0.5\%$	$< \pm 0.5\%$	$< \pm 0.5\%$	$< \pm 0.5\%$	$< \pm 0.5\%$
$1.3 < |\eta| < 1.6$	$< \pm 0.5\%$	$< \pm 0.5\%$	0.5%	$< \pm 0.5\%$	$< \pm 0.5\%$	$< \pm 0.5\%$
$1.6 < |\eta| < 2.5$	$< \pm 0.5\%$	$< \pm 0.5\%$	0.5%	$< \pm 0.5\%$	$< \pm 0.5\%$	$< \pm 0.5\%$
$0.8 < |\eta| < 2.5$	$- 0.5\%$	$- 0.5\%$	$- 0.5\%$	$- 0.5\%$	$< \pm 0.5\%$	$< \pm 0.5\%$

Table 6.7: Preferred α values for the model with modified resolution and identification efficiencies of muons when fitted with nominal templates.

22] GeV and fitted to templates made from a model where the signal was from nominal Monte Carlo. The uncertainty to be applied was derived from preliminary results on tau identification efficiencies from $Z \rightarrow \tau^+\tau^-$[180]. Table 6.8 shows the observed shifts in the preferred value of α for the models varied within $\tau_{\text{had-vis}}$ identification efficiency uncertainties.

	Efficiency up	Efficiency down
$|\eta| < 2.5$	- 0.5%	0.5%
$|\eta| < 0.8$	- 0.5%	0.5%
$0.8 < |\eta| < 1.3$	$< \pm 0.5\%$	0.5%
$1.3 < |\eta| < 1.6$	$< \pm 0.5\%$	0.5%
$1.6 < |\eta| < 2.5$	$< \pm 0.5\%$	0.5%
$0.8 < |\eta| < 2.5$	$< \pm 0.5\%$	0.5%

Table 6.8: Preferred α values for the model with modified identification efficiency of taus when fitted with nominal templates.

6.8.5 Pile-up condition systematics

The stability of the preferred α values with the pile-up conditions was studied in two bins of average number of interactions per event, μ, and is presented in Table 6.9. As the embedding samples were generated from data there was no need to account for differences in the pile-up distribution. This systematic derivation was performed varying only pure simulation samples and fitting to templates constructed from pure simulated samples. Due to statistical limitations, results were given for two $\tau_{\text{had-vis}}$ η regions only.

To evaluate the stability with respect to events where the pile-up is dominated by out-of-time pile-up and events in which the pile-up is dominated by in-time pile-up two subsets of the signal region were formed in both cases.

The difference in preferred α values between pile-up bins and between pile-up categorisations were summed in quadrature and applied as a systematic uncertainty. The same value determined for the region $0.8 < |\eta| < 2.5$ was applied to each forward η region.

	$\mu < 7$	$7 < \mu < 20$
$|\eta| < 2.5$	-0.5%	0.5%
$0.8 < |\eta| < 2.5$	$< \pm 0.5\%$	0.5%

Table 6.9: Preferred α values for subsets of the model in specified bins of pile-up when fitted with nominal templates.

	Out-of-time pileup	In-time pile-up
$|\eta| < 2.5$	1.0%	-1.0%
$0.8 < |\eta| < 2.5$	1.5%	-1.0%

Table 6.10: Preferred α values for different categorisations of pile-up when fitted with nominal templates.

6.8.6 Further cross checks

In addition to the study of systematic uncertainties additional cross checks were performed to ensure the methods used in the analysis were robust. In contrast to the systematic variations described in Sections 6.8.2-6.8.5, where the size of the variations corresponded to the actual confidence on the description of the source of the effect being tested, these checks were performed by performing an exaggerated variation and examining whether it greatly changed the result of the analysis.

$\tau_{\text{had-vis}}$ electron veto

The effect of the $\tau_{\text{had-vis}}$ electron veto was evaluated by generating a model in which the *loose* BDT-based veto used for the analysis was removed. The effect is shown in Table 6.11. Since the effect was very small, it was assumed that the uncertainty on the preferred α values due to the uncertainty in the electron veto efficiency was negligible.

	Electron veto off
$|\eta| < 2.5$	- 0.5%
$|\eta| < 0.8$	- 1.0%
$0.8 < |\eta| < 1.3$	$< \pm 0.5\%$
$1.3 < |\eta| < 1.6$	$< \pm 0.5\%$
$1.6 < |\eta| < 2.5$	$< \pm 0.5\%$
$0.8 < |\eta| < 2.5$	- 0.5%

Table 6.11: Preferred α values for the model with no $\tau_{\text{had-vis}}$ electron veto applied when fitted with nominal templates.

Binning effects

The effect of varying the binning of both the data and template histogram was investigated. It was found that the results were stable around the bin sizes used for the analysis. The effect of the binning was therefore considered negligible.

Approximations in the background estimation

The estimation of the multi-jet background and the determination of the W + jets background, described in Section 6.6, were not repeated for every produced template. Instead the values obtained for the analysis without any $\tau_{\text{had-vis}}$ p_{T} scaling were used. The effect

of this approximation was evaluated by repeating the full background estimation procedure for α values of -10% and +10%. The background estimates for these alpha values were used to construct new sets of templates, which were fitted to the data. The observed deviations in the absolute values of the preferred signal α factors for the modified model are shown in Table 6.12.

	Up-variation of the scale	Down-variation of the scale
$\|\eta\| < 2.5$	$< \pm 0.5\%$	$< \pm 0.5\%$
$\|\eta\| < 0.8$	-0.5%	$< \pm 0.5\%$
$0.8 < \|\eta\| < 1.3$	-0.5%	$< \pm 0.5\%$
$1.3 < \|\eta\| < 1.6$	$< \pm 0.5\%$	$< \pm 0.5\%$
$1.6 < \|\eta\| < 2.5$	0.5%	$< \pm 0.5\%$
$0.8 < \|\eta\| < 2.5$	$< \pm 0.5\%$	$< \pm 0.5\%$

Table 6.12: Preferred α values for the model with modified background estimation, obtained as described in Section 6.12, with respect to the nominal model

Since the observed deviations are small and much less than the change in α applied to the backgrounds the effect was considered negligible.

Tau Identification efficiency further checks

A limited knowledge of the $\tau_{\text{had-vis}}$ identification efficiencies dependence on $\tau_{\text{had-vis}}$ p_T could lead to additional uncertainty in the visible mass distribution. A cross check of the size of possible effects was performed by introducing scale factors varying linearly with $\tau_{\text{had-vis}}$ p_T. The scale factors were constructed to be $\pm 10\%$ for $\tau_{\text{had-vis}}$ p_T of 20 GeV and $\mp 10\%$ value for $\tau_{\text{had-vis}}$ p_T of ≥ 80 GeV. The effect of the application of such scale factors is of order less than 1.5%. Since there was no evidence of such a large dependence of the $\tau_{\text{had-vis}}$ identification efficiency on $\tau_{\text{had-vis}}$ p_T the effect was neglected.

Normalization of the multi-jet background

The normalization of the multi-jet background could suffer from uncertainties in the assumption that the charge correlation is independent of the isolation. In order to estimate the impact of such an effect in the α rescaling factors, an additional control region where the $\tau_{\text{had-vis}}$ identification requirement was reversed and no isolation was applied was built. The $R_{OS/SS}$ ratio was considered in bins of the isolation variables used in the analysis. The maximum deviation from the mean was taken as a conservative estimate of the size of possible deviations from the assumption on the $R_{OS/SS}$ ratio. Models built with variations of the multi-jet background normalisation derived accordingly were compared to the default model, and the effect on α was found to be $< \pm 0.5\%$ in all regions but the regions for tau $0.8 < |\eta| < 1.3$, for which the effect was 0.5%. The effect was therefore neglected.

Pseudorapity distributions for the embedding sample

The embedding sample has pseudorapidity distributions of muons and $\tau_{\text{had-vis}}$ that are affected by the reconstruction efficiencies of muons in the starting $Z \to \mu^+\mu^-$ data sample. A cross-check was made reweighting the embedding sample events with weights derived comparing the pseudorapidity distributions of the signal Monte Carlo and embedding samples. The weights were derived separately for muons and $\tau_{\text{had-vis}}$ but were applied simultaneously in the reweighting. The effect of the reweighting was always found to be within 1%. Given large weights with large statistical uncertainties were applied, the effect was considered negligible.

Normalisation of the embedding sample

The embedding sample was normalised to $Z \to \tau^+\tau^-$ Monte Carlo as described in Section 6.4, that is, after the full selection requirements were applied. It was checked that normalising before the $W \to \mu\nu$ suppressing cuts described in Section 6.5.2 brings no changes to the obtained results.

6.9 Results

The aim of the analysis was to test the validity of the extrapolation of the $\tau_{\text{had-vis}}$ energy scale from the region $|\eta| < 0.8$ covered by the CTB to the region $0.8 < \eta_\tau < 2.47$. For this purpose, the difference in the shifts in the preferred α values for $\eta_\tau < 0.8$ and $0.8 < \eta_\tau < 2.47$ were considered. The observed difference is $(3.0 \pm 2.6)\%$. The shifts for the individual $|\eta|$ regions are $2.5\% \pm 2.5\%$ for the region with $0.8 < |\eta_\tau| < 1.3$, $4.5\% \pm 4.4\%$ for the region with $1.3 < |\eta_\tau| < 1.6$ and $2.0\% \pm 2.7\%$ for the region with $1.6 < |\eta_\tau| < 2.47$. Uncertainties were computed as the quadrature sum of the statistical and systematic uncertainties detailed in the previous sections and summarised in Table 6.13, as all sources of uncertainty are uncorrelated. The main sources of uncertainty are the uncertainties due to the embedding procedure and the data and model statistical uncertainties.

As no significant change in the preferred alpha values as a function of η was observed (see Table 6.3), the extrapolation of the TES described was considered valid.

6.10 Summary

In this Chapter the strategy used in 2011 for the energy calibration of $\tau_{\text{had-vis}}$ objects has been described. The procedure used in 2012 was analogous. The baseline uncertainty on the TES, obtained propagating single particle uncertainties, has been briefly described. An in-situ method complementing the baseline uncertainty determination has been presented. The results obtained from the analysis of 2011 $\sqrt{s} = 7$ TeV data allowed to confirm the validity of the TES extrapolation from the $|\eta| < 0.8$ to the $0.8 < |\eta| < 2.5$ calorimeter region within 3%. This result demonstrated moreover the validity of the analysis concept itself, which was in fact re-iterated and further complemented on the 2012 dataset [125].

Source of uncertainty	$0.8 < |\eta| < 1.3$	$1.3 < |\eta| < 1.6$	$1.6 < |\eta| < 2.5$	$0.8 < |\eta| < 2.5$
Data statistical uncertainty	1.3%	1.7%	1.4%	1.1%
Model statistical uncertainty	1.4%	1.6%	1.4%	1.2%
Embedding systematics	1.2%	3.6%	1.6%	1.5%
Muon systematics	$< \pm 0.5\%$	0.5%	0.5%	1.0%
Tau identification systematics	0.5%	0.5%	0.5%	0.5%
Pile-up conditions	0.7%	0.7%	0.7%	0.7%
Total	2.5%	4.4%	2.7%	2.6%

Table 6.13: Summary of the uncertainties affecting the extrapolation of the tau energy scale from the central barrel ($|\eta| < 0.8$) to the forward region ($0.8 < |\eta| < 2.47$).

H → τ⁺τ⁻: a cut-based analysis

Within the ATLAS collaboration a big effort has been made in order to set up an analysis that could answer the question whether the Higgs boson, observed at $m_H = 125\,\text{GeV}$ in the $H \to \gamma\gamma$, $H \to ZZ^* \to 4l$ and $H \to W^+W^-$ channels, decays to fermions as well, and in particular to τ leptons. First publications were based on sequential cut analyses (cut-based analyses) [135]. The latest official result was obtained on 4.6 pb^{-1} of data collected at $\sqrt{s} = 7$ TeV and 13.0 fb^{-1} at $\sqrt{s} = 8$ TeV, and allowed to set an upper limit to the Higgs boson cross-section times the $H \to \tau^+\tau^-$ branching ratio at 1.9 (1.2 expected) times the SM expectation, with an observed deviation from the background-only hypothesis corresponding to a local significance of 1.1 (1.7) standard deviations [181]. To increase the sensitivity in this channel a multivariate approach, exploiting the correlations between discriminating variables to extract the signal, has been recently developed within the collaboration [4]. Throughout the development of the multivariate analysis a complementary cut-based approach has always been maintained and deemed necessary. Initially, when confidence on the robustness of the MVA analysis still needed to be built, cut-based analyses was considered important supporting analyses. Later new arguments have opened up new perspectives to the role of a cut-based result. First of all in view of the need of extracting the information on the mass of the decaying state, a cut-based analysis offers more straightforward strategies. Secondly the impact of theory uncertainties is more easily defined when using a cut-based approach, where the slicing of the phase-space is more straightforward to understand. Finally the resuming of LHC operations in 2015 poses important concerns on the possibility of quickly adapting an MVA analysis to new challenging data-taking conditions.

The result presented here was developed in parallel with the MVA analysis, and shared several points in common with it. The analysis is presented blinded, that is without looking at data in the signal region, as discussion on cut-based results is still ongoing. The analysis is based on the general strategy outlined in Chapter 3, and uses the MMC reconstructed mass as discriminating variable.

7.1 Data and Monte Carlo samples

For this analysis the dataset collected at $\sqrt{s} = 8$ TeV during 2012 (see Section 2.2.12) was used. The dataset collected with stable beam conditions, for which all relevant sub-

detectors were fully operational and the quality of data was good for analysis corresponds to an integrated luminosity of 20.3 ± 0.7 fb^{-1} [132]. Events collected using single lepton (e/μ) and combined lepton+$\tau_{\text{had-vis}}$ triggers (see Sections 2.3.2, 2.3.3, 2.3.5) were considered:

- `EF_e24vhi_medium1` single electron trigger, requiring an electron with threshold $p_{\text{T}} > 24$ GeV and *medium* quality requirements as determined at trigger level and isolation.

- `EF_mu24i_tight` single muon trigger, requiring a muon with threshold $p_{\text{T}} >$ 24 GeV and *tight* quality requirements as determined at trigger level and isolation.

- `EF_ tau20Ti_medium1_e18vh_medium1` combined electron+$\tau_{\text{had-vis}}$ trigger, requiring an electron with threshold $p_{\text{T}} > 18$ GeV and *medium* quality requirements as determined at trigger level and a $\tau_{\text{had-vis}}$ with threshold $p_{\text{T}} > 20$ GeV and *medium* identification requirements as determined at trigger level and isolation.

- `EF_tau20_medium1_mu15` combined muon+$\tau_{\text{had-vis}}$ trigger, requiring a muon with threshold $p_{\text{T}} > 15$ GeV and *medium* quality requirements as determined at trigger level and a $\tau_{\text{had-vis}}$ with threshold $p_{\text{T}} > 20$ GeV and *medium* identification requirements as determined at trigger level.

A logical OR of the triggers was used. In the following events where a single lepton trigger fired are denoted SLT, while events where the combined trigger and not the single lepton trigger fired are denoted LTT.

In order to model the backgrounds both data and Monte Carlo simulation samples were used.

For the modelling of $Z \rightarrow \tau^+\tau^-$, both for the determination of central values and systematic variations, embedding samples were used (see Section 3.4.1 for a description of the embedding method). The starting dataset was the same considered for the rest of the analysis, except events collected with the same `EF_mu24i_tight` trigger mentioned before and the `EF_mu18_tight_mu8_EFFS` trigger were considered. The second trigger is a di-muon trigger, where the thresholds are $p_{\text{T}} > 18$ GeV with *tight* quality requirements and $p_{\text{T}} > 8$ GeV. Embedding was performed from $Z \rightarrow \mu^+\mu^-$ data events selected requiring exactly two muons with:

- $p_{\text{T}} > 25$ GeV and $|\eta| < 2.5$,

- sum of the p_{T} of the tracks in a $\Delta R < 0.2$ cone around the muon smaller than 20% of the muon p_{T},

- invariant mass of the two muons $m_{\mu\mu} > 40$ GeV.

Corrections were applied to the embedding sample to compensate for various detector and embedding procedure effects and to ensure the correct modelling of lepton and $\tau_{\text{had-vis}}$ distributions.

- **Corrections accounting for effects on muons in the original event**
  Trigger, reconstruction and identification efficiencies of muons were corrected for in order to obtain the correct kinematics for the τ lepton pair decay. Every embedding event was assigned a weight given by the product of the reciprocals of the efficiencies of the muons selected in the event. The efficiencies were obtained from data (see Section 2.3.3 and references therein) and binned in muon p_T and η.

- **Corrections accounting for effects on simulated τ visible decay products**
  In the embedding sample requirements on the presence of b-layer hits for tracks matched to physics objects were applied even in cases where a b-layer hit was not expected (dead Pixel modules). This effected needed to be corrected by assigning each event a weight given by the reciprocal of the efficiency of requiring a b-layer hit when none was expected.
  The effect of the trigger could not be simulated in the embedding procedure, and needed therefore to be emulated. This step was necessary to properly reproduce distributions before applying an overall normalisation factor. The emulation of trigger effects was applied performing the offline selection of candidates, and applying the expected data trigger efficiencies (see Sections 2.3.2 and 2.3.3 and references therein). Spin correlation effects are properly simulated by TAUOLA, but the information on the Z polarisation, that depends on the initial state quark configuration, was not available. The TauSpinner tool (see Section 1.6.1) allows to emulate such spin effects, but since its validation for the $\tau_l\tau_{had}$ channel was not complete at the time the analysis was performed, it was just used to show the effect was expected to be negligible. The same corrections for simulated electrons, muons and $\tau_{had-vis}$ from τ lepton decays that are applied for Monte Carlo simulated samples and described in the following were applied.

The embedding samples were thoroughly validated through comparisons between embedding and $Z \to \tau^+\tau^-$ Monte Carlo simulation (Alpgen + PYTHIA sample), comparisons with data in a validation region and performing the embedding procedure to pairs of muons instead of to pairs of τ leptons (see Ref. [4]). Samples with varied isolation requirements in the data $Z \to \mu^+\mu^-$ event selection and samples with varied subtraction of the energy deposited in the calorimeter by muons were produced, and are further discussed in Section 7.9.9.

The Monte Carlo samples used to model the various backgrounds have already been outlined in Section 3.4. For convenience they are summarised in Table 7.1. Samples used for theory uncertainty estimations are disussed in Section 7.9.11. In all Monte Carlo samples the effects of pile-up were simulated overlaying soft collision events generated by PYTHIA8. Moreover the Monte Carlo simulated samples were weighted or corrected with data-driven factors, obtained as outlined in Chapter 2, to correctly reproduce the following aspects:

- distribution of average number of interactions per bunch-crossing (μ),

- muon momentum scale, resolution and reconstruction, identification, isolation and trigger efficiencies,

- electron energy scale, resolution and reconstruction, identification, isolation and trigger efficiencies,

- $\tau_{\text{had-vis}}$ identification efficiency and electron to $\tau_{\text{had-vis}}$ fake factor,

- jet energy scale,

- b-tagging efficiencies and mis-tag rates,

Special $Z \to \tau^+\tau^-$ and $Z + \text{jets}$ Monte Carlo samples were generated with filters at generator level to enhance the statistics available for VBF-like topologies. The samples were combined with ordinary samples with an overlap removal procedure at generator level to avoid double counting.

7.2 Event selection

The selection of $H \to \tau^+\tau^-$ candidate events includes an event preselection, a categorisation of the events and dedicated background suppression cuts for each category.

7.2.1 Event preselection

Events were required first of all to satisfy basic quality criteria to avoid contamination from non-collision events, such as cosmic ray events and beam-halo induced events. The presence of at least one primary vertex, with at least four associated tracks was required. Cleaning cuts designed to reject events with jets originating from coherent noise in the electromagnetic calorimeter, signal spikes in the end-cap calorimeters and non-collision backgrounds [177, 180] were applied. Events with genuine jets laying in malfunctioning tile calorimeter cells were rejected as well.

The $H \to \tau^+\tau^-$ signature was then identified requiring:

- exactly one muon or electron candidate with $|\eta| < 2.5$ and p_{T} thresholds depending on the trigger fired (see Table 7.2), satisfying `Combined` and *loose* quality requirements respectively,

- muons were required to be isolated, with the sum of the p_{T} of the tracks in a $\Delta R < 0.2$ cone $< 6\%$ of the muon p_{T},

- electrons were required to be isolated, with the sum of the p_{T} of the tracks in a $\Delta R < 0.2$ cone $< 6\%$ of the electron p_{T},

- exactly one $\tau_{\text{had-vis}}$ candidate, with $|\eta| < 2.5$ and p_{T} threshold depending on the trigger fired (see Table 7.2), satisfying *medium* identification criteria and *medium* electron veto (see Section 2.3.5),

- the $\tau_{\text{had-vis}}$ candidate is required to have unitary charge and have 1 or 3 associated tracks.

Sample	Generator	Shower, Hadronisation and UE	PDFs set	Notes
VBF Higgs	POWHEG	PYTHIA8, AU2	CT10	
ggF Higgs	POWHEG	PYTHIA8, AU2	CT10	`hfact`$= m_H/1.2$ (see Section 3.5.2)
WH, ZH Higgs	PYTHIA8	PYTHIA8, AU2	CTEQ6L1	
Z + jets	Alpgen	PYTHIA8, Perugia2011C	CTEQ6L1	Exclusive Z+n partons samples (n up to 4) and inclusive Z+5 partons sample (parton with $p_T > 20$ GeV), samples cover $m_{inv}^{Z/\gamma^*} > 10$ GeV
Z + jets VBF filter	Alpgen	Herwig, Jimmy, AUET2	CTEQ6L1	Same structure as Z+jets samples, filter for at least two truth jets with $p_T > 15$ GeV, $\Delta\eta$ between the two jets > 2.0 and mass of the two jets > 200 GeV
Z + jets TVBF filter	Alpgen	Herwig, Jimmy, AUET2	CTEQ6L1	Same structure as Z+jets samples, filter for at least two truth jets with $p_T > 15$ GeV, $\Delta\eta$ between the two jets > 4.0 and mass of the two jets > 400 GeV
Z + jets VBF	Sherpa	Sherpa	CT10	
W + jets	Alpgen	PYTHIA8, Perugia2011C	CTEQ6L1	Exclusive W+n partons samples (n up to 4) and inclusive W+5 partons sample (parton with $p_T > 20$ GeV)
W + jets VBF filter	Alpgen	Herwig, Jimmy, AUET2	CTEQ6L1	Same structure as W+jets samples, filter for at least two truth jets with $p_T > 15$ GeV, $\Delta\eta$ between the two jets > 2.0 and mass of the two jets > 200 GeV
$t\bar{t}$	MC@NLO	Herwig, Jimmy	CT10	
Single top s-channel and Wt	MC@NLO	Herwig, Jimmy, AUET2	CT10	
Single top t-channel	AcerMC	PYTHIA8, AUET2B	CTEQ6L1	
Diboson qq production, ZZ, WZ	Herwig	Herwig, AUET2	CTEQ6L1	
Diboson qq production, WW	Alpgen	Herwig, Jimmy, AUET2	CTEQ6L1	$WW \to qql\nu$ and $WW \to l\nu l\nu$
Diboson gg production	gg2ww	Herwig, Jimmy, AUET2	CT10	

Table 7.1: Summary of Monte Carlo samples used for the $H \to \tau^+\tau^-$ analysis.

Trigger type	Offline lepton threshold	Offline $\tau_{\text{had-vis}}$ threshold
SLT $\tau_\mu \tau_{\text{had}}$	$p_T^\mu > 26\,\text{GeV}$	$p_T^{\tau_{\text{had-vis}}} > 20\,\text{GeV}$
SLT $\tau_e \tau_{\text{had}}$	$p_T^e > 26\,\text{GeV}$	$p_T^{\tau_{\text{had-vis}}} > 20\,\text{GeV}$
LTT $\tau_\mu \tau_{\text{had}}$	$17 < p_T^e < 26\,\text{GeV}$	$p_T^{\tau_{\text{had-vis}}} > 25\,\text{GeV}$
LTT $\tau_e \tau_{\text{had}}$	$20 < p_T^e < 26\,\text{GeV}$	$p_T^{\tau_{\text{had-vis}}} > 25\,\text{GeV}$

Table 7.2: Lepton and $\tau_{\text{had-vis}}$ thresholds according to the type of trigger fired by the event.

As already introduced in Section 2.3.4, *anti-kt* jets with $R = 0.4$ and LCW+JES calibration were used. Jets with $|\eta| < 2.4$ and $p_T < 50\,\text{GeV}$ were considered only if satisfying $|JVF| > 0.5$. Throughout the analysis the `MET_RefFinal` missing transverse momentum reconstruction with `STVF` pile-up suppression was used, since in the regimes of interest it provides the best performance (see Section 3.3.2).

7.3 Categorisation

Categories were defined to enhance the signal sensitivity making use of the characteristics of the production modes, according to the strategy described in Section 3.5. The categories and relative requirements in this analysis are:

VBF category

1. At least two jets, with threshold $p_T > 40\,\text{GeV}$ for the leading jet and $p_T > 30\,\text{GeV}$ for the sub-leading jet,

2. the two leading jets lie in opposite detector emispheres,

3. the pseudorapidity separation between the two leading jets $\Delta\eta_{jj}$ is > 3.0,

4. the mass of the two leading jets system m_{jj} is $> 500\,\text{GeV}$,

5. the lepton and $\tau_{\text{had-vis}}$ candidates are central to the two leading jets,

6. $p_T^{\text{tot}} < 30\,\text{GeV}$, where the variable p_T^{tot} was defined as

$$p_{T^{\text{tot}}} = (p_l + p_{\tau_{\text{had-vis}}} + p_{j_1} + p_{j_2})_T \tag{7.1}$$

where p_l is the lepton 4-momentum, $p_{\tau_{\text{had-vis}}}$ is the $\tau_{\text{had-vis}}$ 4-momentum and p_{j_1} and p_{j_2} the 4-momenta of the leading and sub-leading jets respectively,

7. the event is SLT,

8. the $\tau_{\text{had-vis}}$ candidate has $p_T > 30\,\text{GeV}$,

9. $E_T^{\text{miss}} > 20\,\text{GeV}$.

Requirements 1-6 individuate the typical topology of VBF Higgs events, with two well separated jets and the Higgs boson decay products in the region between

them. The requirement on the p_T^{tot} variable partially acts as a veto against additional QCD radiation. The choice of using the leading jets instead of the most separated jets in pseudorapidity has some effect in this sense too. Requirement 7 is dictated by the background estimation method, that prevents the use of LTT events in this category (see Section 7.5). Finally requirements 8-9 make use of further characteristics of the selected VBF Higgs events.

Boosted **category**

1. Not in the *VBF* category,

2. $p_T^H > 100\,\text{GeV}$, where the p_T^H is reconstructed as

$$p_T^H = \left(p_l + p_{\tau_{\text{had-vis}}} + p_T^{\text{miss}}\right) \tag{7.2}$$

where the p_T^{miss} 4-momentum is defined as $p_T^{\text{miss}} = (E_x^{\text{miss}}, E_y^{\text{miss}}, 0, E_T^{\text{miss}})$,

3. $0 < x_{\tau_{\text{had-vis}}} < 1.2$, where $x_{\tau_{\text{had-vis}}}$ is the transverse momentum fraction carried by the neutrino system from the τ lepton hadronic decay computed making use of the collinear approximation (see Section 3.2),

4. $0 < x_l < 1$, where x_l is the transverse momentum fraction carried by the neutrino system from the τ lepton leptonic decay computed making use of the collinear approximation (see Section 3.2),

5. the $\tau_{\text{had-vis}}$ candidate has $p_T > 30\,\text{GeV}$,

6. $E_T^{\text{miss}} > 20\,\text{GeV}$.

   Requirements 2-4 characterise boosted topology events. In particular requirements 3-4, impose a good quality of mass reconstruction, which is a characterising feature of boosted topology $H \to \tau^+\tau^-$ events. Requirements 5-6 make use of further characteristics of the selected $H \to \tau^+\tau^-$ events.

The least sensitive zero-jet and one-jet categories were dropped in the preliminary results, both for the ATLAS MVA analysis and cut-based results.

7.4 Background suppression

Several processes can mimic the $H \to \tau^+\tau^-$ signature, and have already been described in Section 3.4. In the following the specific sets of cuts designed in order to suppress them are described. The cuts are defined differently for the two categories.

Suppression of $W + $ jets and multijet events

$W + $ jets events were suppressed mostly using cuts on the transverse mass of the lepton and E_T^{miss} and on the angular variable $\Sigma\Delta\phi$, defined as

$$\Sigma\Delta\phi = |\phi_l - \phi_{E_T}^{\text{miss}}| + |\phi_{\tau_{\text{had-vis}}} - \phi_{E_T}^{\text{miss}}| \tag{7.3}$$

The $\Sigma\Delta\phi$ variable is sensitive to the direction of $E_{\mathrm{T}}^{\mathrm{miss}}$ with respect to the lepton and $\tau_{\mathrm{had\text{-}vis}}$ objects, which is distinctively different between $H \to \tau^+\tau^-$ and $W +$ jets.

The background from multijet was mostly suppressed by the isolation requirements applied at the preselection level. Further suppression against fake $\tau_{\mathrm{had\text{-}vis}}$ objects, and therefore both against the $W +$ jets and multijet backgrounds, was achieved by the $\Delta(\Delta R)$ variable, defined as

$$\Delta(\Delta R) = \Delta R_{\mathrm{act}} - \Delta R_{\mathrm{exp}} \qquad (7.4)$$

where ΔR_{act} and ΔR_{exp} are the actual and expected distances between the lepton and $\tau_{\mathrm{had\text{-}vis}}$ in (η, ϕ) space ($\Delta R = \sqrt{\Delta\phi^2 + \Delta\eta^2}$). The correlation between ΔR and the transverse momentum of the system of the visible decay products $p_{\mathrm{T}}^{l\tau}$ is distinctively different between resonant $\tau\tau$ events and non-resonant background events. The expected ΔR was therefore parametrised as a function of $p_{\mathrm{T}^{l\tau}}$ for the various categories, and the difference between the expected and actual values provided the discrimination power.

Suppression of $Z +$ jets

The background from $Z +$ jets is particularly dangerous in the case where the candidate $\tau_{\mathrm{had\text{-}vis}}$ arises from the misidentification of a lepton. In this case in fact the mass tends to be reconstructed in a region similar to that expected from a $m_H = 125\,\mathrm{GeV}$ signal. The background was already strongly suppressed by the $\tau_{\mathrm{had\text{-}vis}}$ electron and muon vetoes applied at preselection.

Suppression of $t\bar{t}$

Background events due to $t\bar{t}$ events were suppressed by the transverse mass cut applied against the $W +$ jets background. Further suppression was achieved requiring a veto on the presence of a b-tagged jet in the event.

A summary of the cuts applied for each category is given in Table 7.3. An additional cut on the visible mass was applied in the *VBF* category to reject a region populated by fakes and found to be poorly modeled.

Cut	*VBF*	*Boosted*
m_{T}	$< 50\,\mathrm{GeV}$	$< 50\,\mathrm{GeV}$
$\Sigma\Delta\phi$	< 2.8	
$\Delta\Delta R$	< 0.8	< 0.8
b-jet veto	✓	✓
m_{vis}	$> 40\,\mathrm{GeV}$	

Table 7.3: Summary of additional background suppression cuts per category. More details are given in the text.

7.5   Background estimation

The estimation of the backgrounds was performed with two different methods, the *OS-rSS* method for the *boosted* category and the *Fake factor* method for the *VBF* category, due to the different statistics available in the two categories. Throughout this section the uncertainty band on the background prediction in the plots is statistical only.

7.6   The *OS-rSS* method

In the *boosted* a method referred to as *OS-rSS* was used. This method exploits the differences in charge correlations between the signal and those backgrounds that are due to fake $\tau_{\text{had-vis}}$ to infer the background contamination in the signal regions from data. For $H \rightarrow \tau^+\tau^-$ signal and the $Z \rightarrow \tau^+\tau^-$ background the charges of the lepton and $\tau_{\text{had-vis}}$ are typically opposite (OS). The multi-jet background shows almost no charge correlation, whereas the $W + $jets background has a larger asymmetry, with the events with same charge of the lepton and $\tau_{\text{had-vis}}$ (SS) less frequent than the OS ones. The $Z + $jets background is highly OS-SS asymmetric only when a lepton is faking the $\tau_{\text{had-vis}}$ signature. The $t\bar{t}$ and diboson backgrounds show a strong asymmetry. The method relies on two fundamental assumptions:

- The distribution of m_{MMC} for the multi-jet background is the same for selected OS and SS events,

- the background asymmetries determined in dedicated control regions can be extrapolated to the signal region.

Under these assumptions the number of background events in each m_{MMC} bin can be estimated as

$$N_{\text{OS}}^{\text{bkg}} = r_{\text{QCD}} N_{\text{SS}}^{\text{data}} + N_{\text{add-on}}^{Z\rightarrow\tau\tau} + N_{\text{add-on}}^{Z\rightarrow ll(\rightarrow\tau_{\text{had-vis}})} + N_{\text{add-on}}^{Z\rightarrow ll+\text{jet}(\rightarrow\tau_{\text{had-vis}})}$$
$$+N_{\text{add-on}}^{W+\text{jets}} + N_{\text{add-on}}^{\text{top}} + N_{\text{add-on}}^{\text{VV}} \qquad (7.5)$$

where the various terms are defined as follows

- The factor r_{QCD} accounts for the charge asymmetry that is observed in a data sample consisting mainly of multi-jet events, and was defined as $r_{\text{QCD}} = N_{\text{OS}}^{\text{multijet}}/N_{\text{SS}}^{\text{multijet}}$. The asymmetry is due to differences in the jet flavour composition in the two regions. The r_{QCD} factor was determined by a data-driven method, explained in Section 7.6.1

- The term accounting for the $Z \rightarrow \tau^+\tau^-$ background asymmetry was defined as

$$N_{\text{add-on}}^{Z\rightarrow\tau\tau} = k_{Z\rightarrow\tau\tau} \left(N_{\text{OS}}^{Z\rightarrow\tau\tau} - r_{\text{QCD}} N_{\text{SS}}^{Z\rightarrow\tau\tau} \right) \qquad (7.6)$$

where $k_{Z\rightarrow\tau\tau}$ was assumed equal to unity and $N_{\text{OS}}^{Z\rightarrow\tau\tau}$ and $N_{\text{SS}}^{Z\rightarrow\tau\tau}$ are the numbers of OS and SS $Z \rightarrow \tau^+\tau^-$ events respectively. Details about the estimation and modelling of the $Z \rightarrow \tau^+\tau^-$ background are given in Section 7.6.2.

- The term accounting for the $Z \to l^+l^-$ background asymmetry in the cases where the fake $\tau_{\text{had-vis}}$ originates from a lepton was defined as

$$N_{\text{add-on}}^{Z \to ll(\to \tau_{\text{had-vis}})} = k_{Z \to ll(\to \tau_{\text{had-vis}})} \left(N_{\text{OS}}^{Z \to ll(\to \tau_{\text{had-vis}})} - r_{\text{QCD}} \, N_{\text{SS}}^{Z \to ll(\to \tau_{\text{had-vis}})} \right)$$
(7.7)

where $k_{Z \to ll(l \to \tau_{\text{had-vis}})}$ was assumed to be equal to unity, as data-driven corrections to the $l \to \tau$ fake factors were applied as corrections to the simulated samples, and $N_{\text{OS}}^{Z \to ll(\to \tau_{\text{had-vis}})}$ and $N_{\text{SS}}^{Z \to ll(\tau_{\text{had-vis}})}$ are the numbers of OS and SS $Z \to l^+l^-(\to \tau_{\text{had-vis}})$ events respectively. Details about the estimation and modelling of the $Z \to l^+l^-(\to \tau_{\text{had-vis}})$ background are given in Section 7.6.3.

- The term $N_{\text{add-on}}^{Z \to ll + \text{jet}(\to \tau_{\text{had-vis}})}$ was introduced to correct for double-counting of events, since the $Z \to l^+l^-$ background asymmetry in the cases when the fake $\tau_{\text{had-vis}}$ originates from a jet does not show any charge asymmetry. It was defined as

$$N_{\text{add-on}}^{Z \to ll + \text{jet}(\to \tau_{\text{had-vis}})} = k_{Z \to ll + \text{jet}(\to \tau_{\text{had-vis}})} N_{\text{OS}}^{Z \to ll + \text{jet}(\to \tau_{\text{had-vis}})} (1 - r_{\text{QCD}})$$
(7.8)

where the $N_{\text{OS}}^{Z \to ll + \text{jet}}$ is the number of $Z \to l^+l^- + \text{jet}(\to \tau_{\text{had-vis}})$ OS events. More details on the estimation and modelling of the $Z \to l^+l^- + \text{jet}(\to \tau_{\text{had-vis}})$ background are given in Section 7.6.3.

- The term accounting for the asymmetry of the W+jets background, which includes events from $W \to e\nu$, $W \to \mu\nu$ and $W \to \tau\nu$ processes, is defined as

$$N_{\text{add-on}}^{W + \text{jets}} = k_{W + \text{jets}}^{\text{OS}} N_{\text{OS}}^{W + \text{jets}} - r_{\text{QCD}} \, k_{W + \text{jets}}^{\text{SS}} N_{\text{SS}}^{W + \text{jets}}$$
(7.9)

where the $k_{W + \text{jets}}^{\text{OS}}$ and $k_{W + \text{jets}}^{\text{SS}}$ normalisation factors were determined by a data-driven method. More details on the estimation and modelling of the $W + \text{jets}$ background are given in Section 7.6.4

- The term accounting for the asymmetry of the top background, including events from $t\bar{t}$, single-top and Wt production, was defined as

$$N_{\text{add-on}}^{\text{top}} = k_{\text{top}}^{\text{OS}} N_{\text{OS}}^{\text{top}} - r_{\text{QCD}} \, k_{\text{top}}^{\text{SS}} N_{\text{SS}}^{\text{top}}$$
(7.10)

where the $k_{\text{top}}^{\text{OS}}$ and $k_{\text{top}}^{\text{SS}}$ normalisation factors were determined by a data-driven method. More details on the estimation and modelling of the top background are given in Section 7.6.5

- The term accounting for the asymmetry of the diboson (VV) background, which includes events from WW, WZ and ZZ events, considering the qq production

mode as well as the gg production mode for the largest WW contribution. The term was defined as

$$N_{\text{add-on}}^{\text{VV}} = k_{\text{VV}} \left(N_{\text{OS}}^{\text{VV}} - r_{\text{QCD}} \, N_{\text{SS}}^{\text{VV}} \right) \tag{7.11}$$

The k_{VV} normalisation factor is assumed to be unity. More details on the estimation and modelling of the VV background are given in Section 7.6.6.

7.6.1 r_{QCD} determination

The r_{QCD} factor was determined in a data-driven way using a pair of dedicated OS and SS control regions. The common requirements for the two control regions were:

- preselection defined in Section 7.2.1, except for the calorimetric isolation requirement which was reversed (requiring the sum of the transverse energies in a $\Delta R < 0.2$ cone around the lepton direction to be larger than 6%) and the $\tau_{\text{had-vis}}$ identification level which was relaxed to *loose*,

- $m_{\text{T}} < 30\,\text{GeV}$,

- $E_{\text{T}}^{\text{miss}} < 15\,\text{GeV}$.

The resulting regions are enriched in multi-jet events. Residual contributions from top and electroweak backgrounds were subtracted using predictions from simulated samples. The contribution due to $W + \text{jets}$ events was normalised in two regions defined with the same selections except the transverse mass cut which was defined as $m_{\text{T}} > 80\,\text{GeV}$. Since r_{QCD} was found to depend on the calorimeter isolation requirement, the r_{QCD} value for events passing the analysis isolation requirements was extracted by a linear fit of r_{QCD} as a function of the calorimeter isolation cut.

7.6.2 $Z \to \tau^+\tau^-$ background

The $Z \to \tau^+\tau^-$ background was estimated mainly using the embedding samples described in Section 3.4.1 and 7.1. Since the embedding sample was obtained applying a cut on the di-muon invariant mass $m_{\mu\mu} > 40\,\text{GeV}$, it was complemented with Monte Carlo simulated samples at lower masses of the di-tau system. The normalisation of the embedding sample was obtained from a normalisation region defined by:

- Preselection defined in Section 7.2.1,

- $40\,\text{GeV} < m_{\text{vis}} < 70\,\text{GeV}$,

- $m_{\text{T}} < 50\,\text{GeV}$.

The region was defined such that the visible mass window is inclusive of the $Z \to \tau^+\tau^-$ peak and the contribution of signal is negligible. The other backgrounds were subtracted as estimated by the *OS-rSS* method. Distributions for the basic kinematic variables and

m_{MMC} in the normalisation region are shown in Figure 7.1. The distributions are generally fairly modeled, but slopes in the $\tau_{\text{had-vis}}$ p_T spectrum and m_{MMC} are visible. These slopes are covered by systematics uncertainties. In particular a shift of the tau energy scale provides a much better agreement in the region dominated by $Z \to \tau^+ \tau^-$, as shown in Figure 7.2 where the same distributions obtained with a 1σ tau energy scale variation are shown. Even if evidence for a shift of the tau energy scale was found in 2012 with a study similar to that described in Chapter 6, the comparison here is for illustrative purposes only, as other sources of systematic uncertainty could have given rise to the shift.

Normalisation factors were derived separately for $\tau_\mu \tau_{\text{had}}$ and $\tau_e \tau_{\text{had}}$ channel events and for SLT and LTT events. The results are shown in the background estimation summary Table 7.4.

7.6.3 $Z +$ **jets background**

The background from $Z +$ jets was estimated using Monte Carlo simulated samples. In order to distinguish events contributing to the $Z \to ll(\to \tau_{\text{had-vis}})$ and $Z \to ll + \text{jet}(\to \tau_{\text{had-vis}})$ components the generator level information was used. An event was considered for the $Z \to ll(\to \tau_{\text{had-vis}})$ component if the reconstructed $\tau_{\text{had-vis}}$ was matched to a generator level final state electron with $p_T > 8$ GeV arising from the decay of a τ lepton or a Z or W boson, within a cone $\Delta R < 0.2$ or to a generator level final state muon with $p_T > 4$ GeV within the same cone. The event was assigned to the $Z \to ll(\text{jet} \to \tau_{\text{had-vis}})$ otherwise.

The normalisation factor for the $Z \to ll + \text{jet}(\to \tau_{\text{had-vis}})$ component, $k_{Z \to ll + \text{jet}(\to \tau_{\text{had-vis}})}$ was measured in dedicated control regions defined by the following requirements:

- Two opposite sign charge muons of same flavour passing the regular object selection except isolation,

- regular isolation requirement for the leading muon,

- invariant mass of the two muons 61 GeV $< m_{\mu\mu} < 121$ GeV,

- *boosted* category only: $p_T^H > 50$GeV,

- *VBF* category only: $\tau_{\text{had-vis}}$ $p_T > 30$ GeV.

Figure 7.3 shows distributions for the basic kinematic variables and m_{MMC} in the preselection $Z +$ jets control region. The modelling of the distributions is pretty good, in any case acceptable considering this background was found to give small contributions.

7.6.4 $W +$ **jets background**

The $W +$ jets background add-on term was estimated using Monte Carlo simulated samples. The mismodelling of the jet $\to \tau_{\text{had-vis}}$ fake rate was accounted for by normalisation factors (see Eq. 7.9) determined in dedicated control regions. The normalisation factors were determined separately for OS and SS events, $\tau_\mu \tau_{\text{had}}$ and $\tau_e \tau_{\text{had}}$ channels and for
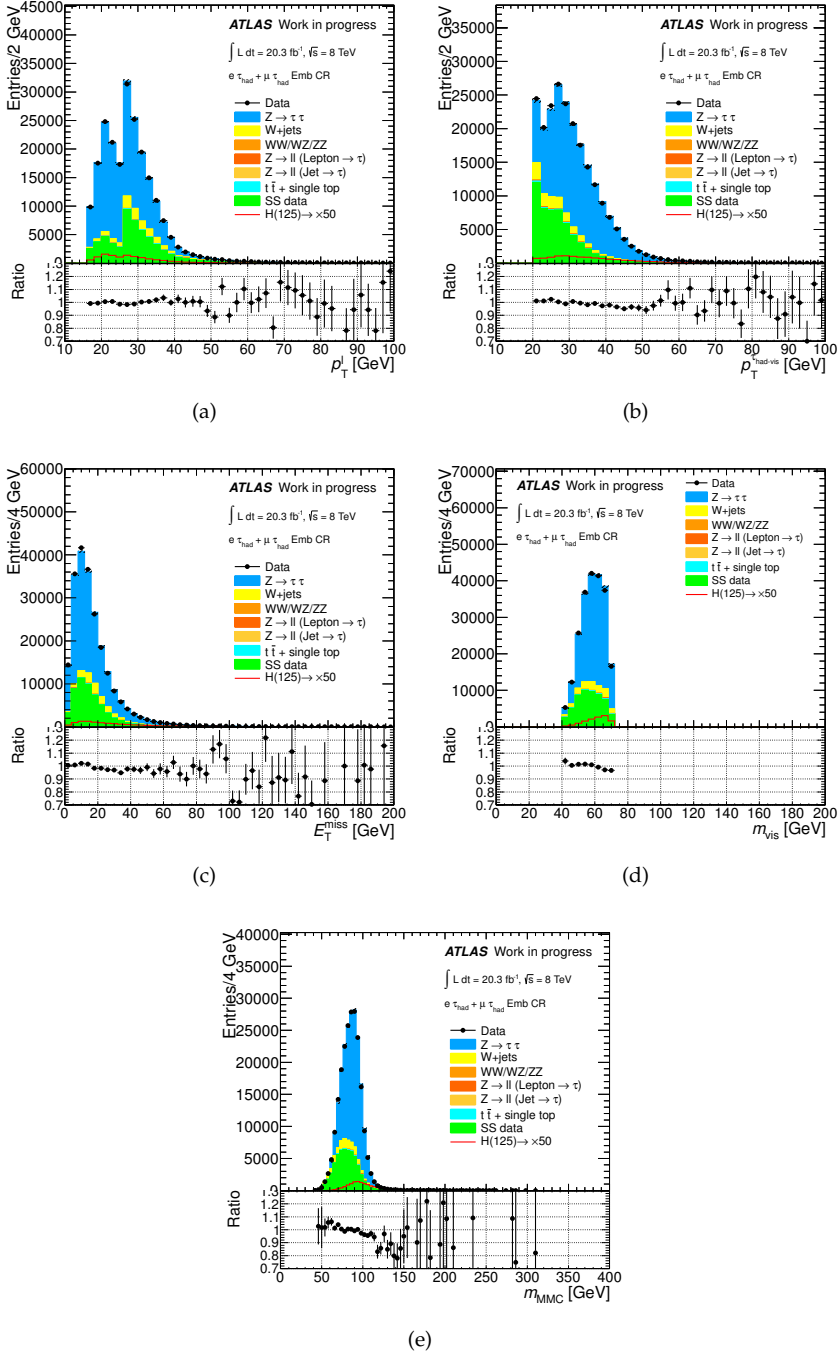
Figure 7.1: Distributions in the embedding normalisation region, (a) lepton p_T, (b) $\tau_{\text{had-vis}}$ p_T, (c) E_T^{miss}, (d) m_{vis} and (e) m_{MMC}.
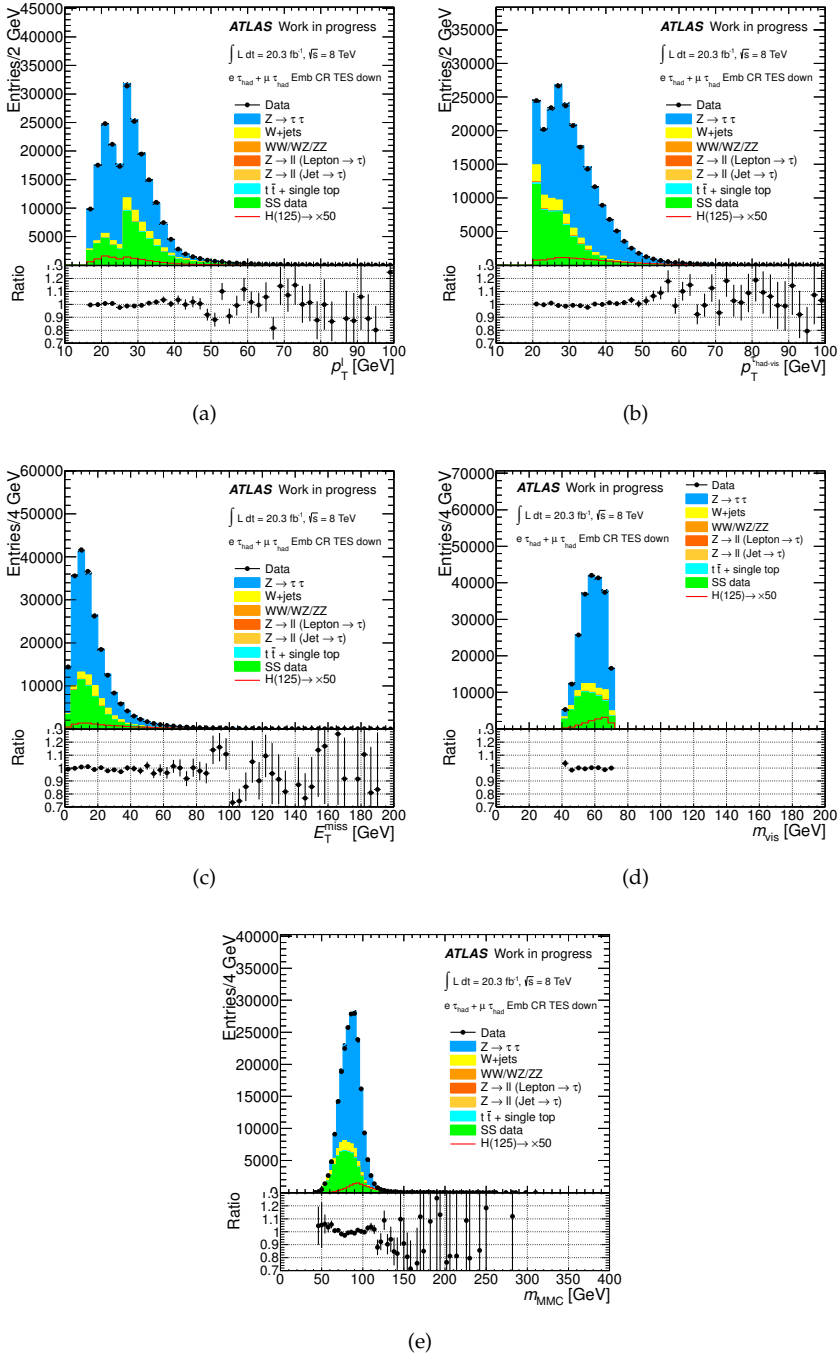
Figure 7.2: Distributions in the embedding normalisation region with a downwards 1σ TES variation, (a) lepton p_T, (b) $\tau_{\text{had-vis}}$ p_T, (c) E_T^{miss}, (d) m_{vis} and (e) m_{MMC}.
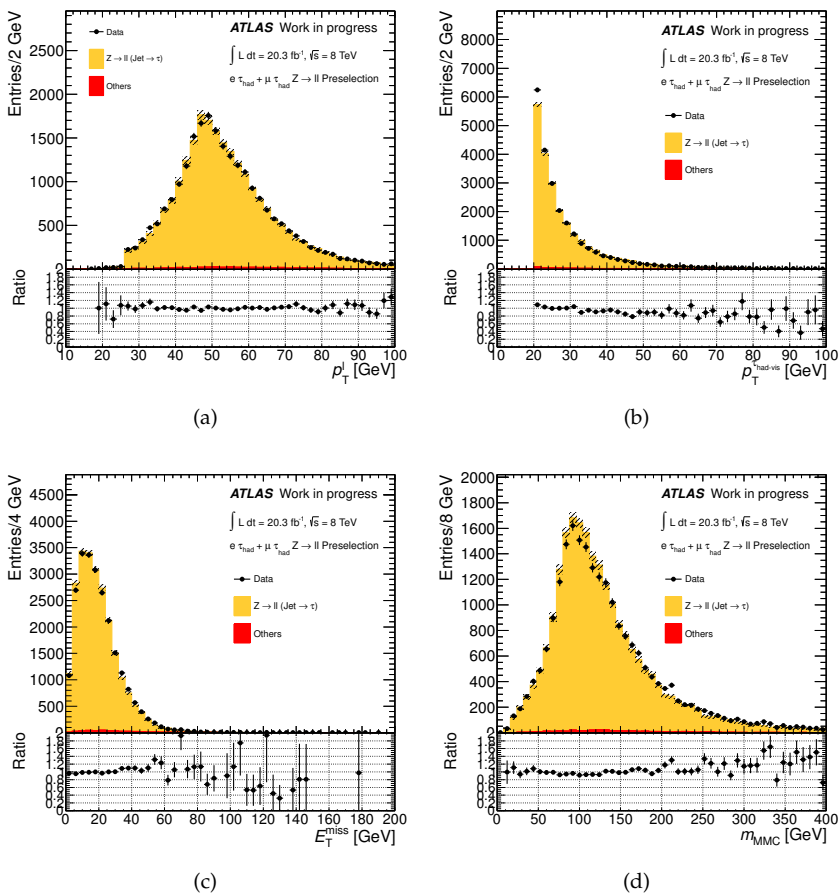
Figure 7.3: Distributions in the preselection $Z + \text{jets}$ control region (a) lepton p_T, (b) $\tau_\text{had-vis}$ p_T, (c) E_T^miss, (d) m_MMC.

preselection and *boosted* category separately to account for the different jet flavour compositions. The control regions were defined by the following requirements:

- preselection defined in Section 7.2.1,

- $m_\mathrm{T} > 70\,\mathrm{GeV}$,

- $E_\mathrm{T}^\mathrm{miss} > 20\,\mathrm{GeV}$,

- *Boosted* category only: not in an analogous control region for the *VBF* region (SLT or less than two jets in the event or leading jet $p_\mathrm{T} < 40\,\mathrm{GeV}$ or $\tau_\mathrm{had\text{-}vis}$ $p_\mathrm{T} < 30\,\mathrm{GeV}$), same cuts as the categorisation apart from $E_\mathrm{T}^\mathrm{miss}$ cut and neutrino transverse momentum fraction cuts.

In order to obtain the normalisation factors other residual backgrounds were estimated using Monte Carlo simulated samples. The normalisation factors determined for the $Z \to l^+l^-$ and top backgrounds were applied to the corresponding Monte Carlo samples. Corrections to the top background as described in Section 7.6.5 were applied.

The shape of the distributions for the W + jets background were corrected to match the data by subsequent reweightings applied as a function of the ratio of the transverse momenta of the lepton and $\tau_\mathrm{had\text{-}vis}$, $p_\mathrm{T}^l/p_\mathrm{T}^{\tau_\mathrm{had\text{-}vis}}$, and of the pseudorapidity difference between the lepton and $\tau_\mathrm{had\text{-}vis}$, $\Delta\eta(l, \tau_\mathrm{had\text{-}vis})$. The correction functions were obtained by fitting a third-order polynomial to the ratio of data to W + jets Monte Carlo after subtraction of the other backgrounds as a function of the corresponding variable. Figure 7.4 shows the $p_\mathrm{T}^l/p_\mathrm{T}^{\tau_\mathrm{had\text{-}vis}}$ and $\Delta\eta(l, \tau_\mathrm{had\text{-}vis})$ and $\Delta R(l, \tau_\mathrm{had\text{-}vis})$ distributions for the control region at preselection level with and without the corrections applied. All background contributions were estimated with the *OS-rSS* method It can be seen that the corrections recover the correct event angular distributions.

Figure 7.5 shows the p_T spectra and m_T distributions for the OS and SS W + jets control regions defined at the preselection level, after all the corrections to the W + jets background were applied, and estimating the various contributions with the same method that was used for the derivation of the corrections factors. All the corrections factors for W + jets were applied. The selected regions are dominated by the W + jets contribution. The modelling was found to be better for the OS W + jets region than for the SS region. The first benefits from a much larger statistics as well. The pretty good modelling of the p_T spectra shows that the assumption of no multi-jet background in the regions was justified. The m_T spectrum was plotted in logarithmic scale in order to show the good modelling of the region dominated by the top background.

Figure 7.6 shows distributions for various variables in the preselection W + jets control region with the background estimated with the *OS-rSS* method. It can be seen that the modelling is generally pretty good. The distribution of the number of jets in the event is not well modeled, but this was expected as correction factors for the W + jets normalisation depend on the jet multiplicity, and for this reason they were derived for the different categories.

Figure 7.7 shows distributions in the *boosted* category W + jets control region, even in this case with *OS-rSS* background estimation. The agreement of the data with the prediction is pretty good.
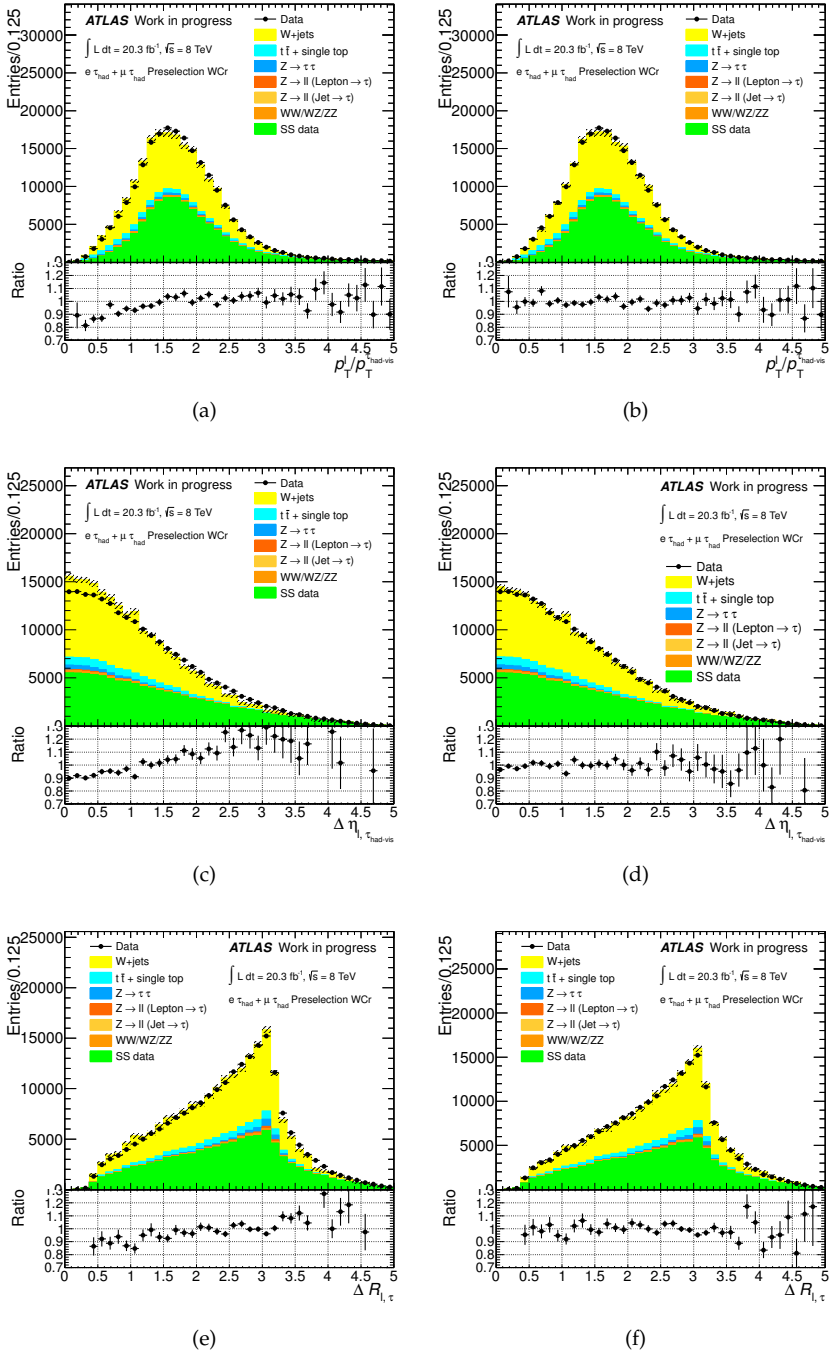
Figure 7.4: Distributions in the preselection W+jets control region (b-d-f) with and without (a-c-e) W+jets shape corrections applied.
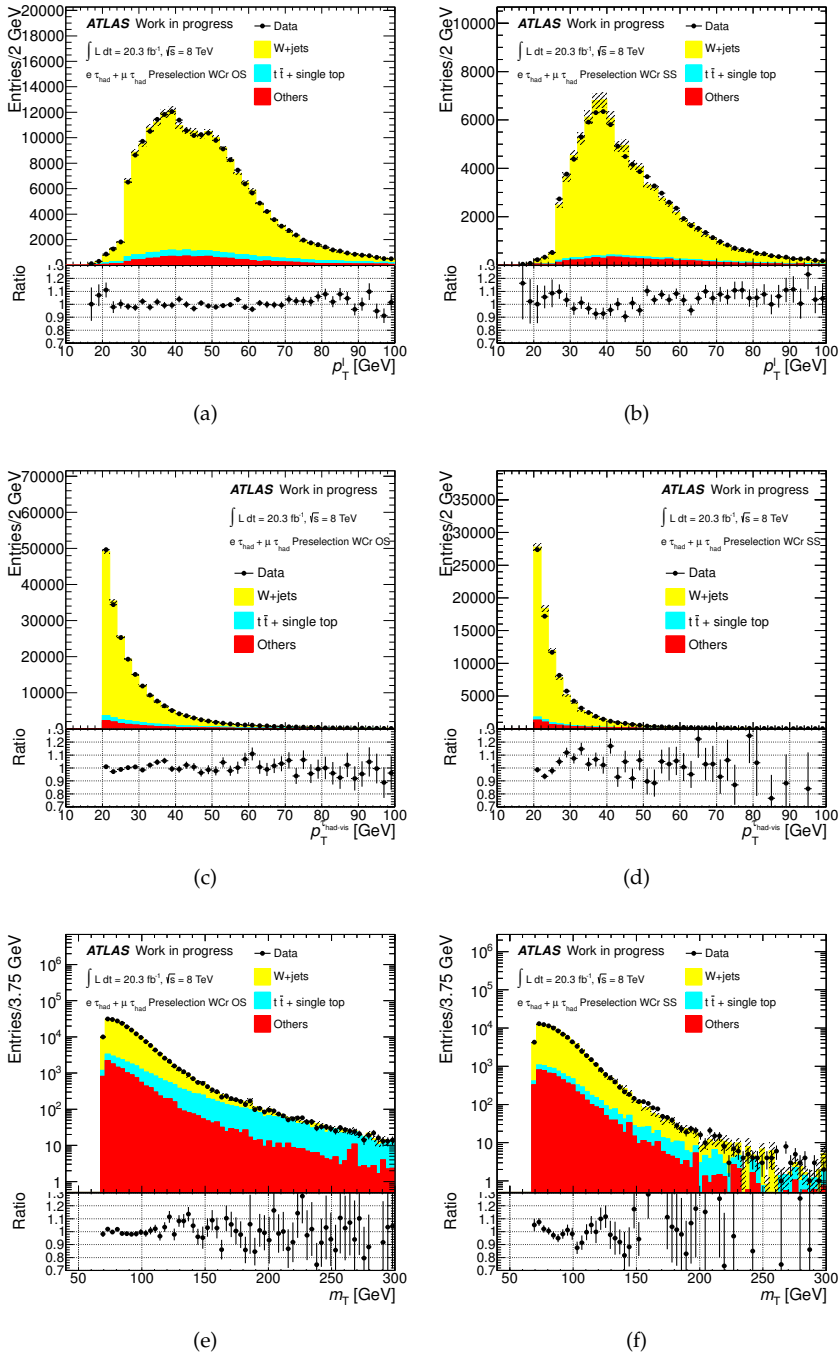
Figure 7.5: Distributions in the (a-c-e) OS and (b-d-f) SS $W + $ jets control regions defined at preselection level. (a-b) lepton p_T, (c-d) $\tau_{\text{had-vis}}$ p_T and (e-f) m_T distributions. More details are given in the text.
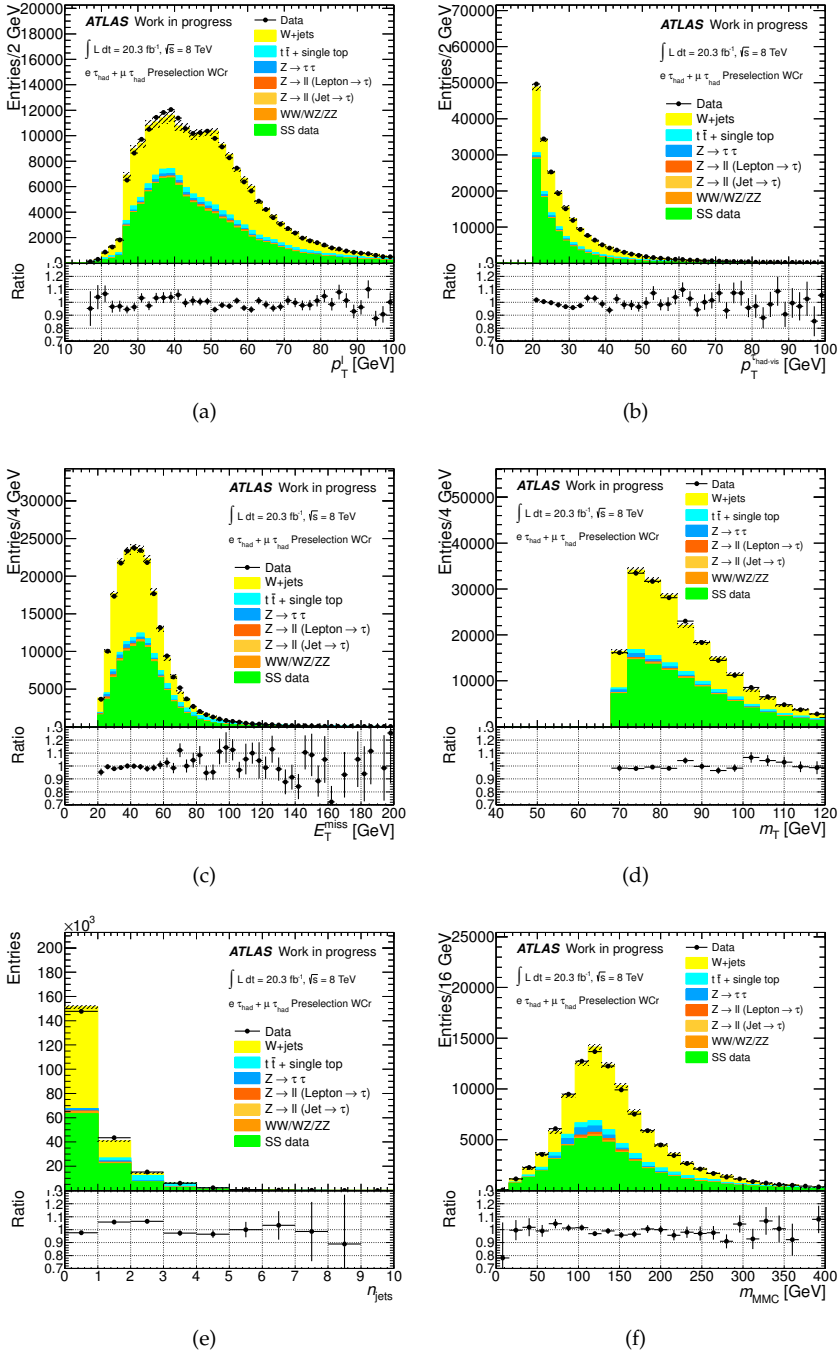
Figure 7.6: Distributions in the W + jets control region defined at preselection level. All background contributions were estimated with the *OS-rSS* method (a) lepton p_T, (b) $\tau_{\text{had-vis}}$ p_T, (c) E_T^{miss}, (d) m_T, (e) number of jets and (f) m_{MMC} distributions.

(a)   (b)

(c)   (d)
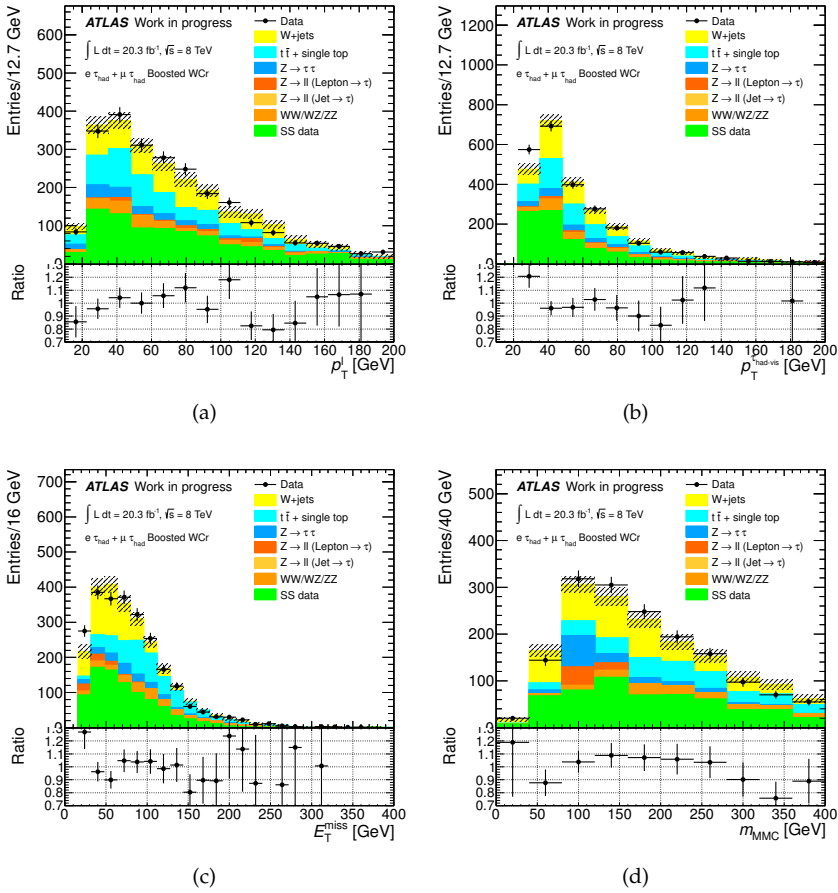
Figure 7.7: Distributions in the W + jets control regions defined for the *boosted* category. All background contributions were estimated with the *OS-rSS* method (a) lepton p_T, (b) $\tau_{\text{had-vis}}$ p_T, (c) E_T^{miss} and (d) m_{MMC} distributions.

7.6.5 Top background

The background due to $t\bar{t}$ and single-top events was estimated using Monte Carlo simulated samples, with normalisation factors derived from data as in Eq. 7.10. Two normalisation factors were determined separately for OS and SS events in a same pair of control regions for the two categories, defined by the following requirements:

- preselection defined in Section 7.2.1,

- ≥ 2 jets with $p_\mathrm{T} > 30\,\mathrm{GeV}$,

- ≥ 1 b-tagged jet,

- $E_\mathrm{T}^\mathrm{miss} > 20\,\mathrm{GeV}$,

- $m_\mathrm{T} > 70\,\mathrm{GeV}$.

The requirements on the transverse mass and b-jet tagging enhance the contribution of $t\bar{t}$ in the region, and ensure the signal contribution is negligible.

Residual other backgrounds, estimated by Monte Carlo simulated samples, were subtracted before comparing the data to the top background Monte Carlo prediction. Corrections were applied to the $Z +$ jets samples as described in Section 7.6.3. A dedicated set of normalisation factors for $W +$ jets samples was derived in a control region defined as the top control region but with a b-tagging requirement instead of a b-veto.

Figure 7.8 shows distributions for the basic kinematic distributions in the OS and SS top control regions with all corrections applied to the top and $W +$ jets background components applied. The various contributions were estimated with the same method that was used for the derivation of the corrections factors. Generally the agreement of the data with the background prediction is good.

Figure 7.9 shows the distributions with all background contributions estimated with *OS-rSS* method. The agreement of the data is good.

7.6.6 Diboson background

Diboson backgrounds were fully estimated from Monte Carlo simulated samples, with data-driven corrections described in Section 7.1 only applied. This background was in fact found to be subleading in all regions of phase space considered.

A summary of the parameters used for the background estimation with the *OS-rSS* method at preselection and in the *boosted* category is given in Table 7.4. Figure 7.10 shows the basic kinematic variables at preselection. The agreement of data with the background prediction is very good apart for m_MMC, for which the same comments as in Section 7.6.2 apply.

7.7 The *fake factor* method

For the background estimation in the *VBF* category a different method was used, as the statistics in the SS region was a limiting factor to the application of *OS-rSS*. The basic
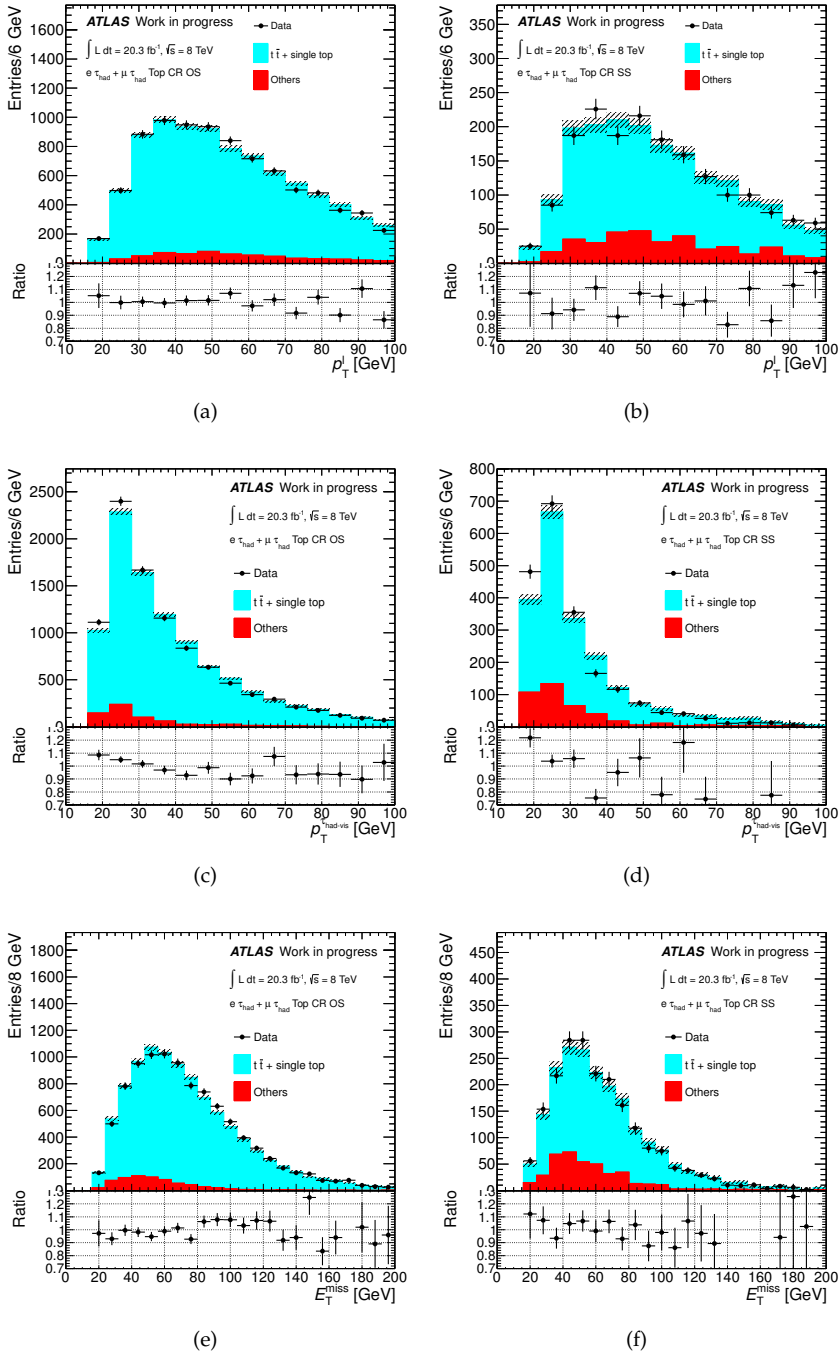
Figure 7.8: Distributions in the (a-c-e) OS and (b-d-f) SS top control regions. (a-b) lepton p_{T}, (c-d) $\tau_{\mathrm{had\text{-}vis}}$ p_{T} and (e-f) $E_{\mathrm{T}}^{\mathrm{miss}}$ distributions. More details are given in the text.
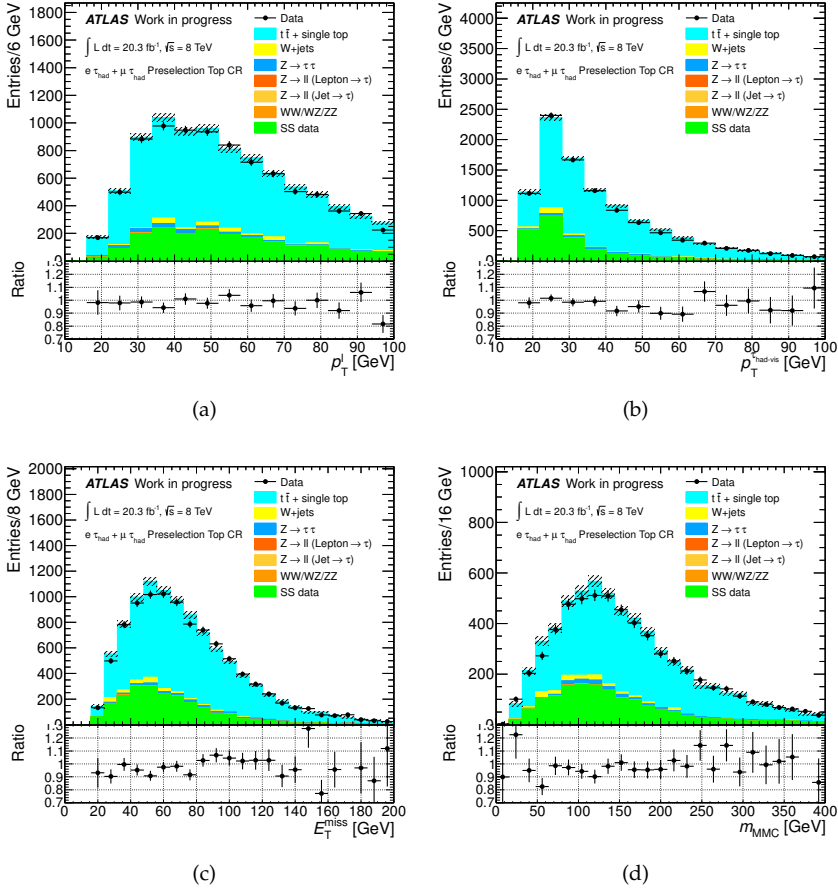
Figure 7.9: Distributions in the top control region. All background contributions were estimated with the *OS-rSS* method. (a) lepton p_T, (b) $\tau_{\text{had-vis}}$ p_T, (c) E_T^{miss} and (d) m_{MMC} distributions.

Parameter	Preselection	Boosted
r_{QCD}	1.05 ± 0.15	
$k_{Z \to \tau^+ \tau^-}$	1 (fixed)	
Embedding normalisation $\tau_\mu \tau_{\mathrm{had}}$ SLT	0.542 ± 0.003	
Embedding normalisation $\tau_\mu \tau_{\mathrm{had}}$ LTT	0.549 ± 0.003	
Embedding normalisation $\tau_e \tau_{\mathrm{had}}$ SLT	0.676 ± 0.006	
Embedding normalisation $\tau_e \tau_{\mathrm{had}}$ LTT	0.676 ± 0.006	
$k_{Z \to ll(\to \tau_{\mathrm{had\text{-}vis}})}$	1 (fixed)	
$k_{Z \to ll(\mathrm{jet} \to \tau_{\mathrm{had\text{-}vis}})}$	0.832 ± 0.007	
$k_{W+\mathrm{jets}}\ \tau_\mu \tau_{\mathrm{had}}$ OS	0.808 ± 0.003	0.691 ± 0.003
$k_{W+\mathrm{jets}}\ \tau_\mu \tau_{\mathrm{had}}$ SS	0.937 ± 0.006	0.89 ± 0.07
$k_{W+\mathrm{jets}}\ \tau_e \tau_{\mathrm{had}}$ OS	0.853 ± 0.004	0.828 ± 0.004
$k_{W+\mathrm{jets}}\ \tau_e \tau_{\mathrm{had}}$ SS	1.012 ± 0.007	1.07 ± 0.09
$k_{W+\mathrm{jets}}\ \tau_\mu \tau_{\mathrm{had}}$ OS for Top CR	0.91 ± 0.02	
$k_{W+\mathrm{jets}}\ \tau_\mu \tau_{\mathrm{had}}$ SS for Top CR	1.05 ± 0.03	
$k_{W+\mathrm{jets}}\ \tau_e \tau_{\mathrm{had}}$ OS for Top CR	1.04 ± 0.03	
$k_{W+\mathrm{jets}}\ \tau_e \tau_{\mathrm{had}}$ SS for Top CR	1.15 ± 0.03	
k_{Top} OS	0.84 ± 0.01	
k_{Top} SS	0.96 ± 0.03	
k_{VV}	1 (fixed)	

Table 7.4: Parameters for the *OS-rSS* background estimation at preselection and in the *boosted* category. Uncertainties are statistical only except for r_{QCD}.
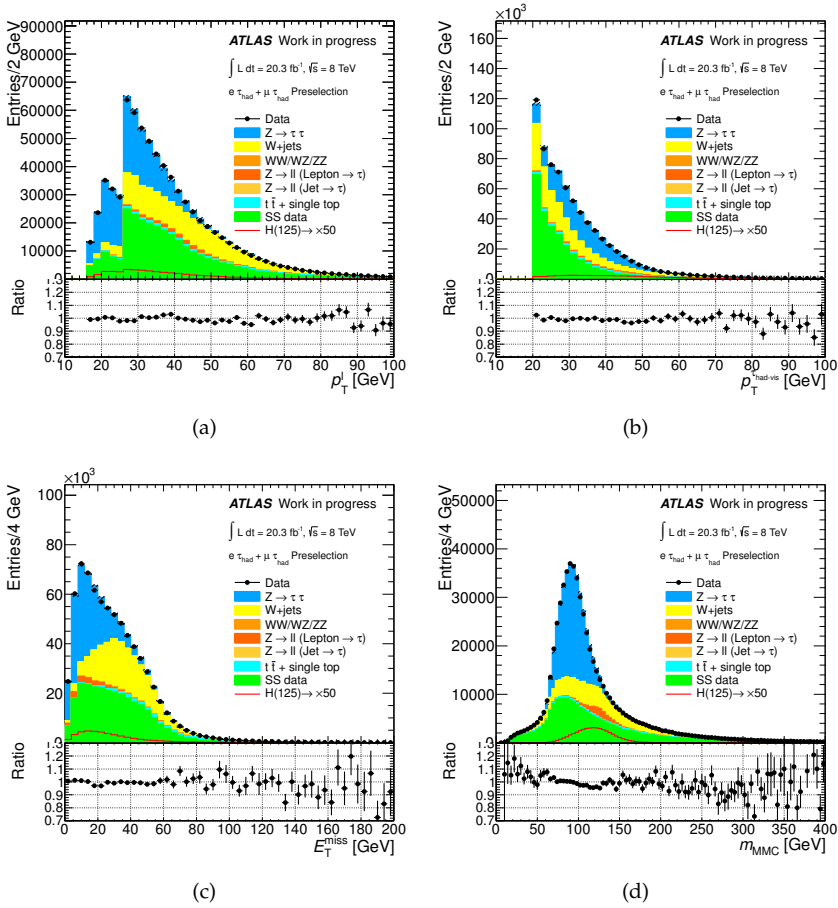
Figure 7.10: Distributions at preselection: (a) lepton p_{T}, (b) $\tau_{\mathrm{had\text{-}vis}}$ p_{T}, (c) $E_{\mathrm{T}}^{\mathrm{miss}}$ and (d) m_{MMC}. All background contributions were estimated with the *OS-rSS* method.

idea of the *fake factor* method is to estimate the multi-jet and W+jets backgrounds, which are essentially due to jets faking the $\tau_{\text{had-vis}}$ signature, using a control region where the $\tau_{\text{had-vis}}$ identification criteria are reversed. This *anti-tau* control region was defined by the following requirements:

- preselection defined in Section 7.2.1, except $\tau_{\text{had-vis}}$ identification was not applied,

- an event is considered separately for each occurrence of a $\tau_{\text{had-vis}}$ candidate failing the $\tau_{\text{had-vis}}$ identification and all relevant event variables except $E_{\text{T}}^{\text{miss}}$ were recomputed according to the $\tau_{\text{had-vis}}$ hypothesis considered,

- the lepton and candidated $\tau_{\text{had-vis}}$ have opposite sign charges,

- same cuts as the categorisation and additional cuts for the *VBF* category.

It should be noted that the *fake factor* method can not be used for LTT events, since $\tau_{\text{had-vis}}$ identification is used at trigger level and this prevents the definition of a valid *anti-tau* region.

The transfer factor from the *anti-tau* region to the signal region is given by the $\tau_{\text{had-vis}}$ identification fake rate, so that the estimate of the background component due to multi-jet and W + jets events is given, for each m_{MMC} bin by:

$$N_{FF} = f_{FF} N_{\text{anti-tau}} \tag{7.12}$$

where $N_{\text{anti-tau}}$ is the number of events in the *anti-tau* region, once other electroweak and $t\bar{t}$ backgrounds have been subtracted, and f_{FF} is defined as the ratio between the events passing the $\tau_{\text{had-vis}}$ identification and those failing it. It was measured in data as explained in the following.

Specific fake factors were needed to account for the different jet flavour composition in W + jets and multi-jet events. The W + jets background is richer in fake $\tau_{\text{had-vis}}$ due to jets initiated by quarks than the multi-jet background. Quark and gluon initiated jets have different characteristics, which make it more probable for the first to fake the $\tau_{\text{had-vis}}$ signature than for the latter.

The f_{FF} factor was therefore obtained as a combination of fake factors for multi-jet and W + jets events, denoted as $f_{\text{multi-jet}}$ and $f_{W+\text{jets}}$ respectively, as

$$f_{FF} = R_{W+\text{jets}}\, f_{W+\text{jets}} + \left(1 - R_{W+\text{jets}}\right) f_{\text{multi-jet}} \tag{7.13}$$

where $R_{W+\text{jets}}$ is given by

$$R_{W+\text{jets}} = \frac{N_{\text{anti-tau}}^{W+\text{jets est}}}{N_{\text{anti-tau}}^{W+\text{jets est}} + N_{\text{anti-tau}}^{\text{multi-jet est}}} \tag{7.14}$$

where $N_{\text{anti-tau}}^{W+\text{jets est}}$ and $N_{\text{anti-tau}}^{\text{multi-jet est}}$ are the estimated numbers of W + jets and multi-jet events respectively. These numbers were estimated as:

$$N_{\text{anti-tau}}^{W+\text{jets est}} = N_{\text{anti-tau, WCR}}^{\text{data}} \frac{N_{\text{anti-tau}}^{W+\text{jets, MC}}}{N_{\text{anti-tau, WCR}}^{W+\text{jets, MC}}} \tag{7.15}$$

$$N_{\text{anti-tau}}^{\text{multi-jet est}} = N_{\text{anti-tau}}^{\text{data}} - \left(N_{\text{anti-tau}}^{W+\text{jets est}} + N_{\text{anti-tau}}^{EW+t\bar{t}} \right) \tag{7.16}$$

To estimate the number of $W + $ jets events in the *anti-tau* region an additional control region enriched in $W + $ jets events was used. The number of events in this *anti-tau WCR* is denoted as $N_{\text{anti-tau, WCR}}^{\text{data}}$, and the transfer factor to the *anti-tau* region was estimated using $W + $jets Monte Carlo simulation and considering the ratio of events in the *anti-tau* region $N_{\text{anti-tau}}^{W+\text{jets, MC}}$ and *anti-tau WCR* region $N_{\text{anti-tau, WCR}}^{W+\text{jets, MC}}$. The *anti-tau WCR* region was defined as

- preselection defined in Section 7.2.1, except $\tau_{\text{had-vis}}$ identification was not applied,

- an event is considered separately for each occurrence of a $\tau_{\text{had-vis}}$ candidate failing the $\tau_{\text{had-vis}}$ identification and all relevant event variables except $E_{\text{T}}^{\text{miss}}$ were recomputed according to the $\tau_{\text{had-vis}}$ hypothesis considered,

- category cuts:

    - *VBF* category: same cuts as the categorisation for the *VBF* category and $m_{\text{T}} > 70\,\text{GeV}$.

The number of multi-jet events was taken as the difference between the total number of events in the *anti-tau* region and the estimated number of $W + $ jets and other EW and $t\bar{t}$ background events.

The fake factor for $W + $ jets events was computed using the numbers of events in the *anti-tau WCR* and in a region defined in the same way except the usual preselection and identification of $\tau_{\text{had-vis}}$ was applied. The fake factor for multi-jet events was computed in analogous regions, where instead of requiring a high transverse mass, the preselection requirements were modified. In particular for the $\tau_\mu \tau_{\text{had}}$ channel events with muons failing the isolation requirements were considered. In the $\tau_e \tau_{\text{had}}$ events with electrons failing the *tight* identification requirements but satisfying *loose* identification were used.

Besides using the *fake factor* method in the *VBF* category is was necessary to complement the $Z \to \tau^+\tau^-$, $Z + $jets and $W + $jets background samples used at various stages of the background estimation with high statistics samples generated with filters for VBF-like topologies (see Section 7.1). The predictions of $Z + $ jets were compared to data in a $Z \to l^+l^-$ control region defined by the presence of two same flavour leptons satisfying the analysis object selection criteria with invariant mass $|m_{ll} - 91.2\,\text{GeV}| < 15\,\text{GeV}$. A reweighting was performed of the $\Delta\eta_{jj}$ variable in order to correctly describe the $\Delta\eta_{jj}$ and m_{jj} distributions [4]. Since a 10% normalisation bias was observed after the *VBF* jet selections, the samples were rescaled by a 1.1 ± 0.1 factor.

The full background estimation in the signal region for the *VBF* category with the *fake factor* method reads:

$$N_{\text{OS}}^{\text{bkg}} = f_{FF} \left(N_{\text{anti-tau}}^{\text{data}} - N_{\text{anti-tau}}^{\text{EW} + t\bar{t}, \text{MC}} \right) + N_{\text{OS}}^{Z \to \tau\tau} +$$
$$+ N_{\text{OS}}^{Z \to ll(\to \tau_{\text{had-vis}})} + N_{\text{OS}}^{Z \to ll+\text{jet}(\to \tau_{\text{had-vis}})} + N_{\text{OS}}^{\text{top}} + N_{\text{OS}}^{\text{VV}} \tag{7.17}$$

where the $N_{\text{OS}}^{Z \to \tau\tau}$, $N_{\text{OS}}^{Z \to ll(\to \tau_{\text{had-vis}})}$, $N_{\text{OS}}^{Z \to ll + \text{jet}(\to \tau_{\text{had-vis}})}$, $N_{\text{OS}}^{\text{top}}$ and $N_{\text{OS}}^{\text{VV}}$ were defined in a way analogous to the add-on terms of the *OS-rSS* method, that is with the same general methodology described for each background term but using only the OS part of each term instead of the full $OS-rSS$ add-on. Embedding samples were used for the estimation of the $Z \to \tau^+\tau^-$ term. The $k_{Z \to ll(\text{jet} \to \tau_{\text{had-vis}})}$ factor was computed in a region and with the method described in Section 7.6.3, and was measured as $k_{Z \to ll(\text{jet} \to \tau_{\text{had-vis}})} = 0.75 \pm 0.02$ (uncertainty statistical only). The term $N_{\text{anti-tau}}^{\text{EW} + t\bar{t}, \text{MC}}$ includes contributions from $Z \to \tau^+\tau^-$ $Z +$ jets, top and diboson backgrounds estimated even in this case in a way analogous to that detailed for the *OS-rSS* add-on terms. In this case the Monte Carlo simulation prediction of $Z \to \tau^+\tau^-$ was used.

Figure 7.11 shows distributions for a region selected as the *VBF* categorisation but with the charge correlation requirement inverted. The comparison is not optimal since the same f_{FF} factors were used as the signal region, while in this region a larger fraction of fakes due to $W +$ jets events is expected. Allowing for the very low statistics, the comparison of the data with the prediction is good, supporting the validity of the *fake factor* method.

Figure 7.12 shows instead distributions in a $W +$ jets control region, built with the following requirements:

- *VBF* categorisation, as described in Section 7.3,

- $m_{\text{T}} > 70 \, \text{GeV}$,

- b-jet veto.

the same comments made for the SS control region apply.
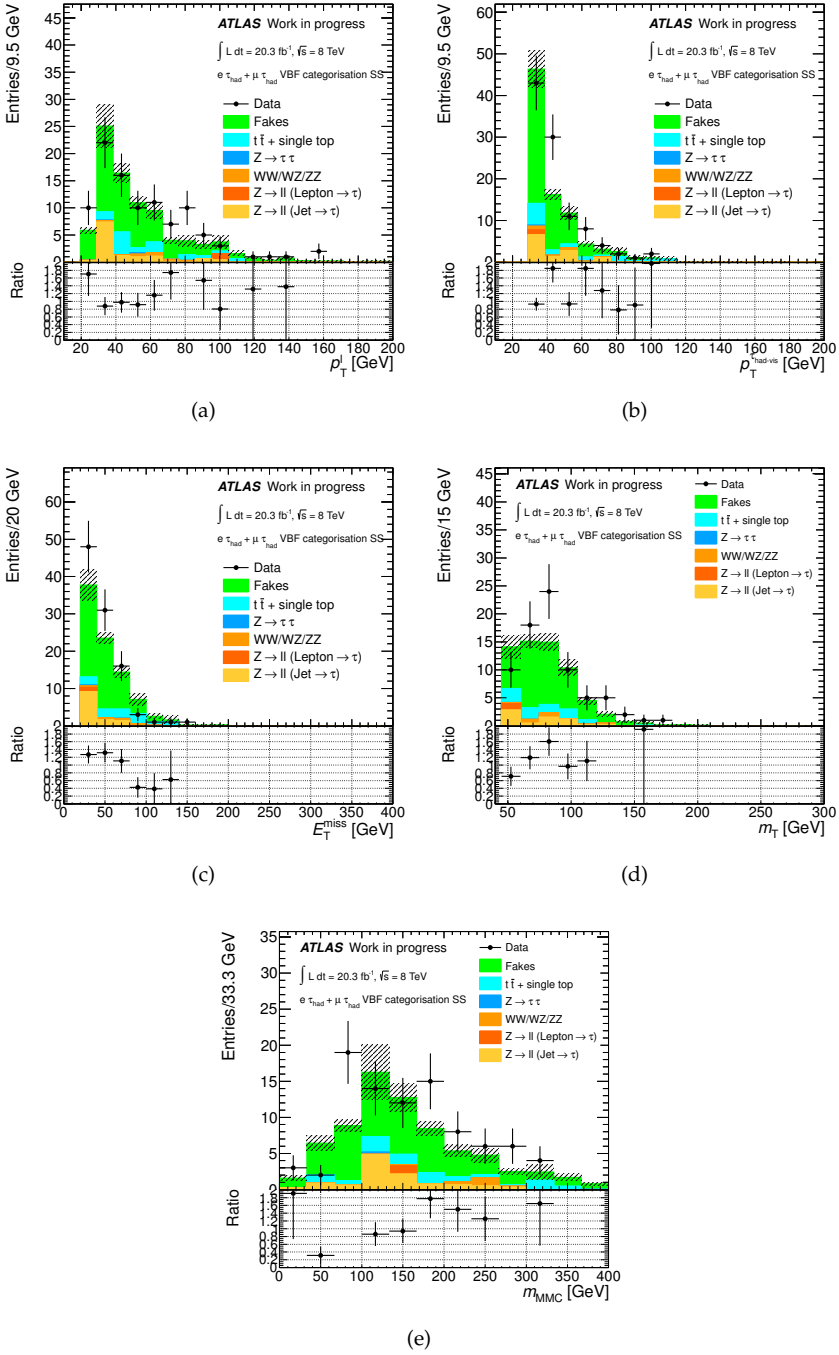
Figure 7.11: Distributions in the *VBF* SS control region: (a) lepton p_{T}, (b) $\tau_{\mathrm{had\text{-}vis}}$ p_{T}, (c) $E_{\mathrm{T}}^{\mathrm{miss}}$, (d) m_{T} and (e) m_{MMC}.

(a)

(b)

(c)

(d)
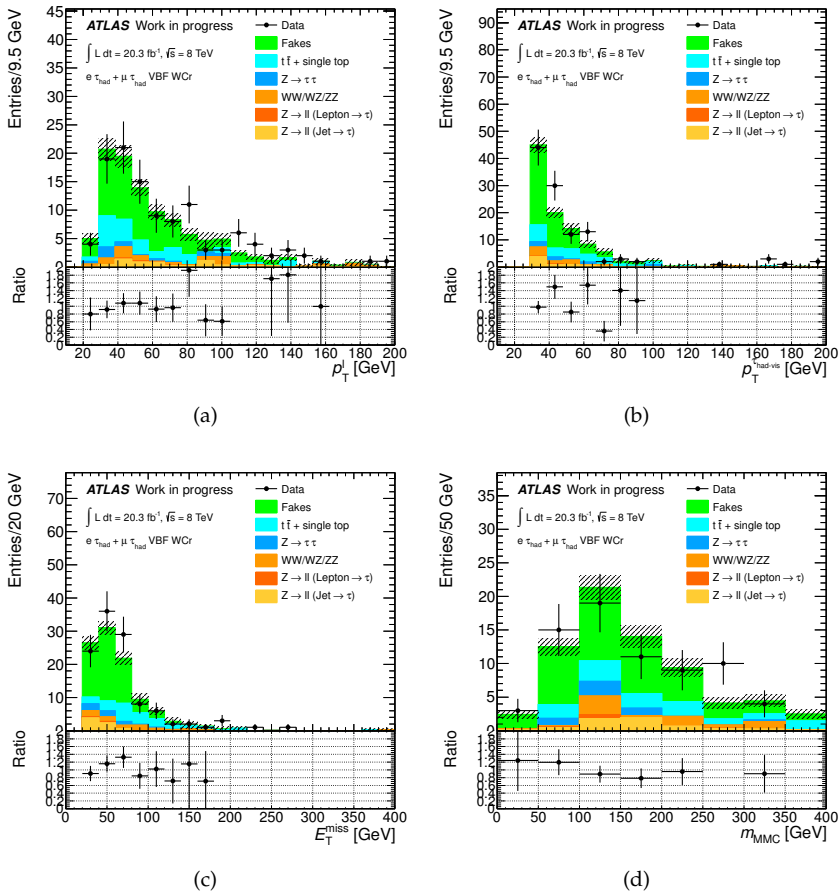
Figure 7.12: Distributions in the *VBF W* + jets control region: (a) lepton p_T, (b) $\tau_{\text{had-vis}}$ p_T, (c) E_T^{miss}, (d) m_{MMC}.

7.8   Control distributions and signal region yields

Since the analysis is blind checks were made at the categorisation level and in dedicated $Z \rightarrow \tau^+\tau^-$ control regions. These control regions were built as the signal regions but with the following additional requirements:

- $m_T < 40\,\text{GeV}$,

- $m_{\text{MMC}} < 110\,\text{GeV}$,

it was checked that these cuts correspond to $< 20\%$ signal efficiency for both categories. Throughout this section the uncertainty band on the background prediction in the plots is statistical only.

Figure 7.13 shows the basic kinematic variables for the *boosted* category at categorisation level, while Figure 7.14 shows variables that are used for background suppression. The agreement of the data with the background prediction is very good. It can be seen that the major background after $Z \rightarrow \tau^+\tau^-$ is the top background, which is mostly rejected by the b-tagging requirement. The $\Delta\Delta R$ and m_T distributions have rejection power as well. The distributions in the $Z \rightarrow \tau^+\tau^-$ control region shown in Figure 7.15 show a good agreement between the data and the background prediction as well.

Figure 7.19 shows the blinded m_{MMC} distribution in the *boosted* signal region. The peak of $Z \rightarrow \tau^+\tau^-$ is narrow, with few tails extending in the upper mass region, and well reconstructed at the expected position. The other residual backgrounds, mostly due to fakes, have a small contribution and have a quite flat distribution. A $m_H = 125\,\text{GeV}$ signal would appear as a tiny excess laying over the right side of the $Z \rightarrow \tau^+\tau^-$ mass spectrum. The expected yields in the signal region are summarised in Table 7.5. The top, $Z \rightarrow ll + \text{jet}(\rightarrow \tau_{\text{had-vis}})$, $Z \rightarrow ll(\rightarrow \tau_{\text{had-vis}}$ and diboson components were added together as they are in the final fit model. The uncertainties are statistical only.

Component	*Boosted* region yield	VBF region yield
$Z \rightarrow \tau^+\tau^-$	3412 ± 36	56 ± 4
SS/fakes	270 ± 17	11 ± 1
$W + \text{jets}$	148 ± 18	
Rest	191 ± 11	12 ± 2
Total background	4022 ± 364	79 ± 16
VBF H(125)	10.78 ± 0.09	6.55 ± 0.07
ggF H(125)	34.2 ± 0.5	1.5 ± 0.1
WH H(125)	3.85 ± 0.07	0.05 ± 0.004
ZH H(125)	1.91 ± 0.04	0.04 ± 0.002
Total signal	50.7 ± 0.5	8.1 ± 0.2

Table 7.5: Expected yields in the signal regions.

(a)

(b)

(c)
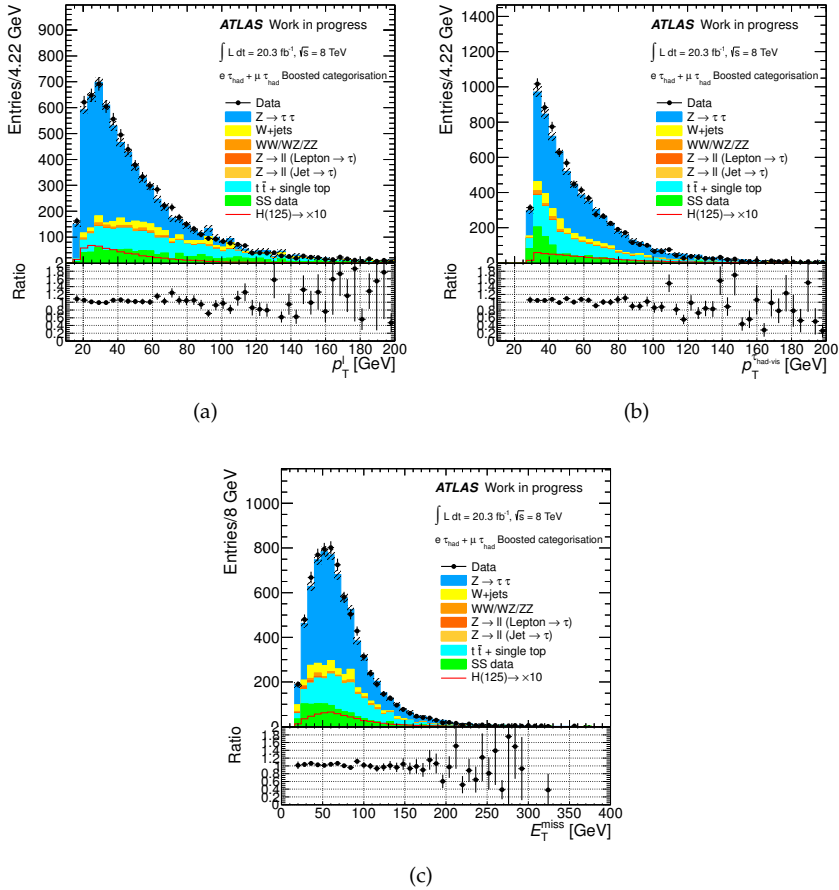
Figure 7.13: Distributions of kinematic variables in the *boosted* category at categorisation level: (a) lepton p_T, (b) $\tau_{\text{had-vis}} p_T$ and (c) E_T^{miss}.
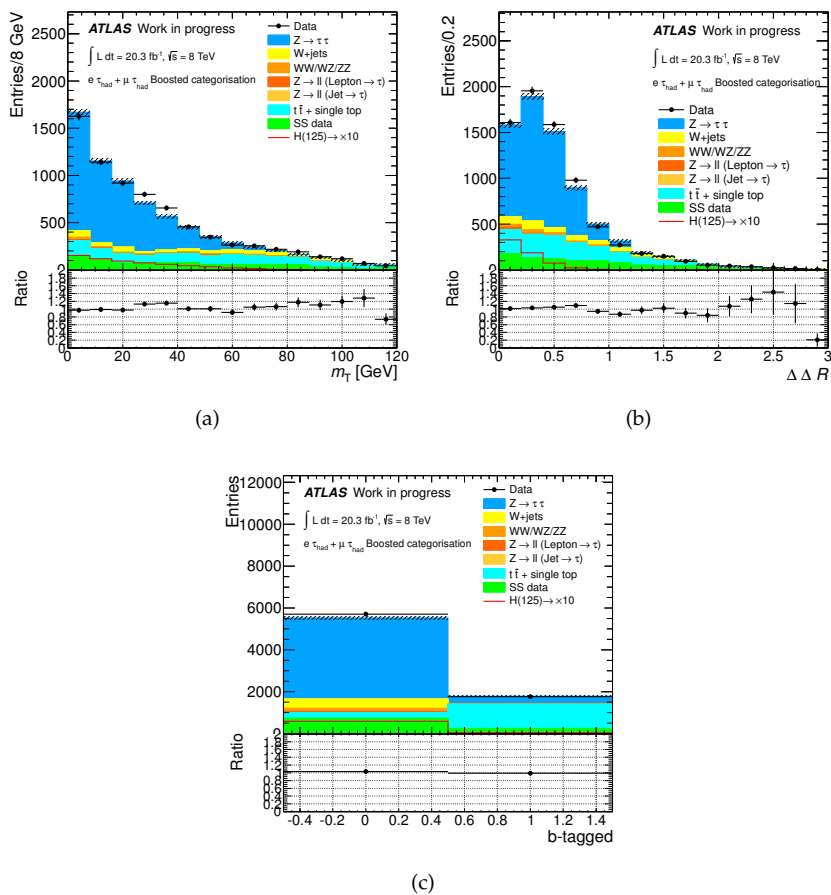
Figure 7.14: Variables used for background suppression in the *boosted* category: (a) m_T, (b) $\Delta\Delta R$ and (c) b-tagging (0 for events with no b-tagged jets and 1 for events with at least one b-tagged jet).
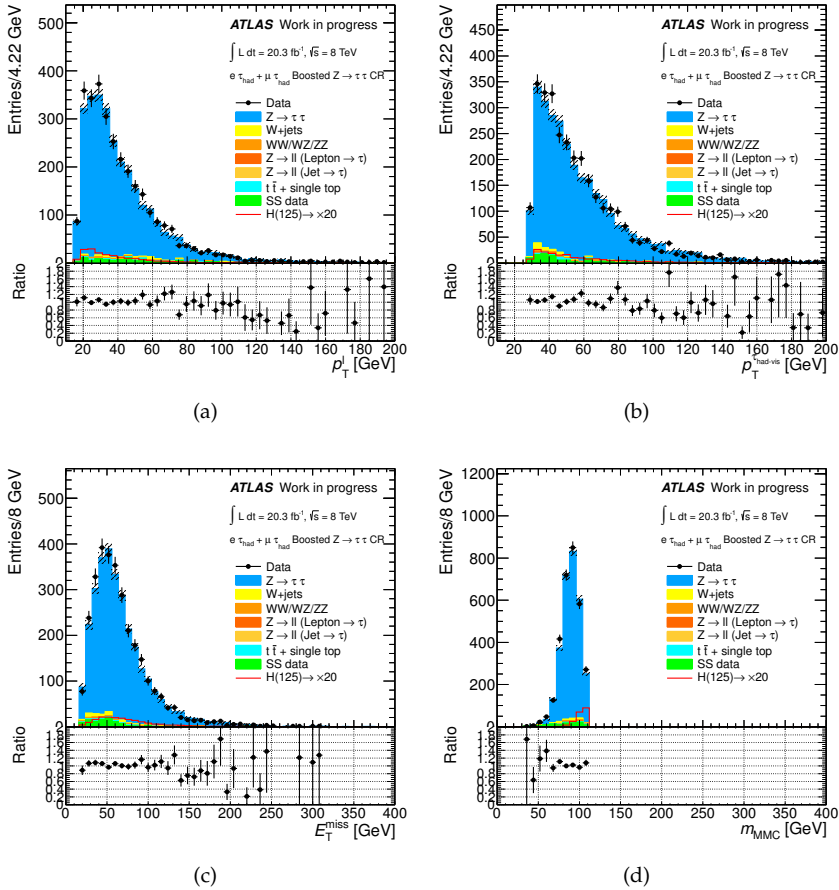
Figure 7.15: Distributions of kinematic variables in the *boosted* $Z \rightarrow \tau^+\tau^-$ control region: (a) lepton p_{T}, (b) $\tau_{\mathrm{had\text{-}vis}}p_{\mathrm{T}}$, (c) $E_{\mathrm{T}}^{\mathrm{miss}}$ and (d) m_{MMC}.

Figure 7.16 shows the basic kinematic variables for the *VBF* category at categorisation level, while Figure 7.17 shows variables that are used for background suppression. The agreement of the data with the background prediction is good. In this case the backgrounds due to $Z \to \tau^+\tau^-$, top and fakes are all important. Cut variables are sensitive in disciminating against fakes and top especially. Figure 7.18 shows some basic distributions in the $Z \to \tau^+\tau^-$ control region, for which the agreement between data and the background prediction is good.

Figure 7.20 shows the blinded m_{MMC} distribution in the *VBF* signal region. The statistics is extremely reduced with respect to the *boosted* category, but a $m_H = 125\,\mathrm{GeV}$ signal would appear as a more sizeable excess enlarging the $Z \to \tau^+\tau^-$ mass spectrum on the larger mass side. The expected yields in the signal region are summarised in Table 7.5. The top, $Z \to ll + \mathrm{jet}(\to \tau_{\mathrm{had\text{-}vis}})$, $Z \to ll(\to \tau_{\mathrm{had\text{-}vis}}$ and diboson components were added together as they are in the final fit model. The uncertainties are statistical only.

7.9 Systematic uncertainties

Several sources of systematic uncertainty that could affect the analysis results, both through effects on the normalisation of the signal and background estimates and on the m_{MMC} distribution were considered. Large emphasis is given to the description of jet energy scale systematics. More details about the effect of the systematic uncertainties are given in Appendix A.

7.9.1 Luminosity

The uncertainty on the total integrated luminosity of the data sample considered is $\pm 2.8\%$, which was determined with the same methodology as described in Ref. [132], from a preliminary calibration of the luminosity scale derived from beam-separation scans performed in November 2012. The uncertainty applied to all steps of signal and background predictions that involved a rescaling by the luminosity.

7.9.2 Pile-up

An uncertainty on the description of the pile-up in the simulation arises from the limited knowledge of the description of the vertex multiplicity in minimum bias vertex multiplicity in soft collision events. It was derived from data and is $\pm 3\%$.

7.9.3 Trigger efficiencies

Trigger efficiencies were measured with tag-and-probe methods (see Sections 2.3.2, 2.3.3, 2.3.5). The uncertainties on the factors applied to correct the Monte Carlo simulated samples were varied to obtain the effect on the analysis. For combined triggers the uncertainties on the efficiencies of the two legs were considered uncorrelated.

(a)

(b)

(c)
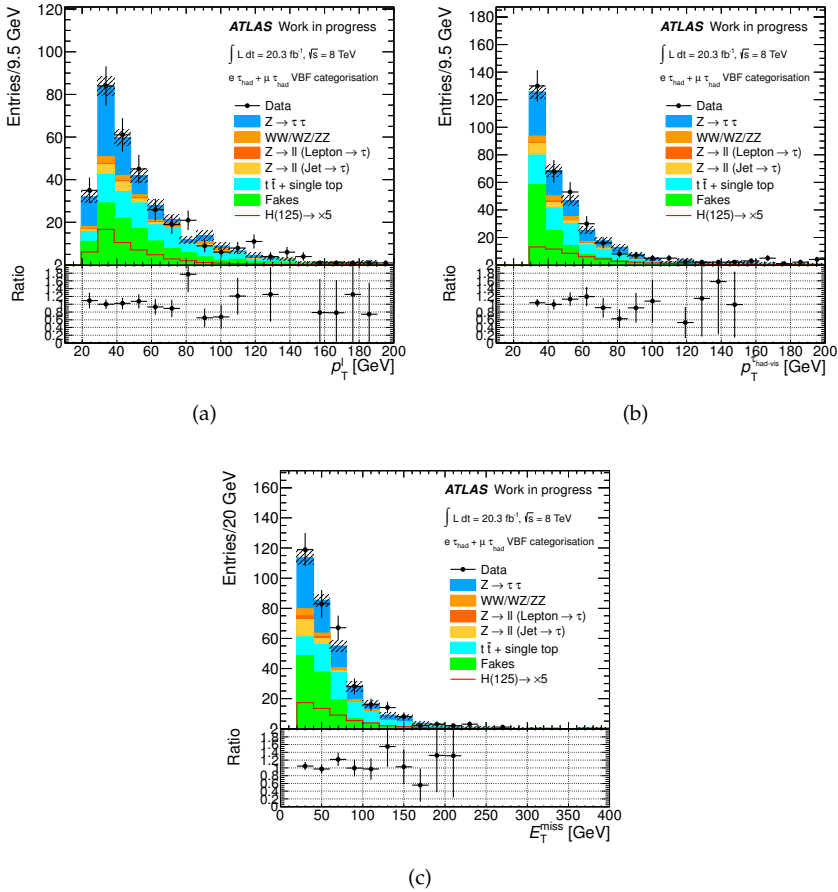
Figure 7.16: Distributions of kinematic variables in the *VBF* category at categorisation level: (a) lepton p_T, (b) $\tau_{\text{had-vis}} p_T$ and (c) E_T^{miss}.
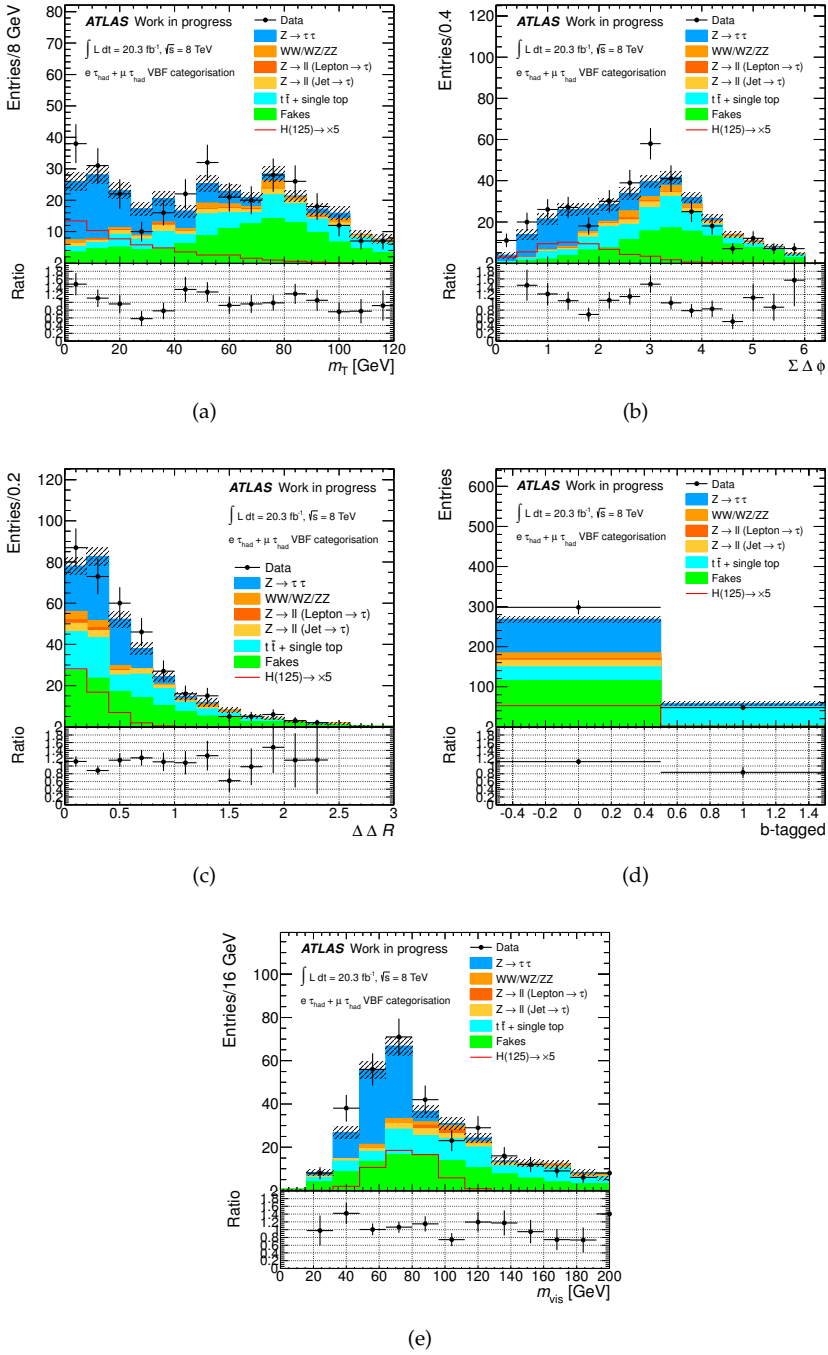
Figure 7.17: Variables used for background suppression in the *VBF* category: (a) m_{T}, (b) $\Sigma\Delta\phi$, (c) $\Delta\Delta R$, (d) b-tagging (0 for events with no b-tagged jets and 1 for events with at least one b-tagged jet) and (e) m_{vis}.
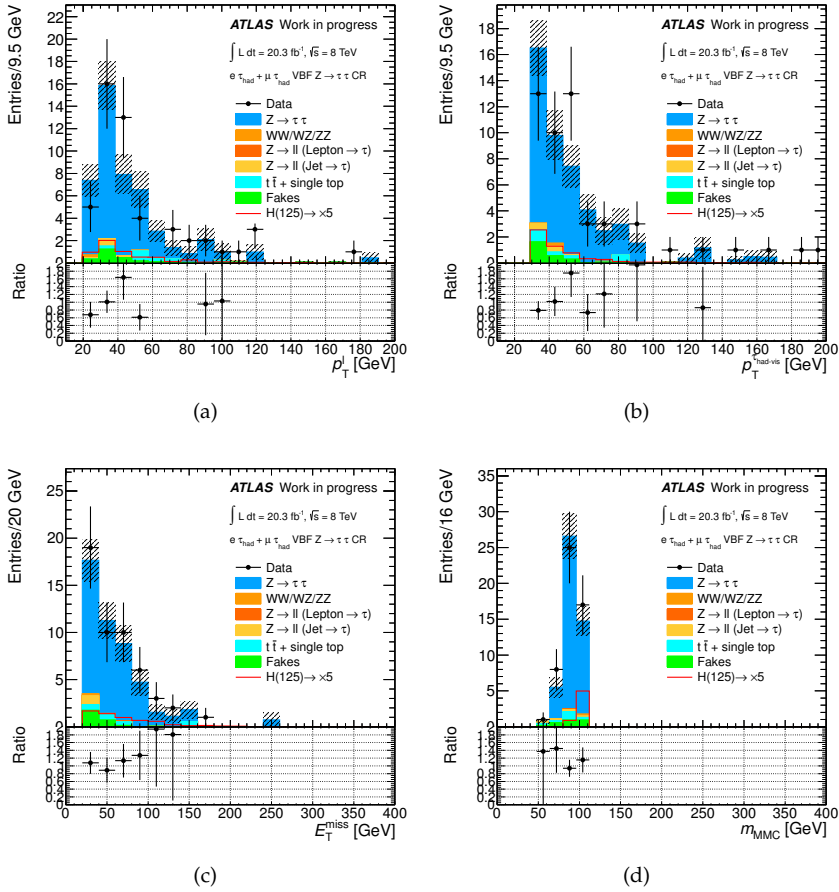
Figure 7.18: Distributions of kinematic variables in the *VBF* $Z \to \tau^+\tau^-$ control region: (a) lepton p_{T}, (b) $\tau_{\mathrm{had\text{-}vis}}p_{\mathrm{T}}$, (c) $E_{\mathrm{T}}^{\mathrm{miss}}$ and (d) m_{MMC}.
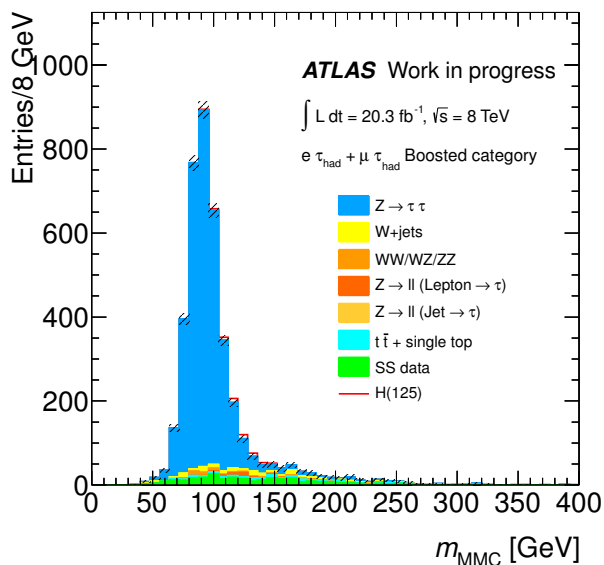
Figure 7.19: Blinded m_{MMC} mass distribution for the *boosted* category.
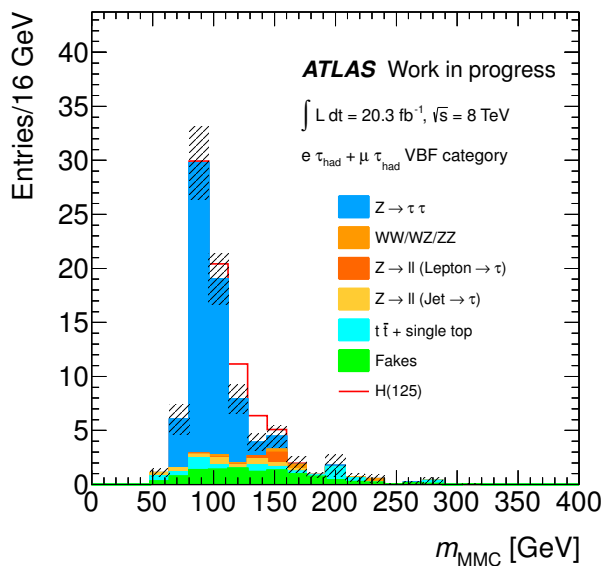
Figure 7.20: Blinded m_{MMC} mass distribution for the *VBF* category.

7.9.4   Electrons

Uncertainties for the reconstruction, identification and isolation efficiencies, determined with tag-and-probe methods were considered. The energy scale and resolution were constrained through studies of the $Z \to e^+e^-$ peak (see Section 2.3.2 and references therein). The uncertainties were applied as scalings and smearings of the electron energies respectively to obtain the effect on the analysis.

7.9.5   Muons

Uncertainties for the reconstruction, identification and isolation efficiencies, determined with tag-and-probe methods were considered. The momentum scale and resolution were constrained through studies of the $Z \to \mu^+\mu^-$ peak (see Section 2.3.3 and references therein). The uncertainties were applied as scalings and smearings of the muon momentum respectively to obtain the effect on the analysis.

7.9.6 $\tau_{\text{had-vis}}$

Uncertainties in the identification efficiency of $\tau_{\text{had-vis}}$ were studied with a $Z \to \tau^+\tau^-$ tag-and-probe analysis (see Section 2.3.5 and references therein). The uncertainties on the rate at which electrons fake the $\tau_{\text{had-vis}}$ signature were derived from a $Z \to e^+e^-$ tag-and-probe analysis (see Section 2.3.5 and references therein). The uncertainties on the factors applied to correct the Monte Carlo simulated samples were applied only on reconstructed $\tau_{\text{had-vis}}$ matched to the correct object at generator level. Only electrons from W, Z and τ decays were considered among generator level electrons for the matching. The uncertainty on the $\tau_{\text{had-vis}}$ energy scale (TES) has been already discussed in Section 2.3.5, Chapter 6 (see references therein as well). The uncertainty used for the analysis was derived from a study analogous to that summarised in Section 6.2. In the analysis the TES uncertainty was decorrelated between true and fake $\tau_{\text{had-vis}}$ candidates.

7.9.7   Jets

The uncertainty on the jet energy scale (JES) has already been partly discussed in Section 2.3.4. The reduction scheme for the sources of uncertainty presented in Table 2.3 was considered.

The effect on yields and shapes of the various uncertainty components was studied and only the relevant ones were retained. The reduction was intended to avoid introducing statistical noise in the signal extraction fit, while preserving the information on the jet energy scale systematic uncertainty. A set of components to be considered as normalisation uncertainties was selected studying for each signal and background component and in each category which uncertainties were relevant and significant. Relevance was defined by requiring the uncertainty to be at least 10% of the leading JES component, while a component was considered significant if at least as large as two times the statistical uncertainty on the shift between nominal and systematically varied yields. This statistical uncertainty was calculated considering the correlation between nominal and systematically varied samples but neglecting two-way migrations. It was tested that the

	Normalisation	Shape
JES_Statistical_1	✓	
JES_Statistical_2		
JES_Statistical_3		
JES_Detector_1	✓	
JES_Detector_2		
JES_Detector_3		
JES_Modelling_1	✓	✓
JES_Modelling_2		
JES_Modelling_3		
JES_Modelling_4		
JES_Mixed_1		
JES_Mixed_2		

Table 7.6: Summary of the in-situ components of the JES uncertainty considered.

	Normalisation	Shape
JES_ EtaIntercalibration Modelling	✓	✓
JES_ EtaIntercalibration StatMethod	✓	

Table 7.7: Summary of the η intercalibration components of the JES uncertainty considered.

sum in quadrature of the dropped components had little importance when compared to the other components.

The effect on the m_{MMC} distribution was found to be often comparable with the MC samples statistical fluctuations. Therefore a further reduction scheme was employed for shape uncertainties. Insight on this was obtained with a test based on the χ^2 of the systematically varied histogram and the nominal histogram, as well as the number of bins with up and down variations in the same direction with respect to the nominal. For signal a list of 7 JES shape-changing terms as shown in Tables 7.6-7.10 was used.

The different JES uncertainties include:

In-situ jet energy corrections uncertainty. The components in this group accounted for bin-to-bin correlations in jet calibration and corrections derived from in-situ techniques, and correspond to groups of physical sources. These components were treated as fully correlated between categories and analysis channels. Table 7.6 summarises the uncertainties components that were considered.

η intercalibration uncertainty. The uncertainty in the intercalibration in different detector pseudorapidity regions has a modelling and a statistical component. The uncertainties were retained as described in Table 7.7. The uncertainties were treated as fully correlated between analysis channels and categories.

	Normalisation	Shape
JES_FlavResp	✓	✓
JES_FlavComp	✓	✓

Table 7.8: Summary of the flavour components of the JES uncertainty considered.

Group	Processes
Quark dominated	VBFH, VH, top, diboson
Gluon dominated	ggFH, V+jets

Table 7.9: Correlation groups for JES_FlavComp uncertainty.

High-P_T jets uncertainty. The component affects only high-P_T ($P_T > 800$ GeV) and is not relevant for any of the analysis channels.

Non-closure uncertainty. The component would affect jets in samples different from the samples used to derive the calibration. Since all samples used in the analysis are of the same type as those used to derive the calibration (full simulation of the detector effects) this source of uncertainty was not considered.

Flavour composition and response uncertainties. These uncertainty components arise from the fact quark-initiated and gluon-initiated jets have different calorimeter responses, and moreover the knowledge of the quark-gluon composition is limited. The uncertainty pertains to light jets only (no b-jets). Conservatively the composition was taken to be $(50 \pm 50)\%$. A summary of how the uncertainties were retained is given in Table 7.8. Since it is known that background and signal components can be more quark or more gluon dominated, two different nuisance parameters were considered as described in Table 7.9. The same background process can enter a different group according to the channel since the mechanism by which the signal signature is faked can be different. These uncertainty components were treated as fully correlated between categories, analysis channels and years.

b-jets uncertainty. The component affects only truth b-jets, and is exclusive with respect to flavour response and composition uncertainties. The uncertainty was applied only as a normalisation uncertainty. The uncertainty was fully correlated between categories.

Uncertainties due to pile-up. The uncertainties due to in-time and out-of-time pile-up (parametrised in terms of μ, the average number of interactions per bunch crossing and NPV, the number of primary vertices) were treated as fully correlated between analysis channels and categories. Two components were then considered for this uncertainty. One component accounted for residual P_T dependence of the correction as a function of NPV and μ, but it was found to be unimportant. The other accounted for residual dependence on the underlying event of the jet energy

Group	Processes
qq initiated	VH, VBF, diboson
qg initiated	V+jets
gg initiated	ggF, top

Table 7.10: Correlation groups for JES_PiluepRhoTopology uncertainty.

	Normalisation	Shape
JES_PileupNPv	✓	
JES_PileupMu	✓	
JES_PileupPt		
JES_PileupRhoTopology	✓	

Table 7.11: Summary of the pile-up components of the JES uncertainty considered.

scale following jet-area based pile-up correction. This uncertainty component was treated as correlated only within three groups differing by initial state, as described in Table 7.10. Table 7.11 summarises which pile-up uncertainty components were retained.

A one-sigma upwards variation in the jet energy resolution was obtained by smearing the energy of every jet with a smearing factor accounting for the uncertainty obtained from resolution in-situ measurement based on a di-jet selection [114].

An uncertainty on the effect of the *JVF* selection cut applied for jets was applied, derived from $Z + $ jets studies.

Uncertainties on b-tagging efficiencies and mistag rates were applied to jets initiated by b-quarks, c-quarks and light quarks or gluons. Their derivation is summarised in Section 2.3.6.

7.9.8 $E_{\mathrm{T}}^{\mathrm{miss}}$

Since the $E_{\mathrm{T}}^{\mathrm{miss}}$ is constructed from the transverse components of the momenta of several objects, when considering systematic variations in the objects they were propagated to the $E_{\mathrm{T}}^{\mathrm{miss}}$ calculation. In addition uncertainties on the $E_{\mathrm{Tmiss,SoftTerm}}$ resolution and scale were considered. These uncertainties were derived as described in Section 2.3.7 and references therein.

7.9.9   Embedding systematics

Two sources of systematic uncertainty affect the embedding procedure: systematics due to the selection of the initial $Z \rightarrow \mu^+\mu^-$ sample in data and systematics affecting the subtraction of muon energy deposits in the calorimeter. To assess the effect of these sources of uncertainty alternative samples with the following requirements were generated:

Variation of the isolation requirements A sample with no muon isolation requirement and a tighter isolation requirement were generated. For the latter the sum of the p_{T} of the tracks in a $\Delta R < 0.2$ cone was required to be smaller than 6% of the muon p_{T} and additionally the sum of the calorimeter deposits in a $\Delta R < 0.2$ cone around the muon were required to be smaller than 4% of the muon p_{T}.

Variation of the muon energy subtraction A conservative estimation was obtained generating samples with the subtracted muon energy in the calorimeter cells varied by 20%.

7.9.10   Background estimation

Several sources of systematic uncertainty arising from the background estimation methods were considered.

Uncertainties on r_{QCD}

Systematic uncertainties on the r_{QCD} value were obtained by varying the track isolation requirement, changing the $\tau_{\mathrm{had\text{-}vis}}$ isolation requirement in the control region varying the extraction fit range and exchanging the roles of the track and calorimeter isolation requirements. The total uncertainty was obtained by the quadrature sum of these uncertainties and was taken to be symmetric.

Uncertainties on the *k-factors*

The limited statistics in the various control regions results in systematic uncertainties in the computed *k-factors* appearing in the add-on terms of both the *OS-rSS* and *fake factor* method. All systematic uncertainties listed beforehand were propagated through the full *k-factors* derivation, so that they are taken into account in the final varied background predictions.

Uncertainties in the $W +$ jets add-on shape correction functions

The statistical uncertainties in the fit performed to derive the shape correction functions for the $W +$ jets add-on described in Section 7.6.4 were considered as systematic uncertainties in the analysis of categories where the background estimation was performed with the *OS-rSS* method. The uncertainties for the $p_{\mathrm{T}}^{l}/p_{\mathrm{T}}^{\tau_{\mathrm{had\text{-}vis}}}$ and $\Delta\eta(l, \tau_{\mathrm{had\text{-}vis}})$ reweightings were considered independent.

Uncertainties in the *fake factor* background estimation

A conservative uncertainty of 50% was taken for the estimation of the multi-jet and $W +$ jets background in the *VBF* category with the *fake factor* method. This uncertainty was estimated from the variation in the m_{MMC} distribution when using $R_{W+\mathrm{jets}} = 0$ and $R_{W+\mathrm{jets}} = 1$.

Normalisation of background estimations with filtered samples

A conservative 10% uncertainty on the normalisation of background estimations with VBF filtered samples was considered as a consequence of the normalisation mismodelling described in Section 7.7. The impact on the analysis is expected to be marginal, since this uncertainty affected only minor aspects of the background estimation procedure.

Extrapolation uncertainties Possible effects of extrapolation systematics from control regions similar to those used in this analysis to the signal region were checked in [4] and found to have negligible effect.

7.9.11   Theory uncertainties

Theory uncertainties affect the predictions of signal and of the tiny fraction of backgrounds for which the prediction normalisation is obtained by the theory cross-section times the acceptance.

The effect of QCD scale uncertainties (see Sections 1.2.1 and 1.2.3) on inclusive signal predictions was estimated by the Stewart-Tackmann method [138, 182]. In this method the QCD scale uncertainties on the inclusive Higgs $+ \geq n$ jets cross-sections are assumed to be uncorrelated and propagated to exclusive jet bins. The inclusive cross-sections were computed with MCFM 6.3 [183] and by varying μ_R and μ_F in the range

$$\frac{1}{2} \leq \frac{\mu_F}{m_H/2} \leq 2 \quad \frac{1}{2} \leq \frac{\mu_R}{m_H/2} \leq 2 \qquad \text{with constraint} \qquad \frac{1}{2} \leq \frac{\mu_F}{\mu_R} \leq 2 \qquad (7.18)$$

For the total inclusive cross-section the values computed in Ref. [184] were used, and for the 2-jets bin the explicit ggF+2jets calculation was used.

The QCD scale uncertainties for backgrounds were taken from [141] after cross-checking the validity at $\sqrt{s} = 8$ TeV.

The dominant uncertainty in the modelling of the Higgs boson transverse momentum spectrum for ggF production is due to the differences in the effect of the inclusion of full quark mass dependence in POWHEG and MC@NLO. The uncertainty was derived by a comparison between the two generators, after taking care of the differences in shower, PDFs, and QCD scale used by the two generators.

The uncertainty due to the underlying event modelling of signal samples was assessed using samples generated with Perugia 2008 alternative underlying event tune.

Simplified uncertainties for the effect of PDFs were taken from Ref. [184] after cross-checks using MCFM.

The uncertainty on the $H \to \tau^+\tau^-$ branching ratio was taken from Ref. [53].

7.10   Fit model

In order to set limits on the signal cross-section in case an excess was not observed or exclude the background only hypothesis, the profile likelihood method [185] with m_{MMC} as discriminating observable was used. Systematic uncertainties were included as nuisance parameters. The binned likelihood was given by:

$$\mathcal{L}(\mu, \theta) = \prod_{\text{category}} \left[\prod_j \text{Pois}(N_j | \mu s_j + b_j) \text{Constr}(\theta) \right] \qquad (7.19)$$

where:

- μ is the signal strenght parameter (see Section 1.5.3),

- θ are the nuisance parameters, that allow to include systematic uncertainties,

- j runs over the bins of the m_{MMC} spectrum,

- s_j and b_j are the signal expectation for bin j respectively, which depend on the values assumed by the nuisance parameters θ.

- $\mathrm{Pois}(n|\mu)$ indicates the value of a poissonian probability density distribution with mean μ at n,

- $\mathrm{Constr}(\theta)$ indicates the gaussian or log-normal constraint for the nuisance parameter θ.

The test statistics q_μ was built according to the profile likelihood ratio:

$$q_\mu = -2\ln \frac{\mathcal{L}(\mu, \hat{\hat{\vec{\theta}}})}{\mathcal{L}(\hat{\mu}, \hat{\vec{\theta}})} \tag{7.20}$$

where $\hat{\mu}$ and $\hat{\vec{\theta}}$ are the signal strength and vector of nuisance parameters that maximize the likelihood respectively, whereas $\hat{\hat{\vec{\theta}}}$ is the vector of nuisance parameters that maximize the likelihood for a given μ.

The spectra of m_{MMC} entering the fit spanned the $[0, 400]$ GeV range with the following binnings:

VBF **category**:
$[0, 60, 80, 90, 100, 110, 120, 130, 150, 180, 400]$ GeV
Boosted **category**:
$[0, 80, 90, 95, 100, 105, 110, 115, 118, 121, 124, 127, 130, 135, 140, 145, 160, 180, 200, 400]$ GeV

The top, $Z \to ll + \mathrm{jet}(\to \tau_{\mathrm{had\text{-}vis}})$, $Z \to ll(\to \tau_{\mathrm{had\text{-}vis}}$ and diboson components were added to a single background component to mitigate low statistics negative effects in the fit. The normalisation of the $Z \to \tau^+\tau^-$ background was allowed to float freely. Because of the high number of nuisance parameters, the fit is subject to numerical instabilities. Therefore a procedure to regularize the fit behaviour was implemented. At first their effect on the fit was separated in a normalization and shape effect. All systematic uncertainties described in Section 7.9 were included as overall normalisation uncertainties provided their effect was larger than 0.5%. In order to avoid the inclusion of shape systematics that were dominated by statistical noise, while avoiding the accidental removal of genuine ones, smoothing and pruning criteria were applied as studied in the context of [4]. The implementation of the fit machinery was based on `HistFactory` in the *RooStat* package [186].

The fit was checked using an Asimov dataset [185] and was found to yield coherent results.

7.11 Results

Expected limits on the ratio of the Higgs boson cross-section times $H \to \tau^+\tau^-$ branching ratio with respect to the SM expectation were obtained using the CLs method [187] at 95% confidence level in the asymptotic approximation [185] and are shown in Figure 7.21 as a function of the Higgs mass hypothesis. The expected limit at $m_H = 125$ GeV is $1.30^{+0.69}_{-0.36}$. Figure 7.21(a) shows the limit for the two categories combined with $\pm 1, 2\sigma$ bands that account for all statistical and systematic uncertainties. Figure 7.21(b) shows the limits for the individual categories as well.

Figure 7.22 instead shows the expected significance of a SM Higgs boson decaying to two tau leptons as a function of mass, the expected significance at $m_H = 125$ GeV is 1.8σ. Even in this case both the combined significance and the significance for the individual categories is shown. As expected the *VBF* category is the most sensitive, but the *boosted* category has a large contribution to the combined significance as well.

7.12 Summary

A cut-based analysis for the search of $H \to \tau_{\text{lep}}\tau_{\text{had}}$ on 20.3 fb^{-1} of ATLAS data collected in 2012 has been presented. The analysis is still kept blind. It is estimated that upper limits on the cross-section times $H \to \tau^+\tau^-$ branching ratio of a SM Higgs boson with $m_H = 125$ GeV could be set to $1.30^{+0.69}_{-0.36}$ times the SM expectation. Moreover it is estimated that the same SM Higgs boson would give rise to a data excess with a significance of 1.8σ.

Cut-based results are useful in complementing MVA analyses with several respects. In the case of $H \to \tau^+\tau^-$, cut-based analyses for all of the $H \to \tau^+\tau^-$ decay channels are still being finalised to support the MVA result, during the development of which there has been continuos exchange between the analyses. The MVA analysis has recently provided a first evidence in ATLAS for the $H \to \tau^+\tau^-$ decay with an observed significance of 4.1σ (3.2σ expected). The best fitted signal strength for the MVA analysis is $\mu = 1.4^{+0.5}_{-0.4}$.

Figure 7.23(a) shows the event yields as a function of $\log(S/B)$, where the signal to background ratio S/B was taken from each event's bin in the MVA discriminator used in the analysis. The data excess can be seen in the last highes S/B bins and is compared both to the $\mu = 1$ and $\mu = 1.4$ expectation. Figure 7.23(b) instead shows a distribution of m_{MMC} obtained weighting the events by $\ln(1 + S/B)$ for all the analysis channels. The excess appears in a position comparable to that expected from a $m_H = 125$ GeV Higgs boson decaying to two tau leptons.
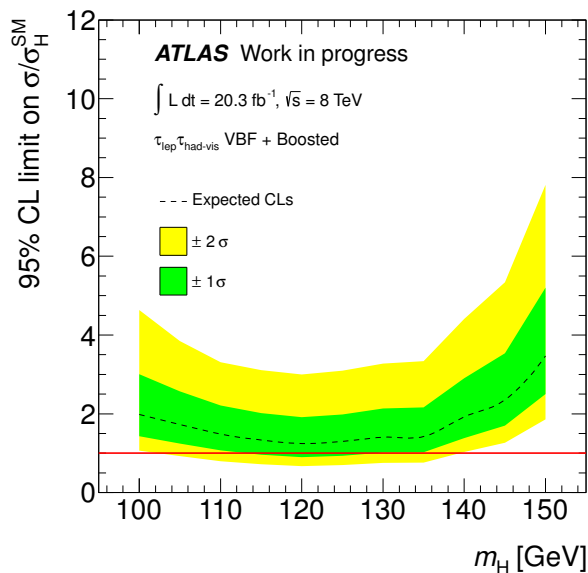
(a)
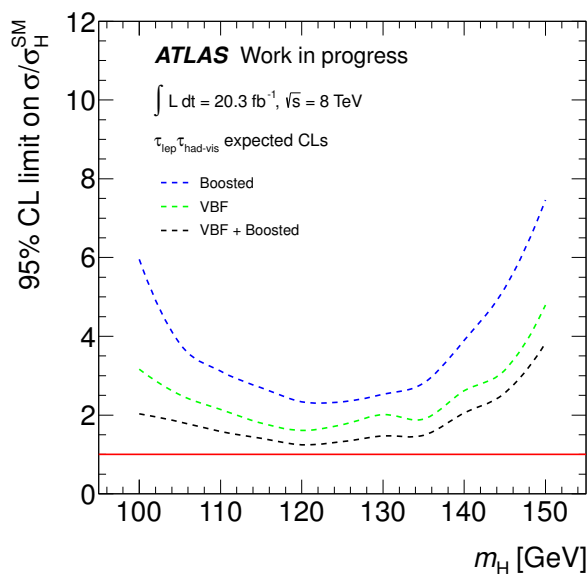
(b)

Figure 7.21: Expected limits on the ratio of the Higgs boson cross-section times $H \to \tau^+\tau^-$ branching ratio with respect to the SM expectation.
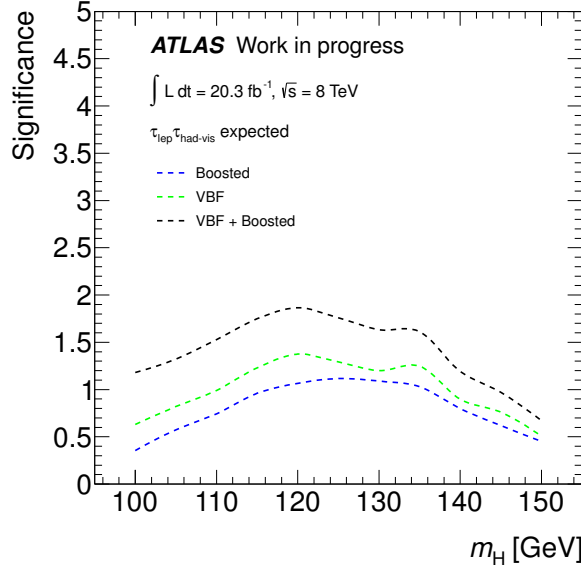
Figure 7.22: Expected significances for a SM Higgs boson decaying to two tau leptons.
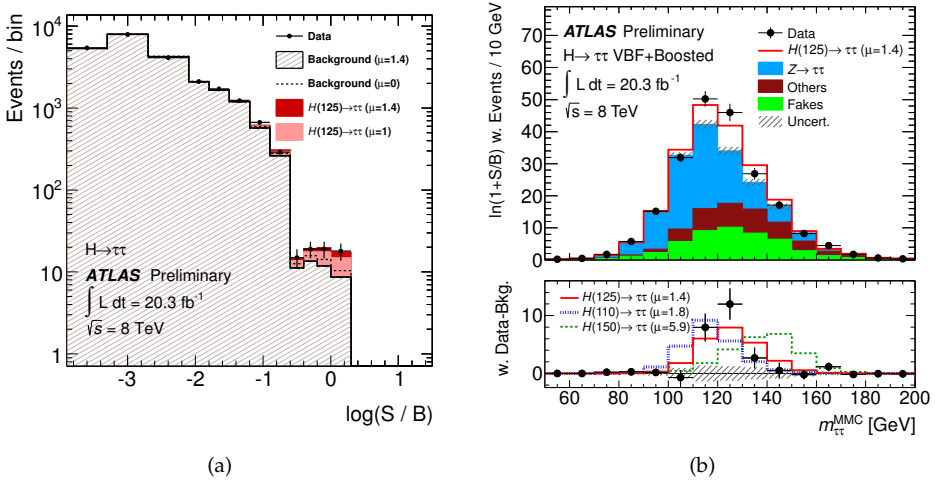
Figure 7.23: (a) event yields as a function of $\log(S/B)$ and (b) distribution of m_{MMC} obtained weighting the events by $\ln(1 + S/B)$ for the ATLAS $H \to \tau^+\tau^-$ MVA analysis [4]. More details are given in the text.

Conclusions

In this work several aspects of the study of di-tau topologies at ATLAS on the data collected during LHC Run-I have been presented. The study of these topologies is experimentally very challenging in the environment of hadron colliders, but it is crucial to the success of the ATLAS Higgs boson physics program.

The very first study in ATLAS real data that allowed to make a measurement in di-tau topologies was the measurement of the cross-section of the $Z \to \tau^+ \tau^-$ process in 36 pb^{-1} of data collected at $\sqrt{s} = 7$ TeV during 2010. The cross-section in the $[66, 116]$ GeV mass window was measured to be 0.97 ± 0.07 (stat) ± 0.06 (syst) ± 0.03 (lumi) nb, in agreement both with theoretical prediction and measurements performed by the CMS collaboration and in other Z boson decay channels. The methodology and theory aspects of this measurement in particular have been discussed.

Hadronically decaying tau leptons play a crucial role in the study of di-tau topologies. Their reconstruction and identification in the detector involves both tracking and calorimetry aspects, that were object of performance preparatory studies.

The ATLAS Pixel detector is designed to provide accurate information on the particle crossing-point in the detector, which allows to obtain an excellent performance of the measurement of the impact parameter of tracks and of the reconstruction of secondary vertices. This information allows to build variables capable of discriminating hadronically decaying tau leptons, whose decay products come from a secondary vertex, from QCD jets, which mainly consist of primary particles. The performance of the determination of the crossing-points of particles in the detector can be improved by dedicated algorithms. In particular the charge sharing clusterisation algorithm and a neural network based algorithms have been discussed. The calibration of the charge sharing algorithm with late 2010 data allowed to improve the resolution in some special cases that were not optimally treated in previous calibrations. The neural network based algorithm instead was designed particularly to recover performance losses in the dense environments typical of hadronically decaying tau leptons and high transverse momentum jets. It has been shown that the improvement in the performance can be large, for example the resolution along the *local-x* coordinate for 4-row clusters was measured in data to improve from 48μm for the charge sharing clustering to 26μm for the neural network based algorithm. In general the performance of the ATLAS measurement of the

tracks impact parameter and of the reconstruction of secondary vertices is improved by the introduction of this approach.

The reconstruction of hadronically decaying tau leptons relies on calorimeter information as well. In particular the measurement of the energy is completely calorimeter based. The determination of the energy response of the detector to hadronically decaying tau leptons is a delicate and crucial task. The calibration strategy used in 2011 and in 2012 samples has been reviewed, together with the baseline determination of the scale uncertainty. An in-situ method for the uncertainty determination, based on the analysis of $Z \to \tau^+\tau^-$ data was developed. The method is based on the sensitivity of the mass reconstructed from visible tau lepton decay products in events where one lepton decays leptonically and the other hadronically. It was first employed in ATLAS real data on a dataset corresponding to 4.26 fb^{-1} collected at $\sqrt{s} = 7$ TeV in 2011, allowing to cross-check the pseudorapidity intercalibration of hadronically decaying tau leptons, measuring a difference in scale between $\tau_{\text{had-vis}}$ pseudorapidity region $|\eta_\tau| < 0.8$ and $0.8 < |\eta_\tau| < 2.47$ of $(3.0 \pm 2.6)\%$. This result allowed to strengthen the confidence in the simulation description of the detector response in regions not covered by test-beam data and to prove the analysis concept, which was re-iterated and complemented on data collected in 2012. Even if the information on the tau energy scale given by this in-situ method is inclusive, and does not allow to separate the various sources of uncertainty, it is deemed to be and important piece of information on one of the most important experimental uncertainties in the study of di-tau topologies.

Since the reconstruction of mass is a complex and crucial task in the study of di-tau topologies, validation studies and preliminary studies for the improvement of the mass reconstruction algorithm used in ATLAS have been presented.

The search for Higgs boson decays to two tau leptons is one of the main motivations for the study of di-tau topologies at ATLAS. The preparatory studies already mentioned have been part of the path that culminated in the evidence of the existence of the $H \to \tau^+\tau^-$ process obtained at ATLAS. The analysis is based on a multi-variate strategy complemented by cut-based results for the different channels. A cut-based analysis for the search of $H \to \tau_{\text{lep}}\tau_{\text{had}}$ process is presented. The analysis shares several points in common with the ATLAS multi-variate results, as the analyses have been developed in close contact and continuous exchange of information. The expected significance of an excess is expected to be 1.8σ, still insufficient to claim for evidence even if an excess is present. The role of a cut-based analysis is however not to be undervalued and is not merely confined to confirm the multi-variate results. Rather, the simplicity of this approach could allow in the future a more straightforward handling of the mass measurement, theory uncertainties and more challenging data-taking conditions of LHC Run-II.

Bibliography

[1] ATLAS Collaboration, *A search for high mass resonances decaying to $\tau^+\tau^-$ in the ATLAS detector*, ATLAS-CONF-2012-067, CERN, Geneva, Jul, 2012. https://cds.cern.ch/record/1460263.

[2] ATLAS Collaboration, *Performance of the ATLAS Detector using First Collision Data*, JHEP **1009** (2010) 056, arXiv:1005.5254 [hep-ex].

[3] https://twiki.cern.ch/twiki/bin/view/AtlasPublic.

[4] *Evidence for Higgs Boson Decays to the $\tau^+\tau^-$ Final State with the ATLAS Detector*, ATLAS-CONF-2013-108, CERN, Geneva, Nov, 2013. http://cds.cern.ch/record/1632191.

[5] D. Perkins, *Introduction to high energy physics*. Cambridge University Press, Cambridge, 2000.

[6] J. Aitchison and A. Hey, *Gauge theories in particle physics: a practical introduction*. Hilger, Bristol, 1989.

[7] R. Cahn and G. Goldhaber, *The experimental foundations of particle physics*. Cambridge University Press, Cambridge, 2009.

[8] J. Beringer and et al. (Particle Data Group), *The Review of Particle Physics*, Phys. Rev. D **86** (2012, and 2013 partial update for the 2014 edition.) no. 010001, . http://pdg.lbl.gov/.

[9] http://users.phys.psu.edu/~cteq/.

[10] https://nnpdf.hepforge.org/.

[11] http://durpdg.dur.ac.uk/hepdata/mrs.html.

[12] T. Sjostrand, S. Mrenna, and P. Z. Skands, *PYTHIA 6.4 Physics and Manual*, JHEP **0605** (2006) 026, arXiv:hep-ph/0603175 [hep-ph].

[13] T. Sjostrand, S. Mrenna, and P. Z. Skands, *A Brief Introduction to PYTHIA 8.1*, Comput.Phys.Commun. **178** (2008) 852–867, `arXiv:0710.3820 [hep-ph]`.

[14] `http://www.thep.lu.se/~torbjorn/Pythia.html`.

[15] G. Corcella, I. Knowles, G. Marchesini, S. Moretti, K. Odagiri, et al., *HERWIG 6: An Event generator for hadron emission reactions with interfering gluons (including supersymmetric processes)*, JHEP **0101** (2001) 010, `arXiv:hep-ph/0011363 [hep-ph]`.

[16] M. Bahr, S. Gieseke, M. Gigg, D. Grellscheid, K. Hamilton, et al., *Herwig++ Physics and Manual*, Eur.Phys.J. **C58** (2008) 639–707, `arXiv:0803.0883 [hep-ph]`.

[17] T. Gleisberg, S. Hoeche, F. Krauss, M. Schonherr, S. Schumann, et al., *Event generation with SHERPA 1.1*, JHEP **0902** (2009) 007, `arXiv:0811.4622 [hep-ph]`.

[18] The ATLAS Collaboration, *Further ATLAS tunes of PYTHIA6 and Pythia 8*, ATL-PHYS-PUB-2011-014, CERN, Geneva, Nov, 2011. `http://cds.cern.ch/record/1400677`.

[19] The ATLAS Collaboration, *Summary of ATLAS Pythia 8 tunes*, ATL-PHYS-PUB-2012-003, CERN, Geneva, Aug, 2012. `http://cds.cern.ch/record/1474107`.

[20] M. L. Mangano, M. Moretti, F. Piccinini, R. Pittau, and A. D. Polosa, *ALPGEN, a generator for hard multiparton processes in hadronic collisions*, JHEP **0307** (2003) 001, `arXiv:hep-ph/0206293 [hep-ph]`.

[21] S. Frixione and B. R. Webber, *Matching NLO QCD computations and parton shower simulations*, JHEP **0206** (2002) 029, `arXiv:hep-ph/0204244 [hep-ph]`.

[22] P. Nason, *A New method for combining NLO QCD with shower Monte Carlo algorithms*, JHEP **0411** (2004) 040, `arXiv:hep-ph/0409146 [hep-ph]`.

[23] M. Cacciari, G. P. Salam, and G. Soyez, *The Anti-k_t jet clustering algorithm*, JHEP **0804** (2008) 063, `arXiv:0802.1189 [hep-ph]`.

[24] C. Buttar, J. D'Hondt, M. Kramer, G. Salam, M. Wobisch, et al., *Standard Model Handles and Candles Working Group: Tools and Jets Summary Report*, `arXiv:0803.0678 [hep-ph]`.

[25] M. Cacciari, G. P. Salam, and G. Soyez, *FastJet User Manual*, Eur.Phys.J. **C72** (2012) 1896, `arXiv:1111.6097 [hep-ph]`.

[26] M. Cacciari and G. P. Salam, *Dispelling the N^3 myth for the k_t jet-finder*, Phys.Lett. **B641** (2006) 57–61, `arXiv:hep-ph/0512210 [hep-ph]`.

[27] UA1 Collaboration, *Experimental Observation of Isolated Large Transverse Energy Electrons with Associated Missing Energy at $\sqrt{s} = 540\,GeV$*, Phys.Lett. **B122** (1983) 103–116.

[28] UA2 Collaboration, *Observation of Single Isolated Electrons of High Transverse Momentum in Events with Missing Transverse Energy at the CERN anti-p p Collider*, Phys.Lett. **B122** (1983) 476–485.

[29] ALEPH Collaboration, DELPHI Collaboration, L3 Collaboration, OPAL Collaboration, SLD Collaboration, LEP Electroweak Working Group, SLD Electroweak Group, SLD Heavy Flavour Group, *Precision electroweak measurements on the Z resonance*, Phys.Rept. **427** (2006) 257–454, `arXiv:hep-ex/0509008 [hep-ex]`.

[30] M. Grunewald, *Experimental tests of the electroweak standard model at high-energies*, Phys.Rept. **322** (1999) 125–346.

[31] UA1 Collaboration, *Studies of Intermediate Vector Boson Production and Decay in UA1 at the CERN Proton - Antiproton Collider*, Z.Phys. **C44** (1989) 15–61.

[32] K. Melnikov and F. Petriello, *Electroweak gauge boson production at hadron colliders through $O(\alpha(s)^2)$*, Phys. Rev. **D74** (2006) 114017.

[33] R. Gavin, Y. Li, F. Petriello et al., *FEWZ 2.0: A code for hadronic Z production at next-to-next-to- leading order*, `arXiv:1011.3540 [hep-ph]`.

[34] S. Catani, L. Cieri, G. Ferrera, D. de Florian, and M. Grazzini, *Vector boson production at hadron colliders: a fully exclusive QCD calculation at NNLO*, Phys. Rev. Lett. **103** (2009) 082001.

[35] The ATLAS Collaboration, *Measurement of the $W \to \ell\nu$ and $Z/\gamma^* \to \ell\ell$ production cross sections in proton-proton collisions at $\sqrt{s} = 7$ TeV with the ATLAS detector*, JHEP **1012** (2010) 060, `arXiv:1010.2130 [hep-ex]`.

[36] The CMS Collaboration, *Measurement of the Inclusive W and Z Production Cross Sections in pp Collisions at $\sqrt{s} = 7$ TeV*, JHEP **1110** (2011) 132, `arXiv:1107.4789 [hep-ex]`.

[37] The CMS Collaboration, *Inclusive W/Z cross section at 8 TeV*, CMS-PAS-SMP-12-011, CERN, Geneva, 2012. `https://cdsweb.cern.ch/record/1460098`.

[38] F. Englert and R. Brout, *Broken Symmetry and the Mass of Gauge Vector Mesons*, Phys. Rev. Lett. **13** (1964) 321.

[39] P. W. Higgs, *Broken symmetries, massless particles and gauge fields*, Phys. Lett. **12** (1964) 132.

[40] P. W. Higgs, *Broken Symmetries and the Masses of Gauge Bosons*, Phys. Rev. Lett. **13** (1964) 508.

[41] G. S. Guralnik, C. R. Hagen, and T. W. B. Kibble, *Global conservation laws and massless particles*, Phys. Rev. Lett. **13** (1964) 585–587.

[42] T. W. B. Kibble, *Symmetry breaking in non-Abelian gauge theories*, Phys. Rev. **155** (1967) 1554–1561.

[43] S. Weinberg, *A Model of Leptons*, Phys.Rev.Lett. **19** (1967) 1264–1266.

[44] A. Salam, *Weak and Electromagnetic Interactions*, Conf. Proc. **C680519** (1968) 367–377.

[45] J. Ellis, M. K. Gaillard, and D. V. Nanopoulos, *A Historical Profile of the Higgs Boson*, `arXiv:1201.6045 [hep-ph]`.

[46] D. Rainwater, *Searching for the Higgs boson*, `arXiv:hep-ph/0702124 [HEP-PH]`.

[47] M. Spira, *QCD effects in Higgs physics*, Fortsch.Phys. **46** (1998) 203–284, `arXiv:hep-ph/9705337 [hep-ph]`.

[48] A. Djouadi, J. Kalinowski, and M. Spira, *HDECAY: A Program for Higgs boson decays in the standard model and its supersymmetric extension*, Comput.Phys.Commun. **108** (1998) 56–74, `arXiv:hep-ph/9704448 [hep-ph]`.

[49] J. Butterworth, F. Maltoni, F. Moortgat, P. Richardson, S. Schumann, et al., *The Tools and Monte Carlo working group Summary Report*, `arXiv:1003.1643 [hep-ph]`.

[50] A. Bredenstein, A. Denner, S. Dittmaier, and M. Weber, *Precise predictions for the Higgs-boson decay $H \to WW/ZZ \to 4\,leptons$*, Phys.Rev. **D74** (2006) 013004, `arXiv:hep-ph/0604011 [hep-ph]`.

[51] A. Bredenstein, A. Denner, S. Dittmaier, and M. Weber, *Radiative corrections to the semileptonic and hadronic Higgs-boson decays $H \to WW/ZZ \to 4\,fermions$*, JHEP **0702** (2007) 080, `arXiv:hep-ph/0611234 [hep-ph]`.

[52] A. Bredenstein, A. Denner, S. Dittmaier, A. Mück, and M. M. Weber, *Prophecy4f: A Monte Carlo generator for a proper description of the Higgs decay into 4 fermions*, `http://omnibus.uni-freiburg.de/~sd565/programs/prophecy4f/prophecy4f.html,`.

[53] LHC Higgs Cross Section Working Group, *Handbook of LHC Higgs Cross Sections: 3. Higgs Properties*, `arXiv:1307.1347v2 [hep-ph]`.

[54] LHC Higgs Cross Section Working Group, *Handbook of LHC Higgs Cross Sections: 1. Inclusive Observables*, `arXiv:1101.0593 [hep-ph]`.

[55] `https://twiki.cern.ch/twiki/bin/view/LHCPhysics/CrossSections`.

[56] LEP Working Group for Higgs boson searches, ALEPH Collaboration, DELPHI Collaboration, L3 Collaboration, OPAL Collaboration, *Search for the standard model Higgs boson at LEP*, Phys.Lett. **B565** (2003) 61–75, `arXiv:hep-ex/0306033` `[hep-ex]`.

[57] TEVNPH (Tevatron New Phenomena and Higgs Working Group), CDF Collaboration, D0 Collaboration, *Combined CDF and D0 Upper Limits on Standard Model Higgs Boson Production with up to 8.6 fb^{-1} of Data*, `arXiv:1107.5518` `[hep-ex]`.

[58] The ATLAS Collaboration, *Observation of a new particle in the search for the Standard Model Higgs boson with the ATLAS detector at the LHC*, Phys.Lett. **B716** (2012) 1–29, `arXiv:1207.7214 [hep-ex]`.

[59] The CMS Collaboration, *Observation of a new boson at a mass of 125 GeV with the CMS experiment at the LHC*, Phys.Lett. **B716** (2012) 30–61, `arXiv:1207.7235` `[hep-ex]`.

[60] The ATLAS Collaboration, *Measurements of Higgs boson production and couplings in diboson final states with the ATLAS detector at the LHC*, Phys.Lett. **B** (2013) , `arXiv:1307.1427 [hep-ex]`.

[61] The ATLAS Collaboration, *Measurements of the properties of the Higgs-like boson in the two photon decay channel with the ATLAS detector using* 25 fb^{-1} *of proton-proton collision data*, ATLAS-CONF-2013-012, CERN, Geneva, Mar, 2013. `https://cds.cern.ch/record/1523698`.

[62] The CMS Collaboration, *Updated measurements of the Higgs boson at 125 GeV in the two photon decay channel*, CMS-PAS-HIG-13-001, CERN, Geneva, 2013. `http://cds.cern.ch/record/1530524`.

[63] The ATLAS Collaboration, *Measurements of the properties of the Higgs-like boson in the four lepton decay channel with the ATLAS detector using* 25 fb^{-1} *of proton-proton collision data*, ATLAS-CONF-2013-013, CERN, Geneva, Mar, 2013. `https://cds.cern.ch/record/1523699/`.

[64] The CMS Collaboration, *Properties of the Higgs-like boson in the decay H to ZZ to 4l in pp collisions at sqrt s =7 and 8 TeV*, CMS-PAS-HIG-13-002, CERN, Geneva, 2013. `http://cds.cern.ch/record/1523767`.

[65] The ATLAS Collaboration, *Study of the spin properties of the Higgs-like particle in the* $H \rightarrow WW^{(*)} \rightarrow e\nu\mu\nu$ *channel with 21 fb^{-1} of $\sqrt{s} = 8$ TeV data collected with the ATLAS detector.*, ATLAS-CONF-2013-031, CERN, Geneva, Mar, 2013. `http://cds.cern.ch/record/1527127`.

[66] The CMS Collaboration, *Evidence for a particle decaying to W^+W^- in the fully leptonic final state in a standard model Higgs boson search in pp collisions at the LHC*, CMS-PAS-HIG-13-003, CERN, Geneva, 2013. `http://cds.cern.ch/record/1523673`.

[67] The ATLAS Collaboration, *Search for the $b\bar{b}$ decay of the Standard Model Higgs boson in associated W/ZH production with the ATLAS detector*, ATLAS-CONF-2013-079, CERN, Geneva, Jul, 2013. `http://cds.cern.ch/record/1563235`.

[68] CMS Collaboration, *Search for the standard model Higgs boson produced in association with a W or a Z boson and decaying to bottom quarks*, `arXiv:1310.3687 [hep-ex]`.

[69] `https://twiki.cern.ch/twiki/bin/view/CMSPublic/ Hig13004TWikiUpdate`.

[70] The ATLAS Collaboration, *Combined measurements of the mass and signal strength of the Higgs-like boson with the ATLAS detector using up to 25 fb^{-1} of proton-proton collision data*, ATLAS-CONF-2013-014, CERN, Geneva, Mar, 2013. `http://cds.cern.ch/record/1523727`.

[71] The CMS Collaboration, *Combination of standard model Higgs boson searches and measurements of the properties of the new boson with a mass near 125 GeV*, CMS-PAS-HIG-13-005, CERN, Geneva, 2013. `http://cds.cern.ch/record/1542387`.

[72] L. Landau, *On the angular momentum of a two-photon system*, Dokl.Akad.Nauk Ser.Fiz. **60** (1948) 207–209.

[73] C.-N. Yang, *Selection Rules for the Dematerialization of a Particle Into Two Photons*, Phys.Rev. **77** (1950) 242–245.

[74] Y. Gao, A. V. Gritsan, Z. Guo, K. Melnikov, M. Schulze, et al., *Spin determination of single-produced resonances at hadron colliders*, Phys.Rev. **D81** (2010) 075022, `arXiv:1001.3396 [hep-ph]`.

[75] The ATLAS Collaboration, *Evidence for the spin-0 nature of the Higgs boson using ATLAS data*, `arXiv:1307.1432 [hep-ex]`.

[76] The CMS Collaboration, *Study of the Mass and Spin-Parity of the Higgs Boson Candidate Via Its Decays to Z Boson Pairs*, Phys.Rev.Lett. **110** (2013) 081803, `arXiv:1212.6639 [hep-ex]`.

[77] The CMS Collaboration, *Properties of the observed Higgs-like resonance using the diphoton channel*, CMS-PAS-HIG-13-016, CERN, Geneva, 2013. `http://cds.cern.ch/record/1558930`.

[78] DELPHI Collaboration, *Measurements of the leptonic branching fractions of the tau*, Eur.Phys.J. **C10** (1999) 201–218.

[79] S. Jadach, Z. Was, R. Decker, and J. H. Kuhn, *The tau decay library TAUOLA: Version 2.4*, Comput.Phys.Commun. **76** (1993) 361–380.

[80] Z. Was, *TAUOLA the library for tau lepton decay, and KKMC/KORALB/KORALZ/... status report*, Nucl. Phys. Proc. Suppl. **98** (2001) 96–102, `arXiv:hep-ph/0011305`.

[81] P. Golonka and Z. Was, *PHOTOS Monte Carlo: A Precision tool for QED corrections in Z and W decays*, Eur.Phys.J. **C45** (2006) 97–107, `arXiv:hep-ph/0506026 [hep-ph]`.

[82] Z. Czyczula, T. Przedzinski, and Z. Was, *TauSpinner Program for Studies on Spin Effect in tau Production at the LHC*, Eur.Phys.J. **C72** (2012) 1988, `arXiv:1201.0117 [hep-ph]`.

[83] S. Berge, W. Bernreuther, B. Niepelt, and H. Spiesberger, *How to pin down the CP quantum numbers of a Higgs boson in its tau decays at the LHC*, Phys.Rev. **D84** (2011) 116003, `arXiv:1108.0670 [hep-ph]`.

[84] `www.cern.ch`.

[85] F. Gianotti, *Physics at the LHC*, Physics Reports **403** (2004) no. 0, 379 – 399. `http://www.sciencedirect.com/science/article/pii/S0370157304003382`.

[86] The ATLAS Collaboration, *The ATLAS Experiment at the CERN Large Hadron Collider*, JINST **3** (2008) S08003.

[87] The ATLAS Collaboration, *The ATLAS Inner Detector commissioning and calibration*, Eur.Phys.J. **C70** (2010) 787–821, `arXiv:1004.5293 [physics.ins-det]`.

[88] The ATLAS Collaboration, *Readiness of the ATLAS Liquid Argon Calorimeter for LHC Collisions*, Eur.Phys.J. **C70** (2010) 723–753, `arXiv:0912.2642 [physics.ins-det]`.

[89] The ATLAS Collaboration, *Readiness of the ATLAS Tile Calorimeter for LHC collisions*, Eur.Phys.J. **C70** (2010) 1193–1236, `arXiv:1007.5423 [physics.ins-det]`.

[90] The ATLAS Collaboration, *Commissioning of the ATLAS Muon Spectrometer with Cosmic Rays*, Eur.Phys.J. **C70** (2010) 875–916, `arXiv:1006.4384 [physics.ins-det]`.

[91] The ATLAS Collaboration, *Atlas Computing: technical design report*, ATLAS TDR-017, CERN-LHCC-2005-022, Geneva, 2005. `http://cds.cern.ch/record/837738`.

[92] G. Barrand, I. Belyaev, P. Binko, M. Cattaneo, R. Chytracek, et al., *GAUDI - A software architecture and framework for building HEP data processing applications*, Comput.Phys.Commun. **140** (2001) 45–55.

[93] F. Viegas, R. Hawkings, and G. Dimitrov, *Relational databases for conditions data and event selection in ATLAS*, J.Phys.Conf.Ser. **119** (2008) 042032.

[94] The ATLAS Collaboration, *The ATLAS Simulation Infrastructure*, Eur.Phys.J. **C70** (2010) 823–874, `arXiv:1005.4568 [physics.ins-det]`.

[95] GEANT4 Collaboration, S. Agostinelli et al., *GEANT4: A Simulation toolkit*, Nucl.Instrum.Meth. **A506** (2003) 250–303.

[96] J. Allison, K. Amako, J. Apostolakis, H. Araujo, P. Dubois, et al., *Geant4 developments and applications*, IEEE Trans.Nucl.Sci. **53** (2006) 270.

[97] G. Folger and J. Wellisch, *String parton models in GEANT4*, eConf **C0303241** (2003) MOMT007, `arXiv:nucl-th/0306007 [nucl-th]`.

[98] M. Blann, B. Berman, and T. Komoto, *Precompound model analysis of photonuclear reactions*, Phys.Rev. **C28** (1983) 2286–2298.

[99] H. Bertini, *Intranuclear-cascade calculation of the secondary nucleon spectra from nucleon-nucleus interactions in the energy range 340 to 2900 MeV and comparisons with experiment*, Phys.Rev. **188** (1969) 1711–1730.

[100] B. Andersson, G. Gustafson, and B. Nilsson-Almqvist, *A Model for Low p_t Hadronic Reactions, with Generalizations to Hadron-Nucleus and Nucleus-Nucleus Collisions*, Nucl.Phys. **B281** (1987) 289.

[101] T. Golling, H. S. Hayward, P. U. E. Onyisi, H. J. Stelzer, and P. Waller, *The ATLAS Data Quality Defect Database System*, arXiv:1110.6119. EFI-11-30, Oct, 2011.

[102] *ATLAS internal information*, 2013.

[103] T. Cornelissen, M. Elsing, I. Gavrilenko, W. Liebig, E. Moyse, et al., *The new ATLAS track reconstruction (NEWT)*, J.Phys.Conf.Ser. **119** (2008) 032014.

[104] The ATLAS Collaboration, *Performance of primary vertex reconstruction in proton-proton collisions at $\sqrt{s}$ =7 TeV in the ATLAS experiment*, ATLAS-CONF-2010-069, 2010. `http://cds.cern.ch/record/1281344`.

[105] The ATLAS Collaboration, *Expected electron performance in the ATLAS experiment*, ATL-PHYS-PUB-2011-006, CERN, Geneva, Apr, 2011. `http://cds.cern.ch/record/1345327`.

[106] The ATLAS Collaboration, *Electron performance measurements with the ATLAS detector using the 2010 LHC proton-proton collision data*, Eur.Phys.J. **C72** (2012) 1909, `arXiv:1110.3174 [hep-ex]`.

[107] The ATLAS Collaboration, *Improved electron reconstruction in ATLAS using the Gaussian Sum Filter-based model for bremsstrahlung*, ATLAS-CONF-2012-047, CERN, Geneva, May, 2012. `http://cds.cern.ch/record/1449796`.

[108] The ATLAS Collaboration, *Expected Performance of the ATLAS Experiment - Detector, Trigger and Physics*, `arXiv:0901.0512 [hep-ex]`.

[109] The ATLAS Collaboration, *Preliminary results on the muon reconstruction efficiency, momentum resolution, and momentum scale in ATLAS 2012 pp collision data*, ATLAS-CONF-2013-088, CERN, Geneva, Aug, 2013. `http://cds.cern.ch/record/1580207`.

[110] W. Lampl, S. Laplace, D. Lelas, P. Loch, H. Ma, et al., *Calorimeter clustering algorithms: Description and performance*, , 2008. `http://cds.cern.ch/record/1099735`.

[111] ATLAS Liquid Argon EMEC/HEC Collaboration, C. Cojocaru et al., *Hadronic calibration of the ATLAS liquid argon end-cap calorimeter in the pseudorapidity region $1.6 < |\eta| < 1.8$ in beam tests*, Nucl.Instrum.Meth. **A531** (2004) 481–514, `arXiv:physics/0407009 [physics]`.

[112] T. Barillari et al., *Local hadronic calibration*, ATL-LARG-PUB-2009-001-2, 2009. `http://cds.cern.ch/record/1112035`.

[113] The ATLAS Collaboration, *Jet energy scale and its systematic uncertainty in proton-proton collisions at sqrt(s)=7 TeV with ATLAS 2011 data*, ATLAS-CONF-2013-004, CERN, Geneva, Jan, 2013. `http://cds.cern.ch/record/1509552`.

[114] The ATLAS Collaboration, *Jet energy resolution in proton-proton collisions at $\sqrt{s} = 7$ TeV recorded in 2010 with the ATLAS detector*, Eur.Phys.J. **C73** (2013) 2306, `arXiv:1210.6210 [hep-ex]`.

[115] The ATLAS Collaboration, *Measurement of the W to $\tau\nu$ Cross Section in pp Collisions at $\sqrt{s} = 7$ TeV with the ATLAS experiment*, Phys.Lett. **B706** (2012) 276–294, `arXiv:1108.4101 [hep-ex]`.

[116] The ATLAS Collaboration, *Measurement of τ polarization in $W \to \tau\nu$ decays with the ATLAS detector in pp collisions at $\sqrt{(s)} = 7$ TeV*, Eur.Phys.J. **C72** (2012) 2062, `arXiv:1204.6720 [hep-ex]`.

[117] The ATLAS Collaboration, *Measurement of the Z to tau tau Cross Section with the ATLAS Detector*, Phys.Rev. **D84** (2011) 112006, `arXiv:1108.2016 [hep-ex]`.

[118] The ATLAS Collaboration, *Measurement of the top quark pair cross section with ATLAS in pp collisions at $\sqrt{s} = 7$ TeV using final states with an electron or a muon and a hadronically decaying τ lepton*, Phys.Lett. **B717** (2012) 89–108, `arXiv:1205.2067 [hep-ex]`.

[119] The ATLAS Collaboration, *Search for Neutral MSSM Higgs bosons in $\sqrt{s} = 7$ TeV pp collisions at ATLAS*, ATLAS-CONF-2012-094, CERN, Geneva, Jul, 2012. `http://cds.cern.ch/record/1460440`.

[120] The ATLAS Collaboration, *Search for Supersymmetry in Events with Large Missing Transverse Momentum, Jets, and at Least One Tau Lepton in 7 TeV Proton-Proton Collision Data with the ATLAS Detector*, Eur.Phys.J. **C72** (2012) 2215, `arXiv:1210.1314 [hep-ex]`.

[121] The ATLAS Collaboration, *A search for high-mass resonances decaying to $\tau^+\tau^-$ in pp collisions at $\sqrt{s}$ = 7 TeV with the ATLAS detector*, Phys.Lett. **B719** (2013) 242–260, `arXiv:1210.6604 [hep-ex]`.

[122] The ATLAS Collaboration, *Search for third generation scalar leptoquarks in pp collisions at $\sqrt{s}$ = 7 TeV with the ATLAS detector*, JHEP **1306** (2013) 033, `arXiv:1303.0526 [hep-ex]`.

[123] The ATLAS Collaboration, *Identification of the Hadronic Decays of Tau Leptons in 2012 Data with the ATLAS Detector*, ATLAS-CONF-2013-064, CERN, Geneva, Jul, 2013. `http://cds.cern.ch/record/1562839`.

[124] The ATLAS Collaboration, *Performance of the Reconstruction and Identification of Hadronic Tau Decays in ATLAS with 2011 Data*, ATLAS-CONF-2012-142, CERN, Geneva, Oct, 2012. `http://cds.cern.ch/record/1485531`.

[125] The ATLAS Collaboration, *Determination of the tau energy scale and the associated systematic uncertainty in proton-proton collisions at $\sqrt{s}$ = 8 TeV with the ATLAS detector at the LHC in 2012*, ATLAS-CONF-2013-044, CERN, Geneva, Apr, 2013. `http://cds.cern.ch/record/1544036`.

[126] The ATLAS Collaboration, *Measurement of the b-tag Efficiency in a Sample of Jets Containing Muons with 5 fb^{-1} of Data from the ATLAS Detector*, ATLAS-CONF-2012-043, CERN, Geneva, Mar, 2012. `http://cds.cern.ch/record/1435197`.

[127] The ATLAS Collaboration, *Measuring the b-tag efficiency in a top-pair sample with 4.7 fb^{-1} of data from the ATLAS detector*, ATLAS-CONF-2012-097, CERN, Geneva, Jul, 2012. `http://cds.cern.ch/record/1460443`.

[128] The ATLAS Collaboration, *Measurement of the Mistag Rate with 5 fb^{-1} of Data Collected by the ATLAS Detector*, ATLAS-CONF-2012-040, CERN, Geneva, Mar, 2012. `http://cds.cern.ch/record/1435194`.

[129] The ATLAS Collaboration, *b-jet tagging calibration on c-jets containing D^{*+} mesons*, ATLAS-CONF-2012-039, CERN, Geneva, Mar, 2012. `http://cds.cern.ch/record/1435193`.

[130] ATLAS Collaboration, *Pileup corrections for ETmiss*, In preparation.

[131] The ATLAS Collaboration, *Performance of Missing Transverse Momentum Reconstruction in ATLAS studied in Proton-Proton Collisions recorded in 2012 at 8 TeV*, ATLAS-CONF-2013-082, CERN, Geneva, Aug, 2013. `http://cds.cern.ch/record/1570993`.

[132] The ATLAS Collaboration, *Improved luminosity determination in pp collisions at $\sqrt{s}$ = 7 TeV using the ATLAS detector at the LHC*, Eur.Phys.J. **C73** (2013) 2518, `arXiv:1302.4393 [hep-ex]`.

[133] A. Elagin, P. Murat, A. Pranko, and A. Safonov, *A New Mass Reconstruction Technique for Resonances Decaying to di-tau*, Nucl.Instrum.Meth. **A654** (2011) 481–489, `arXiv:1012.4686 [hep-ex]`.

[134] N. Metropolis, A. Rosenbluth, M. Rosenbluth, A. Teller, and E. Teller, *Equation of state calculations by fast computing machines*, J.Chem.Phys. **21** (1953) 1087–1092.

[135] The ATLAS Collaboration, *Search for the Standard Model Higgs boson in the H to $\tau^+\tau^-$ decay mode in $\sqrt{s} = 7$ TeV pp collisions with ATLAS*, JHEP **1209** (2012) 070, `arXiv:1206.5971 [hep-ex]`.

[136] B. P. Kersevan and E. Richter-Was, *The Monte Carlo event generator AcerMC version 2.0 with interfaces to PYTHIA 6.2 and HERWIG 6.5*, `arXiv:hep-ph/0405247 [hep-ph]`.

[137] T. Binoth, M. Ciccolini, N. Kauer, and M. Kramer, *Gluon-induced W-boson pair production at the LHC*, JHEP **0612** (2006) 046, `arXiv:hep-ph/0611170 [hep-ph]`.

[138] LHC Higgs Cross Section Working Group, *Handbook of LHC Higgs Cross Sections: 2. Differential Distributions*, `arXiv:1201.3084 [hep-ph]`.

[139] J. Alwall, S. Frixione, V. Hirschi, F. Maltoni, et al., *To appear*, .

[140] *aMC@NLO*, `http://amcatnlo.web.cern.ch/amcatnlo/`.

[141] `http://theory.fi.infn.it/grazzini/codes.html`.

[142] G. Bozzi, S. Catani, D. de Florian, and M. Grazzini, *Transverse-momentum resummation and the spectrum of the Higgs boson at the LHC*, Nucl.Phys. **B737** (2006) 73–120, `arXiv:hep-ph/0508068 [hep-ph]`.

[143] D. de Florian, G. Ferrera, M. Grazzini, and D. Tommasini, *Transverse-momentum resummation: Higgs boson production at the Tevatron and the LHC*, JHEP **1111** (2011) 064, `arXiv:1109.2109 [hep-ph]`.

[144] E. Bagnaschi, G. Degrassi, P. Slavich, and A. Vicini, *Higgs production via gluon fusion in the POWHEG approach in the SM and in the MSSM*, JHEP **1202** (2012) 088, `arXiv:1111.2854 [hep-ph]`.

[145] The ATLAS Collaboration, *$Z \to \tau\tau$ cross section measurement in proton-proton collisions at 7 TeV with the ATLAS experiment*, ATLAS-CONF-2012-006, CERN, Geneva, Feb, 2012. `https://cdsweb.cern.ch/record/1426991`.

[146] The ATLAS Collaboration, *Charged particle multiplicities in pp interactions at $\sqrt{s} = 0.9$ and 7 TeV in a diffractive limited phase-space measured with the ATLAS detector at the LHC and new PYTHIA6 tune*, ATLAS-CONF-2010-031, 2010. `http://cds.cern.ch/record/1277665`.

[147] A. Sherstnev and R. Thorne, *Parton Distributions for LO Generators*, Eur.Phys.J. **C55** (2008) 553–575, `arXiv:0711.2473 [hep-ph]`.

[148] The ATLAS Collaboration, *Data-Quality Requirements and Event Cleaning for Jets and Missing Transverse Energy Reconstruction with the ATLAS Detector in Proton-Proton Collisions at a Center-of-Mass Energy of $\sqrt{s} = 7$ TeV*, ATLAS-CONF-2010-038. `http://cds.cern.ch/record/1277678`.

[149] The ATLAS Collaboration, *Muon reconstruction efficiency in reprocessed 2010 LHC proton-proton collision data recorded with the ATLAS detector*, ATLAS-CONF-2011-063, CERN, Geneva, Apr, 2011. `http://cds.cern.ch/record/1345743`.

[150] The ATLAS Collaboration, *Measurement of the $W \rightarrow l\nu$ and $Z/\gamma* \rightarrow ll$ production cross sections in proton-proton collisions at $\sqrt{s} = 7$ TeV with the ATLAS detector*, JHEP **12** (2010) 060.

[151] The ATLAS Collaboration. ATLAS-CONF-2011-077, `http://cdsweb.cern.ch/record/1353226`, 2011.

[152] The ATLAS Collaboration, *Measurement of inclusive jet and dijet cross sections in proton-proton collisions at 7 TeV centre-of-mass energy with the ATLAS detector*, Eur. Phys. J. **C71** (2011) 1512.

[153] L. Garren and P. Lebrun, *StdHep 5.06.01 - Monte Carlo Standarization at FNAL*, .

[154] The ATLAS Collaboration. ATLAS-CONF-2011-011, `http://cdsweb.cern.ch/record/1334563`, 2011.

[155] P. M. Nadolsky et al., *Implications of CTEQ global analysis for collider observables*, Phys. Rev. **D78** (2008) 013004.

[156] `http://hepforge.cedar.ac.uk/lhapdf/`.

[157] M. Whalley, D. Bourilkov, and R. Group, *The Les Houches accord PDFs (LHAPDF) and LHAGLUE*, `arXiv:hep-ph/0508110 [hep-ph]`.

[158] The H1 and ZEUS Collaborations, *Combined Measurement and QCD Analysis of the Inclusive ep Scattering Cross Sections at HERA*, JHEP **01** (2010) 109.

[159] L. Lyons, D. Gibaut, and P. Clifford, *How to combine correlated edtimates of a single physical quantity*, Nucl. Instrum. Meth. **A270** (1988) 110.

[160] A. Valassi, *Combining correlated measurements of several different physical quantities*, Nucl. Instrum. Meth. **A500** (2003) 391–405.

[161] The CMS Collaboration, *Measurement of the Inclusive Z Cross Section via Decays to Tau Pairs in pp Collisions at $\sqrt{s} = 7$ TeV*, JHEP **1108** (2011) 117, `arXiv:1104.1617 [hep-ex]`.

[162] G. Aad, M. Ackers, F. Alberti, M. Aleppo, G. Alimonti, et al., *ATLAS pixel detector electronics and sensors*, JINST **3** (2008) P07007.

[163] T. Lari and F. Ragusa, *Study of silicon pixel sensors for the ATLAS detector*. PhD thesis, Milan U., Geneva, 2001. Presented on 12 Dec 2001.

[164] A. Arelli-Maffioli, F. Ragusa, C. Troncon, and T. Lari, *Studio di un algoritmo lineare di ricostruzione analogica della posizione per il rivelatore a pixel di ATLAS*. PhD thesis, Milano U., Milano, 2007. Presented on 24 Apr 2007.

[165] S. Montesano and F. Ragusa, *Commissioning of the tracking system in the ATLAS detector*. PhD thesis, Milano, Università degli Studi di Milano, Milano, 2010. Presented on 21 Jan 2010.

[166] M. Aleppo, *A Measurement of Lorentz angle of radiation hard pixel sensors*, Nucl.Instrum.Meth. **A465** (2000) 108–111, `arXiv:physics/0012050 [physics]`.

[167] ATLAS Pixel Collaboration, A. Andreazza, *Progresses on the ATLAS pixel detector*, Nucl.Instrum.Meth. **A461** (2001) 168–171.

[168] I. Gorelov, G. Gorfine, M. Hoeferkamp, S. Seidel, A. Ciocio, et al., *A measurement of Lorentz angle and spatial resolution of radiation hard silicon pixel sensors*, Nucl.Instrum.Meth. **A481** (2002) 204–221.

[169] F. Ragusa, *Recent developments in the ATLAS pixel detector*, Nucl.Instrum.Meth. **A447** (2000) 184–193.

[170] C. Peterson, T. Rognvaldsson, and L. Lonnblad, *JETNET 3.0: A Versatile artificial neural network package*, Comput.Phys.Commun. **81** (1994) 185–220.

[171] The ATLAS Collaboration, *Determination of the tau energy scale and the associated systematic uncertainty in proton-proton collisions at $\sqrt{s} = 7$ TeV with the ATLAS detector at the LHC in 2011*, ATLAS-CONF-2012-054, 2012. `http://cds.cern.ch/record/1453781`.

[172] C. Pizio, *Studio delle reazioni $Z \to \tau\tau$ con i primi dati di ATLAS ad LHC. Prova generale del canale $A/H \to \tau\tau$*. Master thesis, Milano, Università degli Studi di Milano, Milano, 2007.

[173] S. M. Consonni, *Search for $Z \to \tau\tau$ events in pp collisions at a centre of mass energy of 7 TeV with the ATLAS detector*. Master thesis, Milano, Università degli Studi di Milano, Milano, 2010.

[174] The ATLAS Collaboration, *Muon Momentum Resolution in First Pass Reconstruction of pp Collision Data Recorded by ATLAS in 2010*, ATLAS-CONF-2011-003. `http://cds.cern.ch/record/1326960`.

[175] The ATLAS Collaboration, *Determination of the muon reconstruction efficiency in ATLAS at the Z resonance in proton-proton collisons at $\sqrt{s} = 7$ TeV*, ATLAS-CONF-2011-008. `http://cds.cern.ch/record/1330715`.

[176] The ATLAS Collaboration, *Performance of Missing Transverse Momentum Reconstruction in ATLAS with 2011 Proton-Proton Collisions at $\sqrt{s} = 7$ TeV*, ATLAS-CONF-2012-101, CERN, Geneva, Jul, 2012. `http://cds.cern.ch/record/1463915`.

[177] ATLAS Collaboration, *Selection of jets produced in proton-proton collisions with the ATLAS detector using 2011 data*, ATLAS-CONF-2012-020, CERN, Geneva, Mar, 2012. `http://cds.cern.ch/record/1430034`.

[178] The ATLAS Collaboration, *Performance of the Reconstruction and Identification of Hadronic Tau Decays with ATLAS*, ATLAS-CONF-2011-152. `http://cds.cern.ch/record/1398195`.

[179] ATLAS Collaboration Collaboration, *Muon Momentum Resolution in First Pass Reconstruction of pp Collision Data Recorded by ATLAS in 2010*, ATLAS-CONF-2011-046, CERN, Geneva, Mar, 2011. `https://cds.cern.ch/record/1338575`.

[180] The ATLAS Collaboration, *Private communication*, .

[181] The ATLAS Collaboration, *Search for the Standard Model Higgs boson in $H \to \tau\tau$ decays in proton-proton collisions with the ATLAS detector*, ATLAS-CONF-2012-160, CERN, Geneva, Nov, 2012. `http://cds.cern.ch/record/1493624`.

[182] I. W. Stewart and F. J. Tackmann, *Theory Uncertainties for Higgs and Other Searches Using Jet Bins*, Phys.Rev. **D85** (2012) 034011, `arXiv:1107.2117 [hep-ph]`.

[183] S. Catani and M. Grazzini, *An NNLO subtraction formalism in hadron collisions and its application to Higgs boson production at the LHC*, Phys.Rev.Lett. **98** (2007) 222002, `arXiv:hep-ph/0703012 [hep-ph]`.

[184] M. Grazzini, *NNLO predictions for the Higgs boson signal in the $H \to WW \to l\nu l\nu$ and $H \to ZZ \to 4l$ decay channels*, JHEP **0802** (2008) 043, `arXiv:0801.3232 [hep-ph]`.

[185] G. Cowan, K. Cranmer, E. Gross, and O. Vitells, *Asymptotic formulae for likelihood-based tests of new physics*, Eur.Phys.J. **C71** (2011) 1554, `arXiv:1007.1727 [physics.data-an]`.

[186] `https://twiki.cern.ch/twiki/bin/view/RooStats/WebHome`.

[187] A. L. Read, *Presentation of search results: the CL s technique*, Journal of Physics G: Nuclear and Particle Physics **28** (2002) no. 10, 2693. `http://stacks.iop.org/0954-3899/28/i=10/a=313`.

Further details of H $\to \tau^+\tau^-$ cut-based analysis systematics

Further details on the systematics in the $H \to \tau^+\tau^-$ analysis described in Chapter 7 are given. Only systematics appearing in the final fit model are shown. The systematics appearing in the histogram labels indicate:

- `ATLAS_LUMI_2012`: luminosity uncertainty for 2012 data, described in Section 7.9.1;

- `sys_PU_rescaling`: uncertainty on the pile-up conditions described in Section 7.9.2;

- `sys_sf_el`: electron trigger and identification efficiencies uncertainties described in Sections 7.9.3 and 7.9.4;

- `sys_sf_mu`: electron trigger and identification efficiencies uncertainties described in Sections 7.9.3 and 7.9.5;

- `ElEnResSys` and `ElES_PS`, `ElES_R12`, `ElES_Zee`: electron energy resolution and scale respectively, described in Section 7.9.4;

- `MuSys`: muon momentum resolution and scale, described in Section 7.9.5;

- `sys_sf_tau`: $\tau_{\text{had-vis}}$ identification efficiency uncertainties described in Section 7.9.6;

- `sys_sf_tau_el`: electron to $\tau_{\text{had-vis}}$ fake rate uncertainty described in Section 7.9.6;

- `TES`: $\tau_{\text{had-vis}}$ energy scale systematic uncertainty described in Section 7.9.6;

- `JER`: jet energy resolution uncertainties described in Section 7.9.7;

- `JES_*`: jet energy scale uncertainties described in Section 7.9.7, names are coherent with does used in the text;

- `JVF`: *JVF* associated systematic uncertainty as described in Section 7.9.7;

- `bjet_sys_b`, `bjet_sys_c`, `bjet_sys_m`: systematic uncertainties on b-tagging efficiencies and mis-tag rates as described in Section 7.9.7;

- `METResSys` and `METScaleSys`: $E_{\text{T}}^{\text{miss, soft}}$ term resolution and scale systematic uncertainties as described in Section 7.9.8;

- `METResSys` and `METScaleSys`: $E_\mathrm{T}^{\mathrm{miss,\,soft}}$ term resolution and scale systematic uncertainties as described in Section 7.9.8;

- `isolemb` and `muonsub`: systematic uncertainties due to muon isolation requirements and muon energy subtraction affecting the embedding procedure and described in Section 7.9.9;

- `r_qcd` systematic uncertainty on r_QCD described in Section 7.9.10;

- `k_wj_*`: uncertainties on the normalisation of the $W +$ jets background described in Section 7.9.10;

- `k_Top*`: uncertainties on the normalisation of the top background described in Section 7.9.10;

- `k_zll_jt`: uncertainties on the normalisation of the $Z \rightarrow ll + \mathrm{jet}(\rightarrow \tau_\mathrm{had\text{-}vis})$ background described in Section 7.9.10;

- `ATLAS_ANA_LH12_fakes_vbf`: systematic uncertainty on backgrounds due to fake $\tau_\mathrm{had\text{-}vis}$ in the *VBF* category described in Section 7.9.10;

- `QCDscale_V`: QCD scale uncertainty for $W +$ jets and $Z +$ jets backgrounds described in Section 7.9.11;

- `QCDscale_qqH`: QCD scale uncertainty for VBF Higgs signal described in Section 7.9.11;

- `QCDscale_ggH*`: QCD scale uncertainties for ggF Higgs signal described in Section 7.9.11;

- `QCDscale_VV`: QCD scale uncertainty for the diboson background described in Section 7.9.11;

- `Gen_Qmass_ggH`: uncertainty on heavy quark mass effect on the description of the Higgs boson transverse momentum, described in Section 7.9.11;

- `ATLAS_UE_gg` and `ATLAS_UE_qq`: underlying event uncertainty described in Section 7.9.11;

- `pdf_*` PDFs uncertainty described in Section 7.9.11

- `ATLAS_BR_tautau`: uncertainty on the $H \rightarrow \tau^+\tau^-$ branching ratio described in Section 7.9.11;
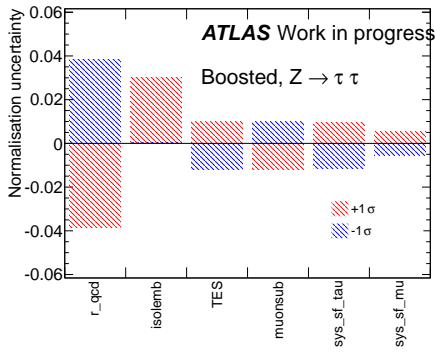
(a)
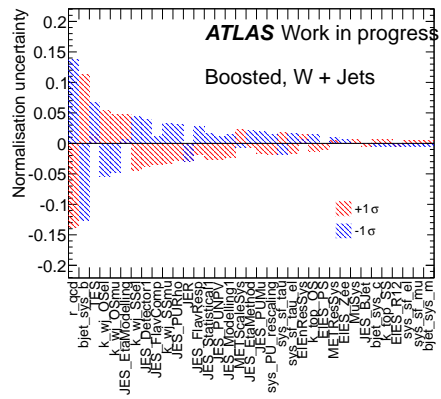
(b)
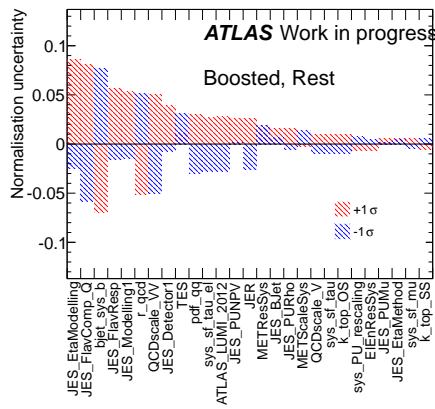
(c)

Figure A.1: Normalization systematics in the *boosted* category for background components.
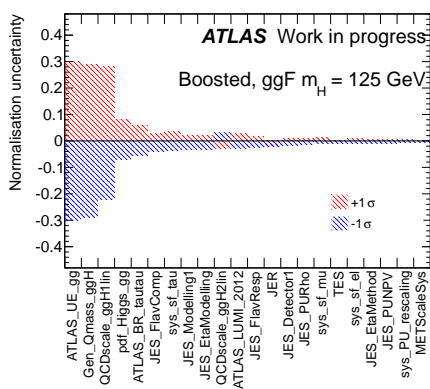
(a)
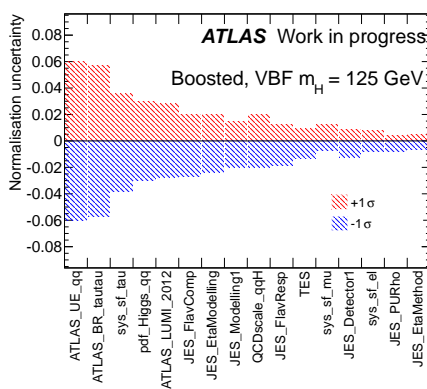
(b)
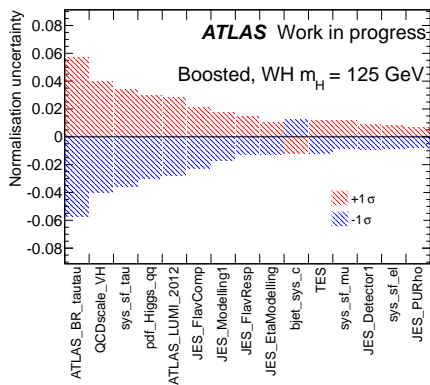
(c)
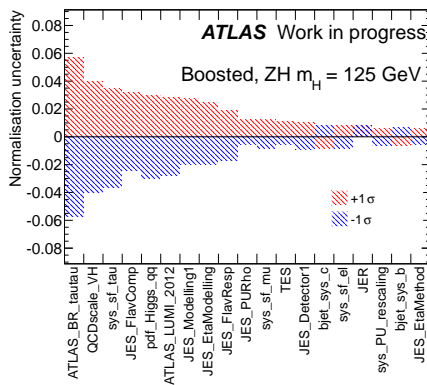
(d)

Figure A.2: Normalization systematics in the *boosted* category for signal ($m_H = 125\,\text{GeV}$) components.

(a)

(b)

(c)
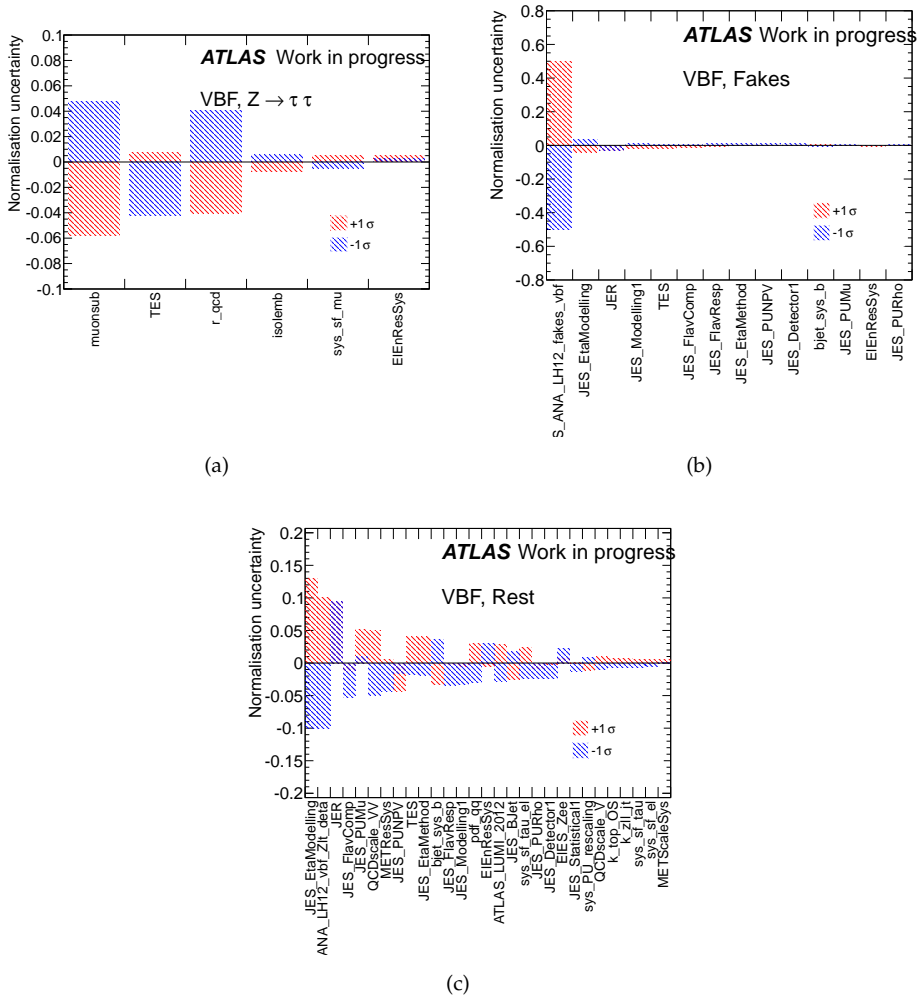
Figure A.3: Normalization systematics in the *VBF* category for background components.
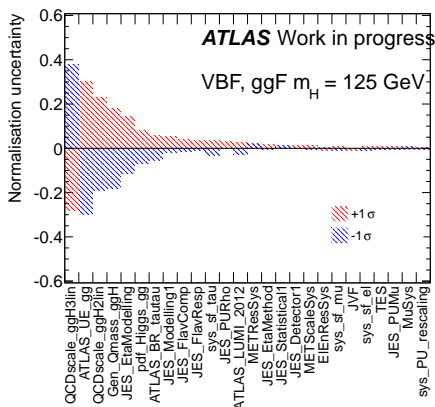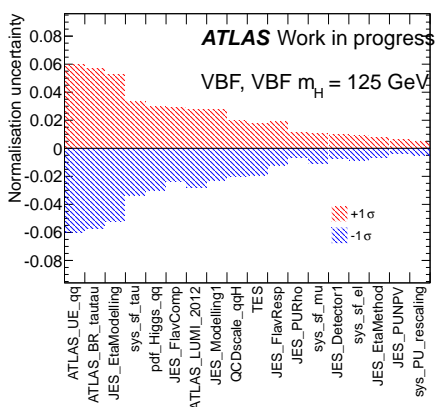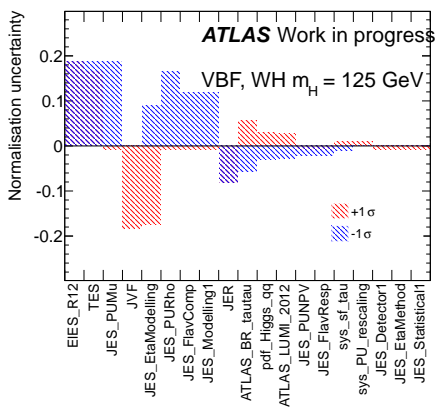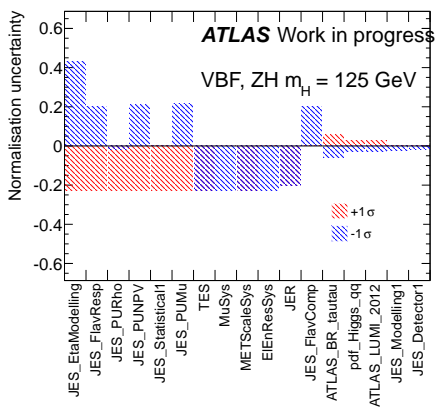
Figure A.4: Normalization systematics in the *VBF* category for signal ($m_H = 125\,\text{GeV}$) components.
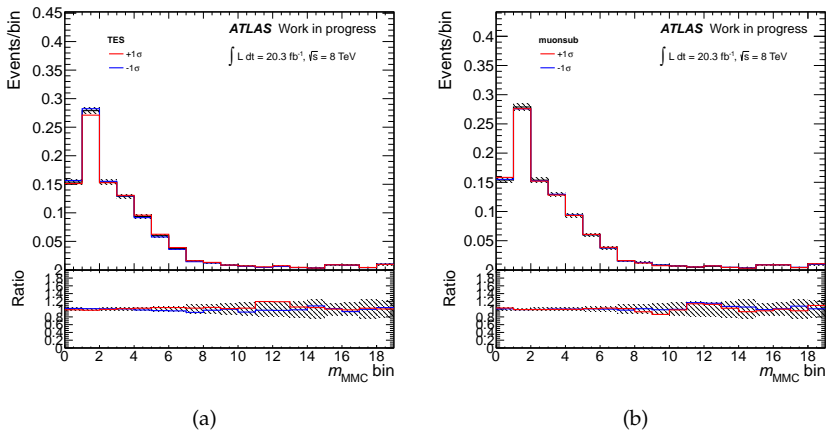
Figure A.5: Shape systematics for the $Z \to \tau^+\tau^-$ background component in the *boosted* category.
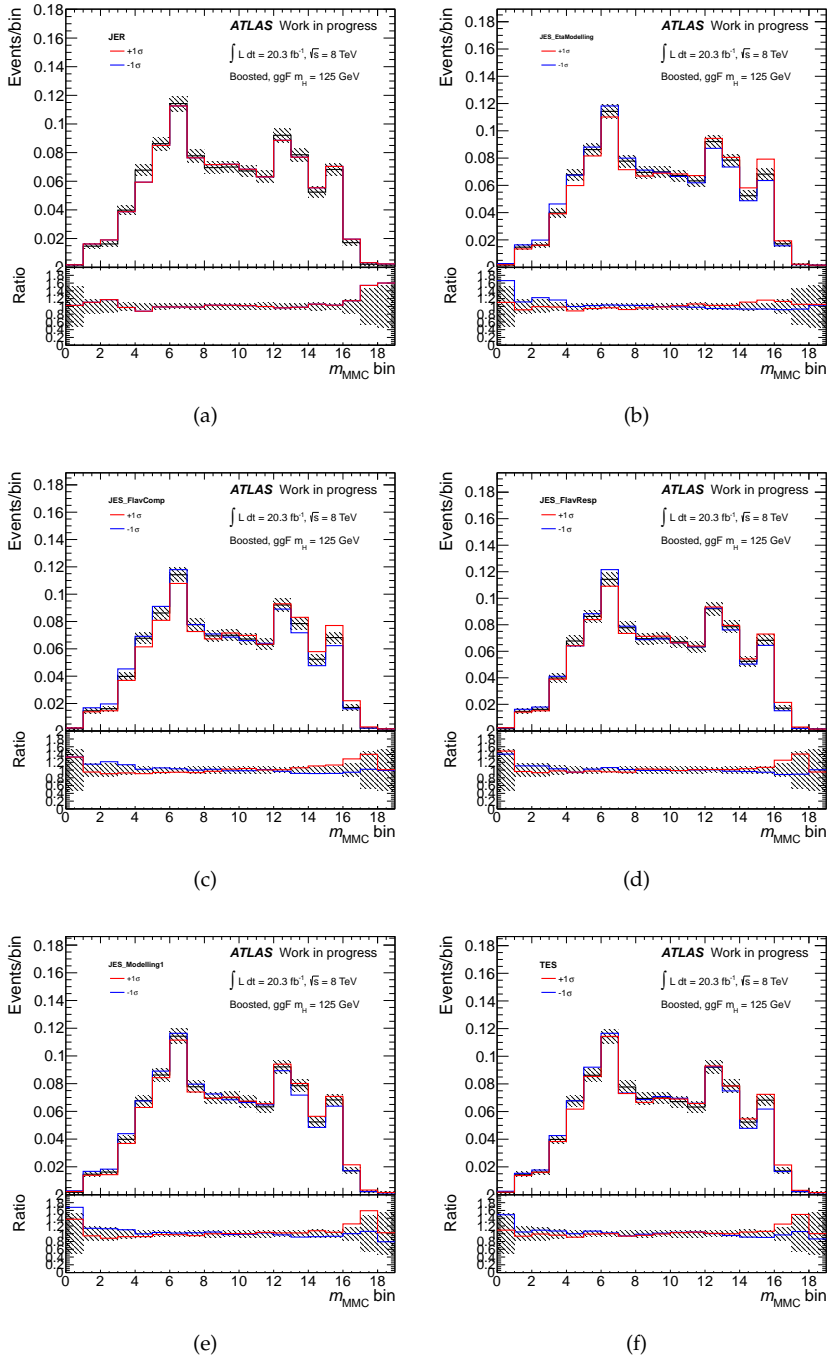
Figure A.6: Shape systematics for the ggF signal component ($m_H = 125\,\text{GeV}$) in the *boosted* category.

(a)

(b)

(c)

(d)

(e)
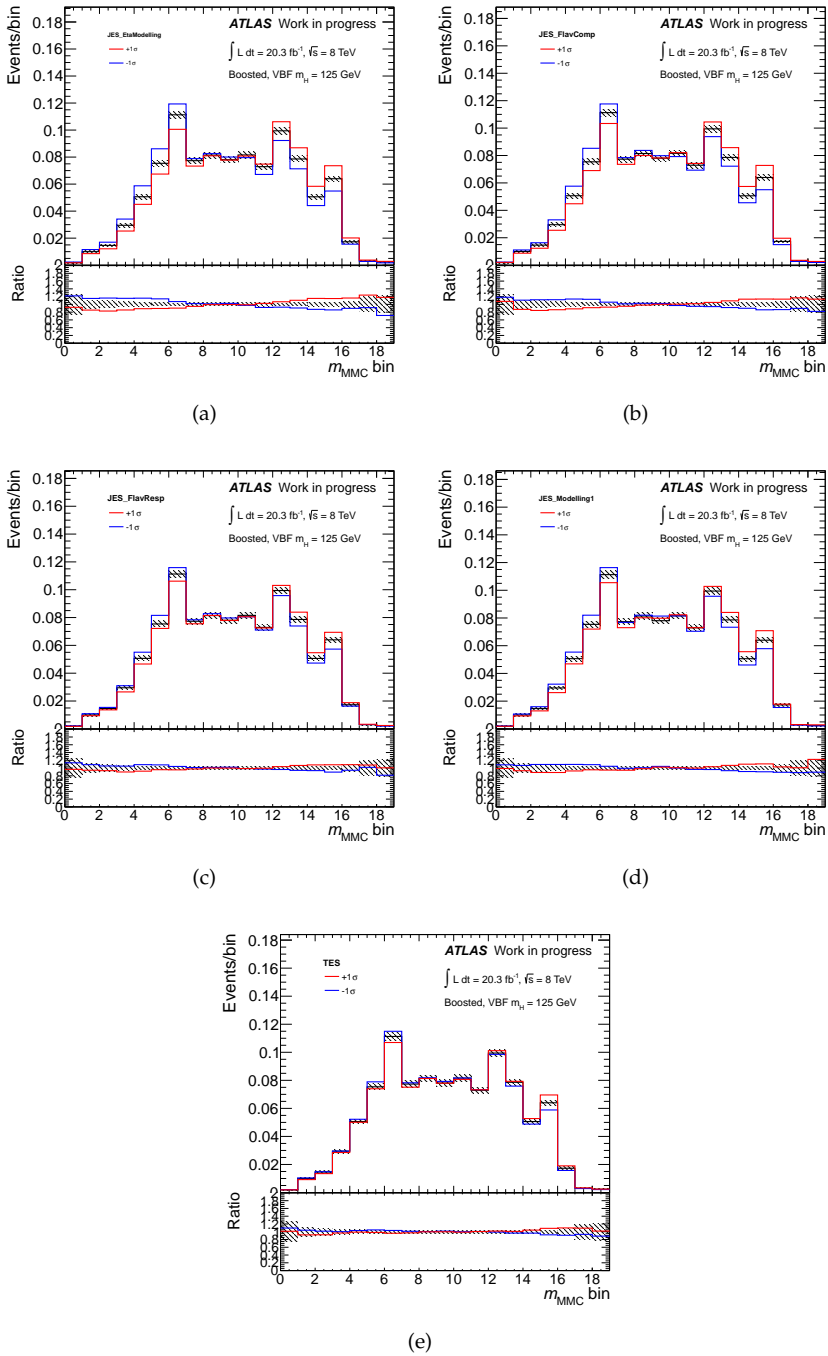
Figure A.7: Shape systematics for the VBF signal component ($m_H = 125\,\text{GeV}$) in the *boosted* category.

(a)

(b)

(c)

(d)

(e)
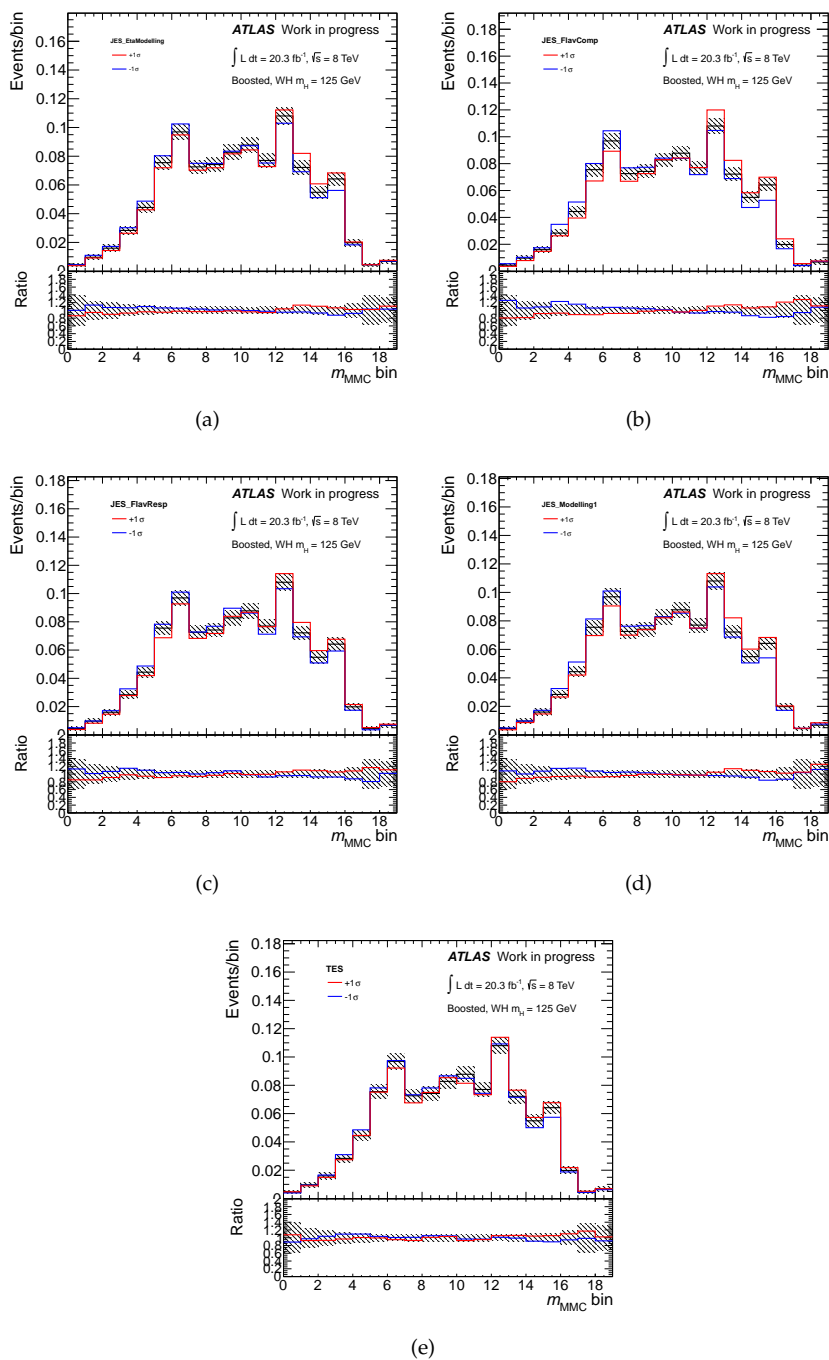
Figure A.8: Shape systematics for the WH signal component ($m_H = 125\,\text{GeV}$) in the *boosted* category.
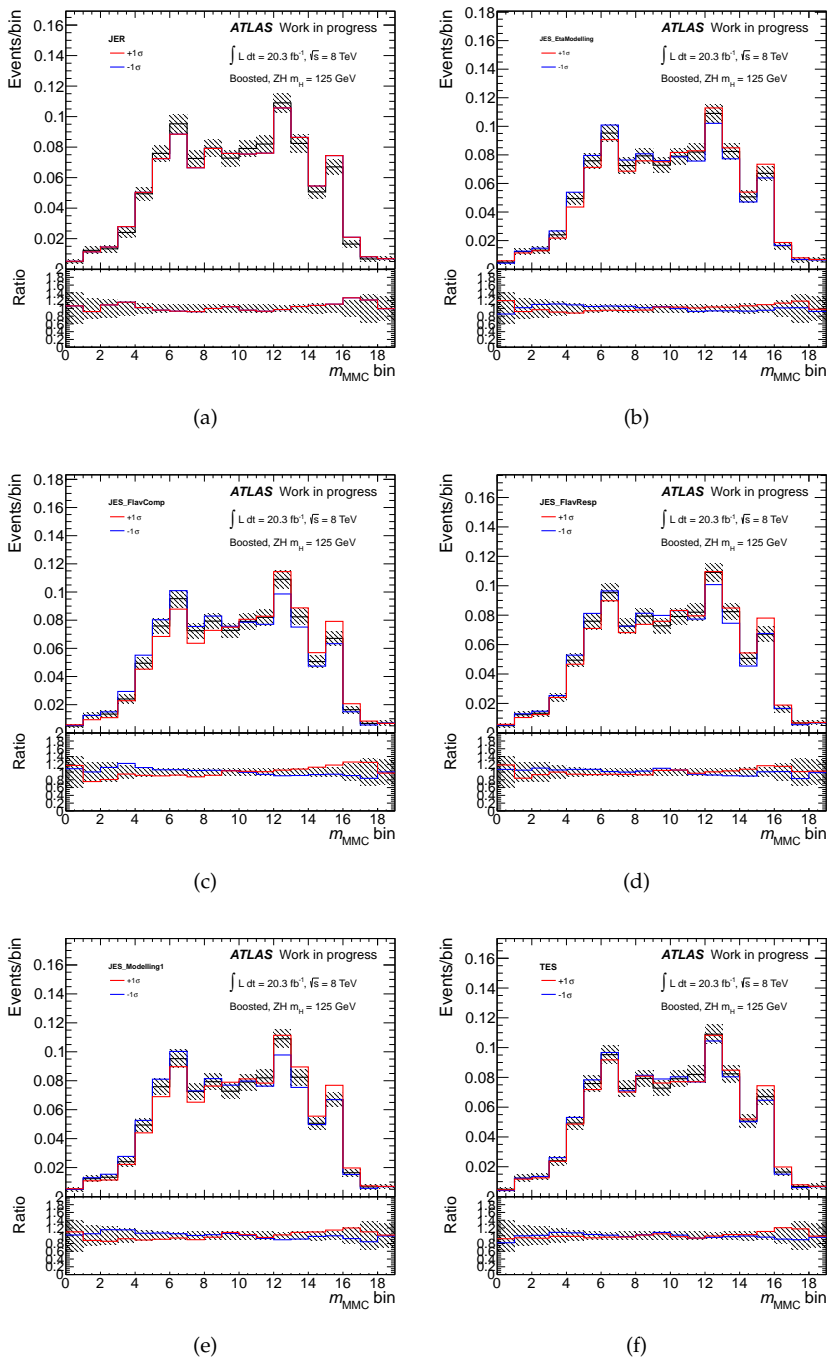
Figure A.9: Shape systematics for the ZH signal component ($m_H = 125\,\text{GeV}$) in the *boosted* category.

(a)

(b)

(c)

(d)

(e)
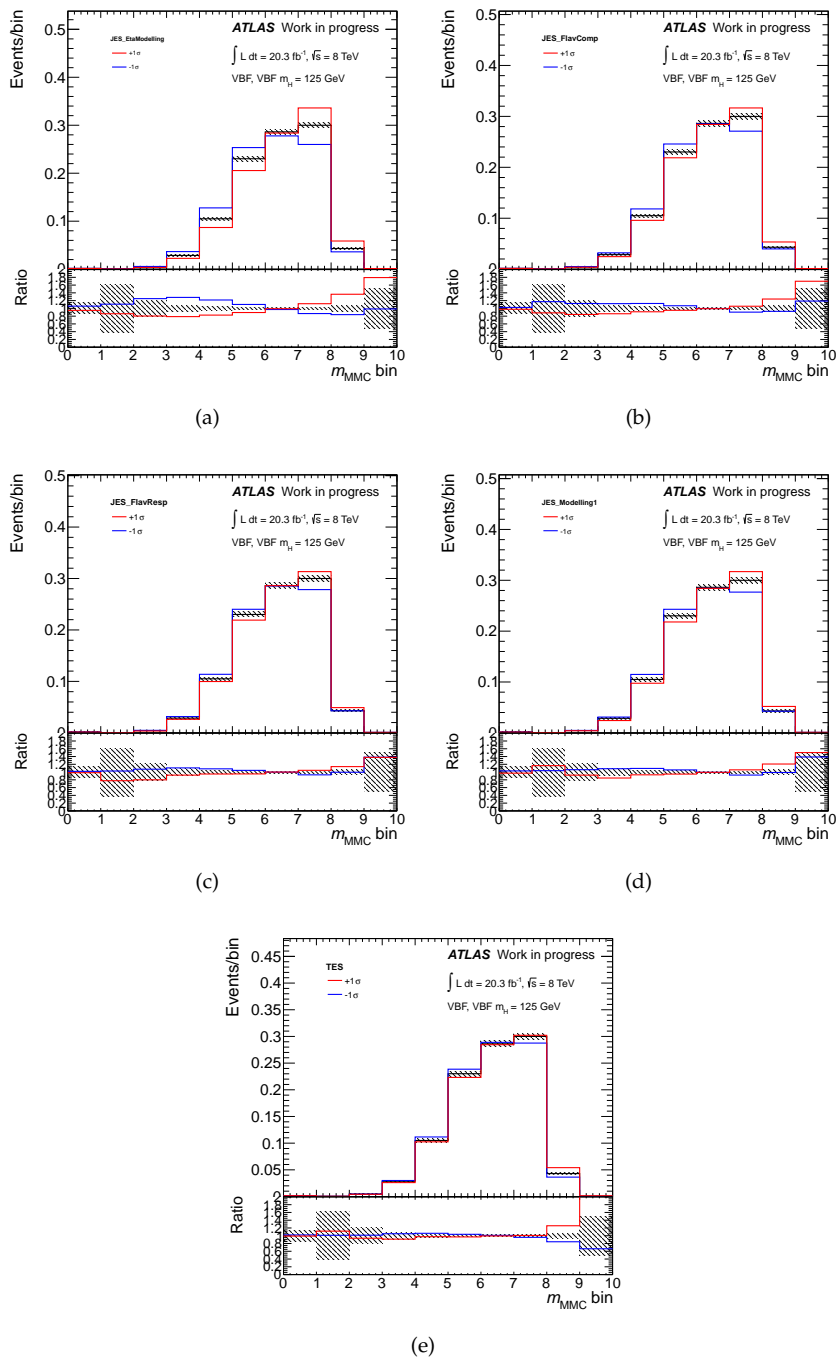
Figure A.10: Shape systematics for the VBF signal component ($m_H = 125\,\text{GeV}$) in the *VBF* category.

(a)

(b)

(c)

(d)
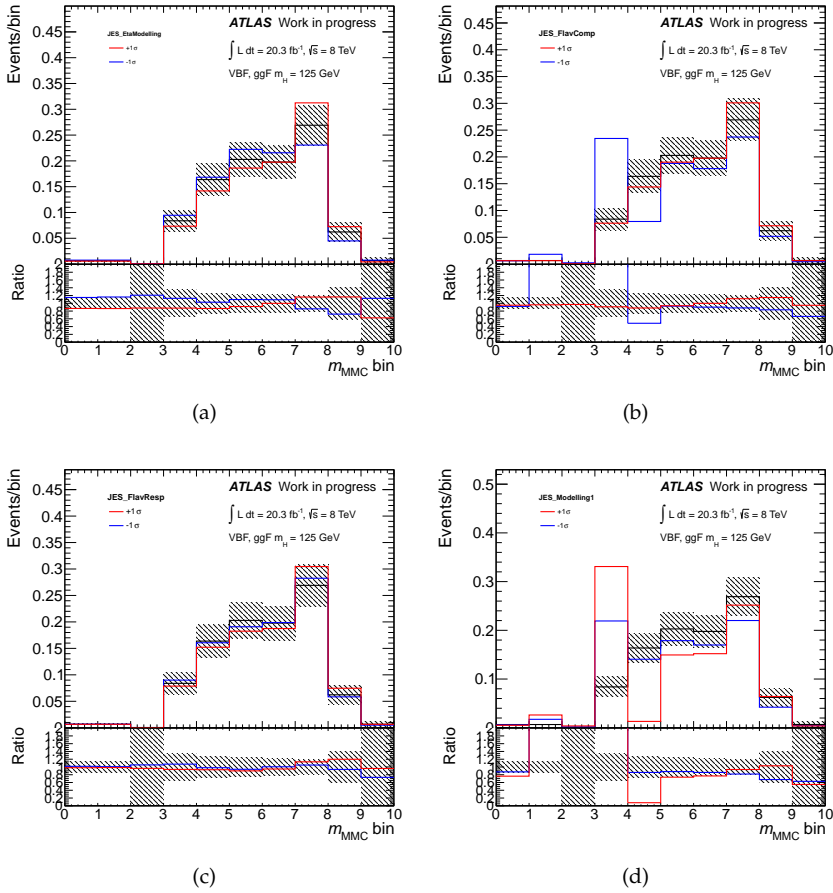
Figure A.11: Shape systematics for the ggF signal component ($m_H = 125$ GeV) in the *VBF* category.

(a)

(b)

(c)

(d)

(e)
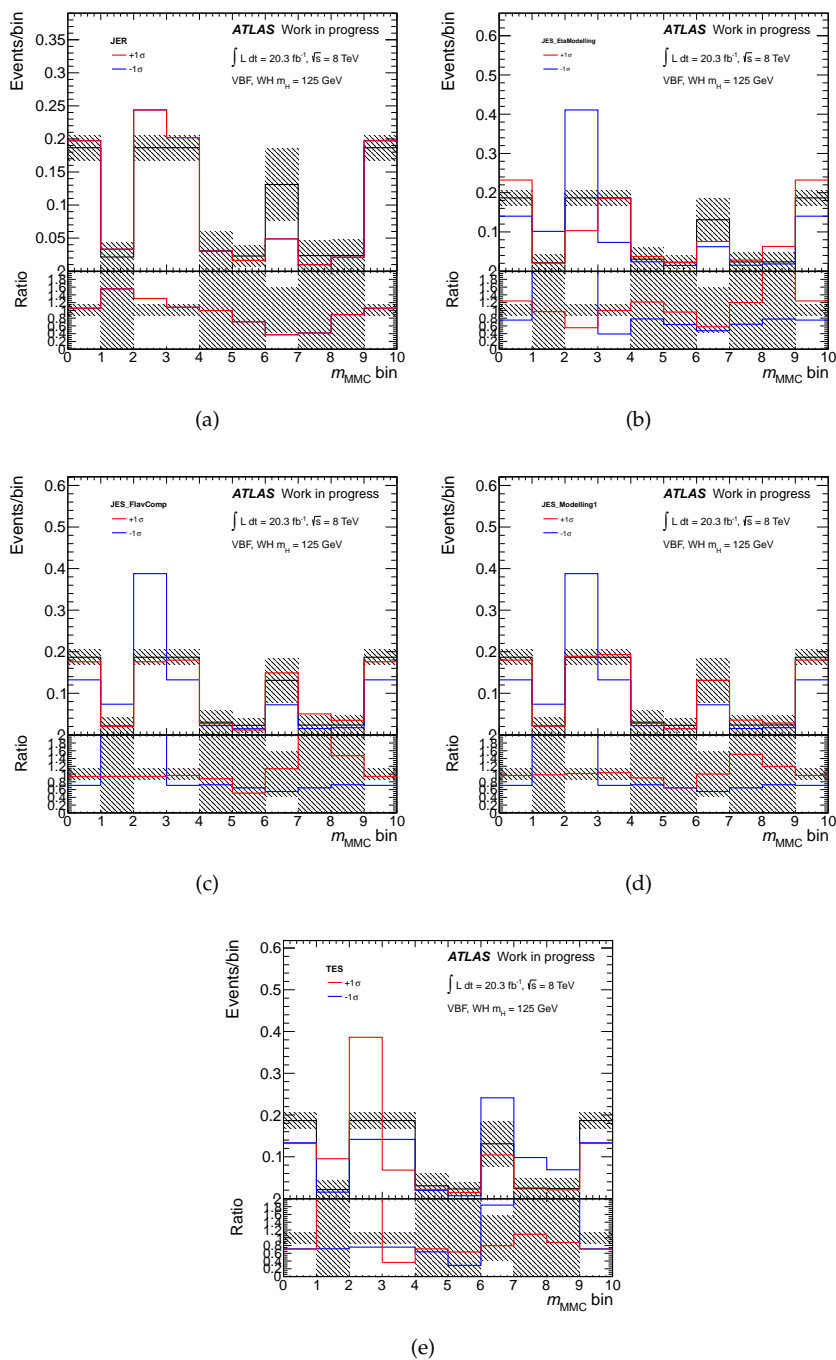
Figure A.12: Shape systematics for the WH signal component ($m_H = 125\,\text{GeV}$) in the *VBF* category.

Figure A.13: Shape systematics for the ZH signal component ($m_H = 125\,\text{GeV}$) in the *VBF* category.

List of Figures

List of Tables

Acknowledgments

There are many people I would like to thank at the end of this work, and my main fear is that I am forgetting somebody that should really be in the acknowledgments.

I would like first of all to thanks the Milano group, starting with Donatella and Attilio for their supervision and patience in reviewing all of this thesis. Thanks to Donatella and the E_T^{miss} girls, Silvia, Rosa and Caterina for the insight on E_T^{miss} and hadronic stuff in general and for discussion on many different topics. And thanks to Attilio for sharing his Pixel omniscience, for the fruitful discussions and anti-depressive candies. Among all of the people in the Milano group I would like to thank in particular Chiara, Francesco, Leonardo, Luciano and Mauro, who have always been very available, for every kind of need, ranging from bureaucracy to physics and for their support, Rosa, Ruggero, Federico and Ilaria, with whom we shared a lot of time while in Genéve. I would like to thank the system administrators for the patience during the hard times with the disks.

I would like to thank people who taught courses both at UniMi and at ESHEP, in particular Attilio, Leonardo, Lucio, Matteo, Peter, John, Riccardo, Gino, Harrison, Gigi and Maurizio.

There are many people who I would like to thank from the $Z \to \tau^+\tau^-$ cross-section analysis. Most importantly Susanne, who has really been a teacher to me and for her friendship. I would like to thank Elias and Anna for their great analysis coordination, Marcin and Ulla for the help and discussion about theory systematics, Claire and Frank for discussions about generators, Kevin and Jon for the very fruitful discussions during the analysis finalisation.

I would like to thank all of the people from the Pixel Clustering Task Force, in particular Andy, Heather and Fares. A special thank to Francesco, that goes to Franca and the children as well, not only for the discussions on physics but also for basically adopting me during the time in Genéve. Staying on Pixels, thanks a lot to all of the people I met from DQ and operations, especially to Lisa, Markus, Kerstin and Mark.

From the tau scale analysis I would like to thanks first of all David, Katy and Elisabetta, with whom I shared this great adventure, thanks to Matteo as well. I would like to thanks a lot Will for all the help and support during difficult times, Stan and Stefania for their great leadership of the tau working group. Thanks to Marco, Francesco, Amelia for continuing the work afterwards.

I thank all of the people in HSG4 from all of the channels. In particular I would like to thank, in random order, Koji, Romain, Thomas, Michel, Jana, Gui, KG, Keita, Yuki, John, Carl and Daniele. Thanks to Dimitris for his efforts in working as a group and friendship, to Alex for his kindness and for the work together on the twiki, to Nils for the very useful discussions on physics and life. Thanks to Lidia, for her friendship and for hosting me for so long when I arrived in Genéve and to Elisabetta, for really being a friend in the most difficult moments during the last year. Thanks to Carlo for his crucial help, Alessio for the passion and work on theory, Rosa for help with the statistics part. I would like to thank David and Sasha for sharing ideas and discussions on MMC, Michael, Bogdan and Richard for the fruitful discussions on jets and TJ and Paolo on E_T^{miss}. Thanks to HSG4 conveners, Stan, Sasha, Elias and Sinead, for taking the group through all of the difficulties of the $H \to \tau^+\tau^-$ analysis, and to Higgs conveners too, especially Marumi for his suggestions, his attentiveness to persons and for accepting to review this thesis.

Thanks to Stan and Giacomo for their presence, support and friendly suggestions throughout these three years.

I would like to thank all of the people in my analyses editorial boards and the persons that carefully reviewed posters, talks and proceedings. I would like to thank the many people who gave me a lot of opportunities to present the work of entire groups to the collaboration or at conferences and to be at CERN for one year.

There are many friends I would like to thank for accompanying me even during difficult times. I am not going to list them all, I would like to mention Simone, who took care of me and fed me so many times in Genéve, Caterina, whose friendship has been fundamental, Maria, Giulia and Marta. Thanks to Agostino and all my friends' children, because with their simplicity they always show what is worth in life.

I would like to thank my family, Giorgio, Daniela and my brother Simeone for all what they have done for me, for always being supportive, for standing me even in the worse moments and for the passion they transmitted to me. Finally I would like to thank Davide for sharing with me these three years, in all of the joyful and sad moments and for always introducing a new perspective on circumstances. Thanks for deciding to take the risk to share all the life with me.